FEDERAL UNIVERSITY OF SÃO CARLOS
CENTER FOR EXACT SCIENCES AND TECHNOLOGY
GRADUATE PROGRAM IN MATERIALS SCIENCE AND ENGINEERING

DESIGN, FABRICATION AND CHARACTERIZATION OF Fe-BASED BULK METALLIC GLASS COMPOSITES BY ADDITIVE MANUFACTURING

Aylanna Priscila Marques de Araújo

São Carlos-SP
2025

FEDERAL UNIVERSITY OF SÃO CARLOS
CENTER FOR EXACT SCIENCES AND TECHNOLOGY
GRADUATE PROGRAM IN MATERIALS SCIENCE AND ENGINEERING

DESIGN, FABRICATION AND CHARACTERIZATION OF Fe-BASED BULK METALLIC GLASS COMPOSITES BY ADDITIVE MANUFACTURING

Aylanna Priscila Marques de Araújo

Thesis presented to the Graduate Program in Materials Science and Engineering as a partial requirement to obtain the title of DOCTOR IN MATERIALS SCIENCE AND ENGINEERING

Supervisor: Prof. Dr. Piter Gargarella
Funding agency: CNPq process n°.:141249/2020-0 (01/03/2020 to 31/03/2021); FAPESP process n°.: 2020/07692-9 (31/03/2021 to 31/10/2023 and 01/11/2024 to 31/03/2025) and FAPESP/BEPE process n°.: 2022/12136-3 (01/11/2023 to 31/10/2024).

São Carlos-SP
2025

VITAE

Master in Materials Science and Engineering – Federal University of São Carlos

(2020)

Bachelor in Materials Engineering – Federal University of Campina Grande – Paraíba

(2017)

UNIVERSIDADE FEDERAL DE SÃO CARLOS

Centro de Ciências Exatas e de Tecnologia
Programa de Pós-Graduação em Ciência e Engenharia de Materiais

Folha de Aprovação

Defesa de Tese de Doutorado da candidata Aylanna Priscila Marques de Araújo, realizada em 09/06/2025.

Comissão Julgadora:

Prof. Dr. Piter Gargarella (UFSCar)

Prof. Dr. Claudio Shyinti Kiminami (UFSCar)

Prof. Dr. Claudemiro Bolfarini (UFSCar)

Prof. Dr. Juliano Soyama (UNICAMP)

Prof. Dr. Marcelo Falcão de Oliveira (USP)

O Relatório de Defesa assinado pelos membros da Comissão Julgadora encontra-se arquivado junto ao Programa de Pós-Graduação em Ciência e Engenharia de Materiais.

ACKNOWLEDGMENTS

I would like to express my gratitude to my supervisor, Prof. Dr. Piter Gargarella, who, over the years, has provided me with knowledge, opportunities, and genuine support when I needed it most.

My sincere thanks also go to Prof. Dr. Jürgen Eckert from the Erich Schmid Institute of Materials Science (ESI) of the Austrian Academy of Sciences – Montanuniversität Leoben, for the opportunity to carry out part of this work in Leoben, Austria. I am grateful to all the wonderful people I had the luck to meet at ESI/Leoben: Dr. Parthiban, Dr. Lidija, Dr. Fereshteh, Dr. Megan, Dr. Florian, Dr. Eray, Huanqing, Lei, Nicole, Alan, Marco, Felix, Sabine, Philipp, Isabela, Carol, and Pastor João.

I would like to thank Prof. Kiminami for all his support during my PhD.

I would like to thank the São Paulo Research Foundation (FAPESP) for the financial support that made this study possible, under the following grants: n°. 2020/07692-9 and n°. 2022/12136-3 (BEPE/FAPESP).

Additionally, I would like to thank to the Conselho Nacional de Desenvolvimento Científico e Tecnológico - Brasil/CNPq, under the process n°.:141249/2020-0.

This study was financed in part by the Coordenação de Aperfeiçoamento de Pessoal de Nível Superior - Brasil (CAPES) - Finance Code 001.

Many thanks to all my colleagues, professors, laboratory technicians, and other university staff at UFSCar. I also acknowledge the facilities of LCE/DEMa/UFSCar and CCDM/DEMa/UFSCar.

I am especially grateful to my friends – Adriel, Gabriel, Sarah, Ivero, Elenara, Geovana, Talita, Erlifas, Bruno, Vitor, Diogo, and Nair – and my family – Aguinaldo, Marinalva, Alan, Ana Maria, Roselaine, and Oscar.

Most importantly, I would like to thank the two loves of my life, my husband Jaderson and my daughter Yanna, for their endless encouragements and support. You have been, are, and always will be my motivation, my strength, and, in the end, all that truly matters.

Finally, I thank God for granting me the health and patience to reach this point.

ABSTRACT

Bulk Metallic Glasses (BMGs) possess unique properties such as high strength, large elastic limits, excellent magnetic behavior, and corrosion resistance, primarily due to their disordered atomic structure. However, their limited ductility at room temperature, caused by nonhomogeneous deformation, restricts widespread use. To overcome this, Bulk Metallic Glass Composites (BMGCs), which incorporate a ductile second phase into a glassy matrix, offer enhanced ductility while retaining strength. Among BMGs, Fe-based alloys are particularly attractive due to their favorable magnetic, mechanical, and corrosion-resistant properties and low cost. Yet, their poor glass-forming ability (GFA) and need for rapid cooling rates limit practical applications and component size and geometry. This study explores the feasibility of using Laser Powder Bed Fusion (LPBF), an additive manufacturing method offering high cooling rates (10^3-10^6 K/s), to fabricate Fe-based BMGCs in the Fe-Mo-P-C-B system. Six alloy compositions were designed through theoretical modeling and synthesized via arc melting. The most promising alloys, selected through microstructural and mechanical evaluation, were scaled up using Vacuum Induction Melting (VIM) and then gas atomized to produce powders suitable for LPBF. The atomized powders were processed by LPBF under various parameters to produce dense samples with retained glassy phase. While process optimization reduced defects (cracks and pores down to 1%) and achieved glassy phase fractions up to 24%, these conditions were not simultaneously met. The microstructure included ultrafine bcc Fe-Mo-C grains in the melt pool and mixed crystalline phases in the heat-affected zone. Compression tests showed no plastic deformation, but the LPBF samples demonstrated excellent wear resistance, combining low coefficients of friction and wear rates. Overall, the study reveals the trade-off between high density and glass formation in LPBF-fabricated Fe-based BMGCs, highlighting both the potential and the challenges of using additive manufacturing for producing such advanced materials.

Keywords: Additive manufacturing; Laser Powder Bed Fusion; Alloys design; Bulk metallic glass composites; Fe-based alloys; Glassy steel.

RESUMO

DESIGN, FABRICAÇÃO E CARACTERIZAÇÃO DE COMPÓSITOS METÁLICOS VÍTREOS EM VOLUME À BASE DE FERRO POR MANUFATURA ADITIVA

Materiais metálicos vítreos em volume (*BMGs*) possuem propriedades excepcionais, como alta resistência mecânica, elevado limite elástico, excelente desempenho magnético e resistência à corrosão. Essas características decorrem de sua estrutura atômica desordenada, sem ordenação de longo alcance. No entanto, a baixa ductilidade à temperatura ambiente — causada por deformação não homogênea concentrada— limita suas aplicações estruturais. Uma estratégia promissora para superar essa limitação é a produção de compósitos vítreos metálico em volume (*BMGCs*), que combinam uma matriz vítrea com uma segunda fase dúctil, promovendo maior ductilidade ao material, sem sacrificar significativamente sua resistência. Ligas à base de ferro (Fe) se destacam entre os *BMGs* por apresentarem boas propriedades mecânicas, magnéticas, resistência à corrosão e baixo custo. Contudo, apresentam baixa habilidade de formação vítrea (*GFA*) e requerem altas taxas de resfriamento para sua formação, o que restringe o tamanho e a geometria das peças produzidas por métodos convencionais. Neste estudo, foi investigada a viabilidade de utilizar a técnica de manufatura aditiva Fusão de Leito de Pó (*LPBF*) — que permite taxas de resfriamento extremamente altas (10^3-10^6 K/s) — para fabricar *BMGCs* do sistema Fe-Mo-P-C-B. Utilizando simulações, seis composições foram projetadas, sintetizadas por fusão por arco, e avaliadas quanto à composição química, microestrutura e propriedades mecânicas. As ligas mais promissoras foram escaladas por fusão por indução a vácuo (*VIM*) e atomizadas a gás para produção de pós adequados à *LPBF*. Os pós foram processados por *LPBF* em diferentes condições. Foram produzidas amostras com frações de fase vítrea de até 24% e percentuais de defeitos (trincas e porosidade < 1%), mas essa combinação não ocorreu simultaneamente. As amostras exibiram microestrutura ultra refinada embebida em matriz vítrea. Apesar da ausência de deformação plástica sob compressão, excelente desempenho tribológico foi atingido. O estudo destaca o potencial da *LPBF*, mas também os desafios de equilibrar

densificação e formação vítrea em *BMGCs* à base de Fe.

Palavras-chave: Manufatura aditiva; Fusão de Leito de Pó; Design de ligas; Compósitos metálicos vítreos em volume; Ligas à base de Fe; Aço vítreo.

PUBLICATIONS

Scientific papers:

- **ARAUJO, AYLANNA P. M. DE**; MICHELOTI, L.; KIMINAMI, C. S.; GARGARELLA, P.. **Microstructure, phase formation and properties of rapid solidified Al-Fe-Cr-Ti alloys.** Materials Science and Technology. p. 1-10, 2020.

- **ARAUJO, A. P. M. DE**; MICHELOTI, L C..; KIMINAMI, C. S.; BOLFARINI, C.; UHLENWINKEL, V.; GARGARELLA, P. **Morphological and microstructural characterization of $Al_{95}Fe_2Cr_2Ti_1$ powders produced by two different gas atomizers.** Tecnologia em Metalurgia, Materiais e Mineração, 2021.

- **ARAUJO, AYLANNA P.M. DE;** PAULY, SIMON; BATALHA, RODOLFO L.; COURY, FRANCISCO G.; KIMINAMI, CLAUDIO S.; UHLENWINKEL, VOLKER; GARGARELLA, PITER. **Additive manufacturing of a quasicrystal-forming Al95Fe2Cr2Ti1 alloy with remarkable high-temperature strength and ductility.** Additive Manufacturing, v. 41, p. 101960, 2021.

- **DE ARAUJO, AYLANNA P.M.;** KIMINAMI, CLAUDIO S.; UHLENWINKEL, VOLKER; GARGARELLA, PITER**. Processability of recycled quasicrystalline Al-Fe-Cr-Ti composites by selective laser melting - A statistical approach.** Materialia, v. 22, p. 101377, 2022.

- **DE ARAUJO, AYLANNA P.M.;** KIMINAMI, CLAUDIO S.; UHLENWINKEL, VOLKER; GARGARELLA, PITER**. High-temperature tensile properties of an aluminum quasicrystal-forming alloy manufactured by laser powder bed fusion.** Materials science and engineering A-Structural materials properties microstructure and processing, v. 886, p. 145670, 2023.

- **DE ARAUJO, AYLANNA PRISCILA MARQUES;** CARMELO, FELIPE B. DO M.; ROCHA, ERLIFAS M.; KIMINAMI, CLAUDIO S.; GARGARELLA, PITER**.**

Effects of Process Parameters on Cold Spray Additive Manufacturing of Quasicrystalline Al93Fe3Cr2Ti2 Alloy. Powders, v. 2, p. 525-539, 2023.

- DE ARAUJO, AYLANNA P. M.; TEODORO, NICOLE S.; PEREIRA, LEANDRO H.; KIMINAMI, CLAUDIO S.; UHLENWINKEL, VOLKER; GARGARELLA, PITER**. Comparing the Properties of Metastable Quasicrystal-Forming Al95Fe2Cr2Ti1 Alloy Prepared by Uniaxial Hot Compaction and Powder Bed Fusion-Laser Beam.** JOM, v. 1, p. 1-12, 2024.

- DE CAMPOS FERNANDES, DIOGO; **DE ARAUJO, AYLANNA P.M.**; FERREIRA, TALES; UHLENWINKEL, VOLKER; GARGARELLA, PITER. **Enhanced wear resistance of a novel Al-based quasicrystalline phase-forming alloy obtained by laser powder bed fusion.** Materials letters, v. 382, p. 137936, 2025.

Conference presentation:

- **A. P. M. de ARAUJO,** D. R. MARTINS, C. S. KIMINAMI, V. UHLENWINKEL and P. GARGARELLA, Physical characterization of Al alloys powders for powder bed fusion additive manufacturing. Oral presentation in 22° Simpósio em Ciência e Engenharia de Materiais (SICEM), São Carlos-SP-Brazil, October 2020.

- **DE ARAUJO, AYLANNA P.M.;** KIMINAMI, CLAUDIO S.; UHLENWINKEL, VOLKER; GARGARELLA, PITER**.** Microstructure and mechanical properties of an aluminum quasicrystal-forming alloy produced by uniaxial hot compaction and additive manufacturing**.** Oral presentation in VI International Conference of the Institute of Solid-State Chemistry and Mechanochemistry SB RAS, Novosibirsk State University, Russia, November 2022.

- ARAUJO, AYLANNA P.M. DE; MICHELOTI, L C..; BATALHA, RODOLFO L., PAULY, SIMON;, KIMINAMI, CLAUDIO S., GARGARELLA, PITER. Influence of Selective Laser Melting Parameter Variation on the Density, Microstructure, and Hardness of the Recycled AlFe-Cr-Ti Quasicrystalline Phase Former Alloy. Oral

presentation in ABM week, São Paulo-SP-Brazil, June 2022.

- **ARAUJO, A. P. M.;** PAULY, SIMON ; KIMINAMI, C. S. ; UHLENWINKEL, V. ; GARGARELLA, P., selective laser melting of recycled Al95Fe2Cr2Ti1 quasicrystalline phase former alloy. Oral presentation in 24° Congresso Brasileiro de Engenharia e Ciência dos Materiais, CBECiMat, Águas de Lindóia-SP-Brazil, November 2022.

- **ARAÚJO, AYLANNA P. M.**; RAMASAMY, P ; JURGEN, E. ; GARGARELLA, P. Combining theoretical methods and simulations to propose a novel fe-based bulk metallic glass composite alloy with acceptable laser powder bed fusion processability, 25° Congresso Brasileiro de Engenharia e Ciência dos Materiais (25 CBECIMAT), Fortaleza-CE-Brazil, November 2024.

SUMMARY

1 INTRODUCTION, MOTIVATION, AND GOAL

Glassy alloys are considered advanced materials whose atomic structure is deliberately engineered to achieve superior and functional properties, particularly in terms of mechanical performance. Unlike crystalline metals, metallic glasses exhibit a disordered atomic structure with no long-range order. The lack of structural defects, such as dislocations, results in significantly higher strength compared to their crystalline counterparts. At the same time, there is an increasing industrial need for high-strength materials as high-strength steels. These two points have inspired engineers and researchers to develop new glassy alloys and their composites, especially those based on low-cost materials such as iron (Fe).

The necessity of high cooling rates during solidification to form the glass structure depends on the metallic alloy system and its chemical composition. Some rules, criteria, and parameters in the literature can guide the selection of glassy alloys, but none of them is 100% reliable. Therefore, considering a combination of those has been a good path. The ability of a metallic alloy to form the glassy phase is defined as its *glass-forming ability* (GFA), which is often quantified by the *critical cooling rate* (R_c), where R_c is the minimum critical cooling rate required to suppress crystallization and form a glass.

In general, Fe-based bulk metallic glasses (BMGs) exhibit poor GFA and are brittle at room temperature. However, they offer several attractive features, including relatively low material cost, good soft magnetic properties (such as low coercivity and high permeability), low core losses, as well as high yield strength, high hardness, and excellent corrosion resistance. In order to handle the poor GFA, overcoming the plasticity limitations of Fe-based BMGs, but exploring the advantages of these glassy materials, a possible alternative is to produce Fe-based bulk metallic glass composites (BMGCs). In BMGCs, a second phase can be introduced into the glassy matrix—either *in situ* or *ex situ*—to serve as both an obstacle to and a source for shear band propagation, thereby enhancing the composite's balance between strength and ductility.

Laser powder bed fusion (LPBF) is a layer-by-layer powder bed fusion additive manufacturing (AM) technology that uses a laser and is able to effectively

achieve high cooling rates (10^3-10^6 K/s), depending on the process parameters. Because of such characteristics, LPBF can be considered a viable route for the fabrication of BMGs and BMGCs, enabling the production of large and complex parts with an *in situ*-controlled microstructure.

According to the literature, some Fe-based BMGs have already been processed by LPBF. However, none of these alloys were designed for the LPBF process. Consequently, issues related to fragility, low density, and undesired crystallization constituted the major obstacles to obtaining functional LPBFed parts. **The motivation of this work, therefore, was to use the LPBF process to produce low-cost Fe-based BMGCs. Thus, this work aimed to select and design Fe-based alloys able to be successfully processed by LPBF, obtaining Fe-based BMGCs with improved plasticity.**

With these considerations, **the specific goals of this project were:**

i. **To select and design Fe-based bulk metallic glass composites using theoretical and experimental methods;**
ii. **To produce and characterize the atomized powders of the designed alloy;**
iii. **To process the powder by LPBF;**
iv. **To investigate the influence of the LPBF process parameters on the density and phase formation of the LPBFed parts;**
v. **To build parts in different directions, 0°, 45°, and 90°, with relation to the Z-axis;**
vi. **To perform microstructural, mechanical, and wear characterization of the samples obtained by LPBF;**
vii. **To correlate LPBF process parameters with the resulting microstructure, mechanical, and wear properties.**

2 LITERATURE REVIEW

2.1 Metallic glasses

In terms of atomic structure, materials can be classified into three main types:

1) Crystalline: long-range atomic periodicity exists; there are translational and rotational symmetry;
2) Quasicrystalline: only atomic rotational symmetry exists in three dimensions;
3) Amorphous: atomic periodicity does not exist, but some short-range order (SRO) can exist; herein, the atoms are randomly distributed.

As is well known, structure and properties are closely related. Therefore, metallurgy focuses on understanding material structures to establish correlations with the resulting properties of alloys. For example, glassy alloys do not contain dislocations, stacking faults, grain boundaries, or other typical defects found in crystalline structures. As a result, they exhibit strength levels approaching the theoretical limit (as shown in **Figure 2.1**). Additionally, it can be observed that the strength of glassy alloys surpasses that of conventional steels, indicating their potential to replace certain steels in structural applications [1].

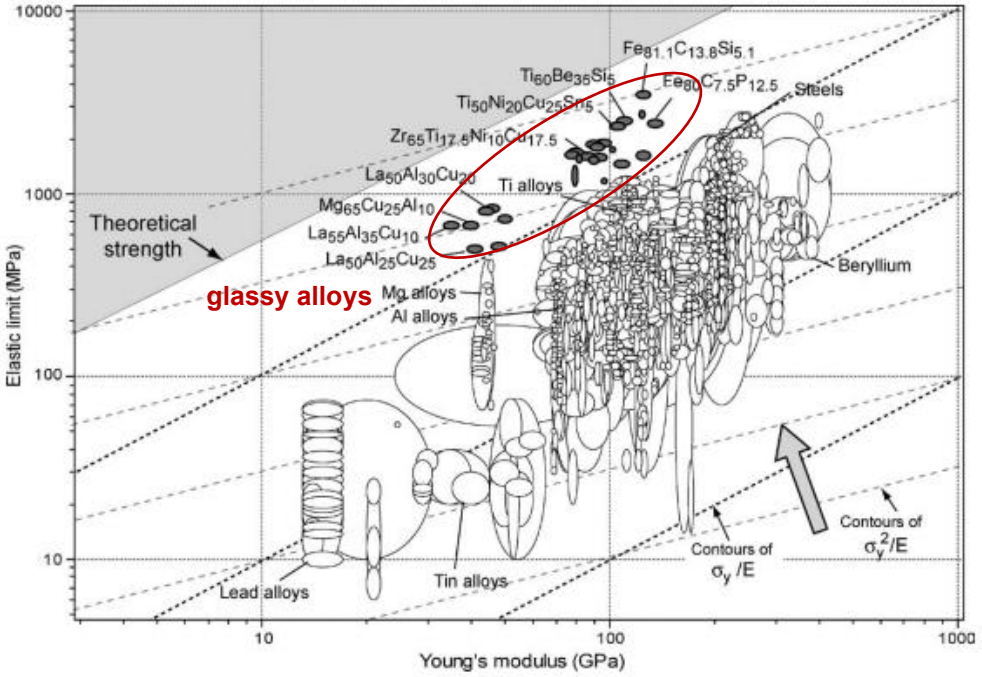

Figure 2.1- Elastic limit versus Young's modulus for 1507 metals/alloys. The metallic glasses results are indicated in the figure by a red circle. Source: [1].

There is an ongoing debate regarding the mechanical properties of glassy alloys, particularly their strength, and whether they behave similarly to oxide glasses. Oxide glasses are brittle materials and present very high strength. However, considering the fracture toughness (**Equation 2.1**), it may be concluded that glassy alloys are not brittle. By considering the geometric factor "Y" equals to 1 in **Equation 2.1**, it is possible to calculate the length "a", which is the critical size of the crack inside the materials before failure during application of stress. From **Figure 2.2**, for ceramic, it can be observed that "a" is very small (~1 μm), indicating that this material will fail catastrophically under a critical stress. In the case of metals, "a" is about 10 mm, and for glassy alloys, this value is around 1 mm. These values are then in the same order of magnitude, proving that glassy alloys are closer to metallic engineering alloys than ceramic oxide glasses.

From **Figure 2.2**, metallic glasses and their composites occupy a region close to conventional Ti- and Ni-based alloys and steels. This suggests significant

potential for metallic glasses to be utilized in engineering applications.

$$K_{IC} = Y\,\sigma\,\sqrt{\pi a} \qquad \textbf{Equation 2.1}$$

Table 2.1- Data from **Figure 2.2** for metal/alloys, ceramic, and metallic glass.

	Metal/alloys	**Ceramic**	**Metallic glass**
σ_y (MPa)	400	3000	1800
K_{IC} (MPa*m$^{0.5}$)	100	10	80
a (m)	20 x10^{-3}	3.5 x10^{-6}	0.63 x10^{-3}
a (mm)	~ 10 mm	~1 μm	~ 1 mm

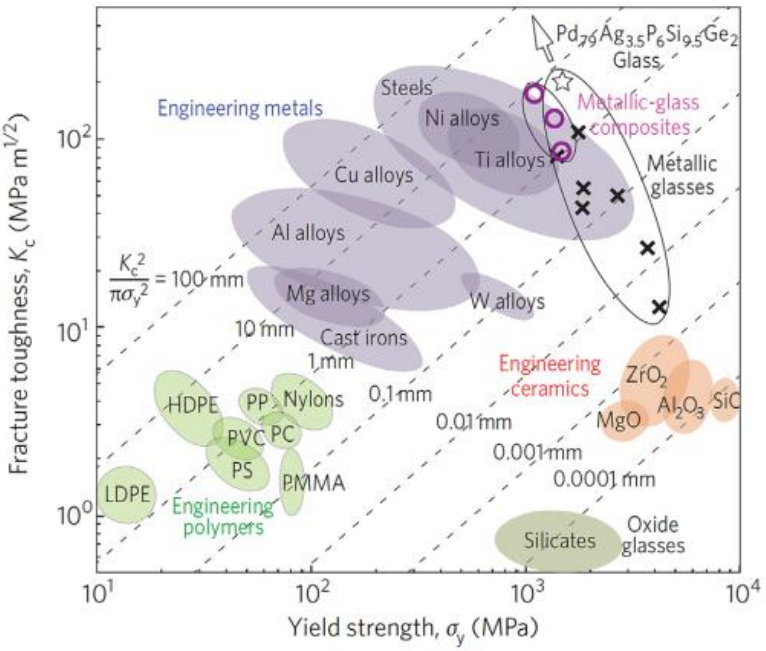

Figure 2.2- Ashby plot displaying yield strength-fracture toughness correlations for various engineering materials depicting the exceptional combinations that metallic glasses can achieve. Diagonal dotted lines show the plastic-zone size, $K_c^2/\pi\sigma_y^2$, where K_c is the fracture toughness and σ_y the yield strength. Source: [2].

In 1960, metallic glass (MG) was obtained by Klement et al. in a small droplet of Au-25%Si (at. %) alloy solidified from the liquid state at rates of about 10^6 K/s [3]. Under high solidification rates, atoms do not have sufficient time or energy to arrange for crystal nucleation, and as a result, the amorphous structure

is maintained [4]. In other words, this structure is achieved by the control of the process's kinetics. By hindering the kinetic energy, it is possible to avoid the arrangement of the atoms, and an amorphous structure is formed. By continuous cooling from the liquid state, there are two paths for the melt as shown in **Figure 2.3**: **1)** the liquid is cooled under such condition that allows the formation of the nucleus just below T_m (melting temperature), and with the decreasing of the temperature, the viscosity increases, these nucleus gets bigger and bigger until all liquid is solidified into a crystal structure. In this case, there is a sudden and significant decrease in the specific volume near T_m, as seen in **Figure 2.3**. **2)** Here, the liquid is cooled under conditions that do not allow nucleus formation; only clusters may be formed. The volume of most of the liquid decreases gradually with decreasing temperature until it reaches the T_g (glass transition temperature). At T_g, there is a slight increase in the specific volume, and the viscosity of the undercooled liquid reaches a value of 10^{12} Pa.s, which is equivalent to the "viscosity" of crystalline solids. Thus, we have a glass solid below T_g for all practical purposes. It is worth mentioning that a sharply defined T_g temperature at which this occurs does not exist. In reality, there is a temperature range in which the liquid becomes glass, and Suryanarayana and Inoue [4] have preferred to call this the glass-transformation interval. From **Figure 2.3**, it is shown that there is no unique T_g value for a given material, which is because of the kinetic nature of the transition rather than thermodynamic [4]; T_g depends on the applied cooling rate. Above T_g (but below the crystallization temperature, T_x), the metallic glass can revert to the supercooled liquid state without crystallization, and this state is usually referred to as the supercooled liquid region. The temperature interval between T_x and T_g is recognized as the width of the supercooled liquid region, that is, $\Delta T_x = T_x - T_g$ [4].

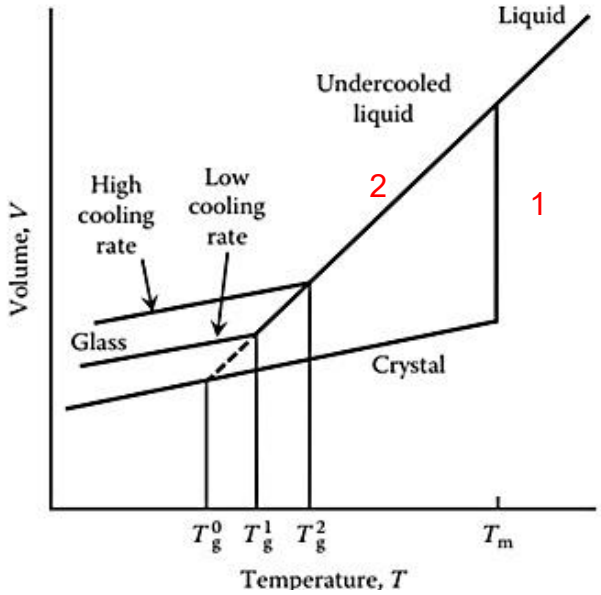

Figure 2.3- Specific volume changes as a function of temperature and cooling rate for 1) normal solidification path and 2) glass-forming path. On increasing the cooling rate, the glass transition occurs earlier. Adapted from [4].

The ability of a metallic alloy to transform into a glassy state is defined as the glass-forming ability (GFA) [4], which is going to be explained in detail in the next section. Each alloy composition has its own capacity to form the glass structure and then requires a specific critical cooling rate (R_c). According to the literature [5], [6], [7], [8], the R_c of metallic alloys ranges between 10^{-2} K/s and 10^6 K/s.

2.1.1 Glass forming ability

As mentioned before, R_c is dependent on the alloy composition: the higher the R_c, the worse the GFA of the alloy. The interplay of thermodynamics and kinetics for crystallization of supercooled liquid results in the typical time–temperature–transformation (T–T–T) diagram shown in **Figure 2.4**. If the alloy is cooled from the liquid state, under such a condition that provides enough time, solidification will occur at temperature T_1, and time t_1, and the product of solidification will be a crystalline solid (curve “1”). On the other side, if the liquid alloy is solidified at a rate faster than the cooling rate represented by curve “2,” which depicts a tangent to the C-curve at its nose (i.e., the temperature at which

the formation of a crystalline phase takes place in the shortest time), then crystal formation will not take place. Instead, the liquid will be retained in a supercooled (or undercooled) condition. If the temperature of this supercooled liquid is further decreased, the liquid viscosity will continue to increase, and at temperatures below T_g, the supercooled liquid will become glass [4]. Hence, the most straightforward and logical criterion one could think of to predict glass formation is that the liquid alloy should be cooled at a rate faster than R_c and to a temperature below T_g. But also, from **Figure 2.4** is possible to theoretically calculate the R_c using **Equation 2.2**.

$$R_C \cong \frac{T_l - T_n}{t_n} \qquad \textbf{Equation 2.2}$$

Where T_n and t_n are the temperature and time at the nose of the C-curve, respectively, and T_ℓ is the liquidus temperature. However, Suryanarayana and Inoue[4] have reported that this expression overestimates R_c since it assumes that the crystallization rate corresponds to the nose of the T–T–T curve throughout the whole temperature interval of T_ℓ to T_n, and therefore results in a value somewhat higher than the experimentally determined value.

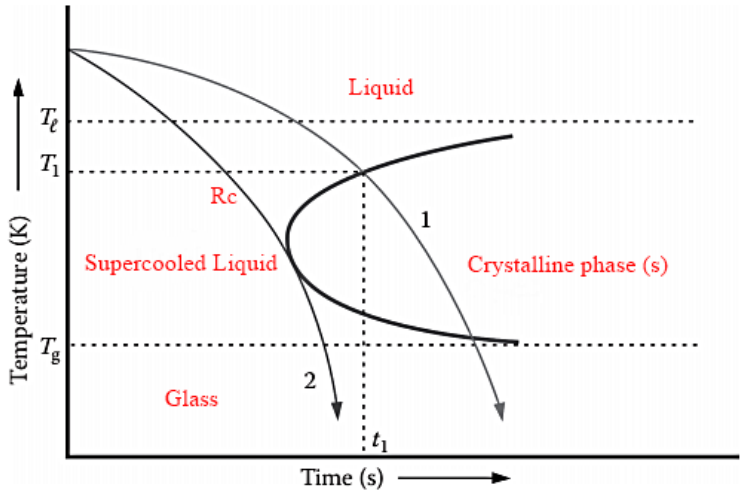

Figure 2.4- Schematic time–temperature–transformation (T–T–T) diagram for a hypothetical composition demonstrating the conditions for glass formation on quenching of the melt. R_c represents the critical cooling rate. Adapted from [4].

Even though R_c is an indicator of the GFA of the alloy melt, it is very hard to predict the glass-forming ability of a composition. Further, the R_c can only be determined when the glassy alloy has been synthesized. Nevertheless, two considerations are very important to form a glass:

1- Addition of alloying elements: changing the chemical composition of alloys by adding different elements has decreased R_c, i.e., increased the GFA. With the presence of alloying elements, the C-curve is shifted to the right; that is, a lower R_c is needed to form the glass. It has been reported [4] that glass formation in pure metals requires an extremely high R_c (typically $>10^{12}$ K s^{-1}), and since it is not easy to achieve such high cooling rates, it is difficult to produce a pure metal in the glassy state by rapidly quenching it from the molten state [4]. However, for binary metallic liquids, the value of R_c is typically in the range of 10^4–10^6 K s^{-1}. Moreover, as the number of components in the alloy system increases, the value of R_c usually further decreases; consequently, for multicomponent alloys, R_c is typically about 10^2 K s^{-1} or less [4].

2- Flux treatment of the melt: to avoid crystallization, the melt should be as pure as possible. In this case, the heterogeneous nucleation is avoided once a fluxing agent helps to remove impurities of the melt; as a consequence, the GFA of the alloy is improved [6], [9].

Nevertheless, the improvement of the glass-forming ability (GFA) is not a linear process with respect to the number of alloying elements. Simply increasing the number of elements does not necessarily lead to higher GFA. Therefore, researchers [4] have been investigating additional criteria to determine whether it is possible to predict the GFA in metallic alloy systems. According to the book [4], some of the most commonly used criteria and parameters for understanding the GFA of a given alloy include the following:

Empirical criteria

- *Reduced glass transition temperature (T_{rg})*: Suggested by Turnbull [10], it is purely based on the kinetics of crystal nucleation and the viscosity of melts; mathematically given by the ratio T_g/T_ℓ. According to Turnbull [10], the higher the T_g value, the higher the viscosity and, therefore, the alloy

melt could be easily solidified into the glassy state at a low R_c. Besides, Turnbull proposed that at $T_{rg} \geq 2/3$, homogeneous nucleation of the crystalline phase is completely suppressed, and a minimum value of $T_{rg} \cong 0.4$ has been found to be necessary for an alloy to become glass.

- *Deep eutectics*: An alloy system in which the eutectic temperature is significantly lower than the melting points of the individual components is referred to as a deep eutectic. In such cases, the T_ℓ of the alloy is the lowest, and, as a result, the T_{rg} reaches its highest value at the eutectic composition. Therefore, this composition is expected to be easily transformed into a glassy state under quenching.

Topological Models

- *Atomic size mismatch*: The size of constituent atoms has a significant role in glass formation. The radius mismatch of the constituents should exceed 15% to increase the liquid stability and sluggish nucleation.
- *Egami and Waseda criterion*: It is based on the destabilization of a crystal lattice when is increased the atomic-level stresses in the solid solution. There is a critical minimum solute concentration (C_B^{min}), where the glassy alloy becomes energetically more favorable than the corresponding crystalline lattice, which is given by:

$$\left|\frac{V_A - V_B}{V_A}\right| C_B^{min} = 0.1,$$

where V_A and V_B are the atomic volume of solvent and solute, respectively.

Inoue empirical criteria

- The alloy must have at least three elements.
- The atomic size difference between the main constituent elements should be larger than 12%.
- There should be a negative mixing enthalpy among the alloy's constituent elements.
- The ΔT_x Criterion: Inoue also proposed that the GFA of alloys is directly related to ΔT_x. A large width of the supercooled liquid region, $\Delta T_x = T_x - T_g$, suggests that the glassy phase produced is very stable and resists crystallization. Thus, with an increase in the ΔT_x value, the R_c decreases.

Parameters based on the transformation temperatures of glasses: Here, two aspects should be considered: first, the stability of the liquid phase, and second, the resistance to crystallization of the glass that has formed. The γ parameter was the first to be proposed; subsequently, many other parameters have been suggested. All of these parameters involve different combinations of the glass transformation temperatures (as shown below), and the higher the parameter's value, the higher the GFA of the alloy.

- The γ Parameter: $\frac{T_x}{T_g + T_l}$
- The α: $\frac{T_X}{T_l}$
- The β Parameter: $1 + \frac{T_x}{T_l} = 1 + \alpha$
- The δ Parameter: $\frac{T_x}{T_l - T_g}$
- The New β Parameter: $\frac{T_x * T_g}{(T_l + T_x)2}$
- The ω Parameter: $\frac{T_g}{T_x} - \frac{2T_g}{T_g + T_l}$
- The θ Parameter: $\frac{T_x + T_g}{T_l} x \left[\frac{(T_x - T_g)}{T_l}\right]^{\alpha}$
- The ζ Parameter: $\frac{T_g}{T_l} + \frac{\Delta T_x}{T_x}$

Since all of these parameters consider the same two points: stability of the liquid phase and the resistance of the glassy phase to crystallization, it would be reasonable to expect similar results from them, but according to the literature [4], they are not. The majority of the parameters have relevance and validity only in some cases. One possible explanation for this is related to the chosen data submitted for analysis by the individual Suryanarayana et al. [4]. Besides, to use these parameters, the transformation temperatures of the glassy alloy, for example, T_g, T_x, T_ℓ, are required. But these temperatures can be obtained only after the alloy has been solidified into the glassy state and submitted to thermal analyses. Then, only after producing the alloy is it possible to know about its GFA. In this respect, these parameters are similar to R_c to predict GFA. Because of

this, until today is very hard to predict a composition that will easily produce the glass, and therefore, many glasses are produced more or less by trial and error. It would be much more efficient if one could predict the GFA of an alloy without actually doing an experiment to produce the glass. Taking all said into account, considering the atomic sizes of the constituent elements and their chemical interaction seems to be the most beneficial approach in selecting good glass-forming alloys. For this reason, in this work, a structural and topological parameter, known as an atomistic approach, was selected, and it will be explained in detail in the next section.

2.1.1.1 Egami's atomistic approach and the subsequent models

Based on the Egami and Waseda criterion (briefly discussed before), Ueno and Waseda [11] developed the λ parameter in the case of multicomponent alloy systems. Subsequently, by extending to multicomponent alloy systems, the topological instability model of Egami and Waseda [12] was then introduced by Botta et al. [13] as a new "lambda (λ) criterion." The new lambda (λ) criterion was used to predict glass formation by combining the average electronegativity difference with the topological instability criterion. The topological instability was calculated from the atomic radii (in simple solid solutions) or molar volumes of the compounds, according to:

$$\lambda \cong \Sigma\, x_i \left|\frac{V_{mi}}{V_{mo}} - 1\right|$$

where: x_i and V_{mi} are the molar fraction, and molar volume, respectively, of the solute element in the compound, and V_{mo} is the molar volume of the compound.

The values of λ are calculated as a function of the composition for a given system. Large values of λ indicate a greater topological instability of the phase under consideration. Botta et al. [13] have also demonstrated a theoretical background and construction of a minimum topological instability λ_{min} map. In this case, after calculating the λ value for all possible crystalline phases, for a given alloy composition, the minimum value of λ, i.e., λ_{min}, is found. The calculation is repeated for *n* compositions of the same system. With all λ_{min} values, a graph is

plotted (λ_{min} values as a function of the compositions of the given system). The interpretation of the λ_{min} graph is that the peaks in the λ_{min} plot correspond to the compositions where the topological instability reaches a local maximum and, consequently, have a better GFA. However, de Oliveira [14] realized that even though λ_{min} appears to be a good parameter to predict the GFA among the competing phases in a given phase diagram, it is not efficient for tracking the GFA, generally. Thus, to better predict the GFA of alloys, de Oliveira [15] proposed an electronic parameter, Δh, defined as:

$$\Delta h = (\Delta\phi)^2 - k(\Delta n_{ws}^{1/3})^2$$

Where $\Delta\phi$ is the average difference of the work function, and $\Delta n_{ws}^{1/3}$ is the average difference of the cube root of the electronic density among the alloy's constituent elements. And, combining into one equation, the Δh parameter, that gives the general behavior of the GFA among the different alloy systems, with λ_{min}, which is used to refine such behavior within the phase diagrams, de Oliveira [14] observed that the simplest combination of $\lambda_{min}+(\Delta h)^{1/2}$ was the best correlation with the critical cooling rates (R_c). Thus, the equation that relates the critical cooling rate, R_c, to the $\lambda_{min}+(\Delta h)^{1/2}$ parameter is given as:

$$\log R_C = 8.21 - 14.06\ (\lambda_{min} + \sqrt{\Delta h})$$

According to the author [14], such linear correlation fitted well for 68 alloys in 30 different metallic systems, proving the criterion ($\lambda_{min}+(\Delta h)^{1/2}$) is much better to predict the R_c. Besides, he asserts that the proposed criterion is in good agreement with the well-known three empirical rules for glass formation proposed by Inoue and concludes that “the new proposed criterion is a fast and easy-to-use tool for guiding the search for new glass-forming alloys, saving time and reducing the number of experimental trials.”

As already said, none parameter or criterion is 100% reliable to predict the GFA of alloys; however, the criterion, proposed by de Oliveira [14], was chosen to be used in this work for the following reasons:

1) It is a topological and atomistic approach, so it does not require T_g, T_x, T_ℓ;
2) It is in agreement with the well-known three empirical rules for glass formation proposed by Inoue;

3) It can be calculated using a computer software already available;
4) It shows promising results for 30 different metallic systems (including Fe-based systems).

2.2 Bulk metallic glasses (BMG)

In 1974, Chen [16] reported the production of long glassy rods, 1-3 mm in diameter and several centimeters in length, by water quenching of ternary alloys of different compositions in the $(Pd_{1-x}M_x)_{0.835}Si_{0.165}$ (with M = Fe, Co, Ni, Cu, Ag, and Au), Pt–Ni–P, and Pd–Ni–P systems. It led to the development of today's well-known Bulk Metallic Glasses (BMGs). Even though more recently researchers tend to consider 10 mm as the minimum diameter or section thickness at which a glass can be labeled as "bulk," generally, metallic glasses with at least 1 mm (diameter or section thickness) are considered "bulk" [4].

MG and BMG have attracted attention because of their excellent physical, chemical, and magnetic properties [17], [18]; their aperiodic structure provides not only unique properties [19] but also an isotropic nature of such properties [20]. Glassy alloys have an elastic limit of almost 2% (**Figure 2.5**) [21], which is far superior to conventional steel, Ti-based alloys, and silicate glasses. Some applications for glassy alloys materials have been outlined [4],[19] as micromotors and precision gears used for Micro Electro Mechanical Systems (MEMS), which can range from several millimeters to less than one micrometer; automobile valve springs; diaphragms for pressure sensors; applications to surface coatings; sporting goods like golf clubs, tennis racket, baseball, softball bats, skis, snowboards, and bicycle parts; and chemical applications as fuel cell systems. Besides that, metallic glasses can store a very high amount of elastic energy due to the high elastic strain limit and very high resilience.

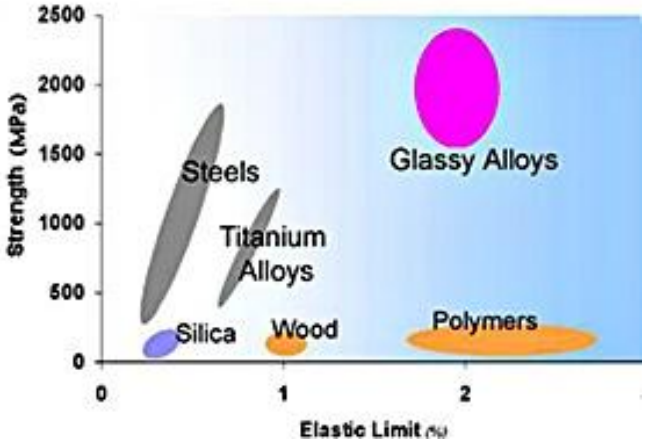

Figure 2.5- Metallic glasses combine higher strength than crystalline alloys with the elasticity of polymers. Source: [21].

Concerning the mechanical properties, even though MG and BMG have a very high elastic energy absorption and ultra-high tensile strength (as shown in **section 2.1**), the plasticity at room temperature is usually poor [22]. Generally, they fail soon after yielding without showing any signs of a reasonable amount of plastic deformation [4]. It has been demonstrated that their plastic deformation follows a manner of localized flow in shear bands at room temperature [23], [24]. This process starts when the shear transformation zones (STZs) are activated [24],[25]. The regions with higher free volume content or more pronounced structural disorder are favored places to the STZs be originated [24], [25]. Authors [26],[27] claim that under loading, small clusters of atoms rearrange spontaneously and cooperatively and form a STZ. Besides, according to Greer et al. [24], heterogeneous sites are fertile places for shear transformation. With increasing load, existing STZs stimulate the activation of STZs in their vicinity, forming a shear band by percolating along the plane of maximum shear stress [27],[28],[29],[30]. When load achieves a critical value, the shear band propagation starts [24],[31],[32]. Thus, in the case of brittle metallic glasses, once shear bands nucleated, they can easily fracture, and the materials show poor plasticity with few shears band formation [33],[34]. As the shear bands are formed to accommodate strain, the space between these structures can provide information about the plasticity of the material [4],[20]. The shear offset in the band relaxes the strain in the vicinity of the shear band, and this determines the

shear band spacing [20]. The more shear bands are created, the closer they will be to each other and the higher the capacity for deformation of the material. Besides, the shear band spacing, which is a macroscopic event, can be correlated with the effective specimen size [20], as shown in **Figure 2.6**. From **Figure 2.6**, it is seen that the bigger the specimen size, the larger the space between the shear bands. As a result, more strain is localized, and the material catastrophically fails sooner. As reported by Sarac et al. [23], "the negligible plasticity in most metallic glasses has been an important barrier obstructing property optimization and their widespread use."

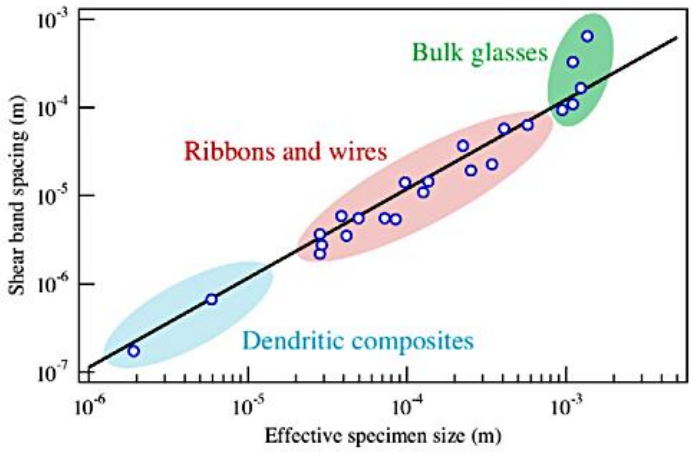

Figure 2.6- Average shear band spacings as a function of characteristic specimen size for a variety of metallic glasses (and some derivative composites) deformed in constrained modes of loading. Source: [20].

2.3 Bulk metallic glasses composites (BMGC)

An alternative to delay the catastrophic failure of metallic glasses when submitted to stress, especially tensile stress, is by increasing the amount of shear bands formed in it. Based on this idea, researchers have been developing the Bulk Metallic Glass Composites (BMGCs) [35],[36],[37],[38], and obtaining enhanced plasticity over the monolithic materials. In BMGCs, a second (reinforcing) phase can act as a source and barrier for the shear bands [24], [39]. According to [24], the reinforcing phase favors the formation of new shear bands at less favorable sites; the multiple shear band formation will promote shear band

interactions [24], [40]. By this mechanism of interaction, the failure of BMGCs can be retarded, and the material will be able to get some amount of plastic deformation [40],[41],[42],[43].

The second phase can be introduced in the glassy matrix via *in situ* or *ex situ* methods. For those *in situ* composites, the second phase precipitates out of the metallic glass matrix, either during processing or after heat treatment of the fully glassy alloy. Differently, when the second phase is added separately during the processing of the alloy, and stays "as is," without much interaction with the matrix, an *ex situ* composite is obtained. When *in situ* BMGC is compared to the *ex situ* BMGC, the former generally presents a stronger interfacial bonding between the reinforcing phase and the glassy matrix, allowing an effective load transfer during deformation [24],[44]. Additionally, all characteristics related to the second phase have a strong influence on the properties of the BMGC produced [4],[37], for instance, atomic structure (crystalline, amorphous, or quasicrystalline), size (micrometer or nanometer [45], [46]), shape (spherical, dendritic, irregular, or elongated [45], [46]), volume fraction, and distribution in the matrix. Schematic illustrations of possible BMGCs' microstructures are presented in **Figure 2.7**.

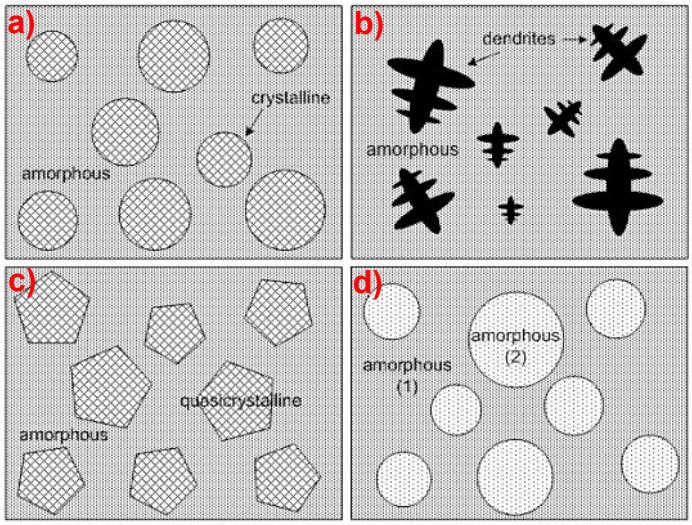

Figure 2.7- Schematic microstructures of BMGCs showing the (a) spherical or (b) dendritic morphology of the crystalline second phase, and (c) quasicrystalline

or (d) amorphous precipitates within an amorphous matrix, which can have nanometer or micrometer size. Source: [37].

Kühn et al. [38] have reported an *in situ* BMGC of the $Zr_{66.4}Nb_{6.4}Cu_{10.5}Ni_{8.7}Al_8$ alloy, where a bcc phase is embedded in a glassy matrix. The bcc phase formed is controlled by the alloy composition and solidification cooling rates. In this case, the compression tests at room temperature revealed significant yielding and plastic deformation before failure [38]. Other researchers [36] have worked with the Zr-Ti-Cu-Ni-Be system and obtained a ductile crystalline Ti-Zr-Nb **β** phase, with bcc structure in a Zr-Ti-Nb-Cu-Ni-Be metallic glass matrix. Here, the samples were submitted to unconstrained mechanical loading, and they showed great development of shear bands, which increased their mechanical properties [36]. Fan & Inoue [47] showed that nanocrystals (~2 nm) embedded in the amorphous matrix of the bulk $Zr_{60}Cu_{20}Pd_{10}Al_{10}$ alloy provide maximum plastic strain. However, they pointed out that the plastic strain increases by increasing the volume fraction of nanocrystals up to a maximum value in the early stage of the nanocrystallization [47]. Additionally, when Leonhard et al. [48] prepared amorphous $Zr_{55}Cu_{30}Al_{10}Ni_5$ and $Zr_{57}Cu_{20}Al_{10}Ni_8Ti_5$ and their micro and nano-composites, they observed that samples with micro-crystals in the amorphous matrix exhibited lower ductility and the same yield strength compared to the fully amorphous samples. For the composites with nano-crystals, the ductility was maintained, and the yield strength was higher than the fully amorphous samples, but only when the volume fraction of nano-crystals was less than 40%; the nano-composites with more than 40% of the nano-crystals presented brittle fracture and reduced fracture strength. Other studies [49] have reported BMGC of $Cu_{46}Zr_{41}Al_7Nb_1Ta_5$ containing Ta-rich particles and the B2 phase, where the stress behavior of the B2 phase dominates the macro-mechanical behavior rather than the shear-banding deformation.

As mentioned before, the strengthening effect observed in the composites is associated with the characteristics of the reinforcement. Thus, using the simple rule of mixture (**Equation 2.3**), it is possible to measure the yield strength of a composite:

$$\sigma_c = V_r \,.\sigma_r + (1 - V_r).\sigma_m \qquad \textbf{Equation 2.3}$$

Where σ_c is the yield strength of the composite, V_r is the volume fraction of the reinforcement, σ_r, and σ_m are the yield strengths of the reinforcement and matrix, respectively. Hence, the presence of hard reinforcements increases the strength to higher values than the softer reinforcements, and the strength increases with increasing volume fraction of the reinforcement. Like monolithic alloys, a fracture strength increase of the BMGCs is also correlated with an increase in plastic strain to failure, and this increase in plasticity is associated with the multiplication of shear bands [4].

The plasticity of BMGCs has been shown to improve significantly with the incorporation of *in situ* ductile dendritic phases [36], [50], [51]. Notably, some studies [52] have reported that transforming the dendritic phase into a more spherical morphology can lead to even greater enhancements in mechanical properties. According to [38], when brittle crystalline or quasicrystalline phases precipitate in BMGCs, the material does not exhibit yielding and strain hardening during room temperature deformation. In contrast, the *in situ* formation of ductile dendritic phases results in a marked improvement in deformation behavior compared to that of monolithic bulk metallic glasses [38].

To produce BMGCs with a ductile phase precipitated *in situ*, the alloy composition should be designed so that the primary crystalline phase precipitates out during the solidification process, usually in the form of a dendritic structure and the remaining liquid solidifies into a glass. Like Zr- [50], Cu- [51], and La-based BMGCs [53], the Fe-based BMGCs are prone to forming dendritic structures as their primary phase during the process of solidification [54], [55], [56], [57]. The Fe-based BMGs and their composites will be discussed in the following sections.

2.4 Fe-based BMGs

In 1995, Inoue et al. [58] synthesized, for the first time, a Fe-based BMG

with a diameter up to 1 mm by copper mold casting the $Fe_{73}Al_5Ga_2P_{11}C_5B_4$ alloy. Since then, Fe-based BMGs have been drawing the researchers' attention due to the high fracture strength of 3000-4000 MPa and high elastic strain of ~0.02, which are significantly different from the conventional Fe-based crystalline alloys [59]. Additionally, Fe-based BMGs exhibit relatively low material costs, good magnetic properties with low coercivity, high effective permeability, and low core losses, as well as high yield strength, high hardness, high corrosion, and wear resistance that overcome those for conventional Fe-Si-B amorphous alloy [60], [61], [62].

In contrast with BMGs based on precious metals, such as Zr and Pd, which present high GFA, Fe-based alloys have a poor GFA, especially the FeB- and FeP(C)-based [60], [61]. To overcome the poor GFA, more elements have been introduced, and the majority of Fe-based BMGs have from 4 up to 9 elements in their chemical composition, for instance, Fe–Co–Mo–P–C–B–Si, Fe–Cr–Mo–P–C–B–Si, Fe–Mo–Ga–P–C–B, Fe–(Cr, Mo)–Al–Ga–P–C–B, Fe–Mo–P–C–B–Si, Fe–Co–Ga–P–C–B–Si, and Fe–Ga–P–C–B–Si [63], [64], [65]. BMGs rods have been reported in the Fe–Ni–Mo–P–C–B [66] and Fe–Ga–P–C–B–Si [67] systems with 2.5 mm diameter and Fe–Mo–P–C–B–Si [63] and Fe–Co–Mo–P–C–B–Si [65] systems with 4 and 6 mm, respectively. Nevertheless, there are some Fe-based systems with fewer than four (4) elements able to produce BMGs parts, such as $Fe_{80}P_{13}C_7$ [68], $Fe_{80}P_{11}C_9$ [69], and, $Fe_{66}Nb_4B_{30}$ [70].

As reported by [60], the chemical composition of Fe-based BMGs regularly has two different types of metalloid elements, consisting of Si and P group with larger atomic sizes and B and C group with smaller atomic sizes. The GFA of Fe-based BMGs strongly depends on the concentration of these metalloid elements in the alloy. By the binary phase diagrams of Fe-C [71], Fe-B [72], and Fe-P [73], the eutectic point is near 17 at. %, which suggests good GFA around this composition. For Fe-based BMGs, the literature [74], [75] has agreed that the total concentration of metalloid additions is in the range of 17 at. % to 25 at.%.

2.5 Fe-based BMGCs

Even though GFA is a challenge to develop Fe-based BMGs, the mentioned properties, alongside cost reduction, have been driving the studies and applications of this type of material. In this direction, some approaches have been proposed: 1- using industrial raw material to produce Fe-based BMGs, 2- producing Fe-based BMGs under uncontrolled atmosphere as low vacuum conditions or even in the air without any inert gas protection, 3- reducing the number of alloying elements, and 4- eliminating expensive elements. However, the drawback of being brittle at room temperature has severely limited the industrial application of these glassy steels [54]. With this regard, an important point that has been considered is to produce Fe-based BMGCs, [76], [77], [78], [79], [80], [81]. According to the literature, to obtain α-Fe plus amorphous phase composite, the alloys should be on the Fe-rich side of the eutectic, forming the α-Fe as the primary phase [54], [82]. McHenry et al. [82] reported that by heating typical Fe-based MGs, crystallization occurs in a two-step process involving primary crystallization of the α-Fe phase, followed by secondary crystallization of a metalloid-enriched amorphous phase. As shown by [54], during the crystallization process of a Fe–(P,C)-based amorphous alloy, the primary bcc α-Fe was formed in addition to the amorphous phases. This fact suggests that Fe-based BMGCs, reinforced only with ductile dendritic α-Fe phase, could be achieved in the Fe–(P,C)-based system via composition design, and this would probably result in enhanced plasticity.

Since Fe-based BMGCs are prone to forming dendritic structures as their primary phase during the solidification process, they may form BMGCs with good ductility. Because of this, researchers have studied the formation of *in situ* dendritic structures in Fe-based BMGCs, and the reported consequences of the dendritic phases are a significant enhancement on the plastic strain and high fracture strength [54], [55], [56], [57], worsening on corrosion resistance [83], [84], and better toughness [85], compared to its monolithic counterparts. One explanation is that the severe interaction between the ductile dendritic phase and the shear bands results in the generation of multiple shear bands and prevention of the rapid propagation of the main shear bands, improving plasticity [54], [78]. However, other authors have reported improvement of properties of Fe-based

BMGCs by nano-crystallization of other phases, as better plasticity [86], [87], higher thermal conductivity [88], and better soft magnetic properties [87], [89]. Other nanocrystalline Fe-based materials designed as *metal/amorphous nanocomposites,* commercially known as FINEMET^{TM} [90], HITPERM [91], NANOPERM^{TM} [92] present excellent soft magnetic properties. Trying to explain the effectiveness of dendrite or other phases in the fracture toughness, researchers [85] have proposed that the intrinsic properties of the precipitate phase may play a more important role than the formation of the dendrite phase.

2.6 Fe-Mo-P-C-B system

When selecting a Fe-based glass-forming alloy, two key factors must be considered: GFA and ductility. Although GFA is often enhanced by multicomponent systems, some Fe-based glass-forming alloys with fewer than four elements—such as $Fe_{80}P_{13}C_7$ [68], $Fe_{66}Nb_4B_{30}$ [70], and $Fe_{80}P_{11}C_9$ [69]—have successfully produced bulk parts. While several theories offer guidance in identifying promising glass-forming alloys, the glass formation process remains inherently complex and difficult to predict, especially in systems with more than three elements, where the formation of competing crystalline phases is often hard to predict. Nevertheless, the adoption of systematic design approaches in the development of advanced steels, including amorphous steels, is increasingly important—helping to move beyond trial-and-error methods and reduce waste of time, energy, materials, and resources [93], [94].

In terms of enhancing the plastic deformation of Fe-based BMGs, the literature [95], [96] clearly indicates that, although most Fe-based BMGs exhibit brittle behavior, careful and systematic compositional design can lead to improved ductility. For instance, a BMG with the composition $Fe_{74}Mo_4P10C_{7.5}B_{2.5}Si_2$ (at. %) achieved a compressive fracture strength of 3.2 GPa and a plastic strain of up to 5.7% in 1 mm diameter rods [97]. In another study, a BMGC with the composition $Fe_{77}Mo_5P_9C_{7.5}B_{1.5}$ (at. %) demonstrated exceptional performance, reaching a compressive plastic strain of 37.5% and a fracture strength of 3.0 GPa—substantially higher than that of the corresponding

monolithic BMGs (<5%) [54]. This level of superplasticity had not been previously reported and was attributed to compositional design; however, the design strategy was not clearly defined by the authors [54]. The scattered findings and absence of a systematic alloy design methodology in studies on Fe-Mo-P-C-B BMGs and BMGCs [54], [56], [84], [85], [98], [99], [100], [101] motivated the present work to focus on investigating this compositional system.

According to the literature, when the main constituents of the MG are ferrous magnetic transition metals (Fe, Co, or Ni) and the metalloid glass formers are (B, Si, P), the alloys exhibit good soft magnetic properties [102]. Considering Mo as an alloying element on the Fe-based BMGs, it is important to point out that it is a transition metal with size and electronegativity higher when compared to Fe. Because of the difference in electronegativity, a low amount of Mo has to be added to the Fe master alloy to attain a higher GFA [100], [101]. Besides, depending on the main metalloid elements, Guo et al. [61] have classified Fe-based BMGs into three groups: FeC(B)-, FeB-, and FeP(C)-based BMGs. Among these three, the FeP(C)-based type presents higher ductility and relatively poor GFA. However, low additions of B in the FeP(C)-based can increase the GFA.

It has been reported that the Fe-Mo-P-C-B system exhibits improved GFA in the presence of certain impurities [103], suggesting the potential to produce Fe-Mo-P-C-B BMGs or BMGCs using commercial materials, as long as the composition is properly designed to favor glass formation, which make it a realistic candidate for applications. In this study, a composition design approach is employed to develop a Fe-based BMGC within the Fe-Mo-P-C-B system. This design is guided by the criterion proposed by de Oliveira [14], as detailed in **Subsection 2.1.1.1.**

2.7 Additive manufacturing (AM) by Laser Powder Bed Fusion (LPBF)

According to the ASTM F2792 [104], additive manufacturing (AM) is a technique described as the process able to build three-dimensional (3D) parts layer-by-layer, where each layer of the material is progressively added, being

guided by a digital 3D model. In contrast with subtractive technologies, the AM allows the production of complex or customized parts directly from the design, without the need for expensive tooling or structures such as punches, dies, or casting molds [105]. This unique feature eliminates geometric limitations present in conventional manufacturing processes. There are seven major categories of the additive manufacturing process: binder jetting, directed energy deposition (DED), material extrusion, material jetting, powder bed fusion (PBF), sheet lamination, and vat photopolymerization [104]. For each category, there are sub-categorizations, and the PBF technique includes, for example, direct metal laser sintering (DMLS), electron beam melting (EBM), selective heat sintering (SHS), selective laser sintering (SLS), and Laser powder bed fusion (LPBF) [104]. The LPBF will be discussed further in this section since this method will be used to process the glass-forming Fe-Mo-P-C-B alloys.

By LPBF, the parts are built using a laser energy source and a 3D-CAD computer model. During the processing, the powder layers are selectively melted, following the 3D CAD model, and once a layer is melted, the base plate goes down according to the selected layer thickness, a new powder layer is deposited by the recoater, and the process is repeated until the part is completely built. The processing takes place under an inert atmosphere (argon or nitrogen), and in the final step, the loose powder is removed, sieved, and reused, while the final parts are removed from the plate.

As previously mentioned, the properties of materials are closely linked to their microstructures, which are, in turn, determined by the processing methods used. In AM technologies such as LPBF, a major challenge lies in accurately characterizing and predicting the properties of the fabricated parts based on the processing parameters [105]. This difficulty arises partly because much of the understanding developed from conventional manufacturing—particularly the processing-structure-property relationships—does not directly translate to AM. The extremely short interaction time between the laser and the powder leads to very high cooling rates in the molten pool, typically ranging from 10^3-10^6 K/s [106], [107], [108]. Due to the complexity of instrumenting the smallest molten volume (the melt pool), tracking microstructural evolution during melting, remelting, and

solidification remains a significant challenge [109].

According to the literature [110], many factors are important for the LPBF. They are based on machine specification (laser type, recoater type, substrate, and chamber size), process parameters (laser power, scanning speed, hatch spacing, focal offset distance or spot size, substrate temperature, building chamber atmosphere, scanning strategy, and building direction), materials feedstock (chemical composition, particle size and shape, thermal properties, flowability, and density). Some of the major LPBF parameters are illustrated in **Figure 2.8**, and they can be combined to quantify the energy input per unit volume during the process, which is often estimated using **Equation 2.4** [111]:

$$E = \frac{P}{t * h * v} \qquad \textbf{Equation 2.4}$$

where P is the laser power (watts), t is the layer thickness (mm), h is the hatching distance (mm), and v is the scanning speed (mm/s). These are the most important parameters that impact the quality of the parts, and during the process, they can be adjusted to obtain high-quality parts.

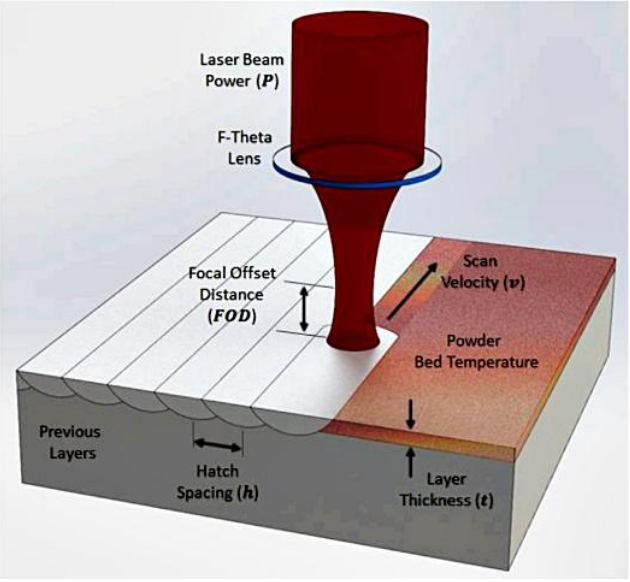

Figure 2.8- Illustration of some parameters of the LPBF process. Source: [111].

In general, there is a relationship between energy input and the relative density of the parts; while low energy density leads to incomplete melt, resulting in fusion errors, excessively high energy promotes evaporation of the melt, and pores are

formed [112], [113]. Besides, the process parameters affect the volumetric energy input and the heat distribution, which directly affect the thermal history of the part additively manufactured. The thermal history strongly influences the microstructure; hence, the material properties are affected. During the parameter's optimization, it is worth starting by selecting the layer thickness, which depends on the powder size, but it is generally in the range of 20-100 μm [110]. Afterward, the laser power and scanning speed should be adjusted by producing single tracks. The hatching or overlapping should be selected from the visual aspect and the width of the single tracks. Su and Yang [114] have reported that the overlapping rate is defined as the ratio of the length of the overlapping zone to the corresponding dimension of the molten pool, mathematically shown in **Equation 2.5**.

$$f_s\ (\%) = \frac{\Delta S}{D}\ x\ 100 \qquad \textbf{Equation 2.5}$$

Where ∆S is the width of the overlapping zone (mm), and D is the width of the single track (mm). The overlap plays a crucial role in producing suitable bounding between tracks, and an inappropriate overlap can reduce the density of the parts. While low overlap implies low energy input, resulting in poor bonding and defects, too high overlaps cause excessive energy input with high heat accumulation, which can affect the residual stress, degrade the surface quality, and facilitate the formation of pores [115]. To predict the effect of an overlap zone on the residual stress induced by the island/chessboard scanning strategy, Chen et al. [116] developed a 3D finite element model, and they observed that the stress decreases first and then increases with the increase of the overlap rate. These authors recommended an overlap rate of 25%–50% for the generally utilized island size [116]. The laser scanning strategy is another process parameter that strongly influences the LPBF parts' porosity, pore distribution, microstructure, and properties [117]. Some of the major scanning strategies are presented in **Figure 2.9**, and each one has been reported as having specific purposes. The chessboard/island (**Figure 2.9 E**), for instance, was developed by the Concept Laser company to alleviate the residual stress of the LPBF parts. However, it is

well-known that laser strategy changes the parts' microstructures, and for the chessboard strategy, the microstructure obtained is composed of elongated columnar grains in the center of each island, and refined misoriented grains between the islands, where a high concentration of cracks is present [118]. Differently, the remelting strategy (**Figure 2.9 F**) is appropriate to increase the relative density and improve the surface roughness [119], [120]. However, in this case, the thermal history of the part is completely modified, affecting its microstructure and properties. So, there is no perfect laser scanning strategy, as it is essential to adjust it to the needs of each alloy. Further, rotation to a certain degree between each melted layer is normally used to reduce the porosity and improve the defects' distribution [121].

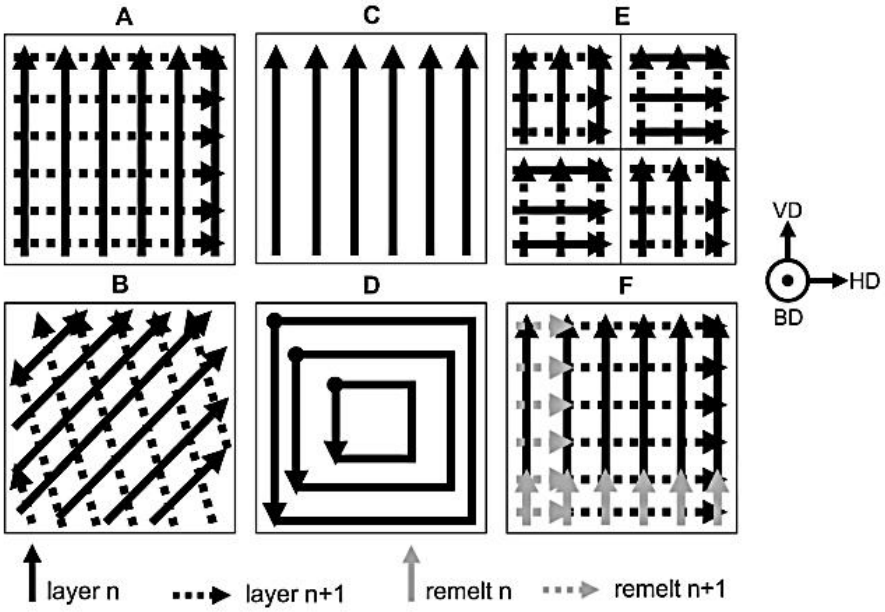

Figure 2.9- Some of the major scanning strategies employed in the LPBF process: A and B: unidirectional scanning with rotation between layers; C: unidirectional scanning without rotation; D: offset scanning; E: chessboard scanning; F: remelting strategy. Where: BD: building direction, VD: vertical direction, HD: horizontal direction. Source: [117].

Even though **Equation 2.4** valuably correlates the main parameters of the LPBF process, other factors, such as powder characteristics, should be appropriately specified for a better understanding of the process. The particle

shape and size distribution, for example, have a crucial influence on the flowability, thermal conductivity, and apparent density of the powders. Powders with high sphericity and normal and unimodal size distribution are, in general, successfully processed by PBF processes [122], [123]. While particles with irregular shapes can influence particle-particle friction and cause physical interlocking during flow, restricting the slippage, spherical shape increases the flow rate of the powders [124]. A symmetric normal size distribution indicates a good batch of powder particles for PBF processes, suggesting a good balance of big and small particles, which results in good powder apparent density [122], [123]. While big particles tend to segregate, small particles tend to agglomerate, and in both cases, the density and surface roughness of the LPBF parts will be compromised [125]. On the other hand, a suitable balance of big and small particles can produce high-quality parts since the small particles can fill the voids between the larger ones, producing dense and uniform powder layers during the processing. Besides, finer particles provide a larger surface area to absorb more laser energy, which, balanced with the big ones, improves the working temperature and thus the melting kinetics [126]. The gas entrapped in the powder particles, which is a pore formed inside the particle during the atomization, is also an important issue for the LPBF process. It contributes to the formation of fusion errors in the LPBF parts; as reported by Olakanmi et al. [127], the entrapped gas can escape when the laser is scanning, resulting in unstable scanning paths (cavities).

Besides the process parameters and powders' properties, Clare et al. [128] have reported the need for alloy design and adaptation for additive manufacturing in order to produce functional parts [128]. That is why, in the first part of this work, a systematic methodology was used to design the chemical composition of the Fe-Mo-P-C-B alloys. After being designed, the selected Fe-Mo-P-C-B alloy was atomized in a gas atomizer available in the Materials Engineering Department at UFSCar.

2.8 Glassy alloys and their composites by AM

Since high cooling rates are, in general, required for the metallic glass formation, BMGs and their composites had been vastly processed by copper-mold suction casting (10-10^2 K/s) [129], gas atomization (10^3-10^5 K/s) [130], and melt spinning (10^4-10^6 K/s) [131]. However, these traditional manufacturing techniques have limits to the achieved cooling rates and size of the components due to the limited heat conduction in bulk. On the other side, the critical cooling rates required for the glassy phase formation are inherent features of the LPBF process, as already mentioned in **section 2.7**. The melt pool in LPBF is very small, and, as a result, the solidification can be achieved very rapidly, bypassing crystallization, and it is possible to obtain a glassy state directly from the metallic melt. At the same time, layer-upon-layer processing allows for producing components with complex geometries. Also, because of the thermal cycling in previous layers, crystals may form by devitrification (crystal formation upon heating of the glassy phase), which provides us with a clue about the use of LPBF to produce BMGCs. Since the maximum cooling rate achieved at the tip of a copper-mold cast wedge (~10^3 K/s) is only comparable to the lower end of the cooling rates typical in LPBF (10^3-10^6 K/s), it is crucial to select alloy compositions with the highest GFA. A higher GFA enhances the likelihood of forming an amorphous matrix during LPBF processing.

In 2004, Fischer et al. [132] reported, for the first time, the processing of an amorphous Pt-Cu-Ni-P alloy by SLS, an AM technique [132]. Afterward, other AM technologies were used to process different glass-forming alloys [133], [134], [135], [136], [137]. However, due to the promising potential of the LPBF for processing MGs, Cu-based [138], [139], Zr-based [140], [141], [142], [143], Al-based [144], [145] and Fe-based [146], [147], [148], [149], [150], [151], [152], [153] alloys have been investigated. From these works, the following conclusions can be highlighted:

- Most of the alloys are partially crystallized, which represents the formation of BMGCs;
- The crystals are formed especially in the heated affected zone (HAZ), the area surrounding the molten pool zone, which suggests crystallization due to the excess heat in the HAZ;

- Most of the alloys presented cracks, suggesting that not only by process parameters optimization, good components are obtained, but that initially, a chemical composition suitable for AM/LPBF, should be carefully selected;
- Several authors reported that higher energy input leads to crystallization, but it improves the density of the parts; on the other hand, at low energy input, the content of the glassy phase is higher, but the powder particles are not completely melted; this suggested that after selecting a suitable chemical composition of the alloy, not only the appropriate energy input should be found, but all process parameters, should be systematically optimized;

Some intrinsic characteristics of the MG alloys can contribute to the porosity of the parts fabricated by LPBF, such as the high liquid viscosity compared to crystalline metals. Additionally, the large thermal gradients inherent to the LPBF process promote uneven thermal expansion and contraction in the parts, resulting in cracks, mainly for those alloys with poor toughness, such as most of the MG alloys [143]. It is known that cracks can occur in any material as long as the applied stress exceeds the fracture strength of that material. As reported by Li et al. [154], the micro-cracks in Fe-based BMGs fabricated by LPBF result from the intense thermal stress concentration around the micro-pores [154]. Other researchers have shown that micro-cracks are mainly localized at the edge between the molten pool and HAZ [155]. These authors also used a finite element model (FEM) to estimate the thermal stress during the LPBF process, and as expected, they found the maximum thermal stress at the edge between the molten pool and HAF, which was about 1.5 GPa. However, this value (1.5 GPa) is far below the fracture strength of the Fe-based BMG, reported at around 3.5 GPa [154]. These results suggest that, in theory, thermal stress is not able to develop micro-cracks by itself if there are no defects in the LPBFed BMG parts [155]. Besides, for LPBFed crystalline parts, heat treatment is a common postprocessing step to stress relief. Differently, stress relief by heat treatment of LPBFed BMGs or BMGCs parts has essentially two challenges: first, the

temperature should be lower than T_x to avoid crystallization events; and second, due to the low thermal conductivity of the metallic glasses, the temperature homogenization would be difficult, especially for large parts.

Intending to achieve high density and amorphization of the LPBFed BMG and BMGC parts, researchers [144], [146], [156] have been working to resolve these two issues *in situ.* For the laser power is well-known that high laser power provides intense crystallization, while a glassy structure is maintained under lower laser power, obviously depending on the chemical homogenization of the molten pool, which, in turn, is a consequence of its thermal fluctuations [156]. Regarding scanning speed, crystallization is favored at low scanning speed, while with increasing the scan speed, the formation of non-stable phases with suppression of crystalline phases occurs. Besides laser power and scan speed, other process parameters modification, especially those related to scanning strategies, have been attempted. For instance, the re-scanning method was used by [144] on an Al-based BMG composite material. The first scanning had high energy input to attain high density, while the second scanning, with low energy, was used to relieve stress. The second scanning not only reduces the stress due to the lower temperature gradient, resulting from the lower heat input, but it is also able to increase the temperature above the supercooled liquid region, where the mobility of the atoms is elevated, and stress is reduced by viscous flow, and then rapidly cool the material to $T < T_g$. In this case, the $Al_{85}Ni_5Y_6Co_2Fe_2$ BMGCs did not present new crystalline phase formation because of the second scanning, and a gear with dimensions of Ø 25 mm and 10 mm of height, free of cracks, was produced [144]. Żrodowski et al. [146] investigated the role of a pulse-random (P-R) remelt strategy on the microstructure of $Fe_{71}Si_{10}B_{11}C_6Cr_2$. By using the checkboard scanning strategy, they melted the first layer and, subsequently, remelted it, using the P-R scanning strategy, which employed random pulses, at least 1 mm apart, to melt the surface. The P-R remelted samples had higher relative density and were four times more amorphous than the samples melted only using the checkerboard melt strategy. Comparing the samples with and without remelting, the aspect ratio (deep/length of the molten pools) was noticeably different, and the authors explained it as a result of the transition

mechanism from conduction to keyhole melting mode. The difference in amorphicity was justified by the variation in laser exposure time. In such a case, after initial melting, the amorphous structure was restored by the P-R strategy, which also reduced stress accumulation enough to allow the production of a crack-free component [146].

Considering the semi-elliptic shape of the molten pool, the literature has reported a temperature decreasing with the increase of the distance from the center of the molten pool [157]. Regarding the thermal history, it has been revealed, for Cu and Al alloys, that the cooling rate decreases from the central part of the melt pool towards its borders [158], [159], [160], [161]. The borders of the molten pools are the heat-affected zone (HAZ). During the LPBF processing of the BMGs and their composites, the additional heat from previous layers may induce structural relaxation or even crystallization in the already solidified glassy parts [142]. Thus, optimizing density, reducing thermal stress, and avoiding crystallization of MG alloys by LPBF is not trivial. Researchers have suggested that crystallization occurs during reheating [143], [138], and/or heat accumulation [162], which can strongly change the microstructures of the parts. Ouyang et al. [143] used a FEM model and indicated that the cooling rate in the melt pool, HAZ, and beyond the HAZ were all sufficient for amorphization of the $Zr_{55}Cu_{30}Ni_5Al_{10}$ alloy, revealing that the reheating at the HAZ results in the formation of nanocrystals, justifying the usual composite structure of this area. However, it is essential to highlight that each alloy composition requires different cooling rates to form the glassy structure. Li et al. [141] have claimed that the partial crystallization events in $Zr_{52.5}Cu_{17.9}Ni_{14.6}Al_{10}Ti_5$ LPBFed result from a nonuniform melt flow at high energy input densities. Thus, the crystals would be a result of the chemical heterogeneity of the supercooled liquid. However, Pauly et al. [140] have opposed this and suggested that these chemical heterogeneities might be a consequence of crystallization rather than their origin [140].

The influence of the substrate temperature on the microstructure of the metallic glass-forming has also been explored. Li et al. [163] processed an Al-Ni-Y-Co-La MG alloy by LPBF using Al-substrates at 25 and 250 ºC and they proved the effect of the substrate temperature on the microstructure of the parts. They

reported that, although with the substrate at 25 ºC, high cooling rates would be expected, due to the lack of bonding between the support and the substrate, the cooling rates were lower, allowing for crystallization. Differently, at 250 ºC, it was more effective to produce strong bonds between the support and the substrate, and larger melt volume, as a result, higher cooling rates, enough to form a glassy structure, were obtained [163].

The main concern regarding crystallization in BMGs/BMGCs produced via LPBF is understanding the role of the crystalline phases on the mechanical properties of the final parts. Thus, one question that arises here is, could, by controlling the LPBF process parameters, the crystalline phases formed in BMGCs be controlled in size and distribution in such a way that the properties of the parts can be improved?

2.9 Main issues of producing MG alloys by LPBF

2.9.1 Powder feedstock characteristics

As well as most additive manufacturing techniques, the powder feedstock for LPBF is mainly fabricated by gas atomization (GA). The powders obtained by GA have typically smooth surfaces, suitable size distribution, and a pretty spherical shape, which are all requirements for the LPBF process. However, some undesirable features as satellite particles and entrapped gas, can also be present in the GA powders, and, depending on their concentration, they may be considered defects for the LPBF. According to the literature, the morphology of MG powders can range from spherical [144], [145], [148], [149], [164],[165], to the elongated shape [148], [163], [164], although the morphology is related to the chemical composition, which leads to the melt viscosity [166]. As well reported [167], the melt of MG alloys has a high viscosity, which avoids atomic rearrangement and crystalline phase formation. Non-spherical particles can reduce the powders' packing, thermal conduction, and uniformity of the deposited layer and, as a result, decrease the density of the LPBFed parts. In addition, owing to the high viscosity of the MG alloys' melt, gas entrapping is highly likely to be formed during the atomization. Malachowska et al. [168] have reported the

difficulty in eliminating the powder porosity in the case of Fe-based MGs during GA. They explained that the entrapped gas formation is related to the gas's kinetic energy during the atomization and the viscosity of the melt [168]. The main consequences of the entrapped gas can be related to defects as pores and cracks, in LPBFed parts MGs [143], [149], [169].

The particle size distribution is crucial in MG powders because the cooling rates are directly related to particle size, so, according to the size, the powder can present a microstructure fully amorphous, partially crystalline, or fully crystalline. Higher amorphous phase content is expected in powders with smaller sizes once small particles achieve high cooling rates. During the LPBF melting process, big particles can have difficulties in being completely melted, especially because of their reduced surface area, which results in lower laser absorption [170], [171]. The fast laser scanning mainly heats the particle surface, and the core should be melted by thermal diffusion [170], [172]. Thus, depending on the process parameters, the big particles might be partially melted, affecting the uniformity of the amorphous/crystalline phase distribution and the final quality of the parts [143], [173]. For instance, Zhang et al. [173] investigated the influence of the particles size of the $Zr_{55}Cu_{30}Al_{10}Ni_5$ alloy in laser-melted layers. They reported that using the same process parameters, the amorphous content was 90.8 %, 78.7 %, and 75.1 % for the 53-75 μm, 75-106 μm, and 106-150 μm powder distributions, respectively. They proposed that using powders size of 53-75 μm, the formed melt pools achieved higher maximum temperature compared to the molten pools formed with 75-106 μm or 106-150 μm sized powder. The high temperature of the melt helps pre-existing crystals and quenched-in nuclei to dissolve, so crystallization is decreased. For the 106-150 μm powders, the thermal conduction and laser absorptivity are lower, as a consequence, pre-existing crystals, nuclei, and atomic clusters inherit from the powder act as crystal nucleation sites during reheating cycles, causing an increase in the crystals content [173]. Balla et al. [174] also processed Fe-Cr-Mo-W-Mn-C-Si-B fine and coarse powders and observed that the incomplete melting of the coarse powder during laser deposition impaired the formation of a fully amorphous structure. Guo et al. [171] showed a reduced volume of the melt when larger $Nb_{52}Si_{20}Ti_{24}Cr_2Al_2$

particles were processed. They claim the discontinues in the laser melt track with the thickness of 200 μm were caused by an inadequate energy absorption in large size particles.

So far, it seems that small particles are more promising for MG powder feedstocks to LPBF. However, it is essential to mention that small particles have a high surface area, which increases their reactivity. This can cause undesirable consequences in the powders, for example, increasing the oxygen content absorbed in the particle surface and other contaminants. Such contaminants can decrease the GFA of the alloys and favor the crystallization once they can act as heterogeneous nucleation sites [175]. Zhang et al. have proposed the oxygen content as the cause of crystallization in $Zr_{65-x}Cu_{27.5}Al_{7.5}O_x$ [176]. Others have claimed that crystallization in HAZ can be reduced by reducing the oxygen content in the virgin powder [173], [177]. Interestingly, Li et al. [178] showed that a critical level of oxygen is effective in enhancing the GFA of a Fe-based BMG. As well as pre-existing nuclei, the oxides can be dissolved by increasing the superheating of the melt; however, excessive superheat can facilitate oxygen absorption due to the increased chemical reactivity of the melt, resulting in oxide-induced crystallization [141]. Other contaminants as Cu, Ni, and Ti have been reported as the apparent cause of crystallization in a laser-melted $Fe_{74}Mo_4P_{10}C_{7.5}B_{2.5}Si_2$ alloy [149]. Nonetheless, it has been reported that even at considerable oxygen content, the high cooling rates achieved by the laser are enough to avoid crystallization for some alloys as those of the Zr-Cu-Al-Nb system [136] and $Ti_{47}Cu_{38}Zr_{7.5}Fe_{2.5}Sn_2Si_1Ag_2$ [179].

2.9.2 Chemical segregation and devitrification in the molten pool

The fast and energetic interaction between the laser and the melted material can cause chemical segregation in the molten pools. For MG alloys, elemental segregation can induce crystallization, even when the cooling rates are higher than the critical cooling rates [141], [145]. According to the literature, the melt can flow by two mechanisms, liquid oscillation and thermo-capillary waves, which then drive the distribution of the elements inside the melt pool [145], [108].

Li et al. have observed a homogeneous elemental distribution when the laser energy density decreased for the $Zr_{52.5}Cu_{17.9}Ni_{14.6}Al_{10}Ti_5$ [141] and $Ti_{47}Cu_{38}Zr_{7.5}Fe_{2.5}Sn_2Si_1Ag_2$ alloys [179]. The researchers [141] found that scanning each melted layer multiple times results in the most homogeneous and amorphous microstructure.

Nevertheless, while re-scanning can improve the homogeneity of the molten pools from a certain number of re-scans, the devitrification phenomenon can occur, especially in the HAZ, as already mentioned. Researchers have explained the devitrification due to the structural relaxation of the HAZ, which creates nuclei and/or small crystals, typically nano-sized and well-rounded. Ouyang et al. [142] investigated the melt pool of LPBF-fabricated $Zr_{55}Cu_{30}Ni_5Al_{10}$ and, by diffraction rings, they proved the HAZ relaxation. Additionally, it is expected that the size of the crystals and the content of crystallization in the HAZ are dependent on the processing parameters. It has been reported that at higher energy densities, the cooling rates are enough for vitrification, however, the time-at-temperature and size of the HAZ are both increased, allowing, as a consequence, nucleation increase and crystals growth [138], [180].

2.10 Fe-based MG alloys by AM/LPBF

In 2013, Pauly et al. [149] reported, for the first time, a Fe-based BMG additively manufactured by the LPBF technique. Since then, Fe-based BMGs and BMGCs have been vastly explored by AM, and especially through LPBF. One can explain this due to their low-cost material, higher strength, hardness, and excellent soft magnetic properties among all BMGs. For instance, compared to the super-high-strength steels, the Fe-based BMGs present strength and hardness 3-4 times higher [181].

According to Zhang et al. [182], the cooling rates achieved in Fe-based glassy alloys during the LPBF process are enough to bypass crystallization. Similar to the other BMGs and their composites, the main challenges of Fe-based MG alloys by LPBF are those related to densification and crystallization control. However, as have reported by [147], [151], [183], stress-induced cracking has

been a common struggle during parameter development of brittle Fe-based MGs. Many studies have been done with different Fe-based systems being processed by LPBF, and some of the main results are going to be mentioned following. Szczepanski et al. [184] obtained a composite structure when LPBFed the $Fe_{79}Zr_6Si_{14}Cu_1$ with low glass-forming ability. While in the HAZ a solid solution of α-Fe(Si) and a low fraction of intermetallic $Fe_{23}Zr_6$ and $FeZr_2$ phases were present, in the center of the molten pool, a nanometric α-Fe(Si) phase and an amorphous matrix were observed. Jung et al. [148] investigated the influence of the LPBF process's laser power and scanning speed on the $Fe_{68.3}C_{6.9}Si_{2.5}B_{6.7}P_{8.7}Cr_{2.3}Mo_{2.5}Al_{2.1}$ alloy. Their results showed that within the range of study, low scan speed (<2500 mm/s) and high laser power (>300 W) produce fully glassy samples with high relative density (>99%). However, all LPBFed samples contained micro-pores and cracks, which requires further tuning of the chemical composition or the processing parameters [148]. Liang et al. [185] fabricated LPBFed porous parts of the $Fe_{70}Cr_5Ni_3Mo_3W_9Si_5B_5$ alloy and observed that the composite nature of the powder was maintained in the LPBFed samples. The identified crystalline phases were α-Fe and Fe_2B, and the volume fraction of the glassy or crystalline phases varied according to the laser power and scanning speed [185]. Other [152] have reported a LPBFed record-large $Fe_{55}Cr_{25}Mo_{16}B_2C_2$ BMG (Ø 45mm x 20 mm), fully amorphous, with the relative density of ~99.0%, nano hardness of 14 GPa, and high yield strength (~4500 MPa). The literature has reported that when Fe-based BMG and their composites are processed by LPBF, a reasonable energy input density is in the range of 30-100 J/mm^3 [185],[186],[187],[188]. Further, as proposed by [182], a multiplicity of phases and microstructures can be produced during printing, even when using a single chemical composition. By carefully controlling the processing of a fully amorphous powder feedstock, LPBF-fabricated components can result from fully glassy structures to dendrite-reinforced metallic matrix composites, or even fully crystalline materials [182].

From a traditional point of view, any alloy composition could form a glassy structure when the applied cooling rate is high enough to that composition [189], [190]. However, the glass structure formation is the result of the suppression of

the nucleation and growth of crystalline phases [190], [191]. Thus, the fabrication of BMGCs needs a favorable combination of chemical composition and processing conditions [192].

3 MATERIALS AND METHODS

This work was developed in different steps: First, the alloy composition was designed, fabricated, and atomized. The resulting powders were then characterized, followed by the fabrication of LPBF samples, which were thoroughly analyzed in terms of microstructure, mechanical properties, and wear behavior. The research was conducted in part at the Department of Materials Engineering (DEMa) at the Federal University of São Carlos (Brazil) and in part at the Erich Schmid Institute of Materials Science (ESI) at the University of Leoben (Austria). The flowcharts in **Figure 3.1** outline the key questions addressed and the methods applied at each stage of the work.

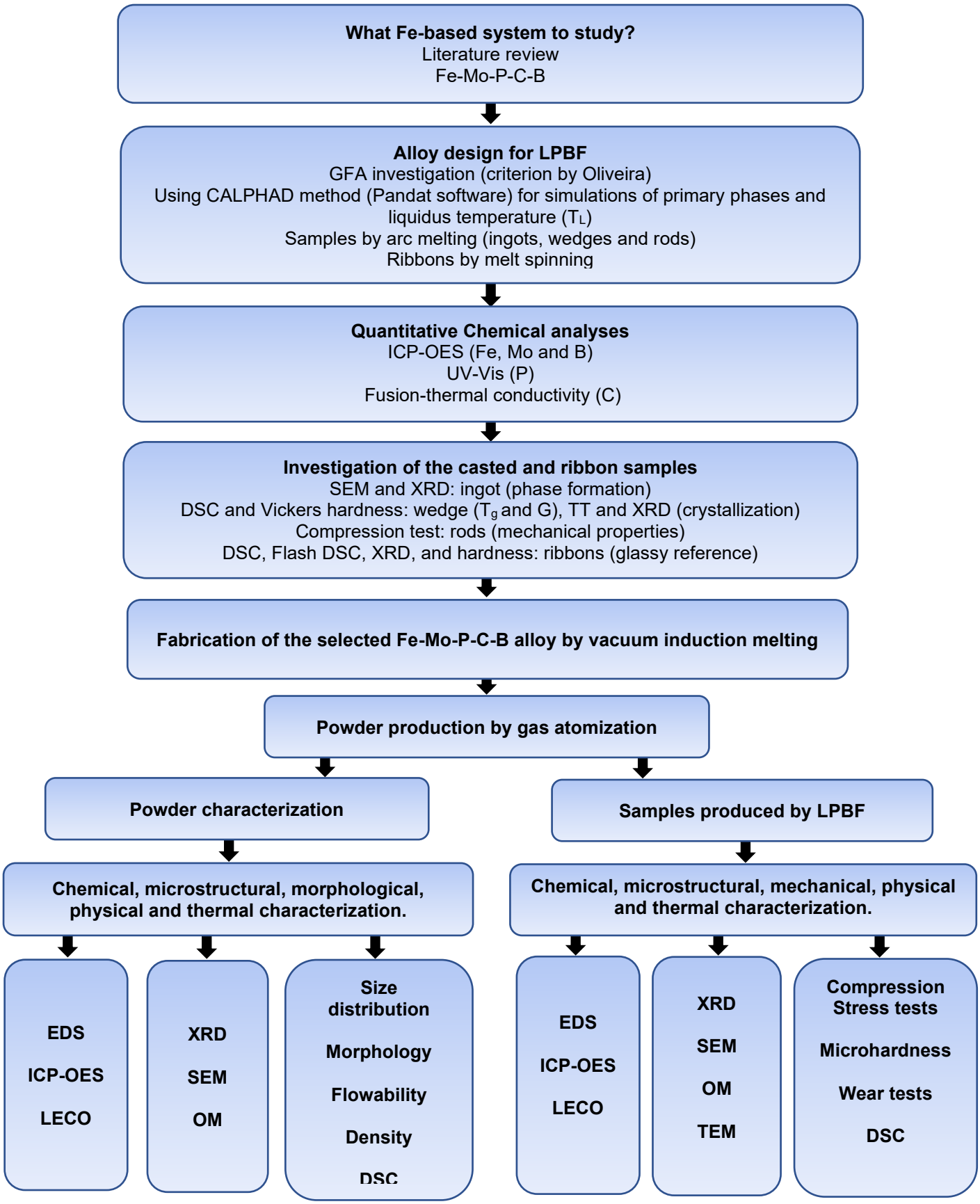

Figure 3.1- Flowchart of the experimental procedure developed in this study.

3.1. Materials

The materials used in this work were all commercial (**Figure 3.2**): 1004 steel, ferroalloys (Fe-60Mo wt%; Fe-25P wt%; Fe-16B wt%), and high-density carbon. The chemical compositions reported in the quality certificate are in **Table 3.1**.

Figure 3.2- Commercial materials used to produce the Fe-Mo-P-C-B alloys.

Table 3.1- Chemical composition (weight %) of the used materials.

Element	1004 steel	Fe-60Mo	Fe-25P	Fe-16B
Fe	99.96	40.00	74.00	84.00
Mo	-	60.00	-	-
C	0.04	-	-	-
P	-	-	26.00	-
B	-	-	-	16.00

3.2. Methods

3.2.1. Design of the Fe-Mo-P-C-B alloys

3.2.1.1 Glass forming ability (GFA) investigation

As the aim of this work was to produce Fe-based glassy alloys using commercial raw materials under low vacuum conditions, the first step was to find a Fe-based system where the presence of some foreign elements does not significantly hinder the glass formation. From the literature [193], molybdenum (Mo) was spotted as a promising alloying element for the Fe-(Si, P, C, B)-based metallic glasses. However, Guo et a. [54] have reported that in Fe–(B, Si)-based alloy systems, brittle Fe–B metastable phases such as $Fe_{23}B_6$ are usually formed instead of precipitation of the equilibrium body-centered cubic (bcc) α-Fe phase during the complicated crystallization processes. On the other hand, they highlighted that for Fe–(P, C)-based glassy alloys, the formation of the (bcc) α-Fe phase as the primary phase seems to be relatively simple [54]. Additionally, works have suggested the Fe-Mo-P-C-B as a system where the glass-forming ability (GFA) is enhanced when some foreign elements are present in the alloy [103]. Further, the authors [54] have shown unprecedented plasticity (>30%) for a Fe-Mo-P-C-B BMG composite. Taking all into consideration, the system (Fe-Mo-P-C-B) was selected to be studied in this work. According to the literature [74], [75], for Fe-based BMGs, the promising range of metalloid additions is 17 to 25 at. %.. To investigate the glass-forming ability (GFA) of this system, the criterion proposed by de Oliveira [14], already explained in **section 2.1.1** (subsection 2.1.1.1), was chosen. The data used to feed the GFA software was collected from the available literature, considering all binary (Fe-Mo, Fe-P, Fe-C, Fe-B, Mo-P, Mo-C, Mo-B, P-C, C-B, and P-B), ternary (Fe-Mo-P, Fe-Mo-C, Fe-Mo-B, Mo-P-C, Mo-P-B, Mo-C-B, P-C-B, P-B-Fe, P-C-Fe, and C-B-Fe), quaternary (Fe-Mo-P-C, Fe-Mo-P-B, Fe-P-C-B, Fe-Mo-C-B, and Mo-P-C-B), and quinary (Fe-Mo-P-C-B) systems. Only those phases formed above 380 °C for the binary, ternary, quaternary, and quinary systems were considered in the calculations because the glass transition temperatures in this system are usually

higher than this temperature. By the data survey, the following phases were found as possible competitors of the glassy phase:

- **Without solid solubility**: Fe_3P_1, Fe_2P_1 (metastable), Fe_1P_1 (metastable), Fe_1P_2, Fe_1P_4, Fe_3C_1, Fe_2C_1, $Fe_{23}C_6$, Fe_2B, Fe_3B (metastable), Mo_2C, Fe_2Mo_6, Fe_7Mo_6, Fe_6C, Mo_6C, Fe_3B, Mo_3C, Mo_3B, MoC, MoB, FeC, FeB, Fe_2Mo_3.
- **With solid solubility**:
- **Austenite**: Fe-Mo (0-1.7 Mo at%); Fe-C (0-9.0 C at%), Fe-P (0-1.7 P at%).
- **Ferrite**: Fe-Mo (0-24.42 Mo at%); Fe-C (0-0.0853 C at%), Fe-P (0-5.0 P at%).

All phases were converted into their stoichiometric chemical unit formula, only considering the integer numbers, since the GFA software does not accept fractional numbers in the formula. Files of competing phases were created according to the requirements of the GFA software. For each simulation, all competing phases (with and without solid solubility, stable and metastable) were considered, as this is the stricter scenario for the glassy phase formation.

This work aimed to produce a Fe-rich glassy alloy and, by the variation in the Mo content, to investigate which metalloid (ML) isopleth (Fe_X-Mo_Y-ML_{17-25} (%at.), where ML= P+C+B) is more promising for the GFA of the system. To select the range of composition to study, some considerations relating to alloy production and theories of metallic glasses were proposed:

1- High content of B (>3 at. %) is good for glassy phase formation, but increases the tendency of the LPBF parts to crack; Precisely controlling the B content in the alloy is challenging for two main reasons: first, due to the low density of the Fe-B, they tend to float to the surface during ingot production; second, B tends to evaporate during the melting process;

2- P element also evaporates; however, the behavior of this evaporation was already understood by the experiments on the arc melt furnace (shown in results section); additionally, P has a lower rate (~2% wt.) of evaporation in the Vacuum Induction Melting (VIM) furnace;

3- When comparing the binary diagrams of Fe-P (T_L=1048°C), Fe-C

(T_L=1148°C), and Fe-B (T_L=1177°C), the Fe-P presents the lowest temperature for the eutectic point, which indicates lower T_L for the alloys with higher content of P;

4- According to the literature [61], in Fe-based BMGs, the electronic density of states in Fe_3M (M=C, B, P) binary alloys demonstrates an increasing metallicity from C through B to P; The increasing metallicity weakens the metal-metalloid connections, lowers the shear modulus, and elevates the Poisson's ratio, which are both desired in this work;
5- Increasing the P content within the metalloid content range of 17 – 25 at. %, the highest content of P achieved is 16 at. %, which is pretty close to the Fe-P eutectic composition (17 at. % P);

From all considerations, the selected content of metalloid elements to be investigated in this work was as follows:

Table 3.2- Content of metalloid elements varied in the simulations.

Total metalloid content (at. %)	P (at. %)	C (at. %)	B (at. %)
17 - 25	8 - 16	7.5	1.5

3.2.1.2 Liquidus temperature and primary phase investigation

From the previous GFA investigations, with the details provided in the results section, the metalloid isopleth of 18 at. % was selected to be further studied, which is the $Fe_xMo_yP_{9.0}C_{7.5}B_{1.5}$ alloy. The content of Mo was varied from 0 to 6 at. %. The phase diagram and path of solidification for the $Fe_xMo_yP_{9.0}C_{7.5}B_{1.5}$ alloy were built to understand the behavior of its liquidus temperature (T_L) and primary phase formation as a function of Mo content. All calculations were executed using the CALPHAD (CALculation of PHAse Diagram) method through the Pandat^{TM} software [194]. Pandat's thermodynamic database for multi-component Fe-rich alloys has the composition range of elements in wt.% of Fe: 50-100; Mo: 0-10; P: 0.-0.1; C: 0-5, B: 0-5 and the binaries

(Fe-Mo, Fe-P, Fe-C, Fe-B, Mo-P, Mo-C, Mo-B, P-C, C-B, P-B) described in [195]. All calculations were carried out using the alloys' chemical composition in atomic percentage (% at.), with the details provided in the results section. The path of solidification was calculated under equilibrium conditions instead of using the Scheil model. It is clear that both conditions are far from the real solidification condition studied in this work; however, the solidification results under equilibrium conditions can be compared with those from the experimental "equilibrium solidification" (ingot). On the other hand, the Scheil model assumes perfect mixing in the liquid and no back solute diffusion in the solid [196], and no experimental results obtained in this work would be similar to this case.

3.2.1.3 Quantitative chemical analyses of the raw material

Before starting the experimental tests, the chemical composition of each material was measured except for the high-density carbon. The 1004 steel was analyzed by spark optical emission spectrometry (S-OES) using a method called Fe-10-F. The carbon content in the 1004 steel was measured through LECO combustion analysis (CS844). The ferroalloys Fe-Mo, Fe-B and Fe-P were analyzed using an Inductively Coupled Plasma Optical Emission Spectrometry (ICP-OES) instrument (Thermo, Model iCAP 7000). The sample decomposition consisted of weighing 100 mg of sample in triplicate and adding 8.0 mL of HNO_3:HCl (1:3 ratio v v^{-1}) to the samples. The analytical blank was prepared using the same procedure without the sample. The samples remained under the action of the acid mixture for 30 min, and immediately afterward, they were kept heating at 100 °C in a closed block digestor for 3 h. After cooling down to room temperature, the samples were transferred to polypropylene tubes and made up to 50 mL with deionized water. To precisely determine the phosphorus content, the Ultraviolet-Visible Spectroscopy (UV-Vis) technique was applied using a Varian instrument, Model: Cary 50 Conc. Here, the sample preparation was the same used for ICP-OES analyses. The chemical compositions of the raw materials are in **Table 3.3**.

Table 3.3- Measured chemical composition (weight %) of the used raw materials.

Element	1004 steel	Fe-60Mo	Fe-25P	Fe-16B
Fe	99.35	37.39	71.90	82.49
Mo	0.001	60.36	-	-
Co	0.006	-	-	-
Cu	0.0043	0.85	-	-
C	0.0467	-	-	-
S	0.017	0.12	-	-
Mn	0.374	-	0.21	-
P	0.024	0.07	26.16	0.034
Si	0.085	1.21	0.48	0.57
Ti	-	-	0.122	-
Cr	0.009	-	0.330	-
V	-	-	0.179	-
Al	0.006	-	0.045	0.044
B	0.002	-	-	16.27

3.2.1.4 Alloys preparation by arc melting

The six alloys selected from the theoretical studies were produced by arc melting using Edmund Bühler GmbH MAM 1 Arc melter. Before melting, the 1004 steel pieces were etched with concentrated HNO_3 for 5 min.

As an inhomogeneity of the element phosphorus in the ferroalloy Fe-25P (wt%) was detected, a specific procedure was used to prepare the load of the alloys. To ensure the chemical homogeneity of the phosphorus in the alloys, at first, 500 grams of the ferroalloy Fe-25P (wt%) were smashed (**Figure 3.3a)**), mixed, and randomized by quartering (**Figure 3.3b)**). Thus, a sample was taken to be analyzed by ICP-OES and UV-Vis, following the procedures mentioned in **section 3.2.1.3**. The Fe-P powder was compacted, using a cold-press machine (**Figure 3.3c)**), in a cylindrical shape (**Figure 3.3d)**) with a varied mass of 4, 3, and 2 grams (**Figure 3.3e)**), and pressures of 15 MPa, 13 MPa, and 10 MPa were used for each mass, respectively. It was used an organic oleic acid ($C_{18}H_{34}O_2$) as lubricant for the mould. The first arc melt experiments were executed to

understand the P evaporation. Here, an evaporation amount of 33.5% at. was observed. Because of this, all loads have considered this evaporation.

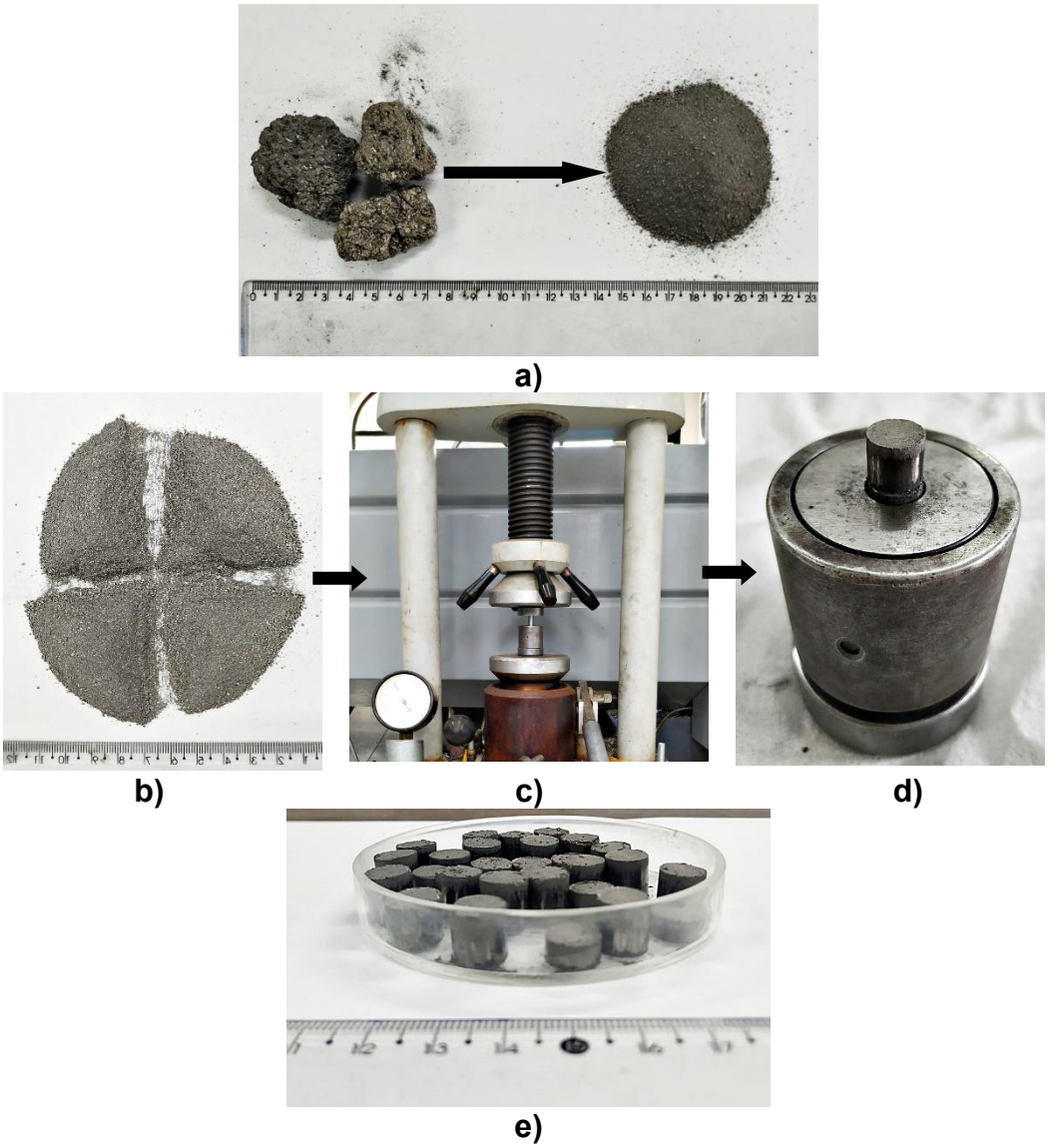

Figure 3.3- Procedure utilized to prepare the ferroalloy Fe-P before being submitted to arc melting. **a)** Fe-P as received and after smashed; **b)** quartering; **c)** cold press machine; **d)** cylinder in the mold after being compacted; **e)** final compacted cylinders.

A load of each alloy was prepared as shown in **Figure 3.4a)**. A button-like

ingot (20g) was produced for each alloy (**Figure 3.4b)**) and remelted five to eight times until they were visually homogeneous. Subsequently, a piece of ~5 grams of each button-like ingot was used to produce a wedge-shaped (**Figure 3.4c)**) sample by suction casting in a water-cooled copper mould. For the most promising alloys, a casted rod-shaped sample (Ø=2 mm x 30 mm) was also produced.

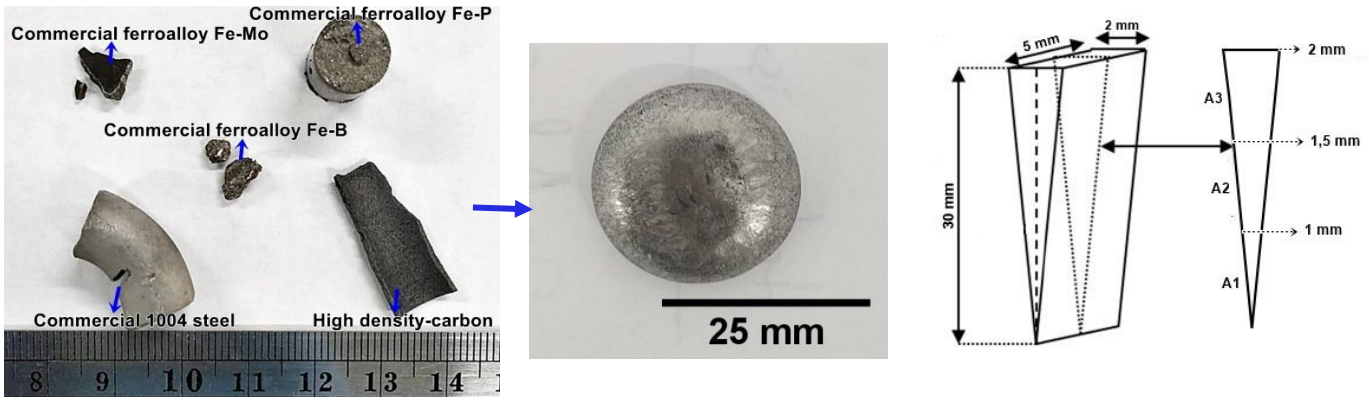

a) **b)** **c)**

Figure 3.4- a) Load of each Fe-Mo-P-C-B alloy, **b)** ingot produced by arc melting, and **c)** geometry of the cast samples.

3.2.1.5 Characterization of the arc-melted samples

The ingots' microstructure of each alloy was first analyzed by Optical Microscopy (OM), Olympus microscope (BX41M-LED), and Scanning Electron Microscopy (SEM-FEI QUANTA 400 model). To measure the chemical composition of the ingots, chemical microanalyses were performed by an energy-dispersive spectrometer (EDS Oxford Instruments, INCAx-sight model) attached to the SEM. By X-ray diffraction (XRD), using a diffractometer Siemens Model D5005 with Cu-K_α radiation with a range of 20-100° and a step size of 2 °/min, the phase formation was also analyzed.

The wedge-shaped samples were cut at the center of the longitudinal section in three areas (A1, A2, and A3) in the transversal section, from the

thinnest to the thickest area (see **Figure 3.4c)**). Then, half of the wedges were embedded and prepared by grinding and polishing, and the other half was used for DSC analyses as described below. To identify the most promising alloy composition to be processed by LPBF, the toughness of the alloys was used as a guideline. Therefore, the toughness of the alloys was investigated, taking into consideration the two conditions (shear modulus (G) < 60 MPa and T_g < 440 °C), as suggested by Demetriou and Johnson[197]. They assessed that Fe-based P-containing BMGs with these two conditions satisfied are tough. Thus, while T_g of the wedges was measured by Differential Scanning Calorimetry (DSC) using a Netzsch DSC 404 calorimeter with the rate of 40 K/min and a protective atmosphere of argon, the G was estimated using **Equation 3.1** [198] and Vickers microhardness (Hv) measurements. These measurements were carried out on the whole section of the wedges using an FM-800 (Future-Tech). The G was estimated using the microhardness of the thinnest area of the wedge (A1). All indents were made at room temperature with a load of 500 gf and a loading time of 10 seconds.

$$G = \frac{H_V}{0.151} \qquad \textbf{Equation 3.1}$$

Additionally, OM and SEM/EDS images were taken from the cross section of the whole area of the wedges using the same devices described above for the ingots' examination. To follow the crystallization process of the V5 and V6 alloys, the A3 area of each wedge was submitted to controlled annealing treatment using the same DSC device used to measure T_g of the wedges. After each annealing step, the same sample was investigated by XRD using a Bruker D2 Phaser (MA, USA), Tabletop XRD system with Co-anode and energy dispersive 1-D detector system LYNXEYE and autosampler, with Co-K_α radiation (λ=1.79026 Å) and Fe as the Kβ filter. Diffraction patterns were recorded between 2θ = 20° and 120° with a step size of 0.02°.

The specimens for the compression test were cut from V5 and V6 casted rods, and each end was polished parallel to each other. The mechanical behavior of 5 cast samples with a diameter of 2.0 mm and an aspect ratio of 2:1 was examined under uniaxial compression using an Instron testing machine at room

temperature with a strain rate of $1x10^{-4}$ s^{-1}. The tests were carried out in a constant-crosshead-displacement-rate controlled manner. The fracture surface morphology results were examined by scanning electron microscopy (SEM).

3.2.2. Ribbons produced by melt spinning

The alloys selected to be gas atomized were also processed by melting spinning in order to obtain a reference for the glassy phase amount. The ingots produced in the arc-melt furnace were used to be rapidly solidified using an Edmund Buhler model D-7400 vacuum melt spinner. 5 g of the alloy was remelted under an argon atmosphere in a quartz crucible whose bottom was in the form circle (Ø=1mm) and ejected onto a rotating Cu wheel (200 mm diameter) with 70 Hz of frequency. The Nozzle-wheel gap was ~2 mm, ejection pressure ΔP=200 Mbar, and 100°C of superheating was used. The as-melt-spun ribbons have been characterized by XRD and DCS using the same devices and parameters used for the wedge samples. Flash DSC measurements were also carried out using ultra-fast calorimeter Mettler Toledo (Ohio, US) FLASH DSC 2+, with an intracooler TC100-MT from Huber Kältemaschinenbau AG (Germany). The sensor chips were high-temperature chips UFH 1, for temperatures up to 1273 K from Mettler Toledo. Vickers hardness was measured using a Shimadzu HMV-G20ST with a load of 0.025 kg and an indentation time of 15 s, at 10 random positions.

3.2.3. Alloy preparation by VIM and powder fabrication

Firstly, ingots of the designed Fe-Mo-P-C-B alloys ($Fe_{79}Mo_3P_9C_{7.5}B_{1.5}$ $Fe_{77}Mo_5P_9C_{7.5}B_{1.5}$ (%at.)) were prepared in a Vacuum Induction Melting (VIM) furnace (**Figure 3.5a)**) and solidified in a graphite mold. The as-cast ingots were chemically analyzed by EDS, ICP-OES, and LECO. The ingots' microstructure was investigated using a FEI Scanning Electron Microscopy (SEM) FEI QUANTA 400 model and chemical microanalyses were performed by an energy-dispersive spectrometer (EDS Oxford Instruments, INCAx-sight model) attached to the SEM. Ingots' samples were etched with aqua regia and observed by an Optical

Microscopy (OM) Olympus microscope (BX41M-LED). The nature of the phases presented in the ingots' samples was investigated by X-ray diffraction (XRD), using a diffractometer Siemens Model D5005 with Cu-Kα radiation with a range of 20-100° and a step size of 2 º/min. Subsequently, the ingots were atomized (**Figure 3.5b)**) in a gas atomizer (PSI Hermiga 75/5VI) using argon as atomization gas with 40 bar of pressure and a gas-to-melt mass flow ratio (GMR) of about 3. The powders produced were sieved and physically (particle size distribution, morphology, density) and microstructurally (phase formation and coarsening of the microstructure) characterized before being processed by LPBF.

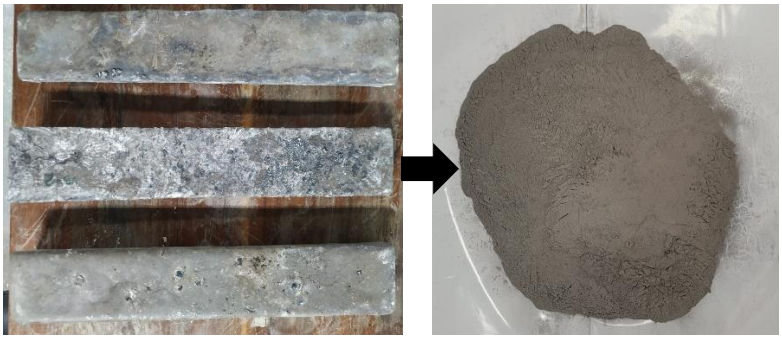

a) **b)**

Figure 3.5- Image of **a)** As-casted VIM ingots and **b)** As-gas-atomized powder.

3.2.3.1 Powders separation and characterization

The total amount of powder produced for each alloy was classified by sieving in the range of +20 µm – -75 µm. In order to characterize the range of interest (+20 µm – -75 µm) the sample volume was reduced by taking a representative subsample from a thoroughly mixed larger sample via the quartering method (ASTM53 C702/C702M- method B) [199]. In this step, a Haver & Boecker EML Digital Plus device and sieves with different mesh were used to carry out the separation. The powders were physically investigated according to the particle size distribution following ASTM B822 and using a Laser Scattering Particle Size Distribution Analyzer 930 brand Horiba. The tapped (ρ_t) density of the powders was performed using a JEL STAV II device (J. Engelsmann AG, Ludwigshafen, Germany) according to the DIN ISO 3953 standard, testing a

mass of 100 g with a frequency of 5 tap/s after 3000 tap cycles. The powders' flowability and apparent (ρ_a) density were also evaluated using the Carney funnel (Ø=5mm and 100g of powder) following the standard ASTM B964 (method 2). The powder shape and microstructure were examined through Optical Microscopy (OM), using an Olympus microscope (BX41M-LED), and by Scanning Electron Microscopy (SEM), using a FEI Scanning Electron Microscopy (SEM) FEI QUANTA 400 model. Chemical microanalyses were performed by an energy-dispersive spectrometer (EDS Oxford Instruments, INCAx-sight model) attached to the SEM. The carbon and oxygen content in the atomized powders was measured using LECO-CS844 and LECO-ONH836 Instruments inert gas fusion (IGF) machines, respectively, and three measurements were made to obtain an average value of C and O concentration. The phase formation of the powders was evaluated by X-ray Diffraction (XRD) experiments using a Siemens Model D5005 diffractometer with Cu-Kα radiation, with a range of 20-100° and a step size of 2º/min. The XRD device Bruker D2 Phaser (MA, USA), a Tabletop XRD system with Co-anode and energy dispersive 1-D detector system LYNXEYE and autosampler, with Co-Kα radiation (λ=1.79026 Å) and Fe as the Kβ filter was also used. Diffraction patterns were recorded between 2θ = 20° and 120° with a step size of 0.02°. The thermal stability of the powders was ascertained by Differential Scanning Calorimetry (DSC) using a Netzsch DSC 404 calorimeter with a heating/cooling rate of 20K/min and 40 K/min and with an argon protective atmosphere. Each sample was subjected to two heating cycles to evaluate the presence and stability of glassy phases.

3.2.4. Fabrication of samples by LPBF

Before each LPBF experiment, V5 and V6 powders were dried at 80°C for 24h in a drying oven with air circulation. For the experiments, three LPBF machines were used:

1- The first exploratory LPBF experiments were conducted to investigate the powders' behaviors during the processing and the alloys' aspects under different LPBF process parameters. An OmniSint-160 machine (Omnitek-Brazil),

equipped with a Yttrium-Aluminum-Garnet doped with Erbium (Yb:YAG) laser and a beam diameter of 90 μm was used. Argon was used as the protective gas, maintaining the residual oxygen < 400 ppm to prevent powder oxidation, and an unheated 1020 carbon steel substrate (Ø=156mm and thickness of 25mm) was used. The powders were melted using the process parameters: uni-directional and chessboard-like (400 μm stroke) laser scanning strategy, layer thickness of 50 μm, and hatch spacing of 30 μm. For each layer, the scanning vectors were rotated by 79°. Here, cubic (6x6 mm) deposits of 10 layers (~0.5 mm thick) were produced systematically varying laser power (P=90, 130, 170, 210, 250, 290, and 330W) and scan speed (V= 100-1000 mm/s). Two sample groups were fabricated, one without remelting and the other with the remelting step for each layer, using the same combination of parameters for melting and remelting.

2- AconityMINI (Germany) with a ytterbium fiber laser and laser spot size of 60 μm. Argon was used as a protective gas, and during the processing, the residual oxygen content was <100 ppm. A 316L steel substrate (Ø=100 mm and thickness of 20 mm) heated at 200°C was used. The powders were melted using the process parameters: chessboard (400 μm stroke) laser scanning strategy, layer thickness of 50 μm, and hatch spacing of 30 μm. For each layer, the scanning vectors were rotated by 79°. Here, cubic (6x6 mm) deposits of 20 layers (~1mm thick) were produced with the most promising laser powers (P=90, 130, 170, and 210W) and scan speed (V=300-1000 mm/s) from the previous experiments. All the samples were fabricated with the remelting step (for each layer), using the same combination of parameters used for the melting.

3- Acconity Midi+ (Germany) with an ytterbium fiber laser and laser spot size of 80 μm. Argon was used as a protective gas, the process started at <600 ppm, and the residual oxygen content achieved less than 100 ppm during the processing. Substrates of CK45 carbon steel (no heated) and 316L steel (Ø=55 mm and thickness of ~12 mm) without and with heating (150 ± 20°C) were used. The powders were melted using different layer thicknesses (50, 70, 90, and 100 μm), and hatch spacing (30, 40, and 50 μm). For each layer, the scanning vectors were rotated by 79°. Here, samples without contour of different geometries (donut, cube, ring, parallelepiped, and cylinder) and sizes (maximum 11mm

height) were built with different combinations of laser powers ($P_{minimum}$=50 W and $P_{maximum}$=210 W) and scan speed ($V_{minimum}$=100 mm/s and $V_{maximum}$=3000 mm/s). Three different laser scanning strategies were also applied: uni-directional (Single Normal-SN), uni-directional randomized (Single Random-SR), and island/chessboard-like (400 μm stroke). Samples were fabricated without and with remelting, some of them using the same combinations of parameters used for the melting, and some using different combinations of parameters. With the best parameters combination, samples for the compression test were built in 0°, 45°, and 90° with respect to the Z-axis. In these experiments, Autodesk Netfabb software was used for designing and building the 3D files before each printing. The slicing and filling were also generated using Netfabb. Python was used to develop a randomizer strip laser strategy.

3.2.5. LPBF samples preparation and density investigation

The LPBF samples were removed from the substrate with a wire electrical discharge machining (EDM) - MV1200-S Advance Type M800. The samples were embedded in polymer resin in the build direction (BD), and two deep (from the side surface), of each sample were ground and polished for defect analysis. Diamond pastes of decreasing particle sizes (down to 1/4 μm) were used for optimal surface finish. An Olympus BX51 optical light microscope and Olympus LEXT OLS4100 laser scanning digital microscope were then used to image the mirror-polished whole cross-section area of the samples using 25x magnification. The software ImageJ/Fiji was then utilized to classify and separate different defect types (pores and cracks) by thresholding and binarizing the samples' images. After that, Fiji's machine learning-assisted segmentation plug-in, the WEKA Trainable Segmentation package, was utilized to isolate pores and cracks and then estimate the area fraction of each (details about the procedure are provided in the Appendix). Besides the relative density quantified from the optical micrographs, the Archimedes density for the densest LPBF samples was measured following ASTM B962 to obtain the bulk property. Samples were measured three times dry and three times submerged, and the results were combined to obtain the average density of each sample by the Archimedes

method. The standard error of the mean for each measured sample was less than 0.07% of the value. The calculated theoretical densities of 7.52 and 7.65 g/cm^3, for V5 and V6, respectively, were assumed as the references for a fully dense material.

3.2.6. Microstructural and thermal characterization of the LPBFed samples

The (micro)structure of the LPBF samples was first characterized qualitatively by optical microscopy imaging of etched cross sections parallel to the building direction. The etching solution, consisting of hydrochloric acid and nitric acid in a 3:1 ratio (aqua regia), was applied to mirror-polished cross sections, and it attacked preferentially the crystalline regions, allowing for detection of their preferential location within melt pools. Etching was carried out by gently rubbing the surface of the sample with a cotton swab moistened with aqua regia for 30-40 s, followed by acetone rinsing and drying with soft paper. After, an Olympus microscope (BX41M-LED) was used to take the images. X-ray diffraction (XRD) analyses were also conducted on mirror-polished cross-sections parallel to the build direction to characterize qualitatively the presence and nature of different phases (glassy/crystalline) in the LPBF parts. For the XRD analyses, a diffractometer Siemens Model D5005 with Cu-Kα radiation with a range of 20-100° and a step size of 2 º/min was used. A XRD device, Bruker D2 Phaser (MA, USA), Tabletop XRD system with Co-anode and energy dispersive 1-D detector system LYNXEYE and autosampler, with Co-Kα radiation (λ=1.79026 Å) and Fe as the Kβ filter was also used. Diffraction patterns were recorded between 2θ = 20° and 120° with a step size of 0.02°. The glassy fraction was additionally quantified by Differential Scanning Calorimetry (DSC) using a Netzsch DSC 404 calorimeter with a protective argon atmosphere using heating rates of 20 K/min and 40 K/min. Each sample was subjected to two heating cycles. The microstructure of the samples was further investigated by Scanning Electron Microscope (SEM) using a Tescan MAGNA, equipped with an electron backscatter diffraction detector (Bruker), and an electron dispersive X-ray detector (Bruker). A Dual-Beam Focused Ion Beam/Scanning Electron

Microscope (FIB-SEM) (Scios 2 DualBeam) with gallium ion beam and platinum deposition was used to prepare thin foil TEM samples. Specimens were removed from the melt pool center (MP) and from the heat-affected-zone (HAZ) for analysis by transmission electron microscope (TEM), using a Talos F200X G2 TEM (TEM/STEM) equipped with a cold field emission gun (X-CFEG) operating at 200 kV.

3.2.7. Mechanical characterization of the LPBFed samples

Nanoindentation measurements on the polished flat side of the LPBF samples (thickness: ~0.5 mm, produced using the OmniSint-160 machine) were carried out at room temperature in air using a nanoindentation apparatus (Anton Paar, NHT2) with a Vickers diamond indenter along with the build direction. Parameters used: linear loading, maximum depth of 500 nm, loading and unloading rate of 250 nm/min, pause of 15 s with a point spacing of at least 15 µm. Six indents were performed for each region (glassy = melt pool center (MPC) and crystallized Heat Affected Zone (HAZ)) of each sample.

Vickers microhardness measurements were carried out at the LPBF samples (thickness: ~1 mm, produced using the AconityMINI machine) using an FM-800 (Future-Tech). All indents were made at room temperature with a load of 500g and a loading time of 10s. All 10 indents analyzed for each sample were placed at random positions in specific regions of the sample.

The LPBF samples produced using the Acconity Midi+ machine were tested in a Vickers microhardness tester, EMCOTEST DURASCAN from ZwickRoell, with a load of 200g and a time of 10 seconds for indentation.

The mechanical behavior of the as-built LPBF samples (P80_V600_SN_0°, 45°, 90°; P80_V600_chess_0°; P70_V400_SN_0°; P70_V400_chess_0°; P60_V100-500_SN and chess_0°) was investigated through compression tests using an INSTRON 5900R-5569/50KN with a constant crosshead speed of 0.048 mm/min (~1×10^{-4} s^{-1}) and coupled with an INSTRON 2663-821 (model AVE 1) advanced video extensometer.

3.2.8. Wear tests of the LPBFed samples

Reciprocating ball-on-flat wear tests were conducted on the LPBF samples (P80_V600_SN_0°, 45°, 90°; and P80_V600_chess_0°) using Plint & Partners TE 67/R equipment. The tests followed ASTM G133-05, procedure A, with a normal load of 25 N, a frequency of 5 Hz, a slip speed of 0.1 m/s, and a total sliding distance of 100 m. Tests were performed at a relative humidity of 50 ± 10% and room temperature (25 ± 5 °C). A deviation from the standard procedure was made due to the use of an alumina pin with a radius of 2.6 mm and a stroke length of 5 mm. The coefficient of friction (COF) was recorded during the tests. Volume loss was determined through 3D topographic analysis of the worn surfaces using an Alicona InfiniteFocus SL optical microscope. The specific wear rate (k) was calculated using the equation $k = V / (W \times L)$, where V is the wear volume loss (mm^3), W is the normal force (N), and L is the total sliding distance (m). Worn surfaces were examined using scanning electron microscopy (SEM; FEI Quanta 400). Vickers hardness measurements were performed using a Shimadzu HMV-G20ST with a 0.5 kg load and an indentation time of 10 seconds, at 7–10 randomly selected positions.

4 RESULTS AND DISCUSSIONS

4.1 Fe-Mo-P-C-B alloys design and selection

The glass-forming ability (GFA) of the alloys is based on their critical cooling rates (R_c (K/s)). The theoretical R_c results of the Fe-Mo-P-C-B alloy are shown in **Figure 4.1a)** and **4.1b)** as a function of the metalloid content. The lower the R_c, the higher the GFA, as lower cooling rates are required to form the glassy phase for that alloy composition. From **Figure 4.1**, one can see that increasing the metalloid content in the Fe-Mo-P-C-B alloy decreases the R_c. In the range of 23-25 % at. of metalloid, the R_c does not change significantly.

For the $Fe_{77}Mo_5P_9C_{7.5}B_{1.5}$ alloy, the R_c predicted by the GFA simulations (~10^4 K/s) agrees with the estimated R_c calculated by **Equation 4.1** [14] and presented in **Table 4.1** (1.17 x 10^4 K/s).

$$R_c \cong \alpha \, \Delta T_n \, \frac{1}{Z_c^2} \qquad \textbf{Equation 4.1}$$

where α is the thermal diffusivity of the alloy and ΔT_n is the undercooling at the nose of the time-temperature-transformation (TTT) diagram for crystallization of the liquid, and $\Delta T_n \sim T_m/3$, where T_m is the melting point in K. Z_C is the critical amorphous thickness experimentally obtained. For the $Fe_{77}Mo_5P_9C_{7.5}B_{1.5}$ alloy, authors have reported Z_C = ~1.00 mm [54], [85]. The estimated R_c and the values of the parameters used in its calculation are shown in **Table 4.2**.

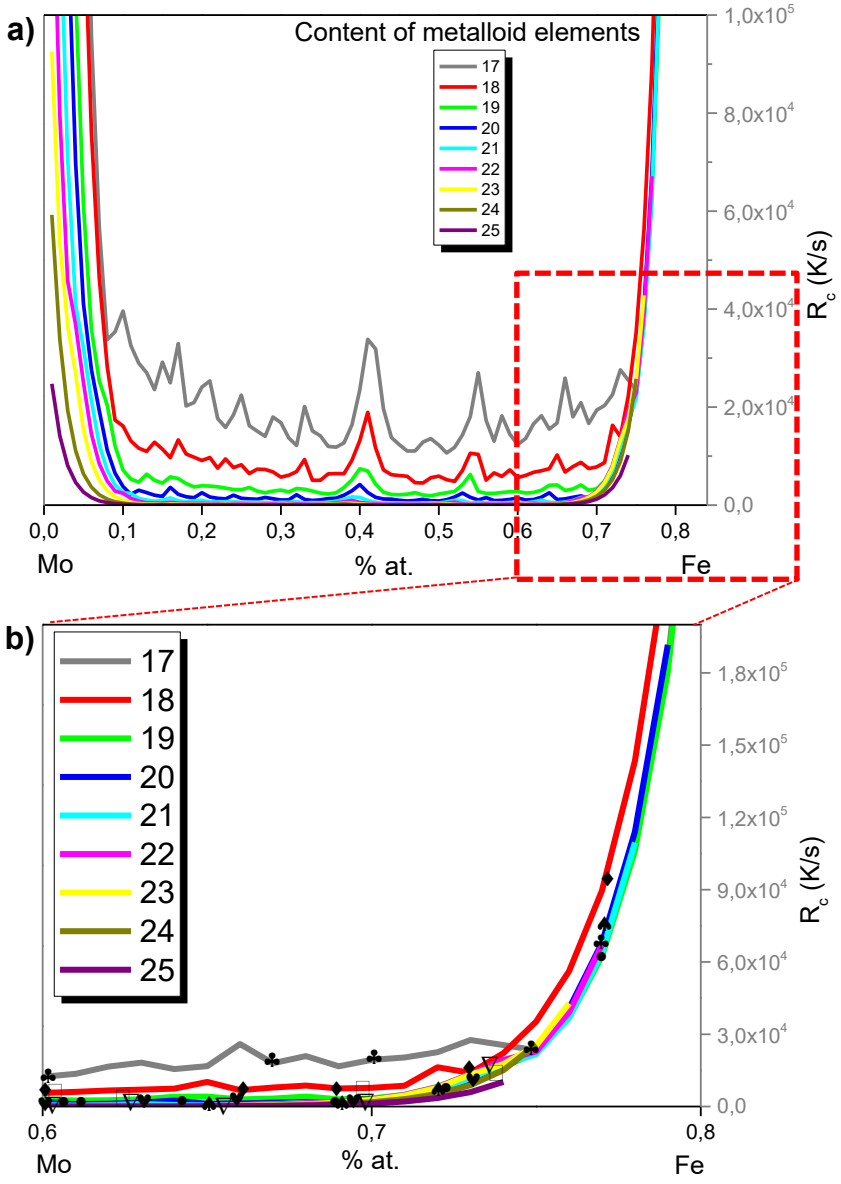

Figure 4.1- a) R_c as a function of the metalloid content in the Fe-Mo-P-C-B alloy, and **b)** magnification of graph a). The symbols in graph b) indicate the promising GFA compositions selected for further investigation.

Table 4.1- Parameters used to estimate R_c for the $Fe_{77}Mo_5P_9C_{7.5}B_{1.5}$ alloy, where λ = thermal conductivity, ρ= density, c= specific heat capacity, and α= thermal diffusivity given in m^2/s.

Parameter	Fe	Mo	P (red)	C (graphite)	B
λ (W/m*K)	34.5	138	35.0	20.0	27.4
ρ (kg/m3)	7870	9136.4	2160	2250	2178
c (J/kg *K)	440	540	770	707.7	29.7
α (mm^2/s)*	9.963	27.97	21.043	12.560	423.58
T_m (K)	1808	2573	863	3825	2890
ΔT_n (K)	602.667	857.67	287.667	1275	963,33
		Alloy in atomic %			
Calculated parameter of the alloy		$Fe_{77}Mo_5P_9C_{7.5}B_{1.5}$			
α (mm^2/s)		18.26			
ΔT_n (K)		642.902			
Experimental Z_c (mm)		1.00			
Estimated R_c (K/s)		1.17×10^4			

***α = λ/ρ*c**

From the R_c results, forty-four (44) Fe-Mo-P-C-B alloy compositions with $R_c < 10^5$ K/s, see **Table 4.2,** were selected to be further analyzed by thermodynamic calculations to obtain the liquidus temperature (T_L) and primary phase formation. In this simulation, graphite, cementite, and diamond phases were suspended. It is observed that the T_L decreases with the increase of metalloid, and considering the alloys with the same content of metalloid, the decrease of Mo content decreases the T_L. Relating to the phase formation, the FCC is a solid solution (γ-FCC), and since it is a ductile phase [200], [201], [202], its presence in the glassy matrix is expected to increase the fracture toughness of the Fe-Mo-P-C-B BMGC. As one can see, no composition is expected to form the FCC or BCC phase as the primary phase. Then, only five compositions precipitated the FCC phase from the remaining liquid, and those with the lowest T_L of each metalloid content were highlighted in light yellow (**Table 4.2**). Between

those five, only two compositions are able to precipitate the FCC phase before the solidus temperature (highlighted in red). For these two compositions, $Fe_{77}Mo_6P_8$ and $Fe_{77}Mo_5P_9$, T_L and the percentage of FCC phase at the final of solidification are 1174 °C and 1165°C, and 0,46 and 0,41, respectively. As mentioned before, the solidification was considered under equilibrium conditions, and it is known that the content of FCC in the final of solidification is most likely not correct, for the real case. Instead, the T_L is probably correct, and because of this, the composition with the lower T_L ($Fe_{77}Mo_5P_9C_{7.5}B_{1.5}$) was selected to be produced experimentally.

Because Mo seems to be a promising element in the Fe– (P, C, B)-based system, especially by increasing the metallicity and the GFA of the alloy, the Mo content was varied from 0 to 5 % at. ($Fe_{77-x}Mo_xP_9C_{7.5}B_{1.5}$). The experimental results will be shown in the next section.

Table 4.2- Forty-four Fe-Mo-P-C-B alloy compositions selected by considering lower R_c (<10^5 K/s). T_L and phase formation, in the order of formation, are also shown.

% metalloid	Alloy (% at.)	T liquidus (°C)	Phases formed in the order of formation	FCC from the remaining liquid?	%FCC in the final of solidification	FCC before Ts?
17	Fe60Mo23P8	1712	HCP; M6C; M3B2;MoP; M2P	NO	-	NO
17	Fe67Mo17P8	1551	HCP; M6C; M3B2;M3P; FCC	YES	0.2	NO
17	Fe70Mo13P8	1422	HCP; M6C; M3B2;FCC;M3P	YES	0.3	YES
17	Fe75Mo8P8	1224	HCP; M3B2; M6C;FCC;M3P	YES	0.43	YES
17	Fe77Mo6P8	1174	M3B2; M6C;FCC;M3P	YES	**0,46**	YES
18	Fe60Mo22P9	1694	HCP; M3B2; M6C;MoP; M2P;M3P;BCC	NO	-	NO
18	Fe66Mo16P9	1529	HCP; M3B2; M6C;M3P;FCC	YES	0.20	NO
18	Fe69Mo13P9	1431	HCP; M3B2; M6C;M3P;FCC	YES	0.28	NO
18	Fe73Mo9P9	1278	HCP; M3B2; M6C;FCC;M3P	YES	0.35	YES
18	Fe77Mo5P9	**1165**	M3B2; M6C;FCC;M3P	YES	**0.41**	YES
19	Fe60Mo21P10	1674	HCP; M3B2; M6C; MoP; M2P;M3P;BCC	YES	0.051	YES
19	Fe63Mo18P10	1595	HCP; M3B2; M6C; MoP; M2P;M3P;FCC	YES	0.1	YES
19	Fe66Mo15P10	1505	HCP; M3B2; M6C; M2P;M3P;FCC	YES	0.18	YES
19	Fe69Mo12P10	1404	HCP; M3B2; M6C; M3C; FCC	YES	0.25	YES
19	Fe73Mo8P10	1243	HCP; M3B2; M6C; M3P; FCC	YES	0.35	NO
20	Fe60Mo20P11	1653	HCP; M3B2; M6C; MoP; M2P;M3P	NO	-	NO
20	Fe65Mo15P11	1512	HCP; M3B2; M6C; MoP; M2P;M3P	NO	-	NO
20	Fe69Mo11P11	1375	HCP; M3B2; M6C; M2B;MoP	NO	-	NO
20	Fe72Mo8P11	1251	HCP; M3B2; M6C; M3P	NO	-	NO
20	Fe77Mo3P11	1127	M3B2; M3P; (FCC exactly on the eutectic)	YES	0.23	NO
21	Fe60Mo19P12	1629	HCP; M3B2; M6C; M2P	NO	-	NO
21	Fe61Mo18P12	1603	HCP; M3B2; M6C; MoP; M2P	NO	-	NO
21	Fe65Mo14P12	1485	HCP; M3B2; M6C; MoP; M2P; M3P; CARBETO	NO	-	NO
21	Fe69Mo10P12	1342	HCP; M3B2; M6C; M2P; M3P; CARBETO	NO	-	NO
21	Fe72Mo7P12	1210	HCP; M3B2; M6C; M3P; CARBETO	NO	-	NO
21	Fe77Mo2P12	1091	M3B2; M3P; M23C6	NO	-	NO
22	Fe60Mo18P13	1604	HCP; M3B2; MoP;M6C; M2P; M3P	NO	-	NO
22	Fe63Mo15P13	1519	HCP; M3B2; MoP;M6C; M2P; M3P	NO	-	NO
22	Fe66Mo12P13	1421	HCP; M3B2; MoP;M6C; M2P; M3P; CARBETO	NO	-	NO
22	Fe69Mo9P13	1307	HCP; M3B2; M2P; M3P; M6C;CARBETO	NO	-	NO
22	Fe73Mo5P13	1195	M3B2; HCP;M2P; M3P; CARBETO; FCC (LOW	YES	0,17	NO
23	Fe60Mo17P14	1577	HCP; M3B2; MoP;M6C;M2P;M3P	NO	-	NO
23	Fe65Mo12P14	1423	HCP; M3B2; MoP;M2P;M6C; M3P; CARBETO	NO	-	NO
23	Fe69Mo8P14	1268	HCP; M3B2; MoP;M2P; M3P; M6C;CARBETO	NO	-	NO
23	Fe73Mo4P14	1177	M3B2;;M2P; M3P;CARBETO	NO	-	NO
24	Fe60Mo16P15	1548	HCP; M3B2; MoP;M6C;M2P; M3P	NO	-	NO
24	Fe65Mo11P15	1389	HCP; M3B2; MoP;M2P; M3P; M6C	NO	-	NO
24	Fe69Mo7P15	1223	HCP; M3B2; MoP;M2P; M3P; CARBETO	NO	-	NO
24	Fe73Mo3P15	1151	M3B2;M2P; M3P; CARBETO	NO	-	NO
25	Fe61Mo14P16	1486	HCP; M3B2; MoP;M2P; M3P; M6C	NO	-	NO
25	Fe65Mo10P16	1351	HCP; M3B2; MoP;M2P; M3P; M6C/CARBETO	NO	-	NO
25	Fe69Mo6P16	1226	M3B2; MoP;M2P; M3P; M6C/CARBETO	NO	-	NO
25	Fe73Mo2P16	1112	M3B2; M2P; M3P; M5C2/CARBETO	NO	-	NO

4.2 $Fe_{77-x}Mo_xP_9C_{7.5}B_{1.5}$ (x=0 – 5) alloys preparation

4.2.1. Arc melt results

Ingots of six $Fe_{77-x}Mo_{x(x=0-5)}P_9C_{7.5}B_{1.5}$ alloys (named V1, V2, V3, V4, V5, and V6) were produced and chemically analyzed using EDS. Measurements of carbon and boron are not presented, as these elements are not detectable by EDS. The differences between the target and actual compositions (see **Table 4.3**) are acceptable, considering the error associated with the ZAF corrections (Z=atomic number, A=absorption, F=fluorescence) applied by the INCAEnergy software during the EDS analysis. Part of each ingot was used to produce a wedge-shaped sample for each alloy via suction casting.

Table 4.3- Chemical composition of the ingots $Fe_{77-x}Mo_xP_9C_{7.5}B_{1.5}$ (x=0 – 5) alloys measured by EDS (%wt).

V1		**Fe**	**Mo**	**P**	**Si**	**Ti**	**Al**	**Mn**
	Targed	92.2	0	5.6	0	0	0	0
	Actual	91.23	0	7.53	0.45	0.42	0.28	0.32
	Deviation	0.59	0	0.55	0.03	0.045	0.11	0.08
	Difference	-0.97	0	1.935	0.4525	0.4225	0.28	0.325
V2		**Fe**	**Mo**	**P**	**Si**	**Ti**	**Al**	**Mn**
	Targed	90.4	1.9	5.6	0	0	0	0
	Actual	89.25	2.49	8.2	0.68	0.52	0.37	0.42
	Deviation	0.57	0.22	0.7	0.1	0.21	0.05	0.007
	Difference	-1.15	0.59	2.6	0.68	0.525	0.375	0.425
V3		**Fe**	**Mo**	**P**	**Si**	**Ti**	**Al**	**Mn**
	Targed	89.5	2.9	5.5	0	0	0	0
	Actual	87.4	3.81	8.6	0.31	0.33	0.32	0.43
	Deviation	1.63	0.22	0.5	0.01	0.04	0.08	0.01
	Difference	-2.1	0.91	3.1	0.31	0.33	0.32	0.43
V4		**Fe**	**Mo**	**P**	**Si**	**Ti**	**Al**	**Mn**
	Targed	88.6	3.8	5.5	0	0	0	0
	Actual	86.62	3.85	8.66	0.68	0.31	0.31	0.36
	Deviation	0.1	0.49	0.67	0.28	0.06	0.09	0.008
	Difference	-1.98	0.05	3.16	0.68	0.31	0.31	0.36
V5		**Fe**	**Mo**	**P**	**Si**	**Ti**	**Al**	**Mn**
	Targed	86.8	5.7	5.5	0	0	0	0
	Actual	84.5	6.2	8.26	0.23	0.34	0.18	0.43

	Deviation	0.17	0.24	0.07	0.02	0.03	0.05	0.11
	Difference	-2.3	0.5	2.76	0.23	0.34	0.18	0.43
V6		**Fe**	**Mo**	**P**	**Si**	**Ti**	**Al**	**Mn**
	Targed	83.26	9.29	5.4	0	0	0	0
	Actual	79.87	9.65	9.77	0.23	0.37	0.24	0.37
	Deviation	0.39	0.44	0.24	0.02	0.1	0.05	0.11
	Difference	-3.39	0.36	4.38	0.23	0.37	0.24	0.37

As proposed in the literature [95], the shear modulus (G) and the glass transition temperature (T_g) govern the shear flow barrier (W) of metallic glasses, where the shear flow barrier refers to the energy required to initiate shear banding [95]. Additionally, Demetriou and Johnson [197] have suggested that tough Fe-based BMGs, particularly those containing phosphorus, should exhibit G < 60 GPa and T_g < 440 °C. Based on the DSC curves (**Figure 4.2**), the T_g of the A1 area (thinnest region) of the wedges from the six alloys (V1, V2, V3, V4, V5, and V6) was measured. For all alloys, T_g was found to be below 440 °C, meeting one of the key criteria established in this study. The shear modulus (G) was estimated using **Equation 4.2** and the Vickers microhardness measured in the A1 area of the wedges. The resulting G values are presented in **Table 4.4**, and it can be seen that all alloys exhibit G < 60 GPa, thus satisfying the second requirement.

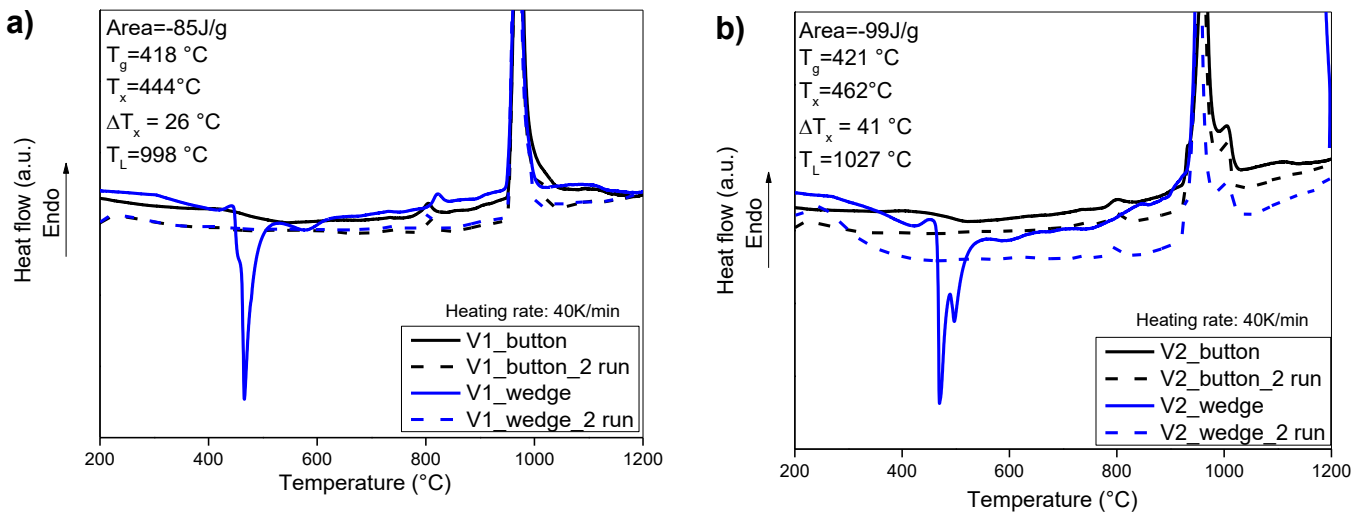

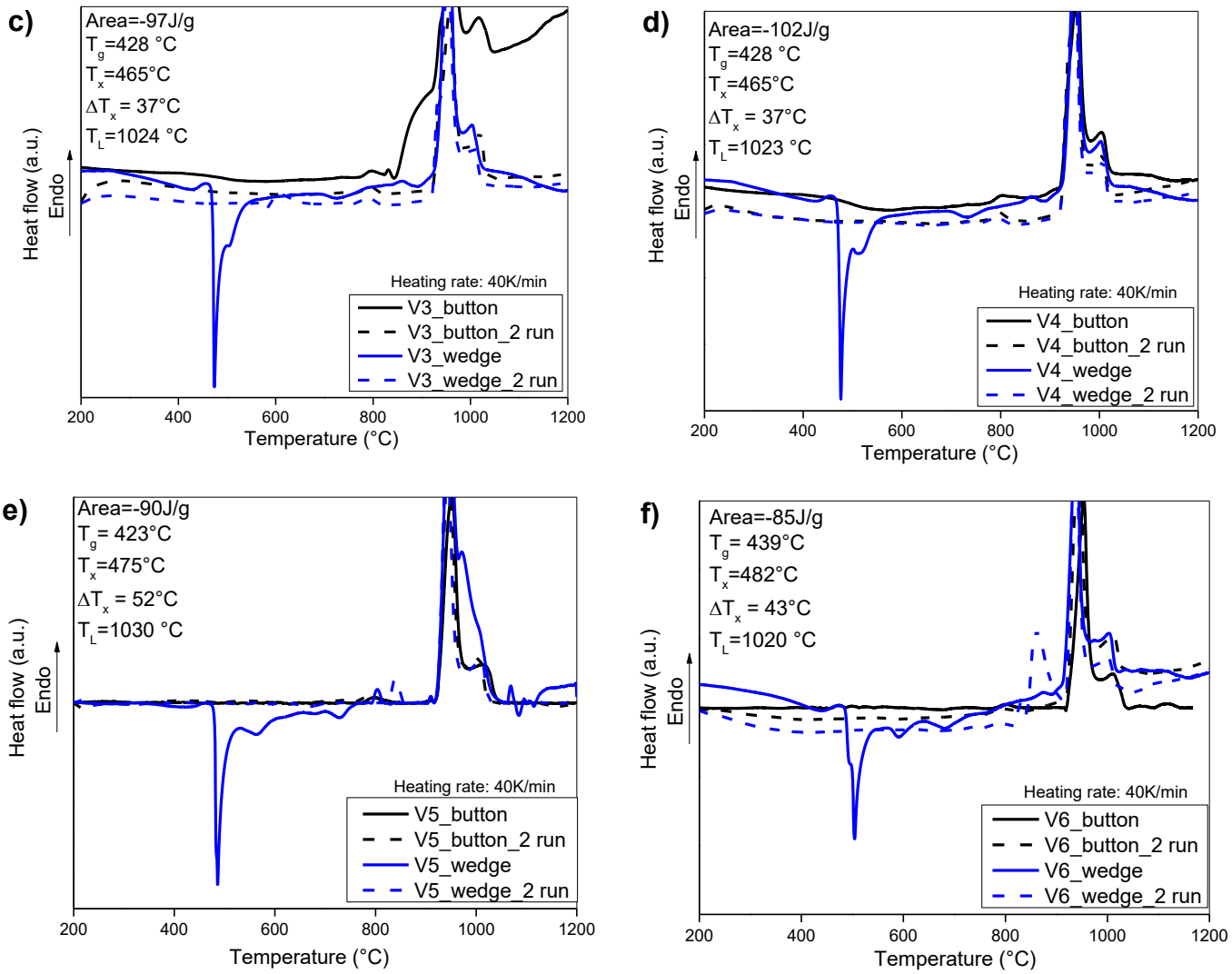

Figure 4.2- DSC results of the ingots (buttons) and A1 area of the wedges for the $Fe_{77-x}Mo_{x(x=0-5)}P_9C_{7.5}B_{1.5}$ alloys **a)** V1, **b)** V2, **c)** V3, **d)** V4, **e)** V5, **f)** V6.

Table 4.4- Summary of the $Fe_{77-x}Mo_{x(x=0-5)}P_9C_{7.5}B_{1.5}$ alloys, the estimated G, T_L and primary phases obtained by simulation, and T_L and T_g obtained experimentally by DSC analyses.

Chemical composition	Alloy ID		(Simulation)		Experimental	
At. %	Name	G (GPa)	T_L (°C)	Primary phase	T_L (°C)	T_g (°C)
$Fe_{82}Mo_0P_9C_{7.5}B_{1.5}$	**V1**	54.1	1041	FCC	998	418
$Fe_{81}Mo_1P_9C_{7.5}B_{1.5}$	**V2**	54.6	1033	FCC	1027	421
$Fe_{80.5}Mo_{1.5}P_9C_{7.5}B_{1.5}$	**V3**	53.1	1024	FCC/M_3B_2	1024	428

$Fe_{80}Mo_2P_9C_{7.5}B_{1.5}$	**V4**	55.9	1049	M_3B_2	1023	428
$Fe_{79}Mo_3P_9C_{7.5}B_{1.5}$	**V5**	57.0	1093	M_3B_2	1030	423
$Fe_{77}Mo_5P_9C_{7.5}B_{1.5}$	**V6**	58.6	1145	M_3B_2	1020	439

Since all six alloys satisfied the G and T_g requirements, their glass-forming ability (GFA) was further investigated using optical microscopy (OM) and differential scanning calorimetry (DSC) analyses of the A2 and A3 regions of the wedges. Based on these results (see OM images **Appendix Figure A.1 e)** and **f)**), only the V5 and V6 alloys exhibited the presence of glassy phases in the A2 and A3 areas, indicating a higher GFA compared to the other alloys. The presence of the glassy phase in these regions was confirmed by DSC analyses, as shown in **Figure 4.3**. The clear appearance of T_g and exothermic events during the first heating run for the A2 and A3 areas of the V5 and V6 wedges confirms the presence of the glassy phase. Therefore, these two alloys were selected to be gas atomized.

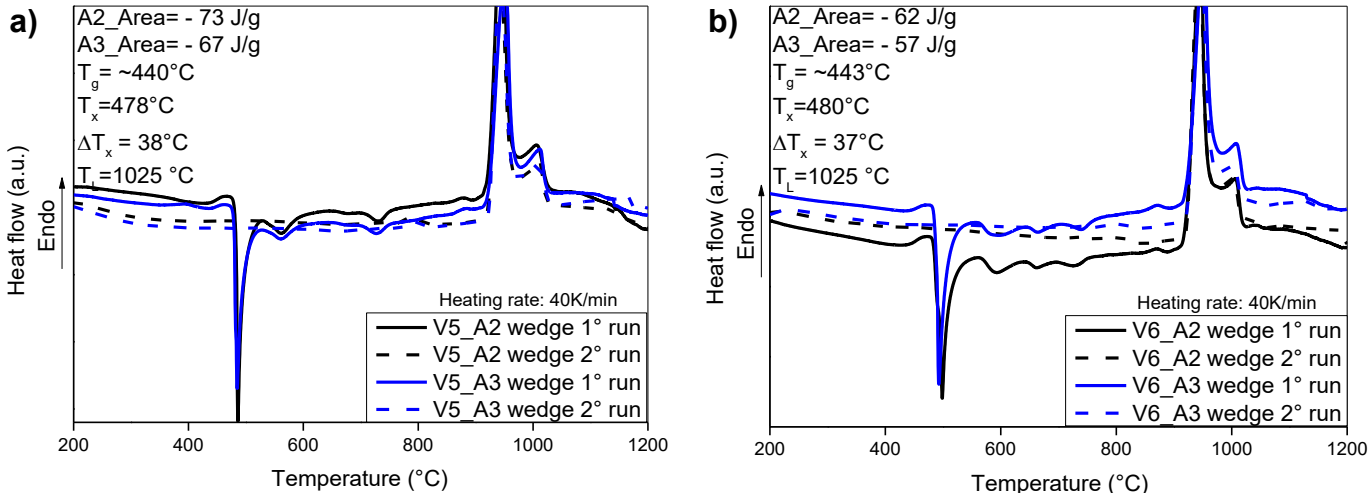

Figure 4.3- DSC results of the A2 and A3 areas of the wedges for **a)** V5, and **b)** V6 alloys.

To better understand the microstructure of the V5 and V6 wedges, the entire wedge area was investigated using SEM. The SEM images of each region,

along with the corresponding hardness values and markings, are presented in **Figure 4.4**. Based on the compositional contrast provided by backscattered electrons (**Figure 4.4a)**), the microstructure consists of a light gray, homogeneous glassy matrix with some spherical crystalline particles dispersed throughout, evidenced by a brighter contrast. A higher concentration of these spherical crystalline particles is observed in the V6 alloy, which can be attributed to its higher Mo content. As shown in the elemental EDX maps in **Figure 4.4b)**, these crystalline particles are rich in Mo. These Mo-rich phases can contribute to the increased hardness of the V6 alloy, as supported by the hardness results.

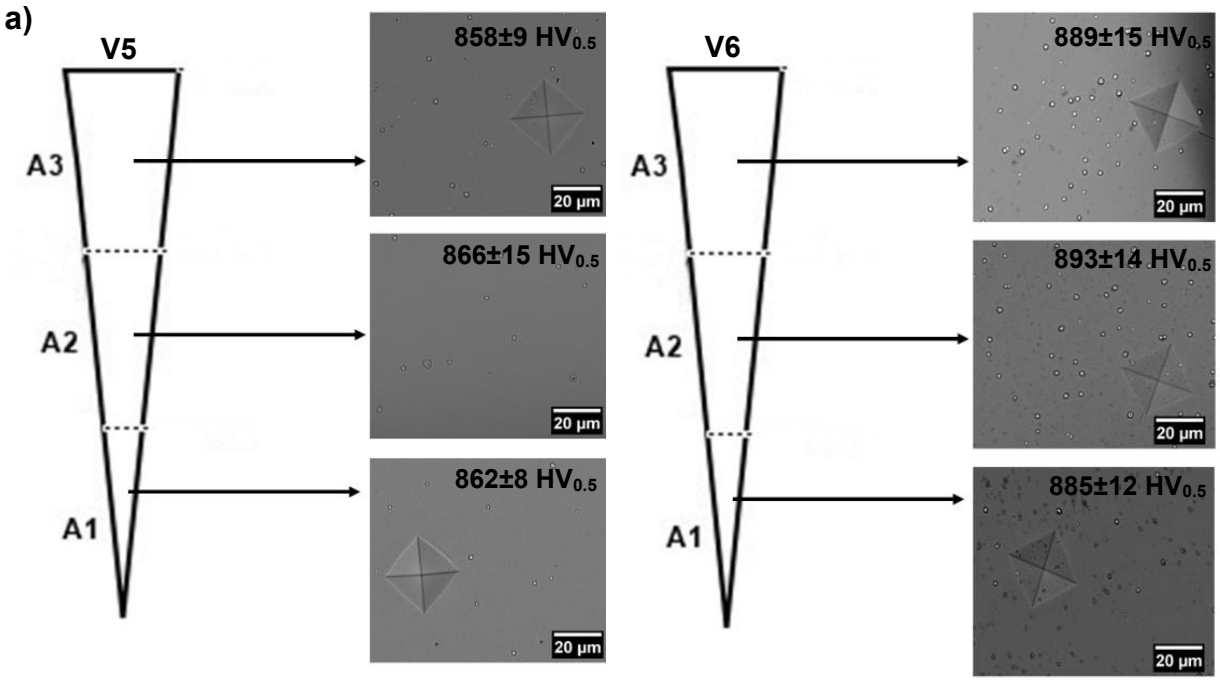

b)

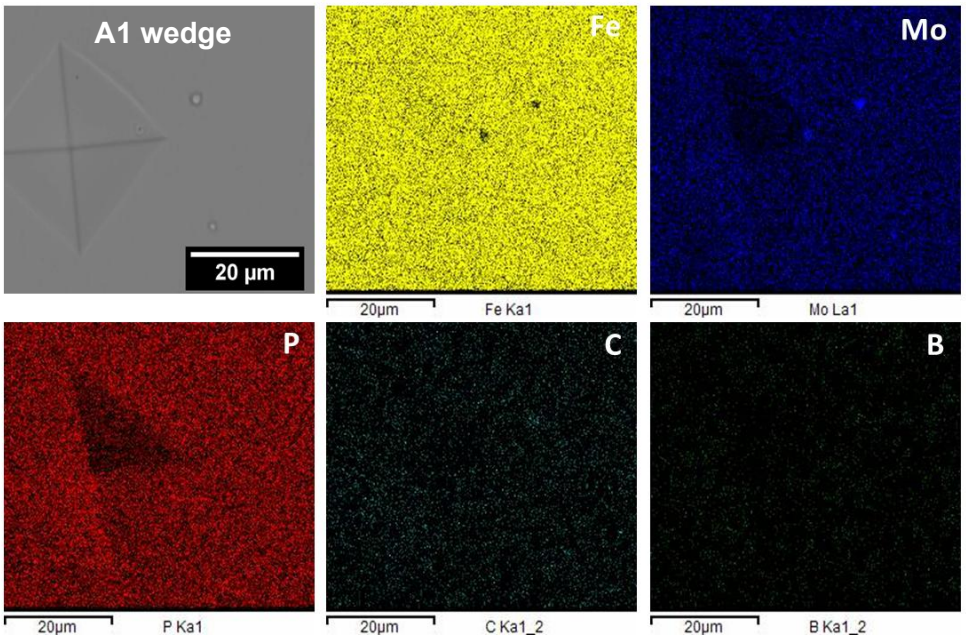

Figure 4.4- a) Schematic of the wedge-shaped cast samples together with SEM images and hardness marks indicated for V5 and V6, and **b)** representative SEM image from A1 area, together with elemental EDX maps using Fe-K_α, Mo- L_α, P-K_α, C-K_α, B-K_α.

From **Figure 4.3**, the V5 and V6 alloys exhibited distinct three- and four-stage crystallization behaviors, respectively. To further investigate the crystallization process, the A3 area of each wedge was selected and subjected to annealing at temperatures just below and above the exothermic peaks observed in **Figure 4.3** (see **Table 4.5**). For each case, the same sample underwent annealing in a DSC, followed by XRD measurement. The annealing steps and corresponding XRD patterns are shown in **Figure 4.5a)-f)**.

Based on the XRD results, the crystallization process is similar for both V5 and V6 alloys, with the formation of Fe_3P, $(Fe,Mo)_{23}(C,B)_6$ and Fe(α) phases occurring immediately after annealing at 475 °C. The more intense Fe_3P peaks after 475 °C annealing indicates increased precipitation of this phase at this stage. For V5, in the range of 475–525 °C, slight differences in the XRD patterns are observed, with the peaks gradually becoming more defined and shifting slightly to the left. A similar trend occurs in the V6 alloy, but within a broader

temperature range of 475–565 °C.

In the range of 645–655 °C, the peaks become more pronounced, particularly those corresponding to the $(Fe,Mo)_{23}(C,B)_6$/ $Fe_{23}(C,B)_6$ and Fe(α) phases. For V5, at 535 °C, a peak at ~50° is decomposed, and after annealing at 695 °C, it clearly appears as two peaks, at 49.4° and 49.9°. At this temperature, new peaks associated with the Fe_3P phase appear, while those related to the $Fe_{23}(C,B)_6$ and Fe(α) phases become significantly more evident. A similar progression takes place at 705 °C for the V6 alloy.

Table 4.5- Selected annealing temperatures for A3 area of V5 and V6 wedges based on DSC results.

	Temperatures (°C)								
Alloy	**T_g**	**T_{x1}-5**	**T_{x1}+5**	**T_{x2}-5**	**T_{x2}+5**	**T_{x3}-5**	**T_{x3}+5**	**T_{x4}-5**	**T_{x4}+5**
V5	440	475	485	525	535	695	705	-	-
V6	440	475	485	555	565	645	655	705	715

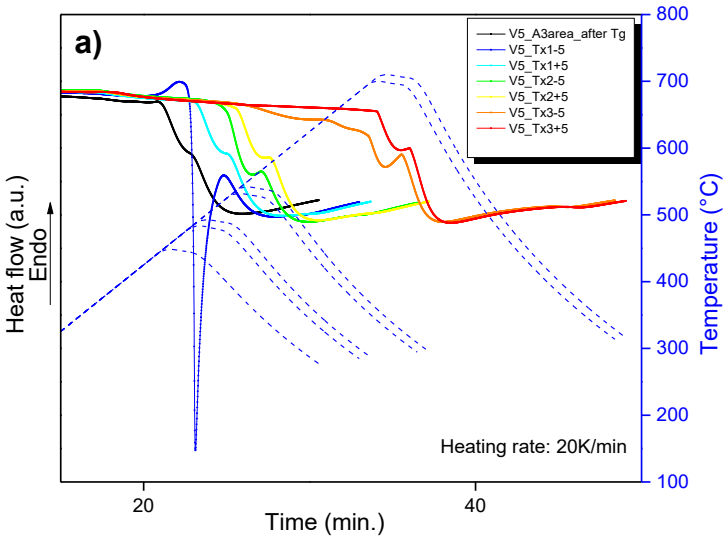

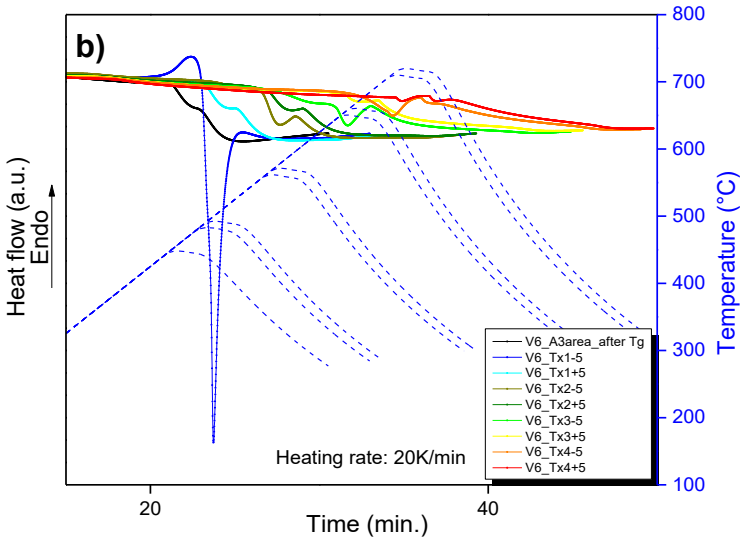

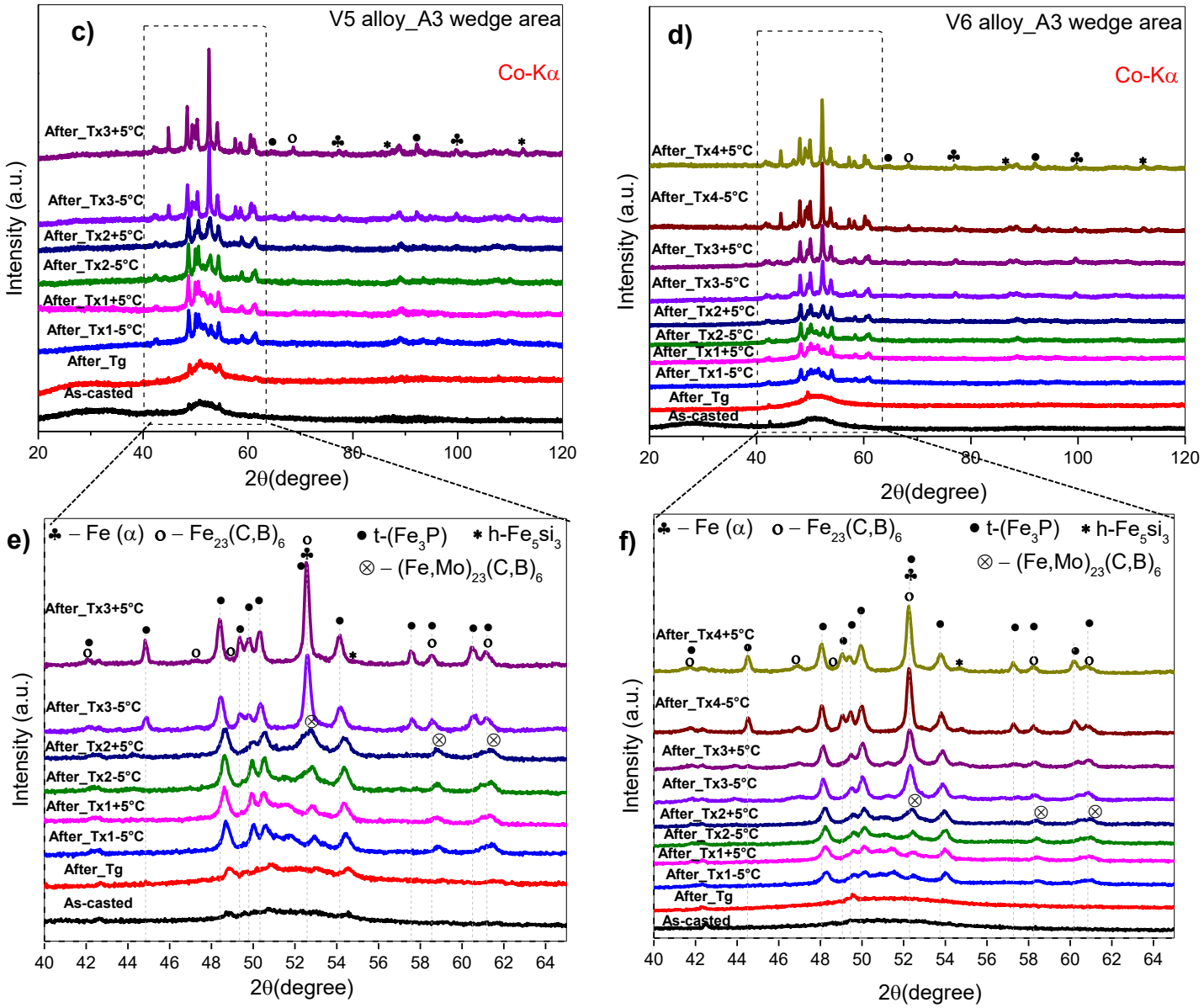

Figure 4.5- DSC curves of the annealing treatment steps for A3 area of the wedge for **a)** V5 and **b)** V6, and corresponding XRD pattern after each annealing for **c)** and **e)** V5 and **d)** and **f)** V6 alloys.

Further investigations into the mechanical behavior of the V5 and V6 alloys were carried out using cast rods. The compressive engineering stress–strain curves at room temperature for 2 mm diameter rods of V5 and V6 are shown in **Figure 4.6a)**.

Although higher compressive strength has been reported for similar systems [100],[203],[204],[205], such performance was not observed in the

present experiments. This discrepancy may be attributed to differences in alloy chemical composition, the raw materials used, and the sample geometry used in mechanical testing. In most reported studies, high-purity elements were used as raw materials, and rods with 1 mm diameter were employed for compression tests. Additionally, microstructural variations resulting from different cooling rates—due to differences in sample diameter—may also contribute. The presence of a small volume fraction of nanocrystals in the glassy matrix, as observed in SEM images (**Figure 4.4**), could also influence the overall mechanical behavior.

Interestingly, the V6 alloy exhibited higher fracture strength (σ_f = 2607 ± 193 MPa) and macroscopic plasticity (ε_p = 2.15 ± 0.13%) compared to V5. This suggests that both strength and plasticity can be simultaneously improved by adjusting the Mo content. The fracture surface of the V6 alloy is shown in **Figure 4.6b)**, and a local magnified view of a well-developed vein-like pattern—a morphology typically observed in the fracture surface of glassy alloys [61]—is presented in **Figure 4.6c)**. The shear direction is indicated by white arrows in the micrograph.

The more negative mixing enthalpies of Mo-atomic pairs, compared to those of Fe, indicate a stronger atomic bonding nature [206]. As a result, the substitution of Fe with Mo can improve alloy strength. While most Fe-based metallic glasses are brittle and exhibit almost no plasticity (<1%), the V6 alloy—with relatively high Fe content and without the addition of typical strengthening alloying elements such as Nb or Ni—exhibited a plastic strain exceeding 2.0%, making it notably different from many other Fe-based bulk metallic glasses.

Figure 4.7a) shows micrographs of the lateral surface of the compressed sample. Fracture occurred along the main shear band, indicating a quite good toughness. A close-up view of area “A” in **Figure 4.7a)** is shown in **Figure 4.7b)**, revealing a high density of multiple shear bands on the side surfaces of the deformed samples, oriented parallel to the fracture plane. The activation of multiple shear bands contributed to the significant plastic strain observed under compressive stress.

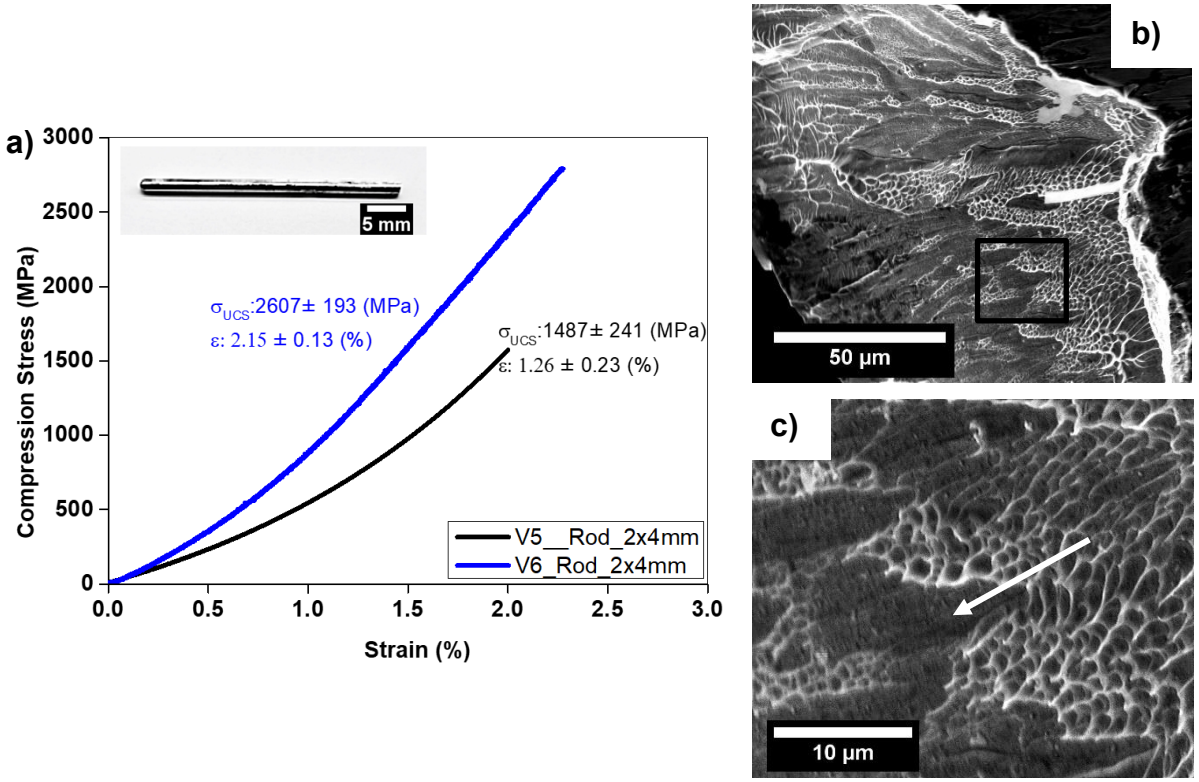

Figure 4.6- a) Compressive stress-strain curves of V5 and V6 as-cast rods with strain rate of $1x10^{-4}$ s^{-1}. **b)** SEM images of the fracture surface morphology of V6. **c)** Partially enlarged views of the fracture of the box in b).

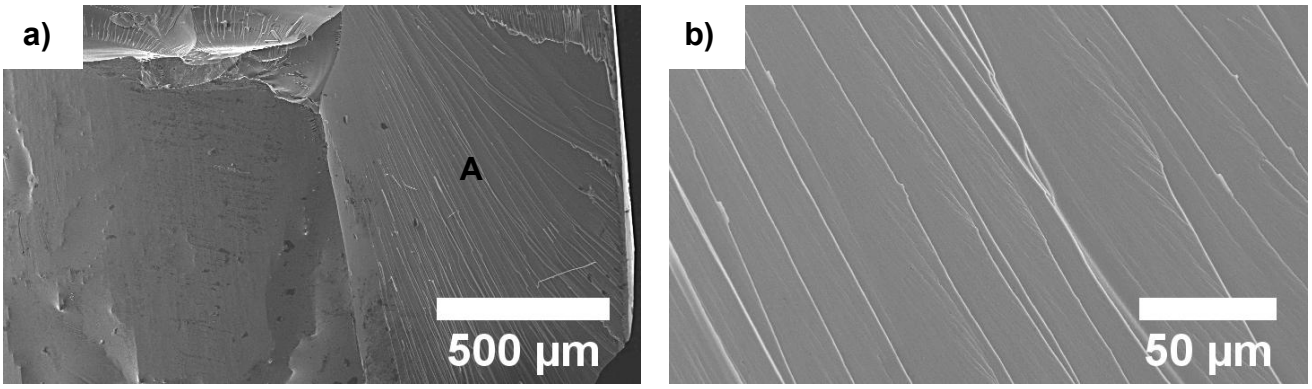

Figure 4.7- SEM images of the V6 sample rod with 2 mm diameter after compression fracture: **a)** lateral surfaces and **b)** a close-up view of the area ‘‘A’’ in a).

4.2.2. Melt Spinning results

Figure 4.8a) shows the XRD patterns of the V5 and V6 melt-spun ribbons. Both patterns exhibit only one broad diffraction peak with no evidence of crystalline phases, which is the typical characteristic of a fully glassy structure.

Figure 4.8b) presents the DSC curves of the melt-spun V5 and V6 ribbons measured at a heating rate of 0.67 K/s. Both curves exhibit distinct glass transition and exothermic crystallization events, further confirming the glassy nature of these ribbons.

Thermal parameters including the glass transition temperature (T_g), crystallization temperatures (T_x), melting temperature (T_m), liquidus temperature (T_L), area of the exothermic peaks, supercooled liquid region (ΔT_x), reduced glass transition temperature $T_{rg}=(T_g/T_L)$, and the glass-forming ability (GFA) parameter $\gamma = (T_x/(T_g+T_L))$, were obtained from the DSC analysis and are listed in **Table 4.6**. It was found that, V5 and V6 are similar regarding to the parameters presented in **Table 4.6**. However, V6 alloy, which has higher Mo content, shows values of T_{rg} and γ parameters slightly higher than V5 alloy, suggesting better GFA.

The Vickers microhardness values for V5 and V6 were 641±38 and 720±30 HV, respectively.

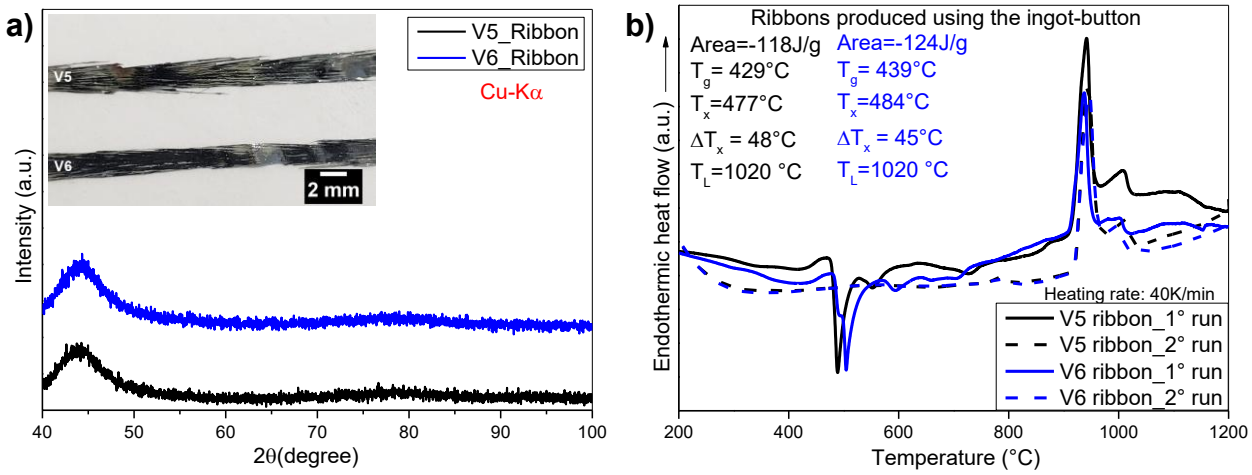

Figure 4.8- a) XRD patterns and **b)** DSC curves with a heating rate of 40 K/min, for V5 and V6 ribbons.

Table 4.6- Glass transition temperature T_g, crystallization temperatures T_{x1} – T_{x5}, melting temperature T_m, liquidus temperature T_l, area of the exothermic peaks, the supercooled region ΔT_x, the reduced glass transition temperature $T_{rg}=(T_g/T_l)$, and the glass-forming ability (GFA) parameter $\gamma = (T_x/(T_g+T_l))$ at 40K/min for V5 and V6 ribbons.

Alloy	$T_{g,inf}$	T_{x1}	T_{x2}	T_{x3}	T_{x4}	T_{x5}	T_m	T_l	Area	ΔT_x	T_{rg}	γ
	±1K	±1K	±1 K	±1 K	±1 K	±1 K	±1 K	±1 K	J/g			
V5	702	750	805	919	-	-	1189	1293	-118	48	0.543	0.376
V6	712	757	772	847	915	962	1184	1293	-124	45	0.551	0.378

To explore the crystallization behavior under varying high heating rates (β) ranging from 200 to 10000 K/s, Flash DSC measurements were carried out. Six representative continuous Flash DSC heating traces for the V5 and V6 ribbon samples at different heating rates—200, 500, 1000, 2000, 5000, and 10000 K/s—are displayed in **Figure 4.9a)** and **b)**. At all heating rates, the Flash DSC heat flow curves exhibit primary crystallization peak, which becomes more pronounced with increasing heating rate.

At heating rates higher than 2000 K/s, the curves exhibit obvious glass transition signals. When the heating rate increases, both the glass transition (T_g) and the primary crystallization (T_x) shift to the higher temperature range, particularly T_x. This behavior is consistent with previously reported thermal responses of metallic glasses and results in a wider supercooled liquid region ($\Delta T_x = T_x - T_g$). Additionally, a wide exothermic peak referred to relaxation appears before the glass transition. Interestingly, this relaxation signal is not detected in conventional DSC measurements performed at low heating rates (e.g., 20 K/min), highlighting a unique feature observable only through Flash DSC.

In additive manufacturing processes, the heating in the heat-affected zone (HAZ) controls the crystallization, whereas the cooling from the melt is generally fast enough to avoid crystallization. According to the literature [207], the HAZ in previous deposited layers in LPBF, can reach temperatures between the T_g and

T_m. For the alloys studied in this work, this range is approximately 430-920°C. Moreover, the LPBF process can achieve extremely high heating rates (~10^6K/s) [208]. Due to cyclic thermal effects in HAZ, crystallization tends to occur upon reheating of the material after solidification [209]. Additionally, it has been reported [208] that crystallization kinetics upon heating are faster than those upon cooling. Therefore, understanding how crystallization progresses in the glassy phase under high heating rates is crucial for describing the structure's behavior of the material during the LPBF process. From **Figure 4.9a)** and **b)**, it is observed that crystallization in the alloys occurs at higher temperatures as the heating rate increases, suggesting that the high heating rates reached in the HAZ during LPBF can suppress crystallization. Furthermore, the V6 alloy crystallizes at higher temperatures compared to the V5 alloy under the same heating rate, indicating a potentially higher glassy phase fraction in V6 samples processed under identical LPBF conditions. However, at the maximum heating rate tested in this study (10,000 K/s), crystallization could not be completely prevented in either alloy.

These findings indicate that Flash DSC at high heating rates is a powerful tool for investigating the crystallization behavior of the glassy phase during LPBF processing.

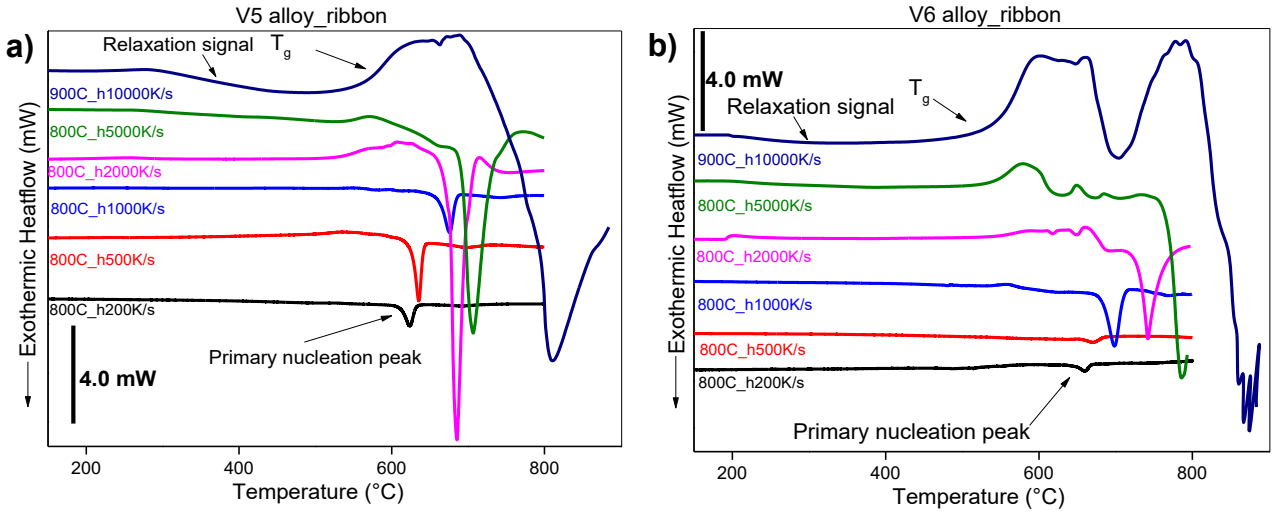

Figure 4.9- Flash DSC heating curves for **a)** V5 and **b)** V6 ribbons, measured at different heating rates (β= 200, 500, 1000, 2000, 5000 and 10000 K/s).

4.2.3. VIM results

The V5 and V6 alloys were produced in a VIM furnace before being submitted for gas atomization. The as-cast ingots were chemically analyzed using ICP-OES, EDS, and LECO techniques, and the results are presented in **Table 4.7**. The results show that the compositions of the alloys are quite close to the target values, except for silicon, which appears as an impurity originating from the raw materials.

Table 4.7- Chemical composition measured by ICP-OES (Fe, Mo, P and B), LECO (C), and EDS (Si) of V5 and V6 ingots produced in the VIM furnace (%wt).

V5	**Fe**	**Mo**	**P**	**C**	**B**	**Si**
Targed	86.80	5.70	5.50	1.80	0.30	0
Actual	86.80	5.87	5.87	1.76	0.253	0.77
Deviation	0.72	0.39	0.39	0.04	0.02	0.1
Difference	0	0.17	0.37	-0.04	-0.05	0.77
V6	**Fe**	**Mo**	**P**	**C**	**B**	**Si**
Targed	83.26	9.29	5.40	1.74	0.31	0
Actual	83.78	8.88	5.60	1.66	0.18	1.1
Deviation	1.00	0.75	0.16	0.01	0.005	0.08
Difference	0.52	-0.41	0.2	-0.08	-0.125	1.1

The microstructure of the V5 and V6 ingots was investigated using optical microscopy (**Figure 4.10**). The microstructure is similar to that of hypoeutectic white cast iron, displaying the cementite phase along with the microconstituents pearlite and ledeburite. SEM imaging and elemental EDS mapping (**Figure 4.11**) revealed that the matrix phase, shown in dark gray contrast, is rich in phosphorus (P), while the phase appearing in light gray contrast is rich in molybdenum (Mo). EDS analysis also confirmed the presence of iron (Fe) in the pearlite dendrites and in the honeycomb-like ledeburite morphology.

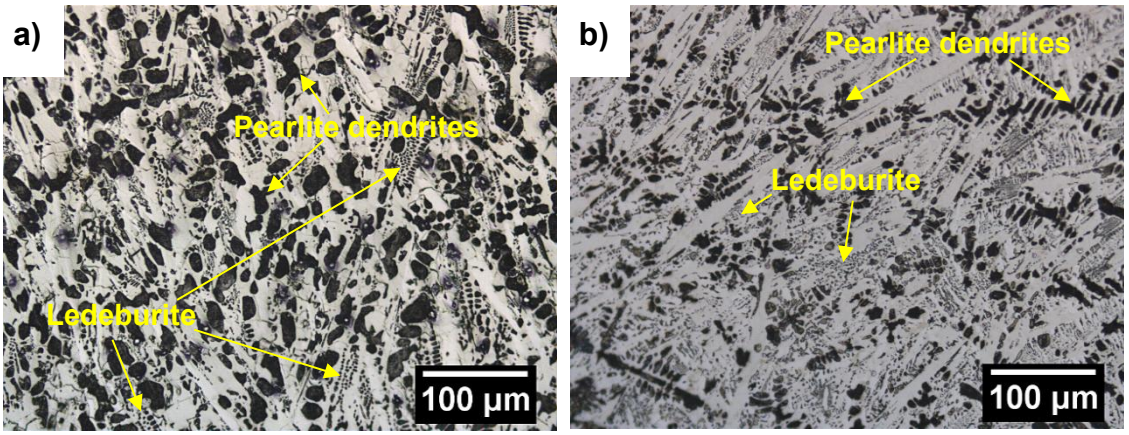

Figure 4.10- Optical images of the as-cast microstructure of **a)** V5 and **b)** V6 ingots produced in the VIM furnace. Microstructure composed of pearlite dendrites (dark areas) and ledeburite (dotted-like areas) (eutectic constituent formed by plates of cementite and pearlite inside the holes).

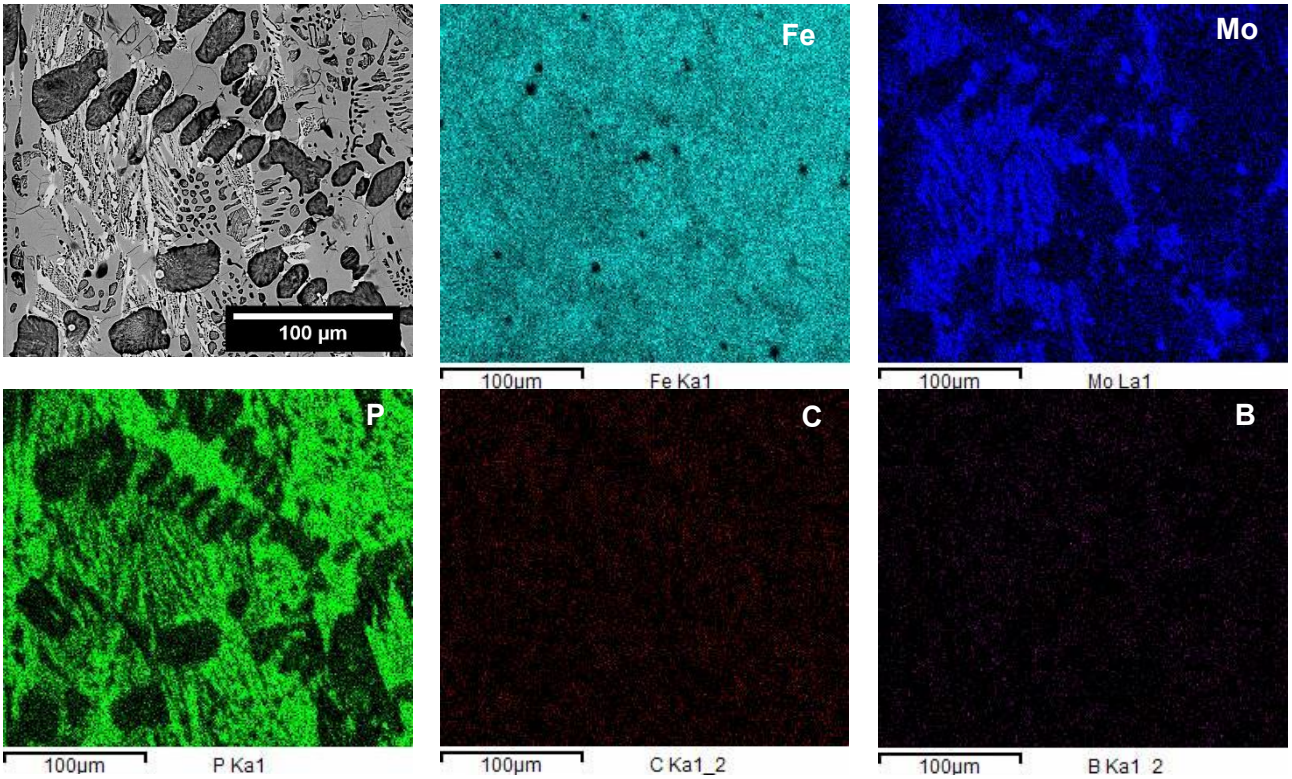

Figure 4.11- SEM image together with elemental EDS maps using Fe-K_α, Mo-L_α, P-K_α, C-K_α and B-K_α for a representative sample of VIM ingot.

The phase formation of the ingots produced using VIM and the arc-melt furnace was compared using X-ray diffraction (XRD) analysis (**Figure 4.12**). From the overview pattern in **Figure 4.12**, it can be observed that all ingots exhibit the Fe (α-bcc) phase. However, the peaks of $(Fe, Mo)_{23}(C, B)_6$ phase are more evident in the ingots produced using the arc-melt furnace, while the peaks of $Fe_3(P,C,B)$ phase (cementite) are more pronounced in those produced via the VIM furnace. This difference can be attributed to the higher cooling rates (~10^1-10^2 K/s [210]) typically achieved in arc-melted ingots compared to the lower cooling rates achieved for the VIM-processed ingots. According to the literature [211], $(Fe, Mo)_{23}(C, B)_6$ phase is richer in transition metals (Fe and Mo) and metalloids (P, C, B) than the $Fe_3(P,C,B)$ phase. With a cubic structure (often FCC-based), the $(Fe, Mo)_{23}(C, B)_6$ phase is stable at high temperatures, ranging from 600 to 950 °C, and exhibits a hardness of approximately 1100 $HV_{0.05}$ [211].

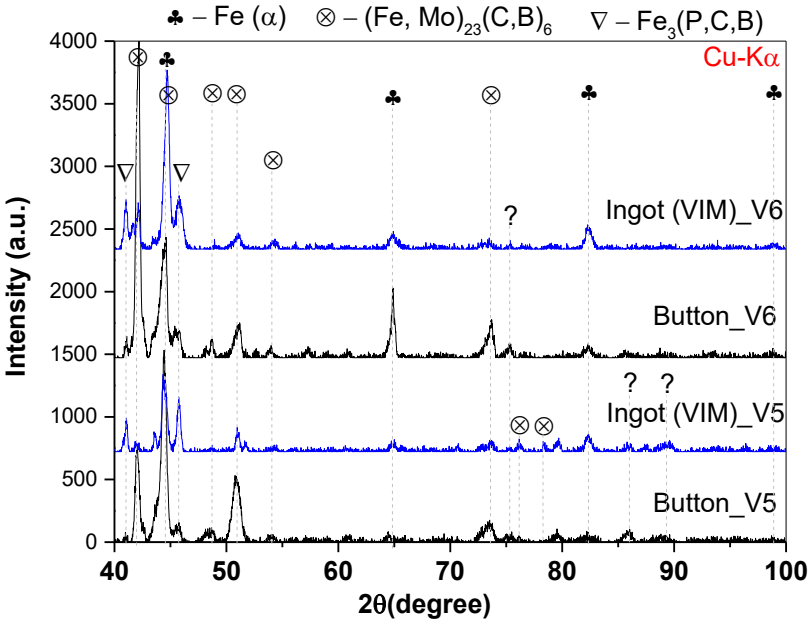

Figure 4.12- X-ray diffractograms of the button-like ingot produced in the arc-melt furnace and the ingots produced in the VIM furnace for V5 and V6 alloys.

4.3 Gas atomized powders

A total of 12.2 kg of V5 and 13.2 kg of V6 VIM-produced ingots were used to feed the gas atomizer. For both atomization, approximately 11.4 kg of powder was obtained, corresponding to yields of 93.4% for V5 and 86.4% for V6. Of the 11.4 kg, about 14% consisted of particles that were too small (<20 μm), and 30% were too large (>75 μm) for use in the Laser Powder Bed Fusion (LPBF) process. These out-of-spec fractions were separated from the main powder batch.

Only the powder fractions with particle sizes in the range of +20 to -75 μm were selected for use in the LPBF process. Consequently, these fractions were the focus of detailed investigation in this work. It is well established that the quality of LPBF-manufactured parts is significantly influenced by the characteristics of the powder feedstock. Key properties include particle size distribution, particle shape, surface morphology, composition, and flowability [105], [112].

Figure 4.13a) and **b)** show the mass fraction and cumulative fraction of each sieved size range for the V5 and V6 powders. Based on these results, improved flowability is expected for the V6 powder, which contains lower content of particles smaller than 20 μm and a higher content of particles in the 53–75 μm range. **Figure 4.13c)** and **d)** display the volumetric frequency and their cumulative as a function of the particle's diameter for the V5 and V6 powders. Both powders exhibit symmetric, approximately normal distributions for their particle size, indicating a good batch of powders for the LPBF process. The median particle diameter is 39.6 μm for V5 and 44.1 μm for V6.

Figure 4.13e) provides a direct comparison of the particle size distributions of V5 and V6 powders. The distribution curve for V6 is slightly shifted to the right, indicating a higher presence of coarser particles, which aligns with the results obtained from sieving.

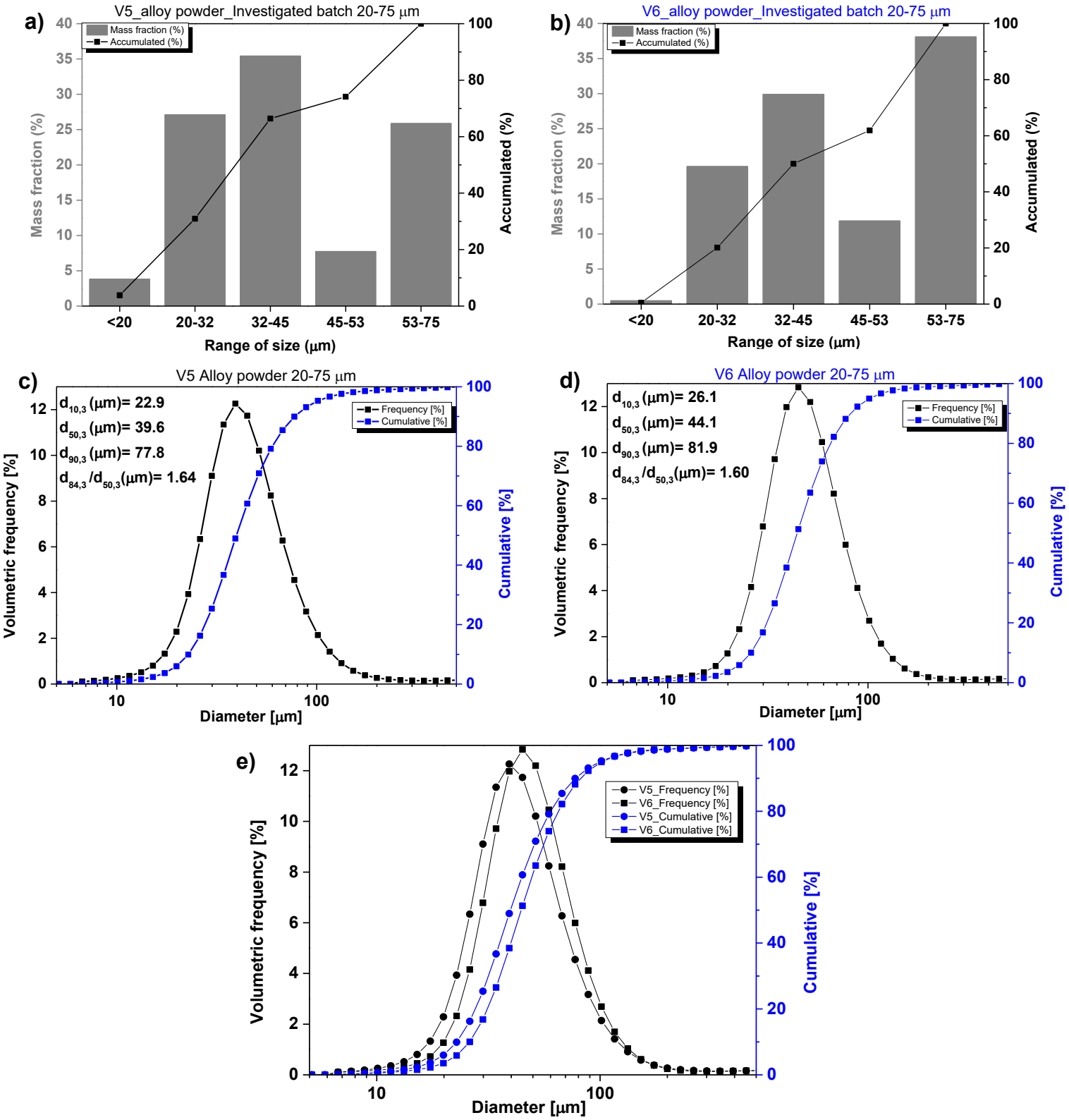

Figure 4.13- The mass and accumulated fractions of the powder retained in each size range after sieving for **a)** V5 and **b)** V6; Particle size distribution of the batch

+20- -75 μm of **c)** V5 and **d)** V6 powders, and **e)** a comparison between V5 and V6 powders size distribution for the batch +20- -75 μm.

The apparent density (ρ_a) and tapped density (ρ_t) of the powders were measured as 4.0 and 4.83 g/cm^3 for V5, and 4.0 and 4.80 g/cm^3 for V6, respectively. Based on these values, the Carr Index (CI = $(\rho_t - \rho_a)/\rho_t$) and the Hausner Ratio (HR = ρ_t/ρ_a), both commonly used as indicators of powder flowability [212], were calculated. The CI and HR values, summarized and compared with reference standards in **Table 4.8**, indicate fair flowability for both powders. This level of flowability suggests that the powders are suitable for LPBF, as they are unlikely to agglomerate and form a rather uniform powder bed. Carney flowability measurements yielded values of 0.85 ± 0.32 g/s for V5 and 1.25 ± 0.25 g/s for V6. These results confirm that the V6 powder exhibits better flowability, consistent with expectations based on its particle size distribution.

.

Table 4.8- Comparison of V5 and V6 powder flow properties (Carr Index, CI and Hausner Ratio, HR) with reference values [212].

Flow Character	**CI (%)**	**HR**
Poor	>26	>1.35
Passable	21–25	1.26–1.34
Fair	16–20	1.19–1.25
Good	11–15	1.12–1.18
Excellent	≤ 10	1–1.11
V5_Fe-based BMG(This study)	17	1.21
V6_Fe-based BMG(This study)	17	1.20

The morphology and surface characteristics of +20 - -75 μm V5 and V6 powders are shown in **Figure 4.14a)** and **b)**. The powders particles have a very smooth surface and the morphology is mostly spherical, although particles exhibiting a high aspect ratio can also be observed. **Figure 4.14c)-f)** shows SEM and optical images of polished cross sections of V5 and V6 powders. By these images, a composite microstructure is revealed for the powders, with some

particles fully glassy and some partially crystalline, with sporadic crystalline phases dispersed in a glassy matrix (see red arrows). By the OM images, one can see that the crystalline phases are etched while the glassy phases are corrosion-resistant, presenting as the unetched regions. From these images, it can be observed that the microstructure is not particle-size dependent, since particles of similar size can present different microstructures. In addition, for some powder particles, there are also some gas pores entrapped inside.

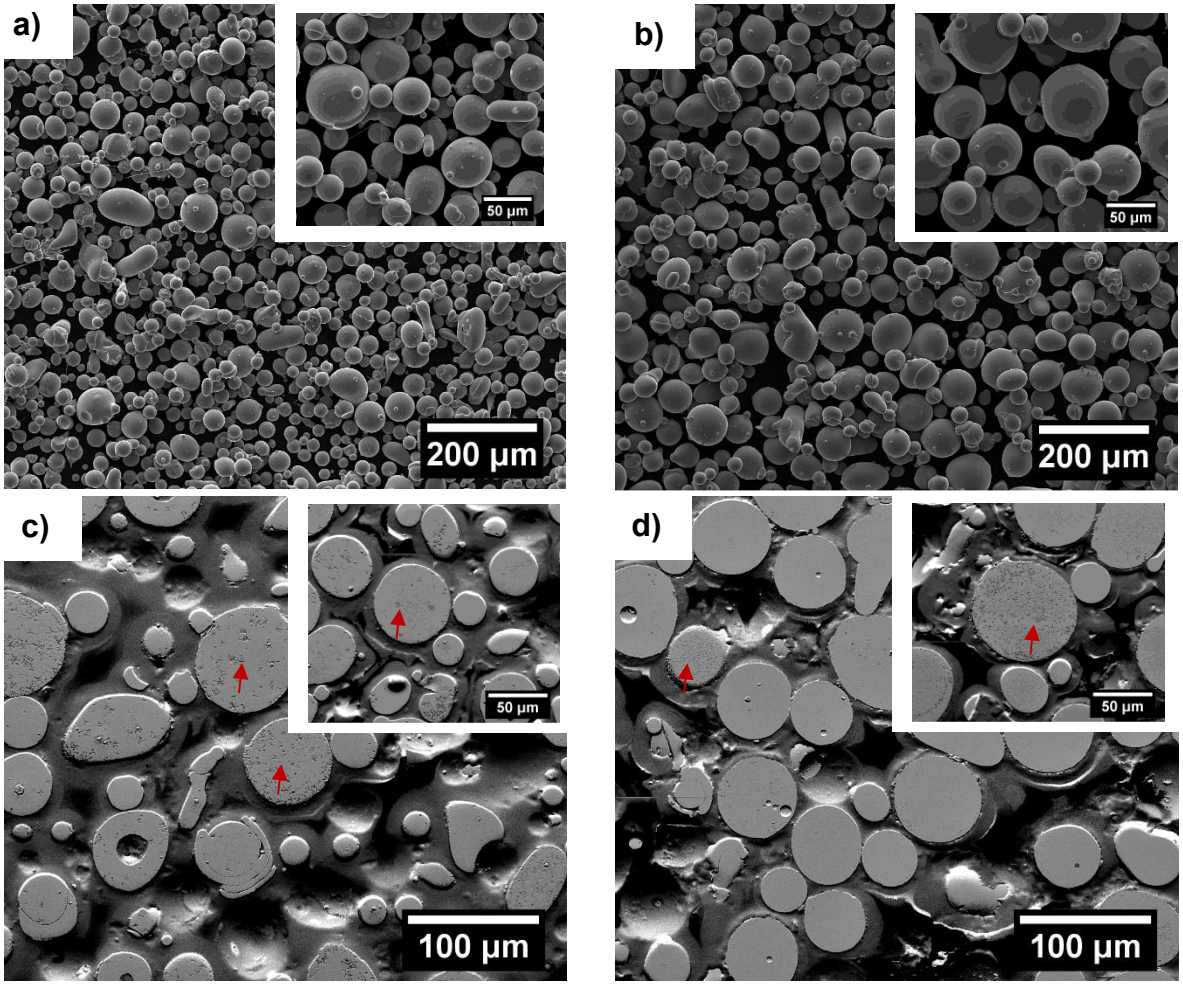

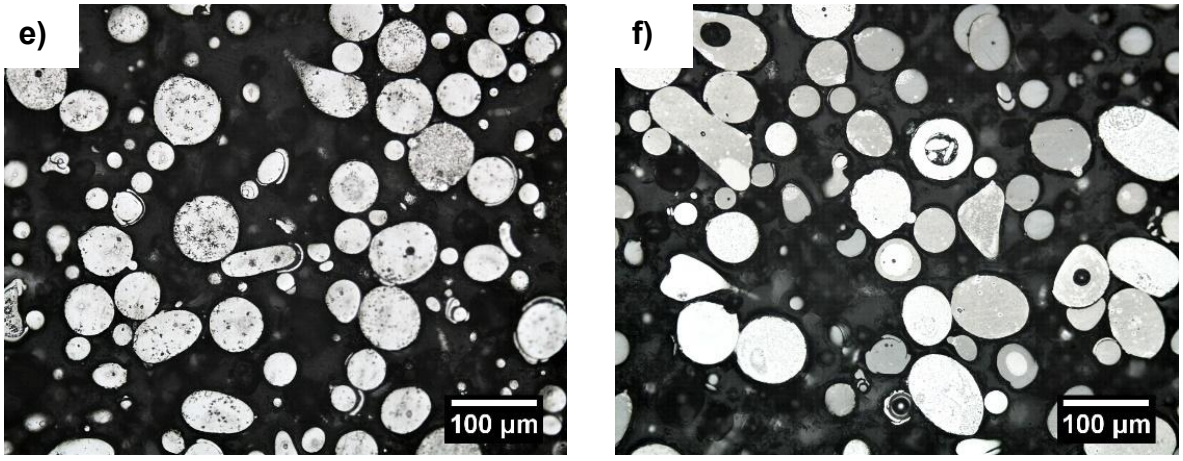

Figure 4.14- Scanning electron images of the loose powders **a)** V5 and **b)** V6; the cross-section of the embedded powders **c)** V5 and **d)** V6, and optical cross-section images of **e)** V5 and **f)** V6 embedded powders after etching. The red arrows in c) and d) indicate some crystalline phases.

The chemical composition of V5 and V6 powders is shown in **Table 4.9**. The elemental contents are close to the target nominal compositions for both powders, except for the Si and O content, which are impurities from the raw commercial material. According to the literature, Fe-based BMGs are less susceptible to oxygen content when compared to Zr and Ti-based BMG, but still the oxygen can act as nucleation sites for crystallization, especially when the oxygen is present as oxides [103], reducing the GFA and leading to the formation of undesired crystalline phases [183]. Thus, a low oxygen content in Fe-based BMG powders is crucial to preserve the glassy structure and ensure optimal mechanical properties of additively manufactured parts [213], [214]. The oxygen content measured for V5 and V6 powders was 80 and 70 ppm, respectively, which can be considered as a low oxygen content. Li et al. [178] have reported that oxygen additions in the range of 0.02 at. % (0.0057 wt.% (57 ppm) to 0.15 at. % (0.043 wt.% (430 ppm)) actually improve the GFA in a FeMoCSiBP BMG. For the same system, Stoica [103] have found an enhancement in the GFA when some foreign elements were present.

Table 4.9- Chemical composition measured by ICP-OES (Fe, Mo, P, B and Si) and LECO (C and O) of V5 and V6 +20 - -75 µm powders produced by gas atomization (%wt).

V5		**Fe**	**Mo**	**P**	**C**	**B**	**O**	**Si**
	Targed	86.80	5.70	5.50	1.80	0.30	0	0
	Actual	85.05	5.4	5.54	1.76	0.38	0.008	1.86
	Deviation	0.99	0.73	0.23	0.02	0.02	0.001	0.09
	Difference	-1.75	-0.3	0,04	-0.04	0.08	0.008	1.86
V6		**Fe**	**Mo**	**P**	**C**	**B**	**O**	**Si**
	Targed	83.26	9.29	5.40	1.74	0.31	0	0
	Actual	81.15	9.01	5.63	1.68	0.43	0.007	2.09
	Deviation	2.40	0.24	0.48	0.01	0.04	0.001	0.09
	Difference	-2.10	-0.28	0.23	-0.06	0.11	0.007	2.09

Although crystalline phases were observed through microscopy analyses, for V5 and V6 +20 - -75 µm powders, only three peaks were revealed by XRD analyses, as shown in **Figure 4.15**. When compared to the fully glassy XRD patterns of the ribbons, three peaks are at the top of the main broad diffraction "halo" for the powders. As indexed in **Figure 4.15** the main reflections correspond to α-Fe, γ-Fe and $M_{23}X_6$. The Bragg peaks have low intensities and are relatively broad, suggesting a sub-micron grain size and a low crystalline volume fraction. Thus, the results confirm the formation of a composite microstructure consisting of a glass matrix with uniformly dispersed refined crystalline phases. This is quite interesting, considering that the FeMoPCBSi system has been presented with relatively high GFA. Consequently, one could expect gas atomized powders to be fully glassy. This can be explained by the use of commercial raw materials to produce the powders, which may have influenced the GFA of the system. Crystallization was fully avoided only under the high cooling rates of melt spinning (10^4-10^6 K/s) [131].

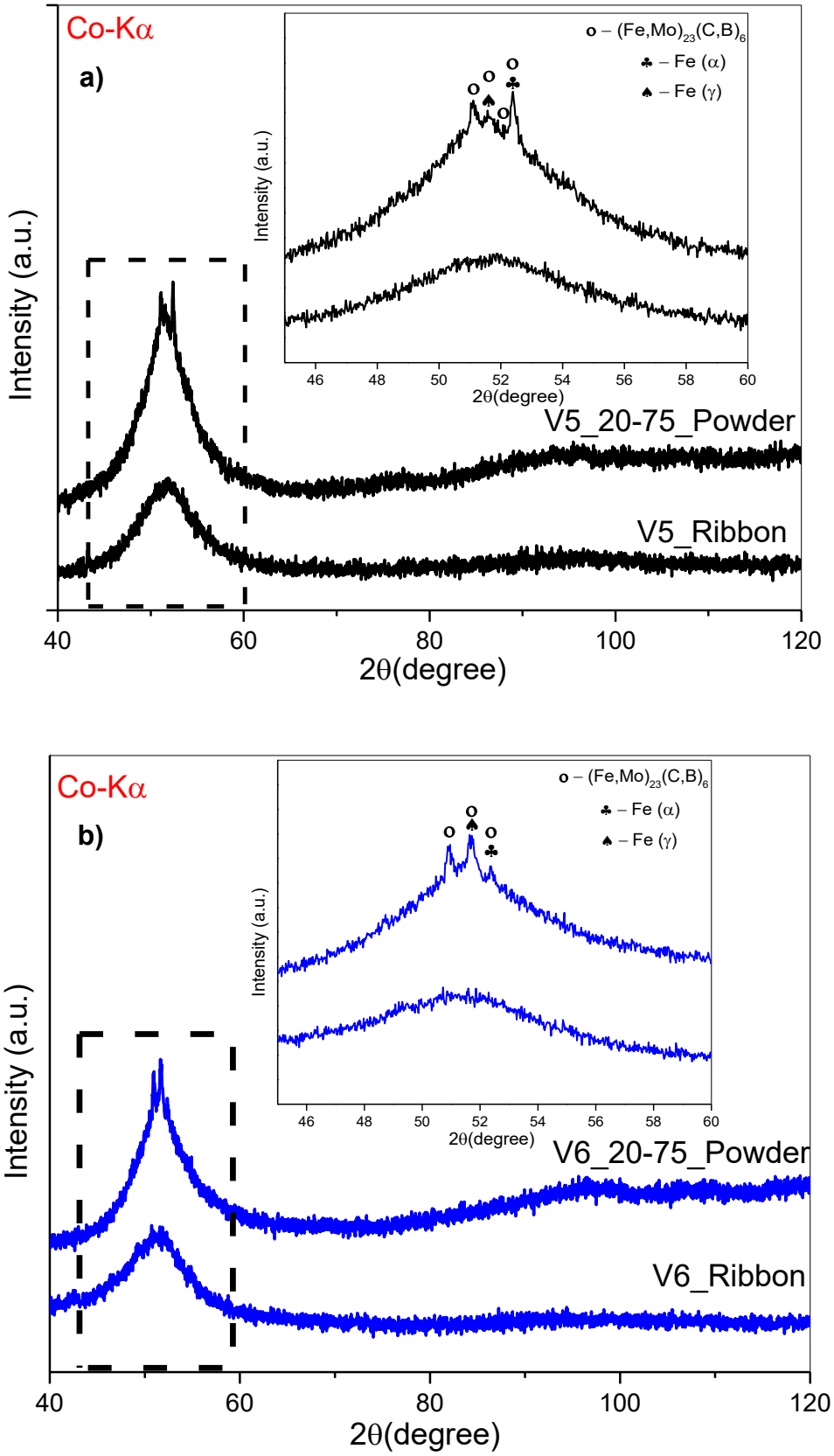

Figure 4.15- X-ray diffractograms of the ribbons and powders of **a)** V5 and **b)** V6.

To understand the crystallization process in the V5 and V6 gas atomized powders, different particle size ranges were investigated by XRD and DSC. **Figure 4.16a)** and **b)** show X-ray diffractograms of V5 and V6 powders, respectively. From these results, powders with a size <45 μm exhibit XRD patterns with only one broad diffraction peak without any evidence of crystalline phases, indicating a fully glassy microstructure. When the powders particles are in the range of 45 μm – 75 μm, one can see sharp reflections being superimposed on the broad glassy halo. For particles bigger than 75 μm, but lower than 150 μm, the XRD patterns present very sharp peaks, revealing the significant presence of crystalline phases, still embedded in a glassy matrix. In general, V5 and V6 powders present quite similar XRD patterns, even though for the range of 75-150 μm the crystalline peaks are more intense. The ICSD database was used for phase identification and the main crystalline phases matched with structures of α-Fe ($Im\bar{3}m$) [215], γ-Fe ($Fm\bar{3}m$) [216], $M_{23}X_6$ ($Fm\bar{3}m$) [217], and Fe_3P ($I\bar{4}$) [218] crystalline phases.

The thermal characterization of the V5 and V6 powders in different ranges is depicted in **Figure 4.16c)** and **d)**. The DSC curves show clear traces of the glass transition with an apparent onset (T_g) at about 388°C and 394°C for V5 and V6 powders, respectively, measured using the midpoint method [219] shown in **Figure 4.16e)** and **f)** at a heating rate of 40 K/min. A plateau indicating the super-cooled liquid region is observed in all curves, but is clearer for the powders with particle sizes <20 μm. There are in total four crystallization events (T_{x1}, T_{x2}, T_{x3}, and T_{x4}), where the largest crystallization enthalpy is observed for the second event. The total crystallization enthalpy for each range of V5 and V6 powders is presented in **Table 4.10**. The subsequent endothermic melting takes place in three steps, with the first onset close to 810°C.

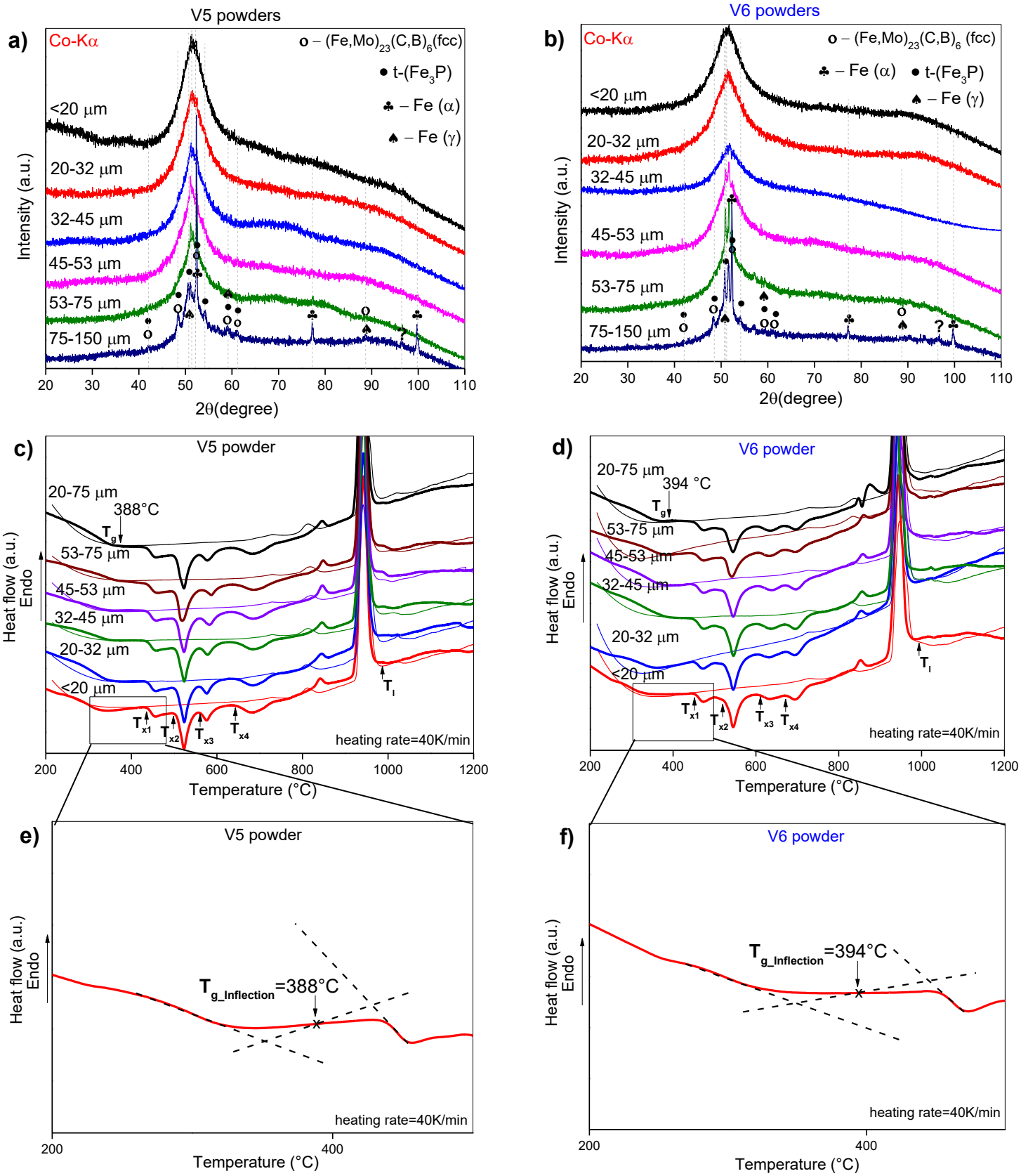

Figure 4.16- X-ray diffractograms of **a)** V5 and **b)** V6 powders in different size ranges; DSC curves with marked points of the glass transition temperature T_g,

crystallization temperatures T_x, melting temperature T_m, and liquidus temperature T_l, of **c)** V5 and **d)** V6 powders in different size ranges; Midpoint method [219] used to determine T_g of **e)** V5 and **f)** V6 powders.

Table 4.10- Area of the exothermic peaks in J/g for each range of size of V5 and V6 powders.

Powder	V5	V6
	Area J/g	
<20 µm	-112.5	-105
20-32 µm	-106.5	-105
32-45 µm	-105	-124
45-53 µm	-114	-99
53-75 µm	-108	-87
20-75 µm	-118	-112

V5 and V6 ribbons were used as a reference for the glassy phase amount present in the +20- -75 µm V5 and V6 powders. Thus, **Figure 4.17** compares the DSC curves of V5 and V6 powders and ribbons at two heating rates 20 K/min (**Figure 4.17a)** and **b)**) and 40 K/min (**Figure 4.17c)** and **d)**). At 20 K/min, V5 powder had a degree of crystallization of ~15%, while V6 powder presented ~36%. When 40 K/min was used, these percentages were about 0% and 10% for V5 and V6 powders, respectively. Such differences can be explained by the small size of the DSC's samples, where the content of each particle size range can slightly differ from sample to sample and cause significant differences in the DSC signal. However, from the XRD results presented in **Figure 4.15**, one can see that the V5 and V6 powders' patterns are very similar, and a similar degree of crystallinity would be expected. Interestingly, when ribbons were produced, V6 alloy presented better GFA (T_{rg} =0.55), see **Table 4.6**, whilst when powders were produced, V5 alloy showed better GFA (T_{rg} =0.53), against a T_{rg} =0.51-0.52, for

V6. It is worth noting that this variation may also be related to the uncertainty in the T_{rg} values used to estimate the GFA of the alloys.

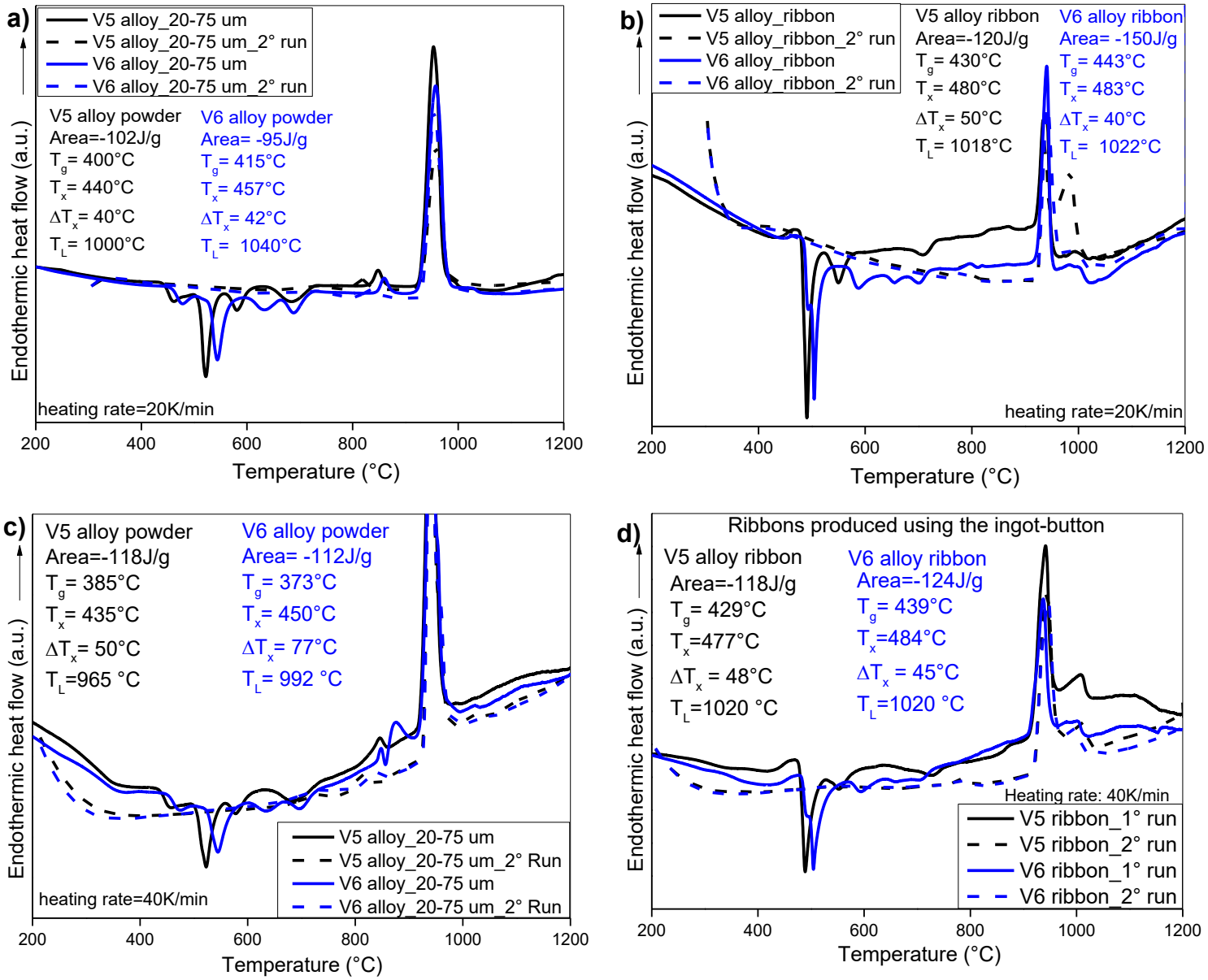

Figure 4.17- DSC curves of V5 and V6 samples: **a)** +20- -75 µm powders and **b)** ribbons at a heating rate of 20 K/min; **c)** +20- -75 µm powders and **d)** ribbons at a heating rate of 40 K/min.

4.4 LPBF experiments

4.4.1. Omnitek machine (unheated substrate)

Exploratory experiments were executed using the LPBF process to investigate the V5 and V6 powders' flowability, as well as the behavior of deposits of a few layers (n=10) produced under different parameters of the process, especially laser power and scan speed. It was decided to begin with the worst-case scenario, so the first experiments were using V6 powder (due to its lower GFA, as indicated in the powders' results section). Different laser power and scan speed were used as shown in **Figure 4.18a)**, combined with two laser strategies, as displayed in **Figure 4.18b)** and **c)**. Here, the samples were labeled using a code in the format PX_VY, where: PX refers to the laser power used during the LPBF process, with X indicating the power in watts, and VY indicates the scanning speed, with Y corresponding to the velocity in mm/s. During the LPBF experiments, the powders did not present any issue relating to the flowability, and the samples produced, without and with remelting, are shown in **Figure 4.18d)** and **e)**. From these pictures, it can be observed that the samples produced with the chessboard-like laser strategy are shinier than those produced using the uni-directional laser strategy. Such a feature was expected, once the literature has reported the role of chessboard laser strategy in increasing the ability of glass formation for Fe-based alloys [182],[188]. It can also be observed that the remelting step makes the samples even shinier, which agrees with the increase of glassy content by the remelting strategy, as has been reported in the literature [146],[151],[182],[188]. To make these eye observations even clearer, the surface of the samples was investigated by optical microscopy, and the images of the respective samples are in **Figure 4.18f)**. From these images, the observations related to glass formation/restoration "made by eyes" were confirmed, but now, it can be noticed that the chessboard strategy results in more porous samples, and that such porosity is reduced by the remelting step. While Pauly et al. [140] have reported higher porosity for samples produced with the chessboard laser strategy, others revealed the remelting step as a tool for glass restoration as well as samples' densification [153],[182]. From our results, the remelting step also

seems to increase the cracks' presence in the samples, but further investigations would be necessary to confirm such observation. Regarding laser power and scan speed, it is visible that 100 mm/s of scan speed is too low, consequently, the samples have a dark appearance. When the laser power is increased above 210 W, the dark appearance is revealed for samples with 200 mm/s as well. The dark appearance is less evident for the samples produced using the chessboard laser strategy, and even less for those remelted ones.

a)

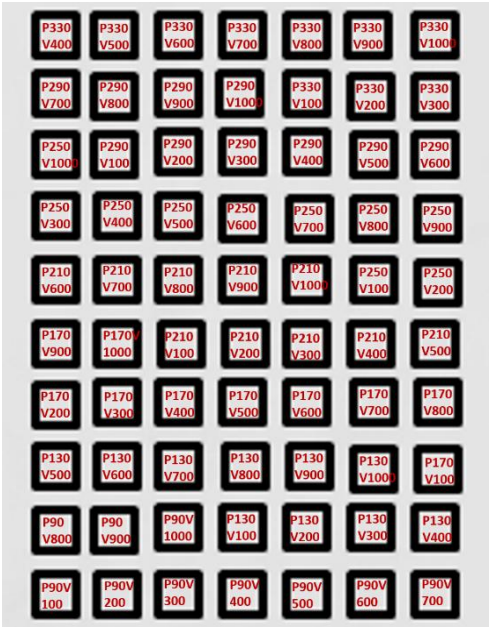

b) Uni-directional laser strategy

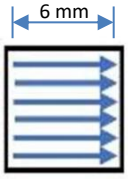

c) Chessboard-like laser strategy

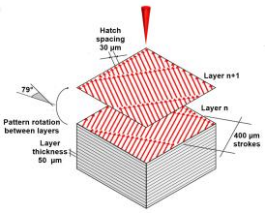

d)

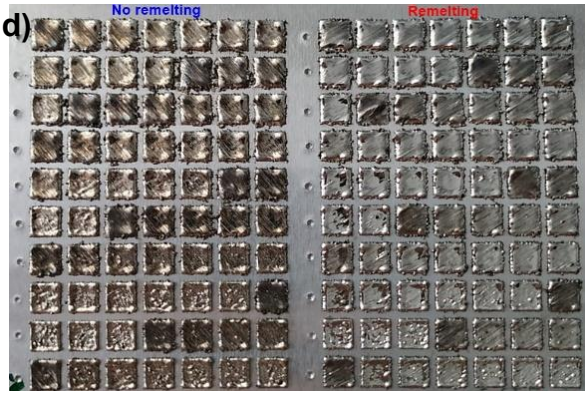

e)

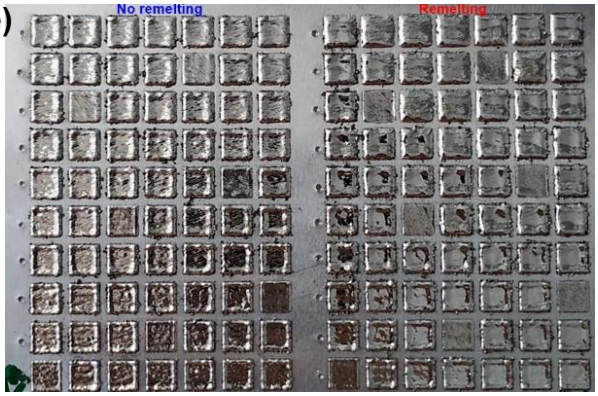

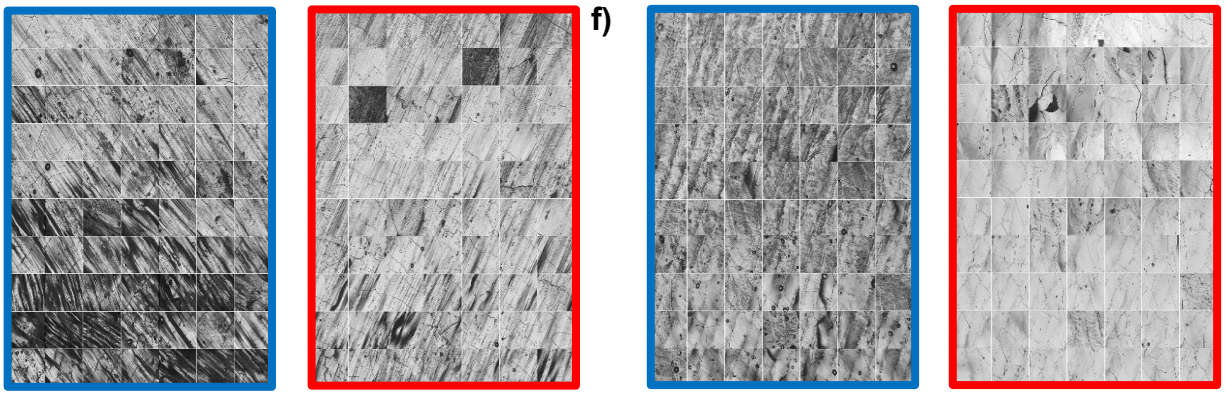

Figure 4.18- Results of the exploratory V6 LPBF experiments. **a)** Scheme of samples position with laser power (P) and scanning speed (V) used, **b)** and **c)** scheme of the two laser strategies used; **d)** and **e)** view of the LPBF samples, side-by-side, without and with remelting step and **f)** optical microscopy imagens of the LPBF samples' surface produced with the two laser strategy, without (blue mark) and with (red mark) remelting.

Since the best results in the V6 LPBF experiments were obtained using the chessboard-like laser strategy, this same strategy was adopted for the exploratory LPBF experiments with the V5 alloy. The produced samples are shown in **Figure 4.19a)**. At a general glance, they appear similar to those of V6 fabricated under the same conditions. As with the V6 LPBF samples, the remelting step enhanced the shiny appearance and reduced porosity. However, as observed in the surface optical microscopy images of the V5 LPBF samples (**Figure 4.19b)**), there are more regions with brighter contrast in the V5 samples compared to the V6 samples when no remelting was applied (indicated by blue marks). This may suggest a better GFA in the V5 alloy, consistent with the observations from the powder results. Conversely, for samples processed with the remelting step (indicated by red marks), the V6 LPBF samples exhibited more prominent bright regions This suggests that remelting is an effective strategy for increasing the glassy phase in the V6 LPBF samples.

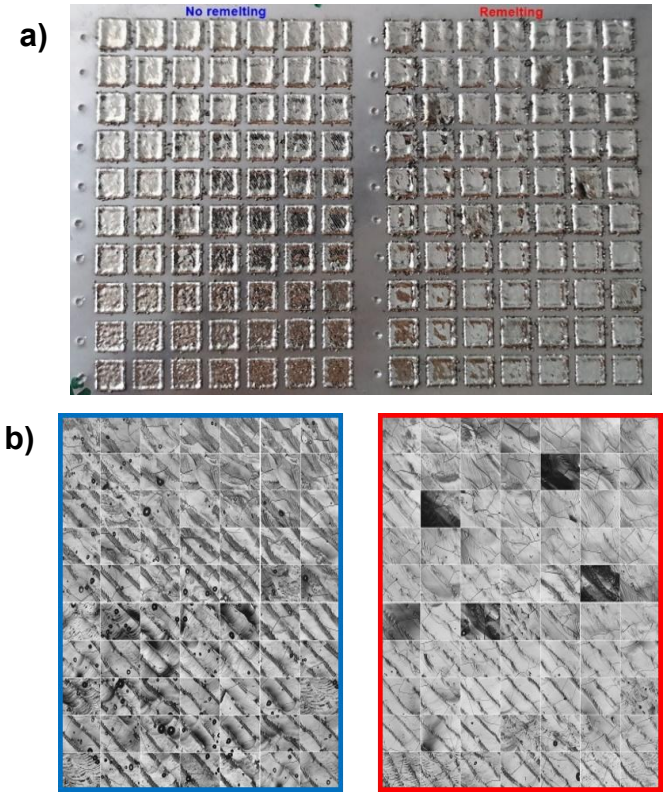

Figure 4.19- Results of the exploratory V5 LPBF experiments using chessboard laser strategy: **a)** view of the samples, side-by-side, without and with remelting step and **b)** optical microscopy images of the surface for the LPBF samples produced without (blue mark) and with (red mark) remelting.

V5 and V6 LPBF samples produced using the chessboard laser strategy and remelting step were selected for further investigation. As shown in the appendix (see **Figure A.2a)** and **b)**), the cross-section of these samples was prepared by grinding and polishing, and the OM images reveal their integrity. From these images, the most suitable range of parameters, considering the range investigated in this work, was in the interval of 90-210 W of laser power and 300-900 mm/s of scan speed. Thus, these four extreme combinations, named as P90_V300, P90_V900, P210_V300, and P210_V900, were selected to be studied in more detail. The corresponding energy input in J/mm^3 is 200 (P90_V300), 67 (P90_V900), 467 (P210_V300), and 156 (P210_V900).

Figure 4.20 shows the XRD and DSC results of the selected V5 and V6 LPBF samples (P90_V300, P90_V900, P210_V300, and P210_V900). From V5

and V6 LPBF XRD patterns (**Figure 4.20a)** and **c)**), it is confirmed the formation of a composite microstructure, where crystalline α-Fe, $M_{23}X_6$ (M=Fe or Mo, and X=C or B), and Fe_3X (X=P or C) phases are together with a glassy matrix (confirmed by the glassy broad peak, similar to the powders' XRD). By the XRD patterns, both alloys can form the same crystalline phases; however, they formed in different amounts. While the α-Fe peaks are more intense in V5 LPBF samples, the peaks corresponding to the $M_{23}X_6$ phase are more intense in V6 LPBF samples. Additionally, for both alloys, the Fe_3X peaks are intensified when the higher energy (467 J/mm^3) input is used to produce the samples (P210_V300). Considering the different combinations of parameters, no significant differences were observed in the XRD diffractograms. The DSC curves for the V5 and V6 LPBF samples are shown in **Figure 4.20b)** and **d)**. The curves had the same character with two overlapping crystallization events. Considering V5 LPBF samples, produced with different combinations of parameters, no significative difference was observed in DSC curves. For these samples, T_g was about 450°C, and on average 28 J/g was released for the crystallization of the glassy phase. For V6 LPBF samples, those produced with the same laser power had similar DSC curves. While the P90 samples released about 12 J/g, those using P210 released about half ~ 6 J/g for the crystallization event. Except for the P210_V300 sample, T_g was around 460°C for the V6 LPBF samples. The results show that V5 can form glassy phases more easily than V6 when processed by LPBF. So, for V6, increasing laser power decreases the amount of glass, even when the scan speed of the laser is increased. Agreeing with the powders' results, V5 has better GFA than V6 by the LPBF process as well.

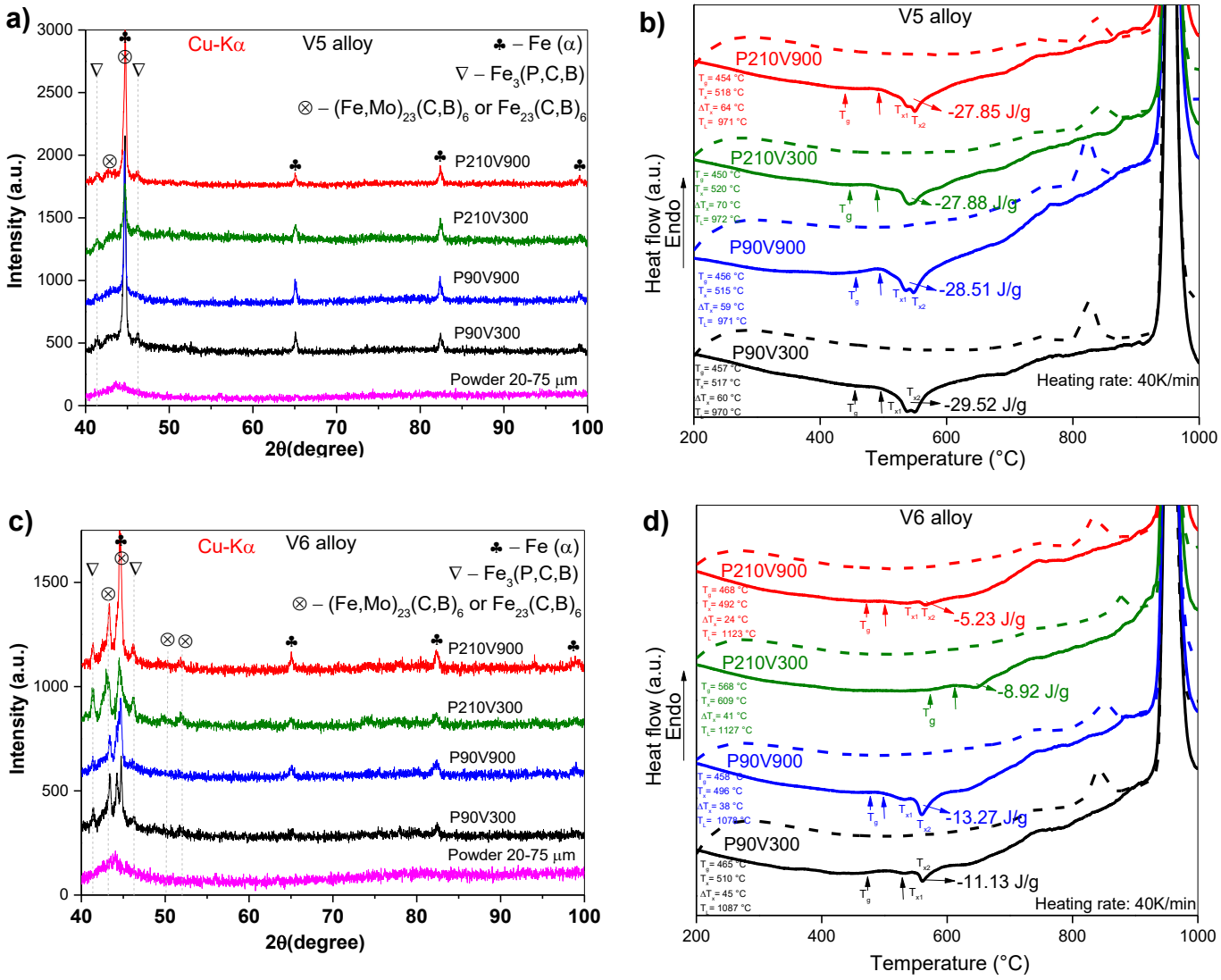

Figure 4.20- X-ray diffractograms and DSC curves of the selected LPBF samples produced with chessboard laser strategy and using remelting step for V5 alloy **a)** and **b)**, and V6 alloy **c)** and **d)**.

OM images of the etched cross-section of the selected V5 and V6 LPBF samples are displayed in **Figure 4.21a)** and **b)**. From these images, the molten pool profile is not so clear, except for V5 LPBF samples produced with P210. Nevertheless, regions with bright and dark contrasts can be clearly observed. Since crystalline phases are more easily etched than glassy phases, the dark contrast is correlated to the crystallized areas, while the bright contrast (unetched regions) is associated with the glassy-rich areas. The crystallized areas are the Heat Affected Zone (HAZ), which resulted from the crystallization of the

overlapping glassy regions during the melting of the neighboring melt pools. Most likely as a result of the remelting step, the glassy phase is randomly distributed, forming distinct regions with crystalline boundaries, similar to what has been previously reported by [151]. In addition, it was revealed that the samples produced with the higher energy input, P210_V300, are heavily cracked along the whole deposit thickness.

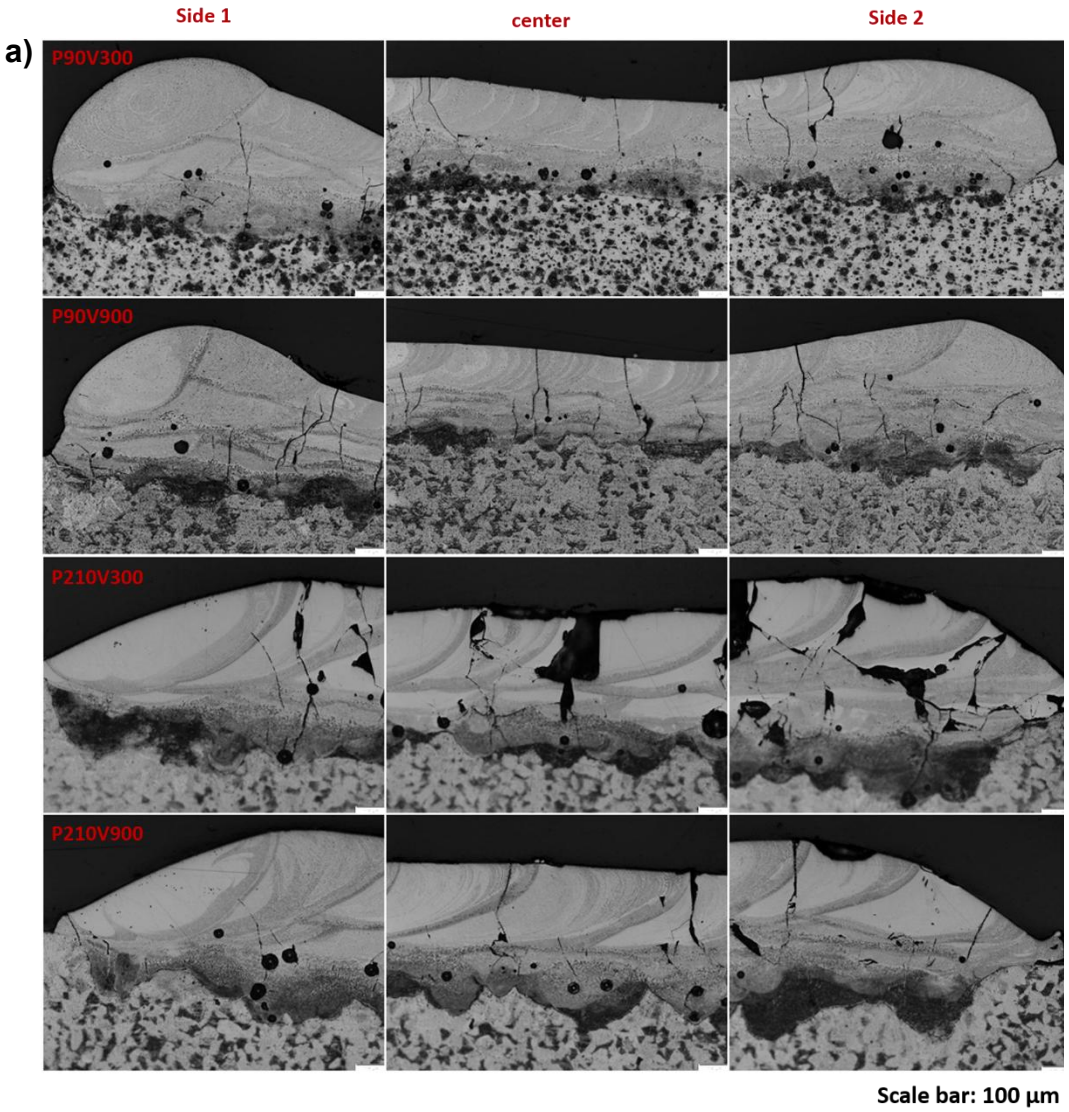

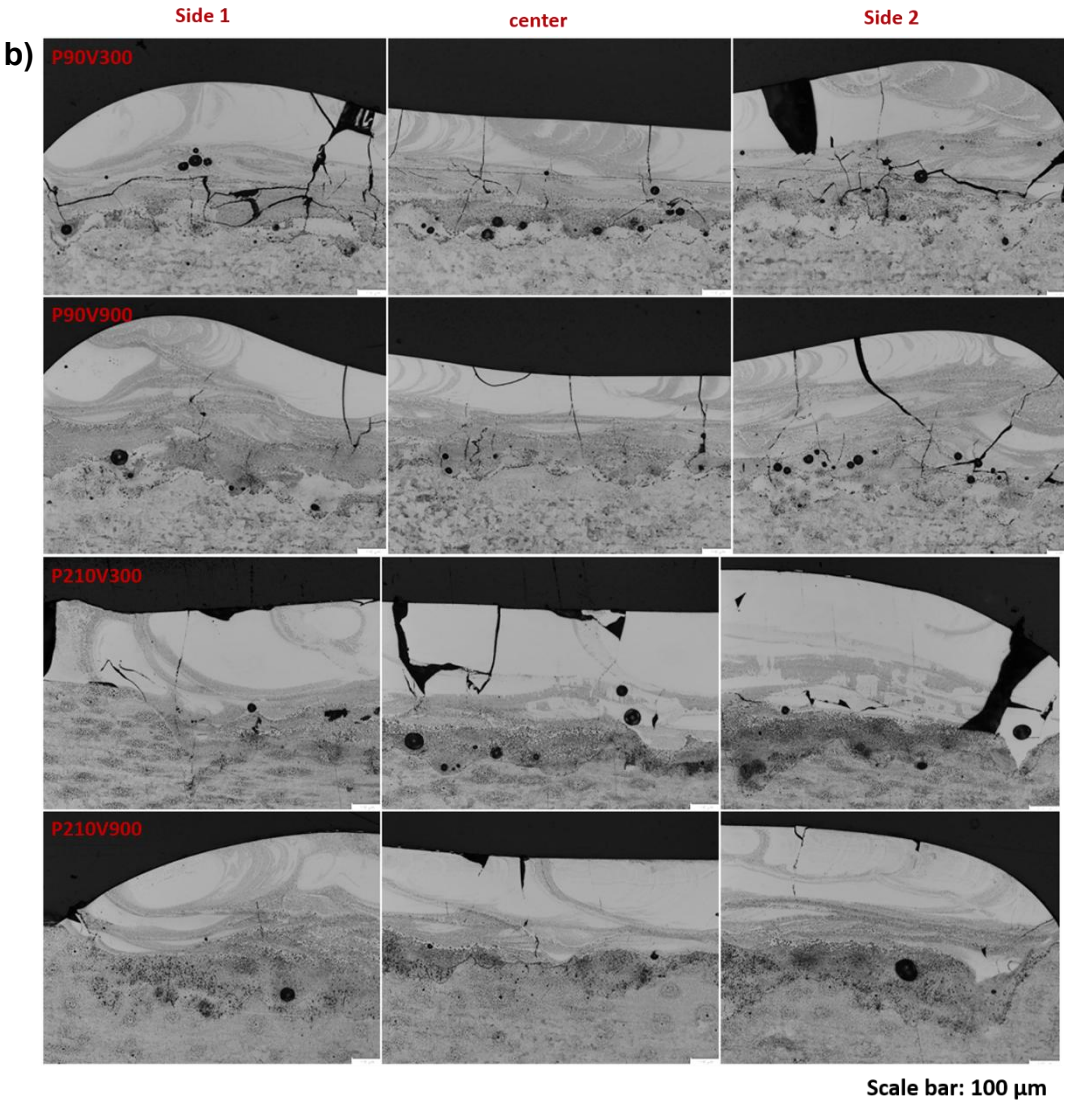

Figure 4.21- Optical microscopy images of the etched cross-section of LPBF samples, produced using P90_V300, P90_V900, P210_V300, P210_V900 for **a)** V5 and **b)** V6.

Intrinsic properties of materials such as atomic bonding strength and bonding energy are typically reflected through hardness and Young's modulus measurements [220]. Thus, the hardness and Young's modulus were investigated for the glassy and crystallized regions of the LPBF samples. Due to the small dimensions of specific melt pool regions, nanohardness measurements were considered. Curves of load versus displacement obtained for the individual molten pool regions of V5 and V6 LPBF samples are presented in **Figure 4.22a)**

and **d)**, respectively. For V5 LPBF samples (**Figure 4.22a)**), independently of the combination of parameters used, the glassy-rich regions (inside melt pool) were always slightly softer than the crystallized ones (HAZ=border of melt pool). According to the literature, the free volume in a glassy microstructure typically features larger interatomic distances and lower atomic bonding energy compared to a crystalline microstructure [221]. It can justify the lower hardness of the glassy-rich regions. Authors [207], [222] also have found higher hardness in the crystallized regions by nanoindentation tests of a LPBF Fe-Co-B-Si-Nb BMG. They assert that the precipitation of crystallite in the glassy matrix for the HAZ can reinforce it, leading to a slight increase in nanohardness. These authors [207], [222] still concluded that the differences in the hardness values of the two regions (glassy-rich and HAZ) are almost negligible, and the same is observed in the present work. Others [223] suggested a gradual increase in the hardness of LPBF samples as a function of increasing the energy input up to a certain limit, from which the hardness tends to drop with further increases in energy input. From the P90V300 sample, an increase in P (P210_V300) or in V (P90_V900), or even in P and V together (P210_V900), slightly softens both regions (glassy and crystallized), but no significant differences can be observed. It indicates that the influence of processing parameters on the hardness of glassy-rich and crystallized regions is very low. It is expected that if different parameter combinations result in samples with the same composite microstructure, i.e., with the same phases, independently of the parameters used, the hardness of each region (glassy-rich and crystallized) in different samples should be maintained. As the hardness of glassy-rich and crystallized regions was quite similar, a mean hardness for each sample was calculated and is presented in **Figure 4.22b)**. A mean Young's modulus for the samples is also given in **Figure 4.22c)**. From the results, considering the standard deviation of the measurements, all samples have an equivalent hardness of about 12.5±1.7 GPa and Young's modulus around 201.5±13.7 GPa.

Differently, for V6 LPBF samples, the load versus displacement curves (**Figure 4.22a)**) reveal that the glassy-rich (bright) and crystallized (HAZ) regions have similar hardness, but, in some cases (low laser power (P90)), the glassy-

rich regions are slightly harder than the crystallized regions. According to the Hofmann et al. [150], the presence of a crystallized phase in the HAZ decreases the LPBF sample's hardness. Luo et al. [207] have reported that the hardness of glassy and HAZ regions can change with the LPBF processing parameters due to two aspects: 1) the presence or absence of finer grains in the melt pool center (glassy-rich region) and 2) the partial or complete crystallization of HAZ. It is explained that when the glassy regions are rich in finer grains, they are harder than the HAZ, whilst the HAZ is harder than the glassy regions when it is partially crystallized, i.e., not fully crystallized [207]. Due to the similarity of hardness and modulus for the two regions, an average of these properties for each sample was calculated, and it is displayed in **Figure 4.22e)** and **f)**. Considering the standard deviation, the samples have similar hardness, on average 11.75±2.6 GPa, and Young's modulus around 200±13.4 GPa. It is noteworthy that these values are comparable to those obtained for V5 LPBF samples.

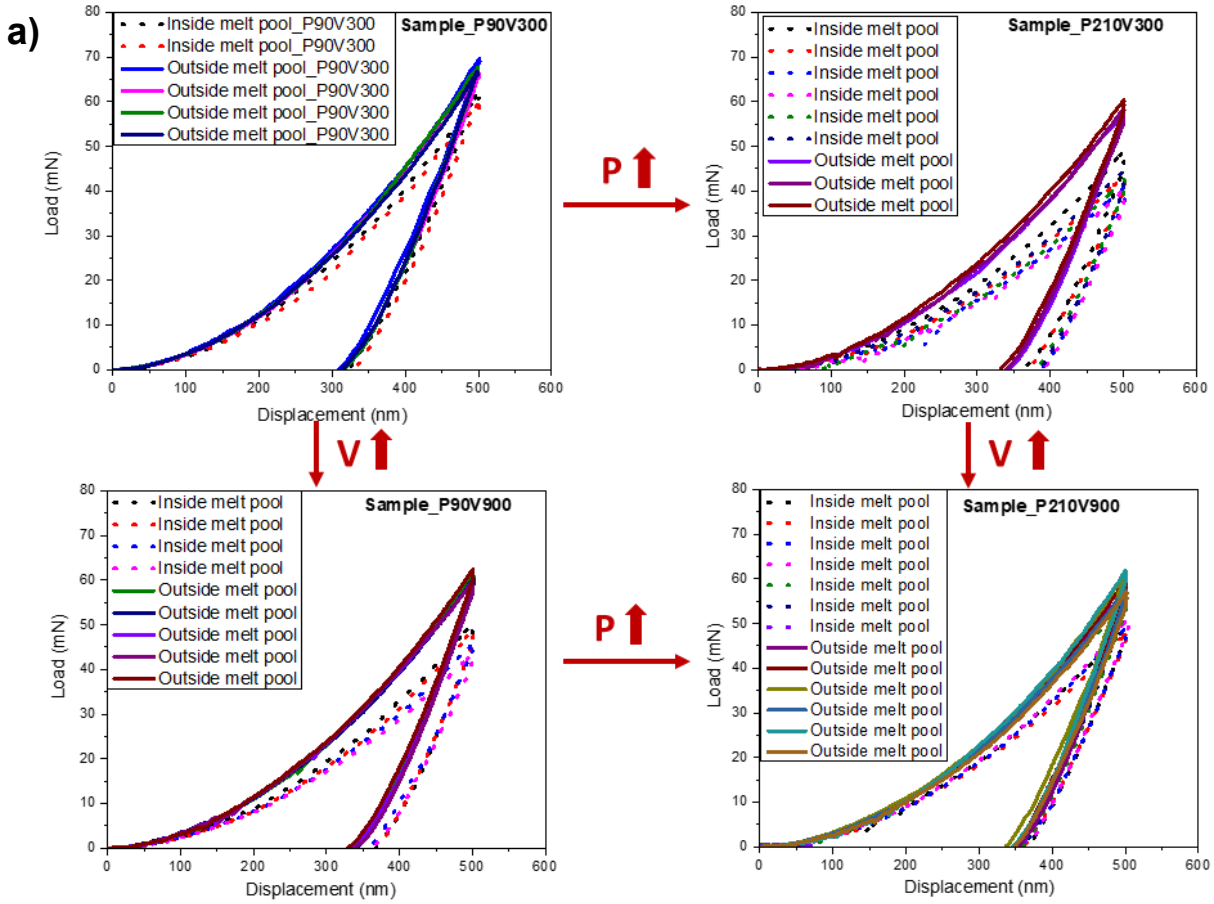
a)
Sample_P90V300
Inside melt pool_P90V300
Outside melt pool_P90V300
Sample_P210V300
Inside melt pool
Outside melt pool
Sample_P90V900
Sample_P210V900
Load (mN)
Displacement (nm)
P
V

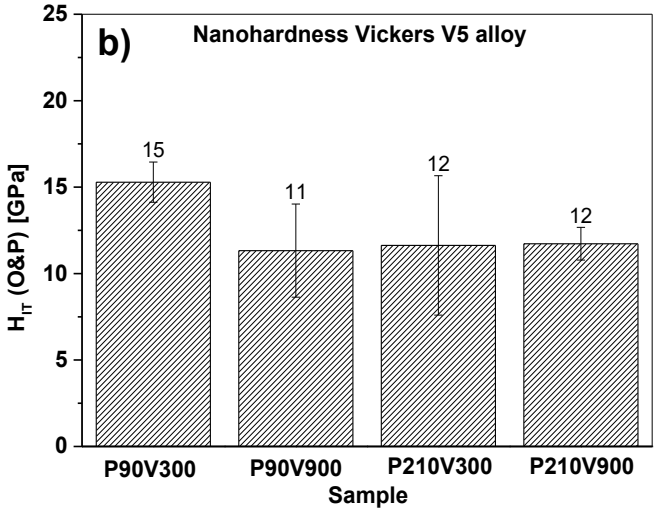
b)
Nanohardness Vickers V5 alloy
H_{IT} (O&P) [GPa]
15
11
12
12
P90V300
P90V900
P210V300
P210V900
Sample

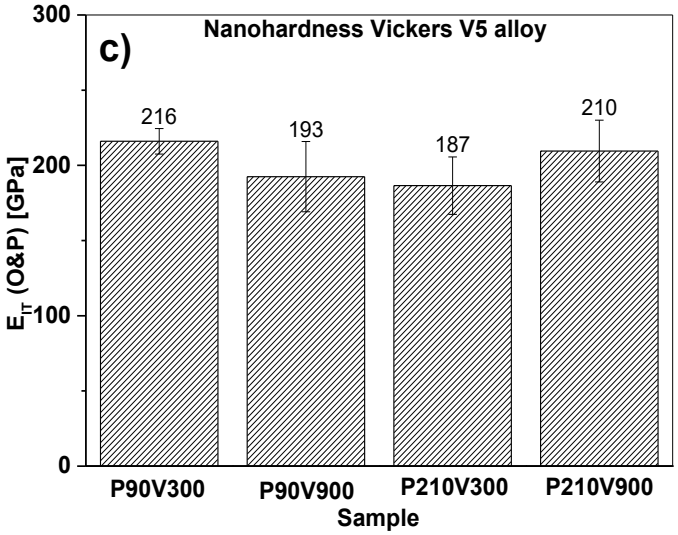
c)
Nanohardness Vickers V5 alloy
E_{IT} (O&P) [GPa]
216
193
187
210
P90V300
P90V900
P210V300
P210V900
Sample

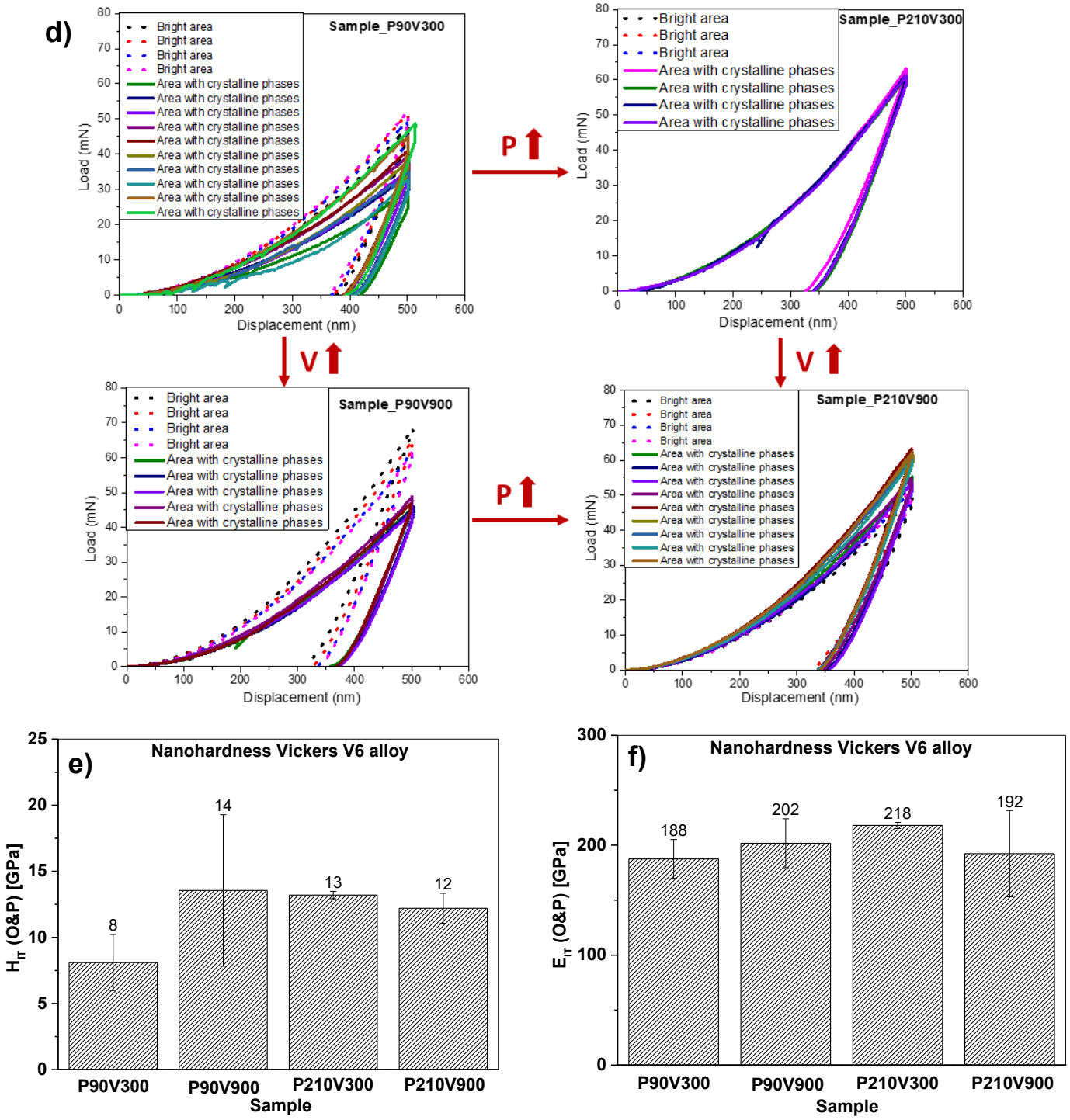

Figure 4.22- Nanoindentation load-displacement (L-D) curves in different regions of **a)** V5 and **d)** V6 LPBF samples. Mean of **b)** and **e)** nanoindentation hardness (H_{IT}), and **c)** and **f)** Young's modulus (E_{IT}) for V5 and V6 LPBF samples.

The backscattered electron (BSE) images of the selected V5 and V6 LPBF samples reveal very similar contrasts. Thus, only one sample (P210_V900) of each alloy was selected as a representative one, and the microstructure is shown in **Figure 4.23**. For V5 (**Figure 4.23a)**, **b),** and **c)**), the molten pool shape is very unclear, but the glassy-rich and HAZ regions are distinguished as indicated in **Figure 4.23b)**. Differently, for the V6 LPBF sample (**Figure 4.23d)**, **e),** and **f)**), the molten pool is well evidenced with the glassy-rich region located in the center of the melt pool and the HAZ region as the border of the molten pool. While V6 shows continuous HAZ (crystallized regions), V5 presents non-continuous HAZ embedded in a featureless glassy matrix. The glassy-rich regions are represented by a homogeneous and featureless microstructure. Even though the same amount of energy was used to produce the samples (156 J/mm^3), it seems the temperatures achieved in the HAZ of V5 caused coarser crystallization than the temperatures reached in V6 HAZ. Whilst the HAZ of V5 is rich in dendrites of ~1-5 µm in size (see **Figure 4.23c)**), the HAZ of V6 is full of round and small (~1 µm) black and white crystalline phases (see **Figure 4.23f)**).

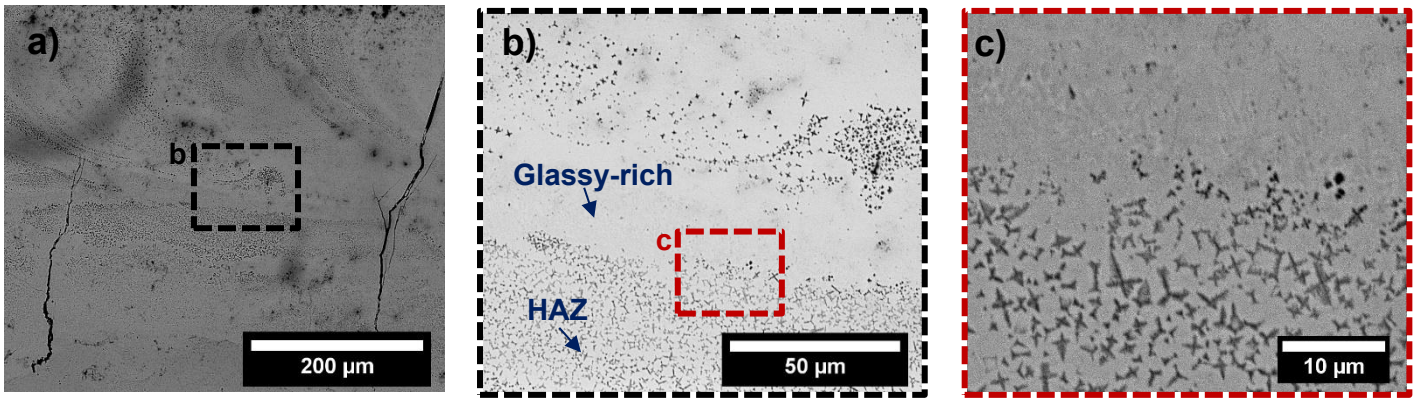

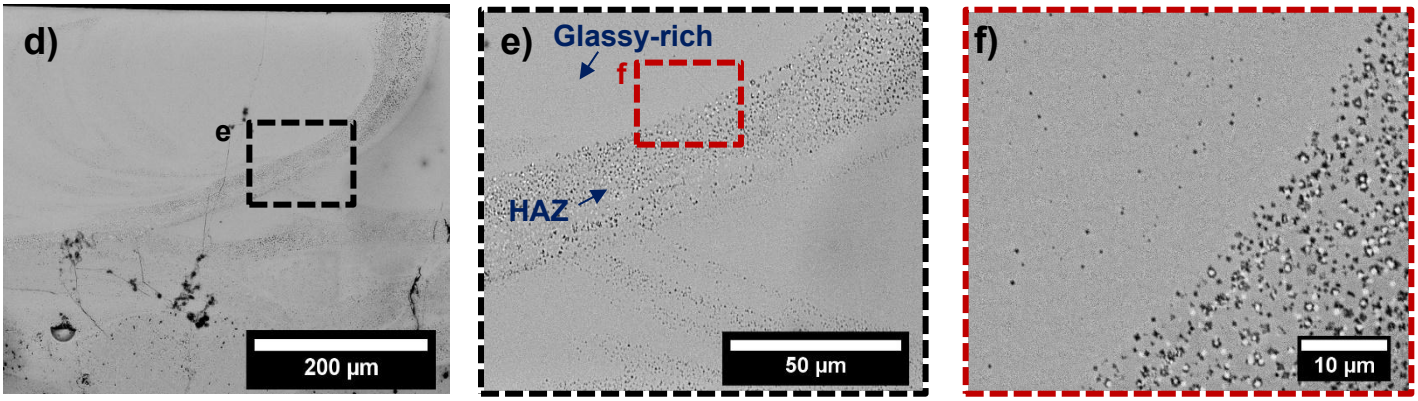

Figure 4.23- Representative SEM images of P210_V900 LPBF samples for V5 **a)**, **b)** and **c)**, and V6 **d)**, **e),** and **f)**.

4.4.1. AconityMini machine (heated substrate)

In order to reduce cracking in the LPBF samples, the use of a heated substrate was considered. Taking into consideration the results of the exploratory experiments executed in the Omnitek machine, the suitable process window (interval of 90-210 W of laser power and 300-900 mm/s of scan speed) was used. A scheme of the laser strategy, laser power and scan speed is shown in **Figure 4.24a)**.

The samples produced in these experiments also used the remelting step, but now, on a 316L steel heated substrate (200°C). The visual appearance of V5 and V6 LPBF samples as-produced is presented in **Figure 4.24b)** and **c)**. For P>170 W, combined with V<600 mm/s, the samples presented the super-elevation phenomenon at around 0.8mm height, and the production of these samples was stopped. When the remaining samples reached 1.2 mm height, those using P>170 W and V>600 mm/s also started to get super-elevation, so the whole process was stopped at this height. The samples that appeared to be fine during the process were detached from the substrate, as shown in the right-side images in **Figure 4.24b)** and **c)**.

The cross-section OM analyses of V5 and V6 LPBF samples revealed that most of the samples are super porous (see **Figure A.3** in Appendix), the only

exception was those produced using 90 W combined with scan speeds higher than 600 mm/s. In addition, the cracks were not reduced, and then, only for comparison, two samples were selected to be analyzed by DSC, P90_V900 and P210_V900.

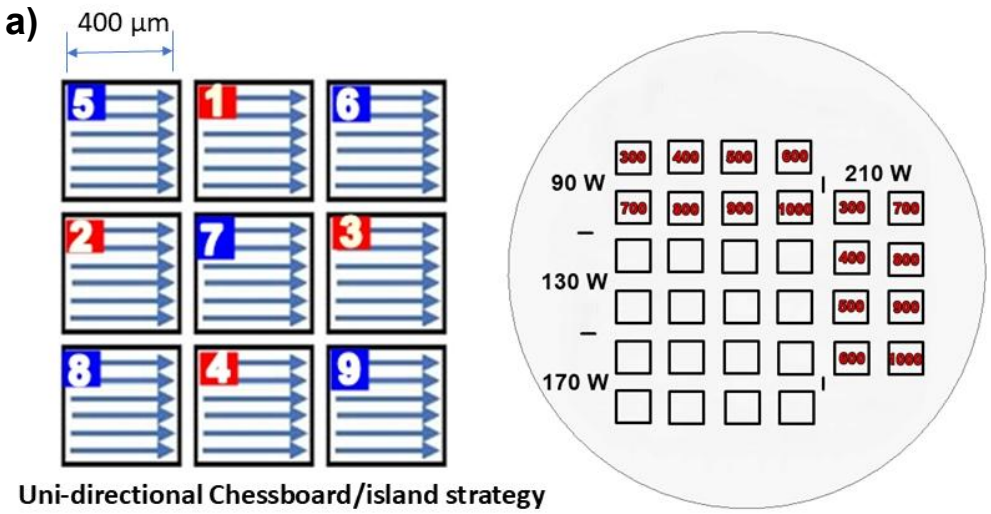

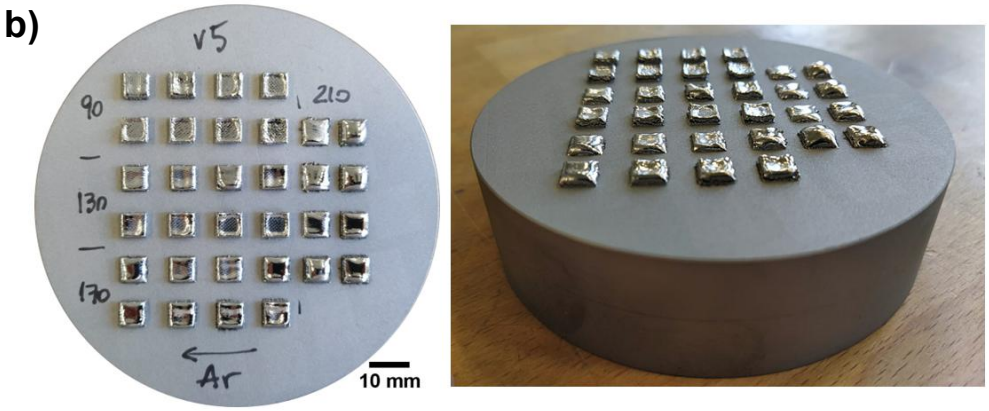

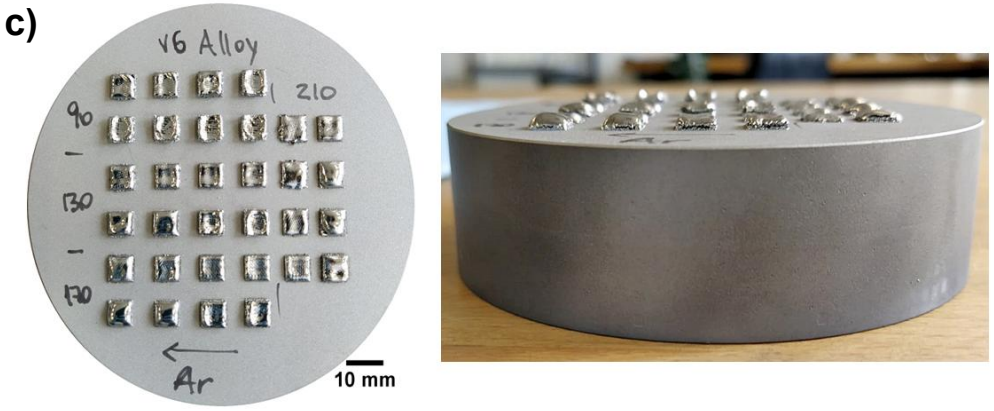

Figure 4.24- a) Scheme of the unidirectional chessboard/island laser strategy and samples position with laser power (P) and scanning speed (V) used to produce the samples; and images of the as-built LPBF samples for **b)** V5 and **c)** V6 alloy.

The DSC curves of the V5 and V6 LPBF samples (P90_V900 and P210_V900) are shown in **Figure 4.25a)** and **b)**. The absence of exothermic events in both curves indicates that the samples have fully crystalline microstructures. SEM analysis was conducted to further investigate their microstructural features. As V5 and V6 were processed using the same parameter sets and exhibited similar microstructures, only the micrographs of the V6 sample are presented in **Figure 4.26**. Both samples display fully crystalline structures; however, the P90_V900 sample (**Figure 4.26a)**, **b),** and **c)**) shows a finer microstructure with rounded phases approximately 1–2 μm in size. In contrast, the P210_V900 sample (**Figure 4.26d)**, **e),** and **f)**) contains phases of varying shapes and sizes, predominantly dendritic, ranging from 5–10 μm. These results suggest that the processing conditions for both samples were insufficient to suppress crystallization. Moreover, the higher energy input of 156 J/mm^3 used for P210_V900 led to significant coarsening in the heat-affected zone (HAZ), whereas the lower energy input of 67 J/mm^{3}used for P90_V900 resulted only in the precipitation of fine-scale crystals (<2 μm).

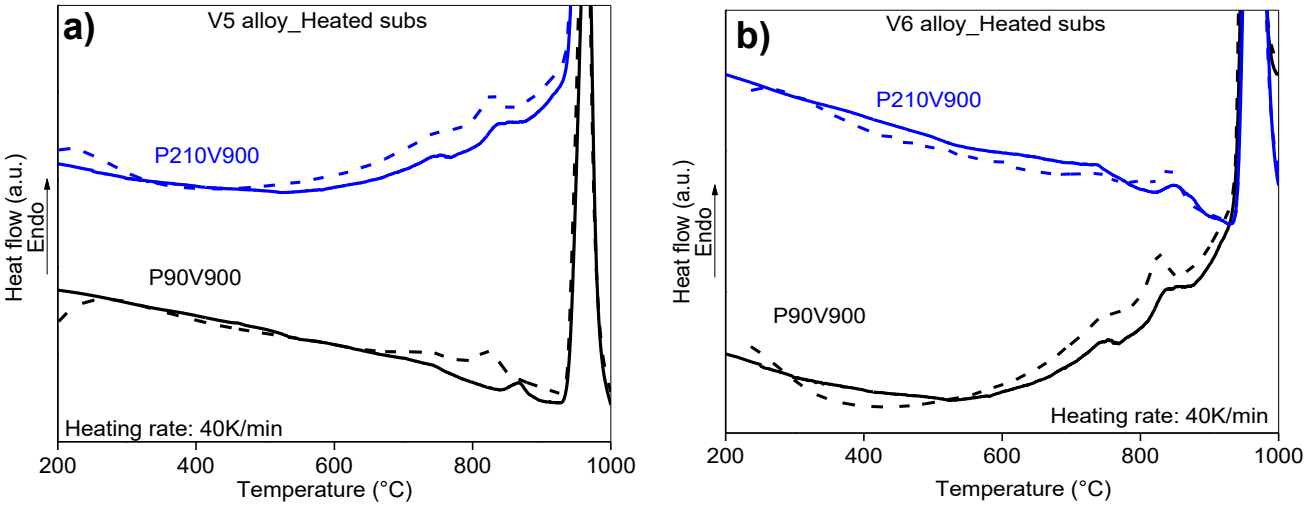

Figure 4.25- DSC curves of the LPBF samples produced using a heated 316L steel substrate (200°C) with P90_V900 and P210_V900 for **a)** V5 and **b)** V6.

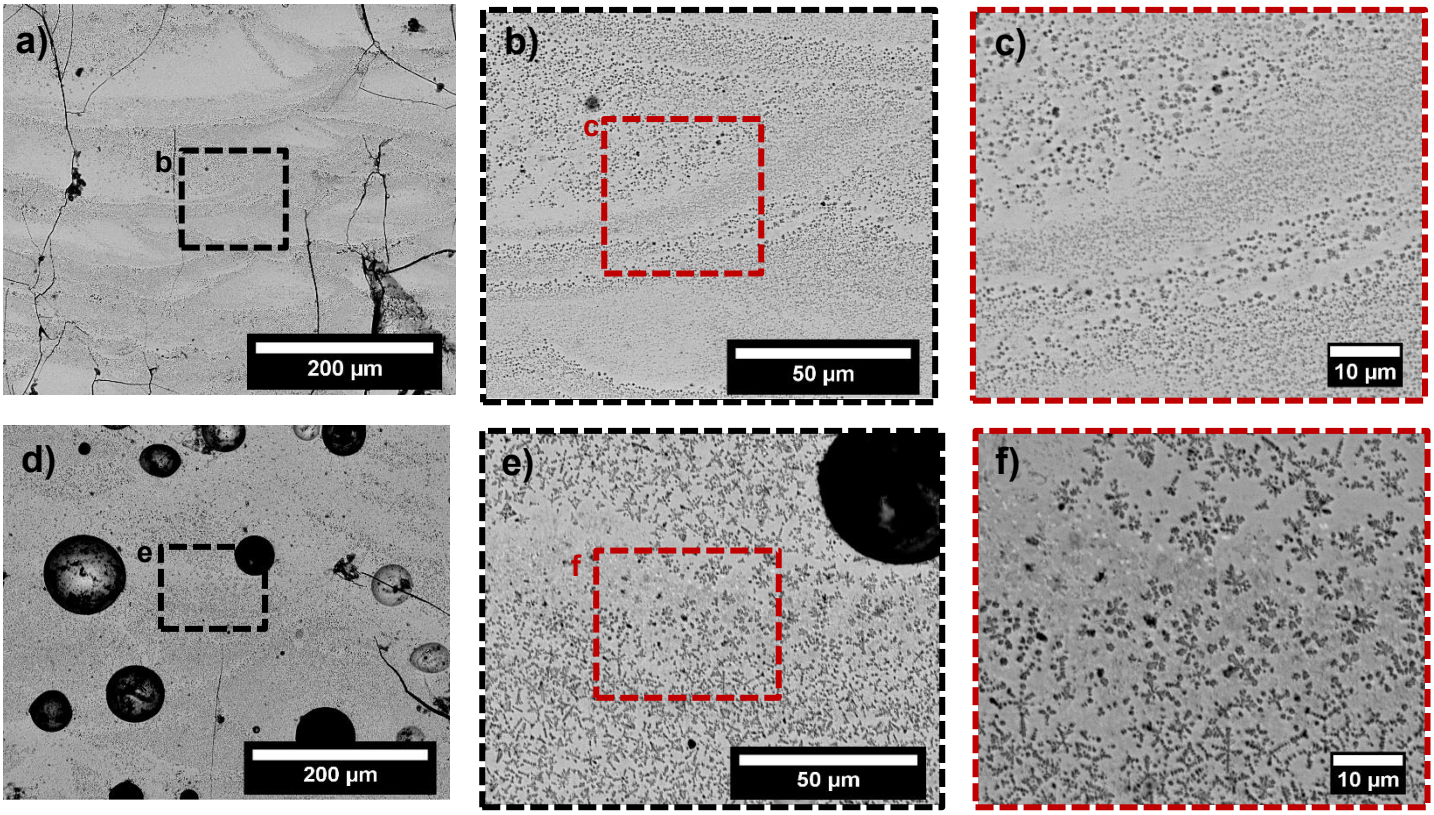

Figure 4.26- Representative SEM images of V6 LPBF samples produced using **a)**, **b)** and **c)** P90_V900 and **d)**, **e)** and **f)** P210_V900.

4.4.2. Acconity Midi+ machine

The most promising process parameters obtained in the previous experiments, i.e., 90, 130, 170 and 210 W of laser power, and 700 mm/s of scan speed, combined with remelting and unheated 1020 carbon steel substrate were tested as a starting point in the search of producing good bulky samples using the Acconity Midi+ machine. Herein, uni-directional/single strategy (SN), uni-directional/single random strategy (SR), and chessboard/island (Chess) were tested.

It was decided to initially process V6 powder, and the first round of LPBF samples is shown in **Figure 4.27**. The samples produced in this round exhibited poor quality, primarily due to inadequate structural integrity. It was not even possible to handle them to carry out other analyses, and the main defects and anomalies encountered during the samples production were: **1)** Super-elevation, which refers to the phenomenon where the height of the printed part exceeds the intended or expected layer height. It can be due to various factors, including improper combination of parameters and thermal effects. **2)** Residual stress/distortion, which is normally inherent to the AM process due to the small size of the molten pool and the repeated heating/cooling cycles. However, when it is intensified by an improper combination of parameters it can cause excessive cracking and delamination in macroscopic or microscopic scale. **3)** Flaking, refers to the delamination or peeling off of material from the printed part, often due to thermal stresses or poor adhesion as a result of using unappropriated process parameters as laser power, laser scanning speed, hatch distance and printing conditions[224]. Taking into consideration the results of this experiment, it was decided to change the parameters one by one, always following what the previous samples indicates as a good processing direction.

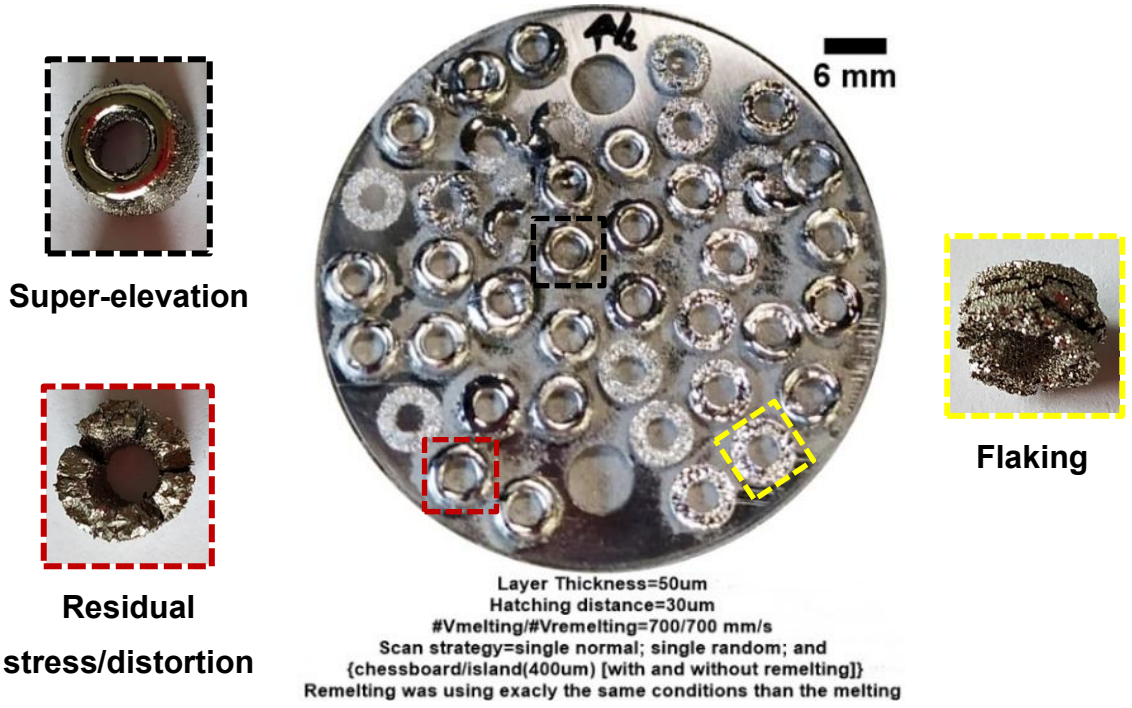

Figure 4.27- Main defects and anomalies encountered during production of the LPBF samples.

To obtain intact samples, the following parameters test sequence was employed (for reference, see the specified samples' rounds in appendix **Figure A.4**):

1) Different combinations of parameters for melting and remelting (2° round).
2) Increase the layer thickness from 50 µm to 70-90-100 µm (3° to 5°rounds).
3) Change the samples' geometry, (4°, 5°, 7° and 8° rounds).
4) Increase the hatching distance from 30 µm to 40 and 50 µm, (6° round).
5) Adjust the laser power for the melting (7° round).
6) Adjust the laser scan speed for the melting (8° round).
7) Finding a suitable combination of melting and remelting's scan speed (9° round).
8) Changing the material of the substrate from CK45 to 316L stainless steel and heating the substrate at 150°±20°C (10° round).
9) Adjusting the combination laser power/scan speed for the melting (11°, 12° and 13° rounds).
10) Using high scan speed for remelting (>1000 mm/s), produce samples

without remelting, change geometry and size of the samples (14° to 16° rounds).

11) Changing samples' size and printing direction (0°, 45° and 90°), (17° to 22° rounds).

12) Decrease laser power and change laser scan strategy, (23° to 28° rounds).

Regarding the influence of each tested parameters on the integrity of the V5 and V6 LPBF samples, a summary can be given:

The **remelting step**, using the same combination of parameters used in the melting, drastically compromised the integrity of the samples. When the energy input is high, the samples get very porous and the surface becomes super elevated in at least 10 times higher than the layer level. When the energy input is low, the samples are severe cracked and is not possible to manually handle them. Even though the literature [153], [182] highlight remelting as a promising approach for vitrification, in this work was observed that the remelting step acted intensifying the presence of cracks and devitrifying the glassy phases. This could be expected, since the glassy phase formed during the melting can easily be decomposed into crystalline phases, during the remelting, especially when the same combination of parameters of the melting is used for remelting. In this case, the molten pool dimensions are the same, and most of the glassy regions can suffer heat treatment enough to crystallization. The use of different parameters combinations for melting and remelting implies in different amount of energy inputs for each step. While the combination high/low energy input could, according to the literature [225], acts densifying and vitrifying the samples, in practice, using this sequence the vitrification promoted by the remelting is completely consumed by the subsequent melting. In this direction, only the last remelted layer can maintain its glassy phase, and in the end, the sample seems to be fully glassy (as can be seen in **Figure 4.28**), but it is actually only a superficial glassy coat.

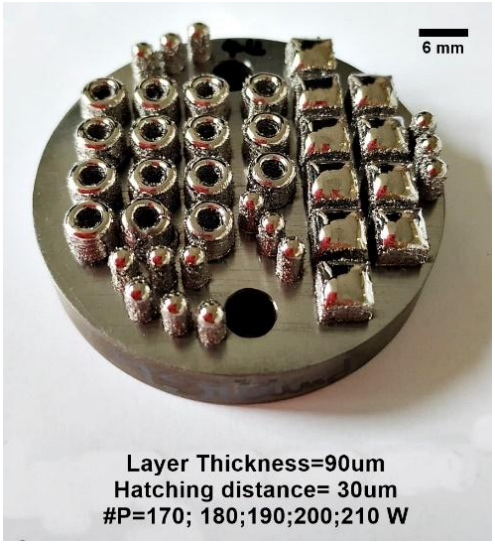

Figure 4.28- Image of LPBF samples produced using the combination of high/low energy input for melting/remelting, showing a glassy visual aspect.

On the other hand, the low/high energy input combination would not make any logical sense, and the explanation follows what was mentioned before. **Figure 4.29** shows the influence of remelting step, when using a combination of parameters different of the melting. One can see that all the samples are heavily cracked, especially when the tested scan speed of the remelting was the lowest (1000 mm/s), combined with the chessboard laser strategy. The best samples produced in this work were those without remelting step.

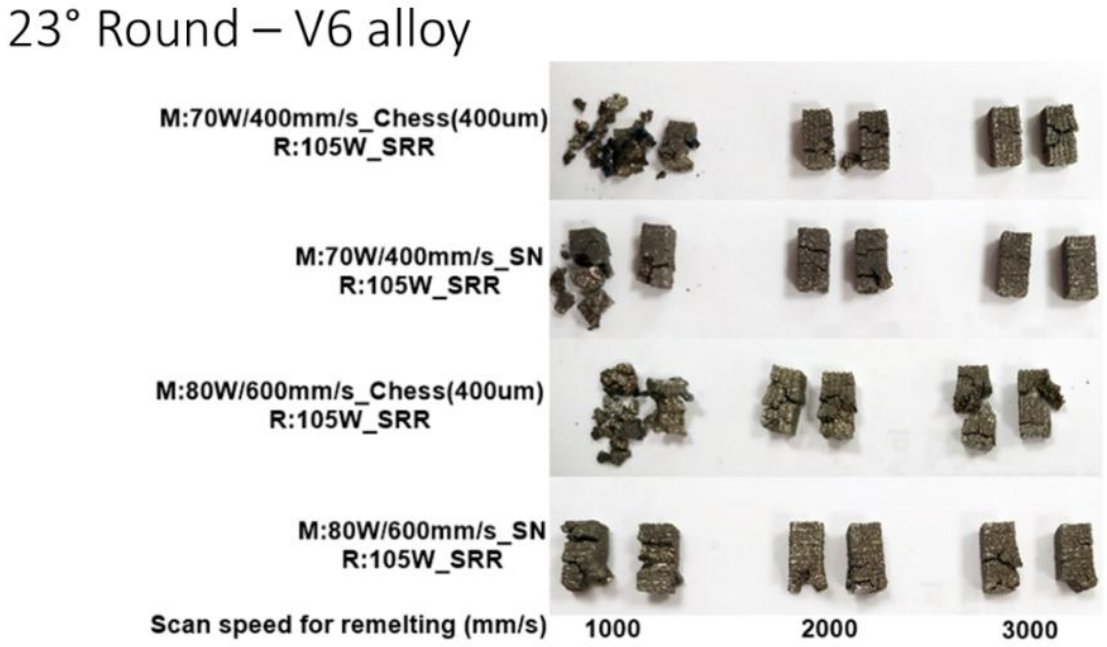

Figure 4.29- LPBF samples produced using different combinations of parameters for melting and remelting, as specified in the image. The influence of different (1000, 2000, and 3000 mm/s) scan speeds for the remelting is shown.

To reduce the influence of the subsequent layer on the previous layer, the **layer thickness** was investigated. It was decided to increase the layer thickness taking into consideration that thicker layers reduce the energy input, which could reduce the super elevation phenomenon, and that thicker layers imply in lower number of layers to build the final height of the sample, reducing as so the number of repeated heating/cooling cycles. In this study, it was observed an improvement of the samples' integrity when the layer thickness was gradually increased up to 100 μm.

When samples with acceptable integrity were produced, the super elevation phenomenon was still present, so the influence of **hatching distance** was explored. It was decided to increase the hatching distance from 30 μm to 40 μm and 50 μm to reduce the energy input and the overlap between tracks. The experiments showed severe cracking when the hatching distance was increased (see **Figure 4.30a)** and **b)**), then it was decided to continue the investigations using 30 μm of hatching distance.

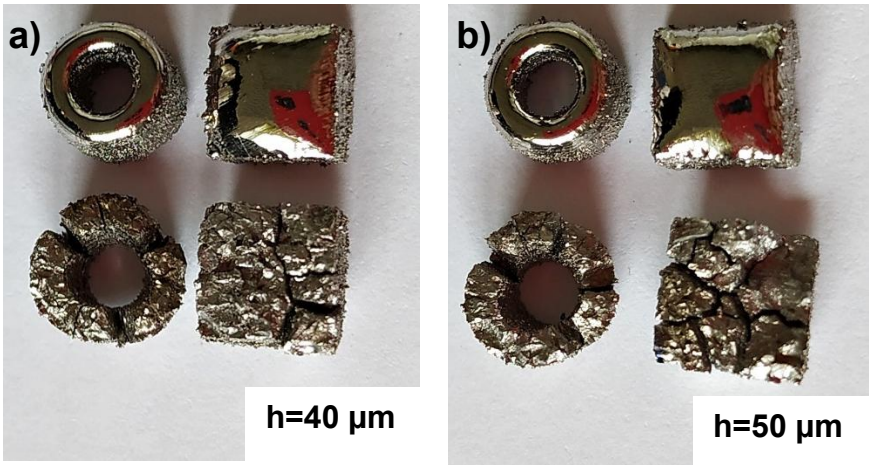

Figure 4.30- Image of the LPBF samples produced with the same combination of parameters, but different hatching distance **a)** 40 µm and **b)** 50 µm.

The phenomena presented by an unadjusted combination of parameters can appear to a greater or lesser degree depending on the **samples' geometry and size**. Here, the super elevation phenomenon was intensified in samples with a smaller surface area (see **Figure 4.31a)**). Cylindrical samples exhibited a greater tendency to crack compared to the square samples of the same height, produced using the same combination of parameters (see **Figure 4.31b)**). In addition, for the same sample's geometry, the smaller ones tend to crack less than larger ones (**Figure 4.31c)**).

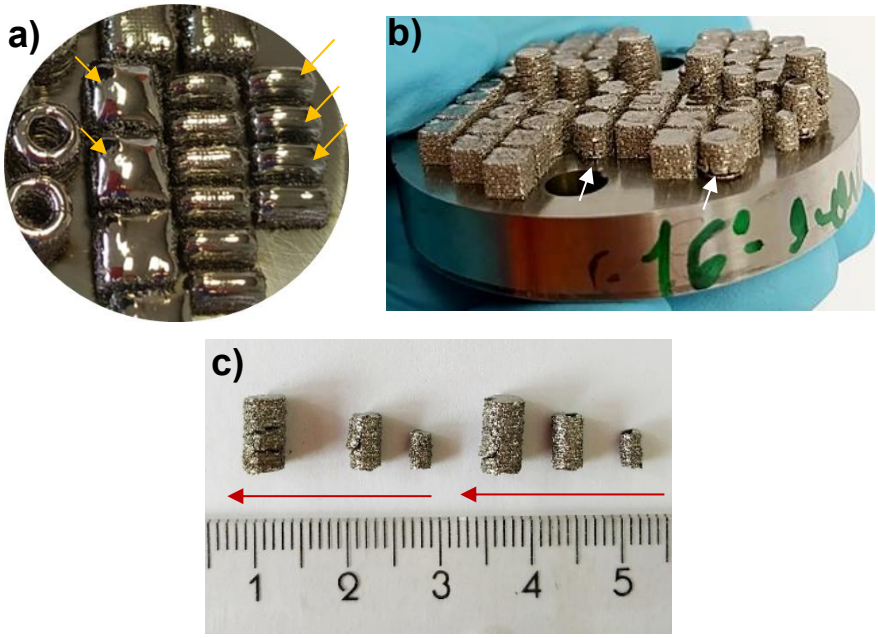

Figure 4.31- Image of LPBF samples showing the influence of: **a)** surface area, **b)** samples' geometry, and **c)** samples' size on the samples' integrity. Yellow arrows indicate super elevation phenomenon, white arrows indicating cracks and red arrows are showing the direction of cracking increasing.

Three different **laser scan strategies** were tested for melting and remelting. Single normal (SN) laser strategy was suitable for melting and remelting, especially for melting, and when combined with appropriate parameters it can successfully densify and vitrify the samples. Single random (SR) laser strategy was not suitable for melting (densification), because it causes a mess in the powder layer (extensive spatter generation). For remelting, it seems promising for vitrifying, but as mentioned before, depending on the parameter combination it does not help. Chessboard/island was a promising laser strategy to increase the vitrification, however, due to the melting pattern, pores can easily be formed. In addition, when chessboard strategy is used with the inappropriate parameters, thermal stress seems to be intensified, inducing severe distortions. **Figure 4.32** shows the influence of SR and chessboard laser strategies for the remelting step. One can see that, when the chessboard strategy is used, the samples are heavily distorted/cracked.

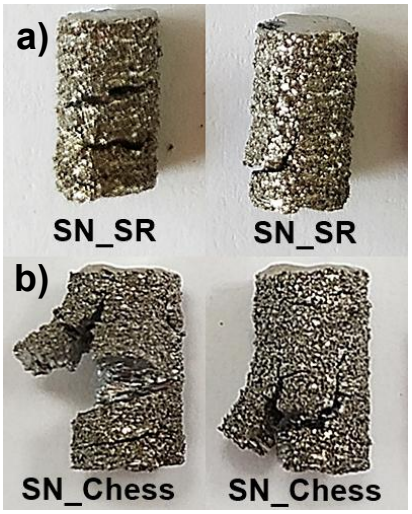

Figure 4.32- Image of the LPBF samples produced with the same combination of parameters, but using different laser strategies for remelting **a)** Single normal and **b)** Chessboard/island.

The influence of **substrate's material** on the samples' integrity is driven by the similarities or dissimilarities between the two materials and their properties. The similarities between the substrate and printed material improve the wettability and bonding of the printed parts. Differently, when the properties of the material's substrate are too dissimilar from the printed material the adhesion is poor and delamination can occur in the firsts 15 layers. The continue of printing, can result in samples with a well cracked base and poor quality. Additionally, regarding samples' integrity, the **temperature of the substrate** affects the thermal stresses of the printed material. By heating the substrate, the thermal stresses can be reduced, which can reduce the cracking tendency. The alloys studied in this work presented a better affinity with 316 L stainless steel than with CK 45 carbon steel. When the substrate was heated at 150±20°C the samples also showed better quality with fewer cracks at the base.

The **laser power** and **scan speed** combination was decisive for processing the alloys in this work. While high laser power (>100 W) or low scan speed (<400 mm/s) were being used to densify the samples, phenomena as super elevation, rough finishing surface, larger cracks and undesirable

dimensions were always linked to this condition. On the other side, low laser power (<100 W) or high scan speed (>500 mm/s) were used to dimensional control and vitrification, but in this condition, pores and thin cracks (not seen by eye) were always an issue. Thus, the range of 50-90 W for laser power, and 400-600 mm/s for scan speed was the most suitable window to process the studied alloys.

After numerous attempts, intact samples of the V5 and V6 alloys were finally produced. However, even at this stage, the samples exhibited a pore fraction of approximately 2–7% and a crack fraction between 0.5% and 3%. Detailed results can be found in Appendix **Figure A.5**, for V5 and V6. Among this set, the sample with the best overall integrity and flattest surface was selected for further investigation, with results summarized in **Figure 4.33**. Due to the similarity between the V5 and V6 results, only the V6 results are presented here. The optical microscopy (OM) and scanning electron microscopy (SEM) images in **Figure 4.33a)** and **Figure 4.33b)** reveal that the microstructure is nearly fully crystalline, featuring phases enriched in Fe, Mo, or P, as confirmed by SEM-EDS mapping. The DSC curve in **Figure 4.33c)** further confirms that the microstructure contains approximately 1% glassy phase.

As 1% of the glassy phase is a very low fraction, further parameter adjustments were made to increase the glassy phase content while reducing porosity and crack formation.

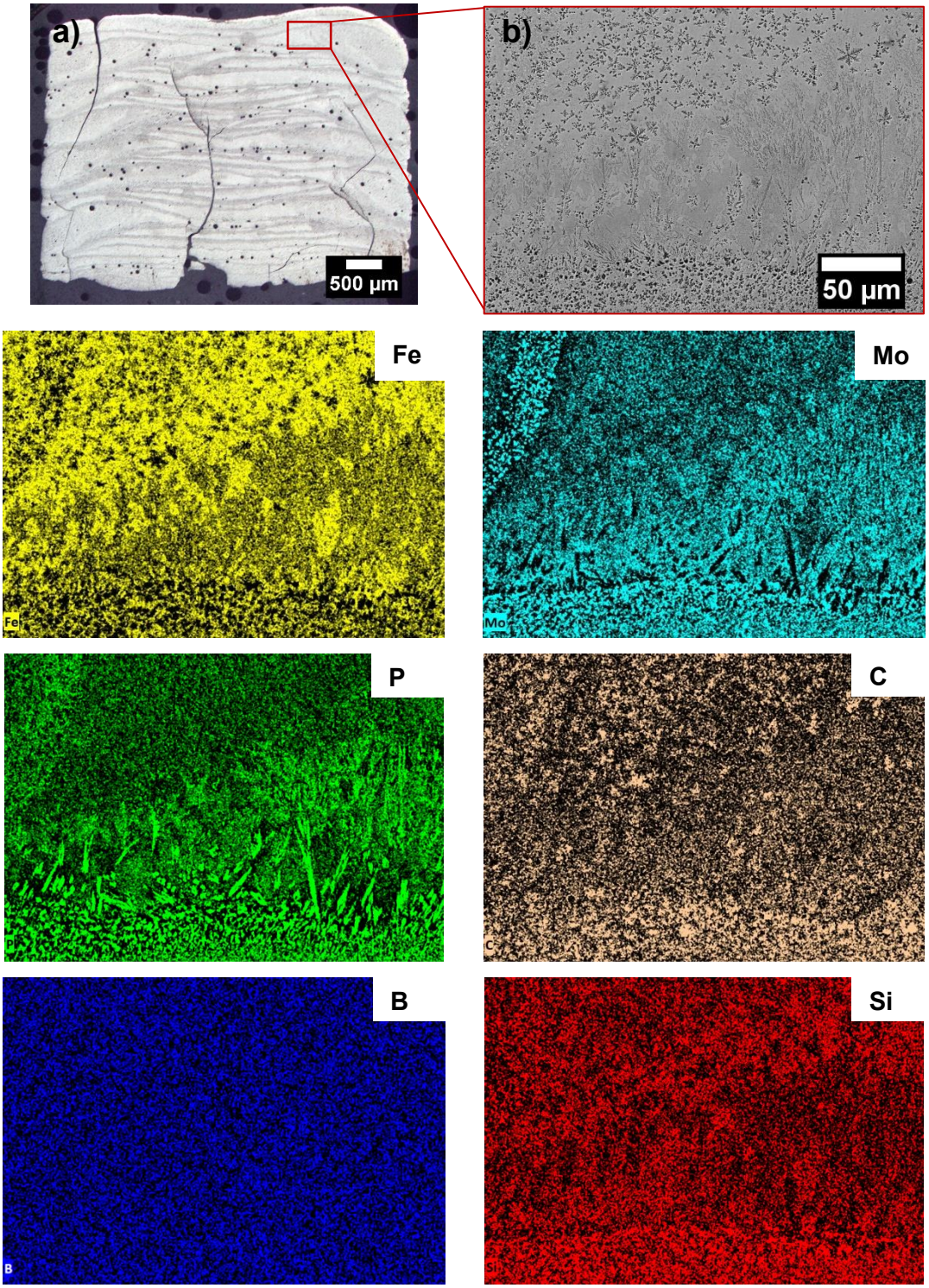
a)
500 µm
b)
50 µm
Fe
Mo
P
C
B
Si

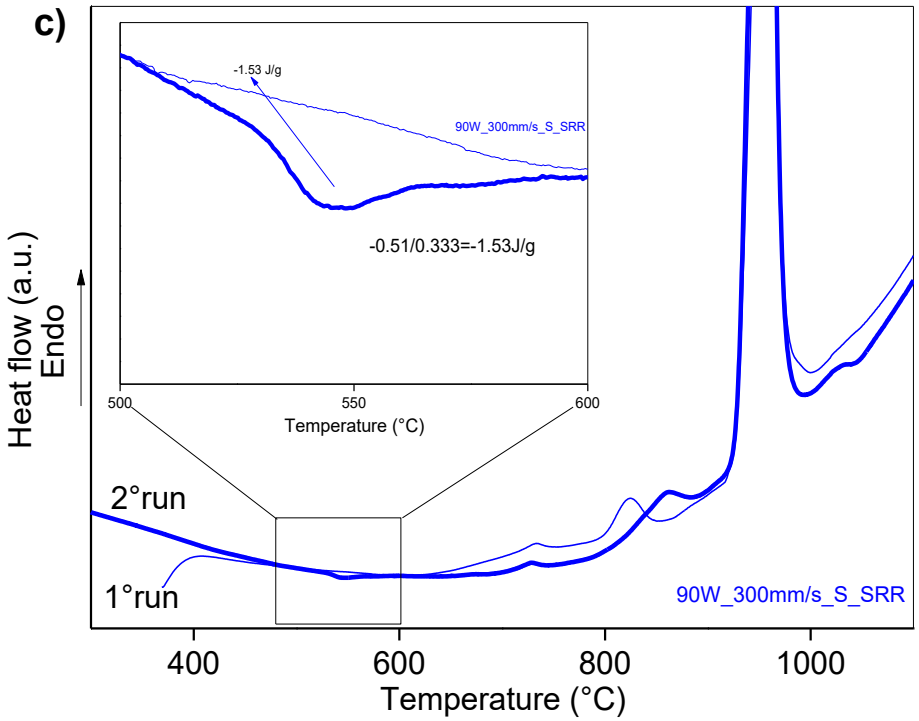

Figure 4.33- a) Optical microscopy image (etched sample), **b)** SEM image together with elemental EDS maps using Fe-K, Mo-L, P-K, C-K, B-K, Si-K, and **c)** DSC curve for a V6 LPBF sample.

Figure 4.34a) shows slice OM images viewed from the side of the LPBF 4x4x4 mm cubes produced using different laser power and scan speeds within the appropriate processing window for V5 and V6. When varying the laser power while keeping the scan speed constant and all other parameters at their default values (layer thickness: 100µm, hatching distance: 30 µm, SN laser strategy, substrate of 316L at 150±20°C), it is expected that lower power results in a thinner and shallower melt pool and, consequently, a narrower scan track, leading to lack of fusion between adjacent tracks and between subsequent layers. This can be seen in the images of 400 and 500 mm/s, as the power increases (in the series of images for 400 and 500 mm/s), there is an optimal value for minimizing porosity, beyond which a gradual increase in randomly dispersed, round-shaped pores is observed. These round-shaped pores are associated with keyhole mode porosity, which occurs when excessive laser power generates a deep melt pool

with intense dynamics, leading to vapor entrapment as the melt pool advances and the vapor cavity collapses. In the intermediate regime where porosity is minimized, only small spherical pores are observed – these are likely metallurgical pores resulting from trapped gas between powder particles. In the series of images in **Figure 4.34a)** it is clear that the keyhole mode porosity increases in quantity with increasing power at 300 and 400 mm/s. The quantitative porosity, cracks, and pore+crack values are plotted in **Figure 4.34b)**. It is shown, as expected, that the optimal laser power for minimal porosity is higher at higher scan speeds, i.e., 70 W_300mm/s; 80W_400mm/s, and 90 W_500 mm/s. On the other hand, for crack and pore+crack percentage, the behavior is not linear. Thus, considering a balance between flat surface, few cracks and lower porosity, the samples produced using 70 W_400mm/s, and 80 W_600 mm/s were selected to be further investigated.

It is important to note that the samples produced using 70 W_400 mm/s and 80 W_600 mm/s were also subjected to remelting, applying different energy densities (14, 18, and 23 J/mm³) in combination with SN and chess laser scanning strategies. In all cases, the remelted samples showed a similar pore fraction compared to those without remelting but, exhibited an increase in crack percentage of approximately 15%, which justifies the omission of their results from this section.

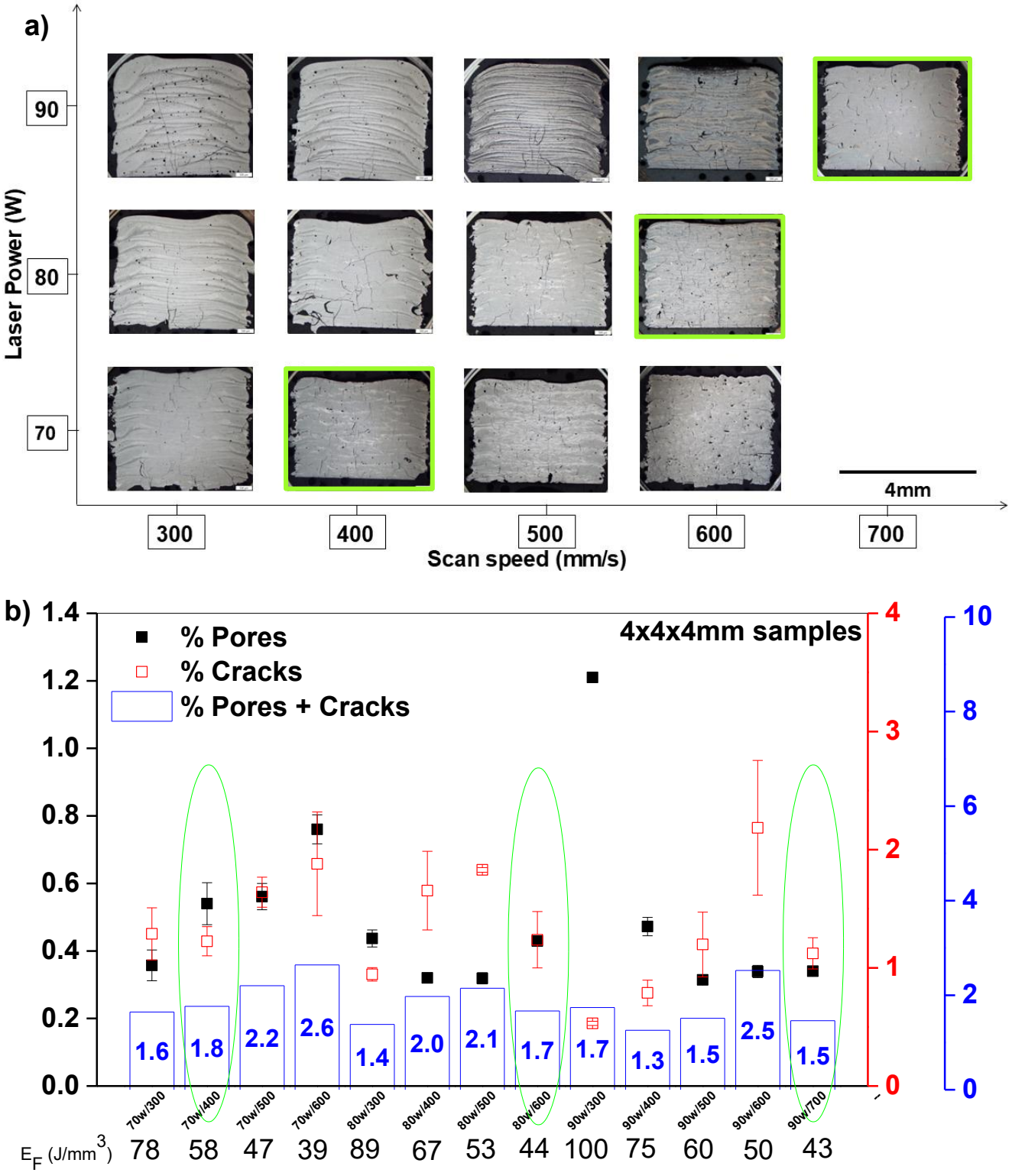

Figure 4.34- a) Schematic with OM images showing the microstructure of etched 4×4×4 mm LPBF samples as a function of laser power (W) and scan speed (mm/s). **b)** Quantitative porosity, crack and pore+crack percentage of LPBF

samples as a function of parameter combinations. Green markers indicate the samples selected for further investigation.

Since sample height and printing direction are also LPBF process parameters, the best parameter combinations identified in previous experiments (70 W_400 mm/s and 80 W_600 mm/s) were tested on 4x4x8 mm samples and printed at 0°, 45° and 90° with respect to Z-axis for both V5 and V6 alloy. The quantitative results for porosity, cracks, and the combined percentage of pores and cracks, along with their corresponding representative etched OM images, are shown in **Figure 4.35a)** for the V5 alloy and **Figure 4.35b)** for the V6 alloy. Compared to the expected pore percentage (0.5–0.6%), the V5 LPBF samples generally exhibited a lower percentage (<0.4%) (see **Figure 4.35a)**), while the V6 LPBF samples showed values close to the expected pore percentage (~0.5%) (see **Figure 4.35b)**). In contrast, regarding crack percentage, the V5 LPBF samples fell within the expected range (1.0–1.5%), whereas the V6 LPBF samples exhibited higher crack percentages, exceeding 1.5%. For both alloys, the combined percentage of pores and cracks generally increased with the printing angle, from 0° to 90°. Previous study [123] have shown that increasing the printing angle tends to result in a higher occurrence of defects such as pores and cracks. As the laser scans longer distance in comparison to samples built at 0°, the probability of defect formation increases, potentially leading to lower density. The influence of sample orientation on the porosity of LPBF parts has also been previously reported by other researchers [226].

The Archimedes density was measured for V5 and V6 LPBF samples produced with 70W_400mm/s, combined with SN laser strategy, built at 0°, without remelting, and using a 150°C heated 316L steel substrate. Compared to the theoretical density of V5 (7.52 g/cm^3) and V6 (7.65 g/cm^3), the measured Archimedes densities of 7.11±0.06 (V5 LPBF), and 7.22±0.06 g/cm^3 (V6 LPBF), are equivalent to a density of 94.5% and 94.4% for V5 and V6, respectively.

When the V5 and V6 LPBF samples were printed at 0° using the same parameters but with the chessboard laser scan strategy (see **Figure 4.35c)**), the percentage of pores and cracks increased significantly—by at least 10 times for

pores and twice for cracks. The worst results were observed with the 80 W_600 mm/s condition, corresponding to a lower energy input (44 J/mm³). This behavior can be attributed to insufficient overlap between the scan islands; when the overlap is inadequate, large lack-of-fusion (LoF) defects may form. The literature has also reported a decrease in sample density due to an increase in defects when the chessboard strategy is applied [227]. Interestingly, under the chessboard strategy, the V6 alloy showed better results than the V5 alloy in both parameter conditions (70 W_400 mm/s and 80 W_600 mm/s).

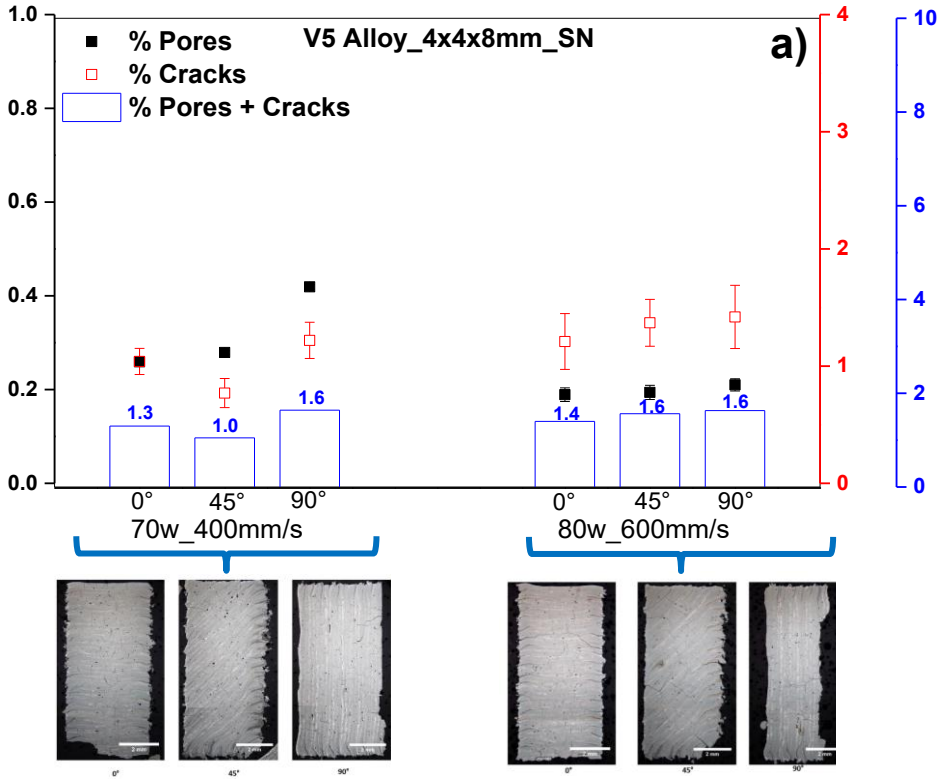

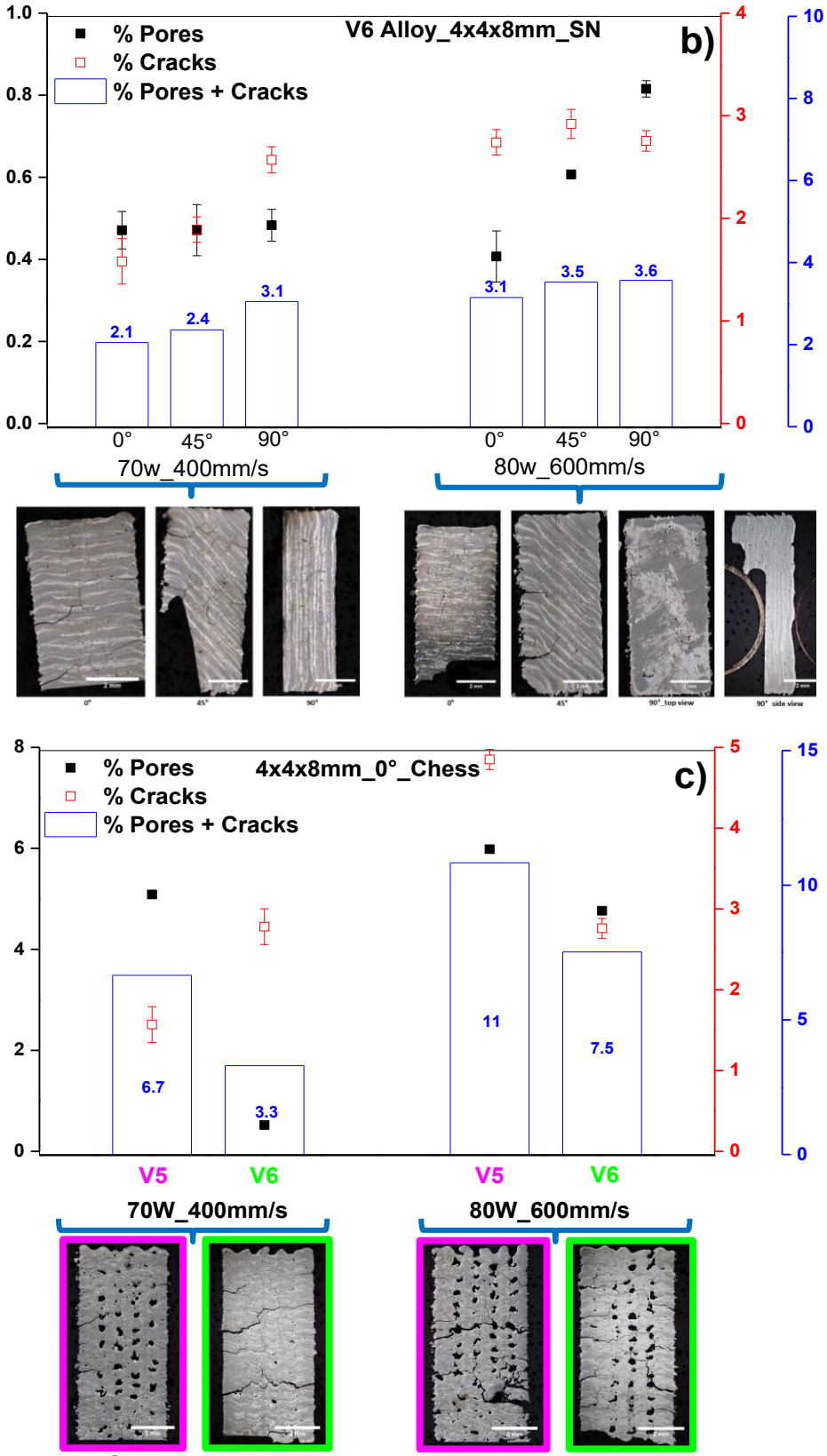

Figure 4.35- Quantitative porosity, crack and pore+crack percentage of 4×4×8 mm LPBF samples produced with 70 W_400 mm/s and 80 W_600 mm/s as a function of printing direction (0°, 45°, and 90°), along with their corresponding

representative etched OM images for: **a)** V5 alloy, and **b)** V6 alloy. **c)** Porosity and crack percentage behavior of 4×4×8 mm V5 and V6 LPBF samples built at 0° using the chess scan strategy with 70 W_400 mm/s and 80 W_600 mm/s.

To investigate the potential for increasing the glassy phase content in the LPBF samples, the laser power was reduced to 60 W and 50 W and tested with scan speeds ranging from 100 to 500 mm/s. A schematic with OM images showing the microstructure of unetched and etched 4×4×4 mm LPBF samples for the V5 and V6 alloys is presented in **Figure 4.36a)** and **Figure 4.36c),** respectively. As expected, the optimal scan speed for minimizing porosity was lower at lower laser power—specifically, 60 W_200 mm/s and 50 W_100 mm/s. The presence of cracks was reduced, for the same direction (decreasing scan speed) although not entirely eliminated. However, by reducing scan speed, the white contrast observed in the etched samples (indicative of the glassy phase) is clearly diminished. Quantitative comparison of the results for 50 W and 60 W in both V5 and V6 samples (see **Figure 4.36b)** and **Figure 4.36d)**) shows that the samples processed with 60 W are better, with a lower combined percentage of pores and cracks. Consequently, the V5 and V6 LPBF samples produced at 60 W with scan speeds of 200 mm/s and 500 mm/s (highlighted with green circles) were selected for further investigation.

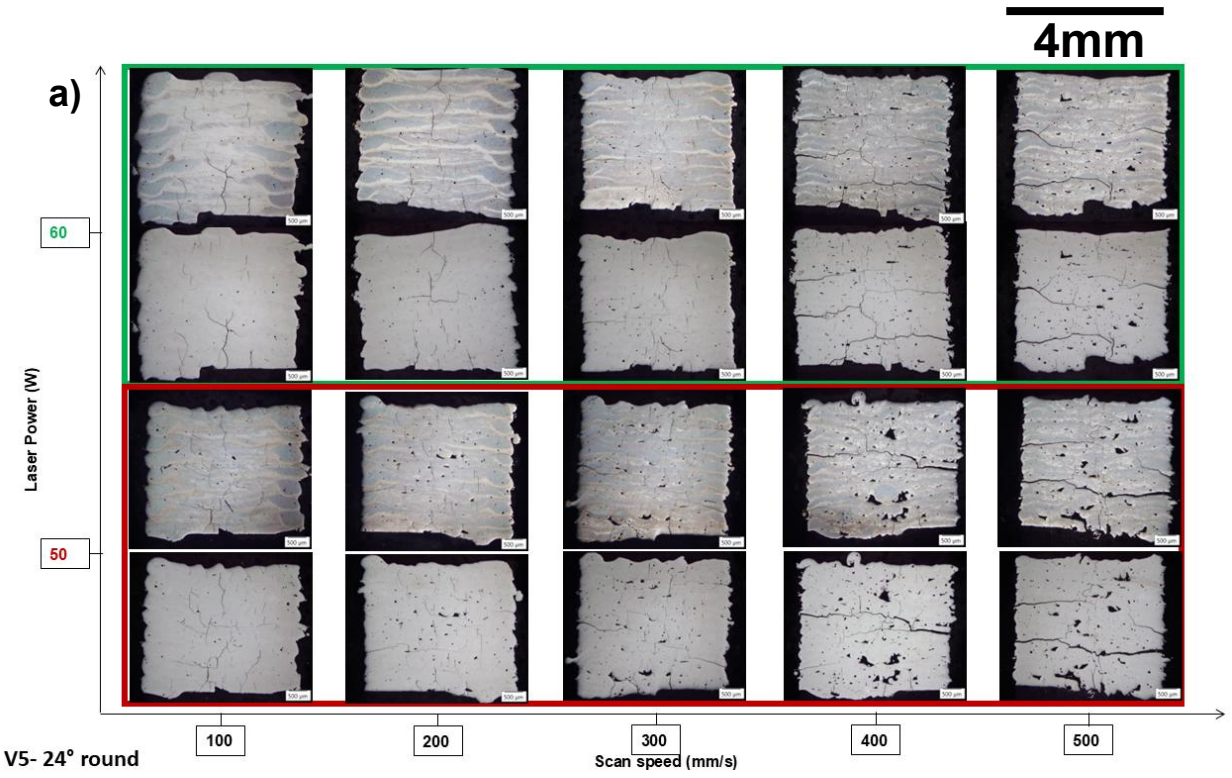
4mm
a)
60
50
Laser Power (W)
100
200
300
400
500
Scan speed (mm/s)
V5- 24° round

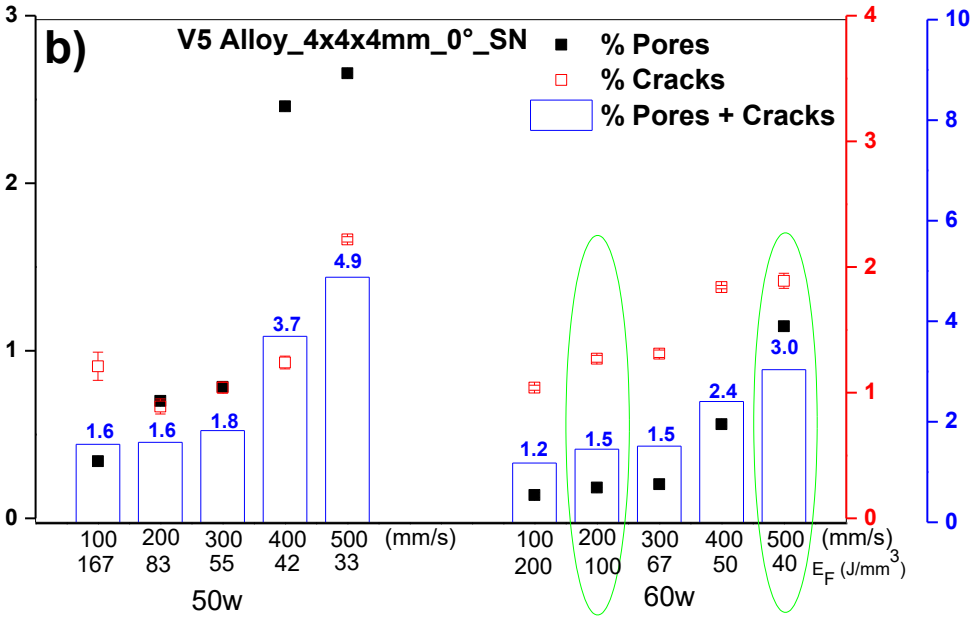
b)
V5 Alloy_4x4x4mm_0°_SN
% Pores
% Cracks
% Pores + Cracks
1.6
1.6
1.8
3.7
4.9
1.2
1.5
1.5
2.4
3.0
100 200 300 400 500 (mm/s)
167 83 55 42 33
50w
100 200 300 400 500 (mm/s)
200 100 67 50 40
60w
E_F (J/mm^3)

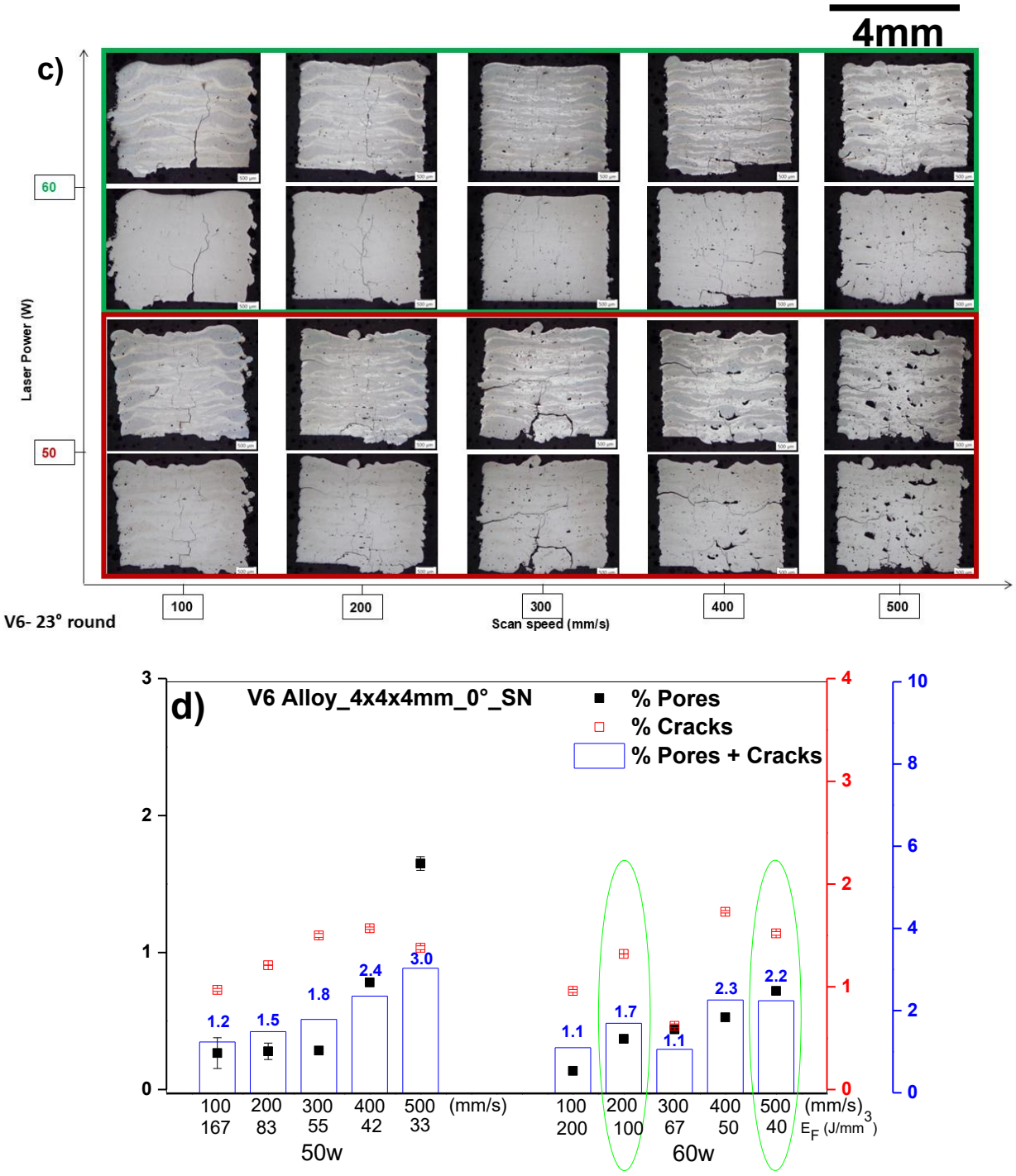

Figure 4.36- Schematic with OM images showing the microstructure of unetched and etched 4×4×4 mm LPBF samples as a function of laser power (W) and scan speed (mm/s) for: **a)** V5 alloy, and **c)** V6 alloy. Quantitative porosity, crack and pore+crack percentage of LPBF samples as a function of parameter combinations for: **b)** V5 alloy, and **d)** V6 alloy. Green markers indicate the samples selected for further investigation.

Samples of the V5 and V6 alloys were produced using 50 W and 60 W laser power, combined with scan speeds ranging from 100 to 500 mm/s, printed at 0° and using the chessboard laser scan strategy. The quantitative results for porosity, cracks, and the combined percentage of pores and cracks, along with their corresponding representative etched OM images, are shown in **Figure 4.37a)** for the V5 alloy and **Figure 4.37b)** for the V6 alloy. As can be seen, for a fixed laser power, the white contrast—indicative of the glassy phase—increases with increasing scan speed. However, porosity and crack formation also increase in the same direction. Once again, the samples processed at 60 W yielded better results. Nonetheless, compared to those produced with the SN scan strategy, the combined pores and cracks percentage is significantly higher when using the chessboard strategy—at least twice as high at lower scan speeds, and above five times higher at higher scan speeds. In addition, using the chessboard laser scan strategy, the V6 alloy showed better results than the V5 alloy. Based on the results, the samples produced at 60 W with scan speeds of 200 mm/s and 500 mm/s were selected for further investigation.

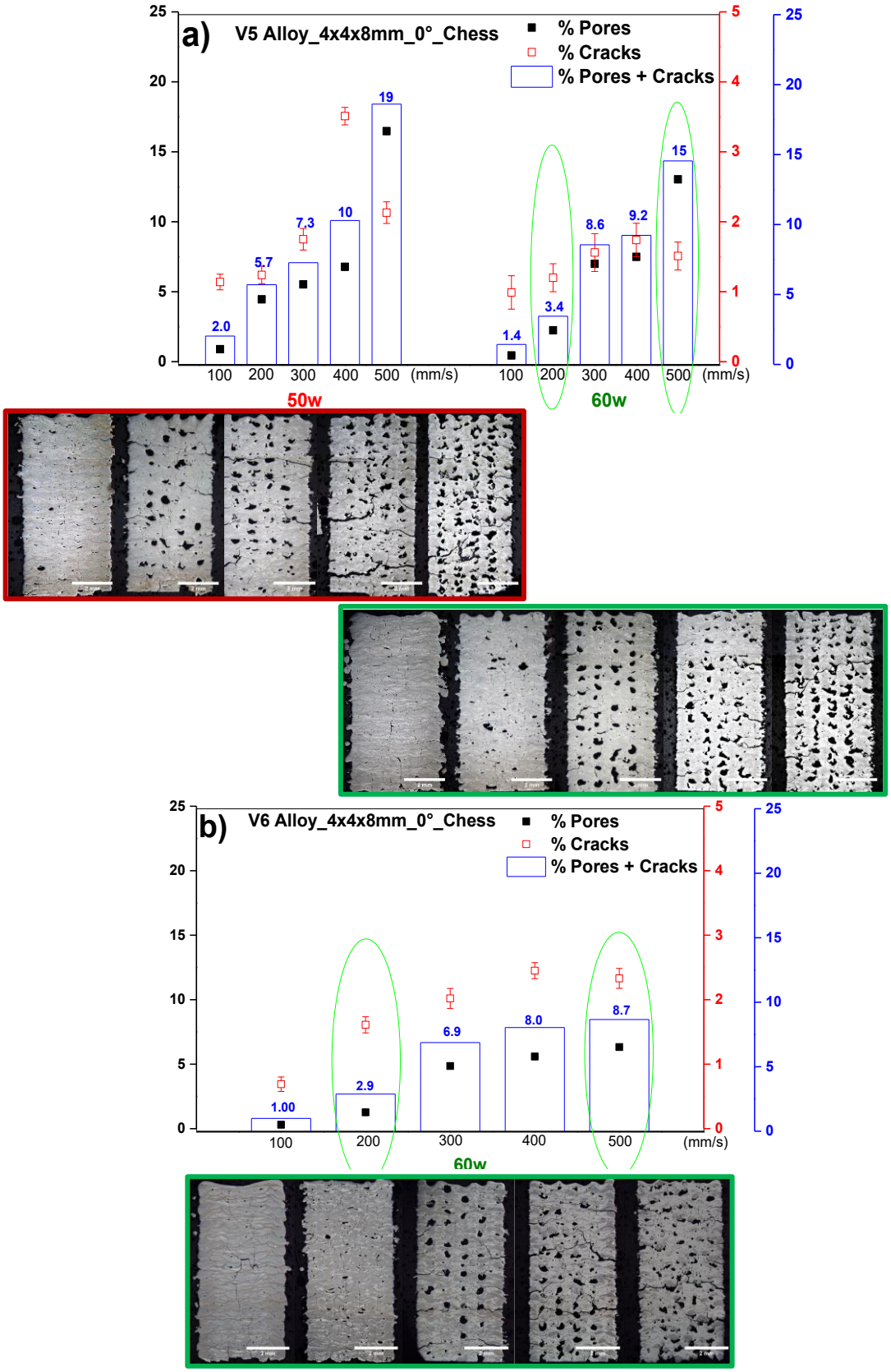

Figure 4.37- Quantitative porosity, crack and pore+crack percentage of etched 4×4×8 mm LPBF samples produced with 50 W and 60 W and chessboard laser

strategy at 0° as a function of scan speed (100-500 mm/s), along with their corresponding representative etched OM images for: **a)** V5 alloy, and **b)** V6 alloy.

4.4.2.1 Chemical and microstructural characterization

Table 4.11 displays the chemical composition of V5 and V6 +20 - -75 µm powders and LPBF samples (%wt.) measured by ICP-OES (Fe, Mo, P, B and Si) and LECO (C and O). Because the energy input used to produce the LPBF samples can be high enough to cause selective evaporation of alloying elements, it is essential to analyze the chemical composition of the samples. Zhang et al. [112] have reported that the preferential evaporation of specific elements can inevitably lead to deviations from the nominal alloy composition, which in turn change the alloys properties. Comparing the measured chemical compositions with the target values, a slight decrease was observed in the Fe, Mo, and C contents, while P and B showed a slight upward deviation. Additionally, the presence of O and Si in the alloys was expected, due to the use of commercial raw materials and oxygen contamination occurring during atomization and LPBF processing. Nonetheless, considering the standard deviation of the measurements, the chemical composition of the alloys remains close to the nominal values.

For both alloys, a comparison between the oxygen content of the powders and that of the LPBF samples (see **Table 4.11**) reveals an increase—approximately fourfold for V5 and twofold for V6. This observation aligns with findings in the literature [228], which show that LPBF parts generally exhibit higher oxygen content than the starting powders. This increase occurs despite the use of high-purity argon atmospheres, as residual oxygen levels can persist and react with the molten metal, especially at the high temperatures of the laser-induced melt pool.

Table 4.11- Chemical composition measured by ICP-OES (Fe, Mo, P, B and Si) and LECO (C and O) of V5 and V6 +20 - -75 µm powders and LPBF samples (%wt.).

V5 Samples	**Fe**	**Mo**	**P**	**C**	**B**	**O**	**Si**
Targed	86.80	5.70	5.50	1.80	0.30	0	0
Powder +20 - - 75 µm	85.05±0.99	5.4±0.73	5.54±0.23	1.76±0.02	0.38±0.02	0.008±0.001	1.86±0.09
P60_V200	85.16±0.35	4.91±0.26	5.66±0.31	1.76±0.02	0.41±0.04	0.03±0.001	2.10±0.09
P60_V500	85.32±0.93	4.81±0.06	5.58±0.07	1.76±0.02	0.41±0.02	0.03±0.001	2.09±0.05
V6 Samples	**Fe**	**Mo**	**P**	**C**	**B**	**O**	**Si**
Targed	83.26	9.29	5.40	1.74	0.31	0	0
Powder +20 - - 75 µm	81.15±2.40	9.01±0.24	5.63±0.48	1.68±0.01	0.43±0.04	0.007±0.001	2.09±0.09
P60_V200	82.76±1.27	7.57±0.18	5.40±0.16	1.70±0.01	0.40±0.01	0.01±0.001	2.16±0.03
P60_V500	82.87±0.42	7.43±0.49	5.37±0.37	1.68±0.03	0.49±0.09	0.01±0,001	2.15±0.15

Table 4.12 summarizes the oxygen content (%wt.) measured by LECO in V5 and V6 powders (+20 to –75 µm) and their corresponding LPBF samples. The results show that the virgin powders of both V5 and V6 alloys had similar oxygen contents, ranging from 0.007 to 0.008 %wt. For V5, the LPBF samples produced during the 4° round of printing—initiated with a chamber oxygen level of approximately 500 ppm—showed an oxygen content of 0.030 %wt., which is more than three times higher than that of the virgin powder.

In the case of the V6 alloy, the first ten rounds of printing were also started with a chamber oxygen level of ~500 ppm. From the 11° round onward, printing only began when the chamber oxygen level dropped to ~200 ppm. Notably, the LPBF samples from the 5° and 10° rounds exhibited oxygen levels at least twice as high as those from the 14° and 17° rounds.

These findings indicate that when printing began at a chamber oxygen level of around 500 ppm—as in V5 (4° round) and V6 (5° and 10° rounds)—the resulting LPBF samples had significantly higher oxygen contents. Conversely, initiating the LPBF process at a lower oxygen level (~200 ppm), as done for V6 (1°, 14°, and 17° rounds), led to reduced oxygen content in the final parts. Therefore, it can be inferred that the oxygen content in the LPBF chamber plays

a more decisive role in determining the final oxygen content of the LPBF samples than the oxygen content of the starting powder.

Compared to the virgin V5 and V6 powders, the oxygen content of the powders after all printing rounds was increased by approximately 2.6 times. However, it's important to note that the V5 powder was reused for 7 printing rounds, while the V6 powder was reused 19 times. Additionally, during the 15t° round, the V6 reused powder was mixed with a portion of virgin V6 powder to obtain the required volume for printing larger samples.

The literature [229] has reported that reused powders tend to accumulate oxide layers due to repeated exposure to heat and residual oxygen, leading to a progressive increase in oxygen content over multiple builds. For example, a study on Ti-6Al-4V powders showed that powders' oxygen content increased during LPBF processing, even when oxygen concentrations in the chamber were maintained below 100 ppm [229].

However, the results from this study indicate that the oxygen content in LPBF samples was not significantly affected by powder reuse. Instead, the oxygen level in the processing chamber played a more critical role. Therefore, to minimize oxygen uptake in LPBF parts, it is essential to keep the chamber oxygen level as low as possible.

Table 4.12- Oxygen content measured by LECO (O) of V5 and V6 virgin powders (+20 - -75 µm), the same powders after all printing's rounds, and the LPBF samples (%wt.).

Sample	Oxygen (wt.%)
V5	
Virgin powder +20 - - 75 µm	0.008±0.001
Print - 4° round	0.030±0.001
Powder after all LPBF +20 - - 75 µm	0.021±0,001
V6	
Virgin powder +20 - - 75 µm	0.007±0.001
LPBF - 1° round	0.007±0.001
LPBF - 5° round	0.016±0.001
LPBF - 10° round	0.022±0.001
LPBF - 14° round	0.008±0.001

LPBF - 17° round	0.010±0.001
Powder after all LPBF +20 - - 75 μm	0.021±0.001

Figure 4.38 a)-c) depicts XRD patterns of the selected LPBF V5 and V6 samples within a wide 2θ range (20°-120°). The measurements, qualitatively, confirm the presence of a glassy/crystalline composite microstructure in all LPBF samples. The composite consists of a wide glassy hump centered around 52°, superimposed with sharp diffraction peaks corresponding to the α-Fe, Fe_3P and $(Fe, Mo)_{23}(C, B)_6$ phases, which cannot be clearly distinguished by XRD, and to the $Fe_{0.75}Mo_{0.122}C_{0.128}$ phase. Based on the XRD data, α-Fe is the dominating phase accompanied by lower volume fraction of the Fe_3P and $(Fe, Mo)_{23}(C, B)_6$/$Fe_{0.75}Mo_{0.122}C_{0.128}$ phases. Phase identification was carried out using the ICSD database, and the main crystalline phases matched the following structures: α-Fe ($Im\bar{3}m$) [215], $M_{23}X_6$ ($Fm\bar{3}m$) [217], $Fe_{0.75}Mo_{0.122}C_{0.128}$ ($I\bar{4}3m$) [230], and Fe_3P ($I\bar{4}$) [218] crystalline phases.

The primary difference among the XRD patterns lies in the intensity of the glassy hump. In **Figure 4.38a)**, it can be inferred that V6 LPBF samples exhibit a more pronounced glassy character than V5 samples, when processed at 80W-600mm/s_SN_0° with a height of 4 mm. From **Figure 4.38b)**, it is not evident which printing direction yields a higher fraction of glassy phase. However, when comparing **Figure 4.38a)** and **Figure 4.38b)**, it becomes clear that samples with an 8 mm height contain less glassy phase than the 4 mm samples. **Figure 4.38c)** reveals that, at a fixed laser power of 70 W, increasing the scan speed enhances glassy phase formation, as indicated by the reduced intensity of crystalline peaks. Comparing **Figure 4.38c)** and **Figure 4.38a)**, it can be concluded that for the V5 alloy, when 4 mm-high samples were printed at 0° using a SN scan strategy, the combination of 80W_600mm/s promotes significantly more glassy phase formation than the 70W_400mm/s combination.

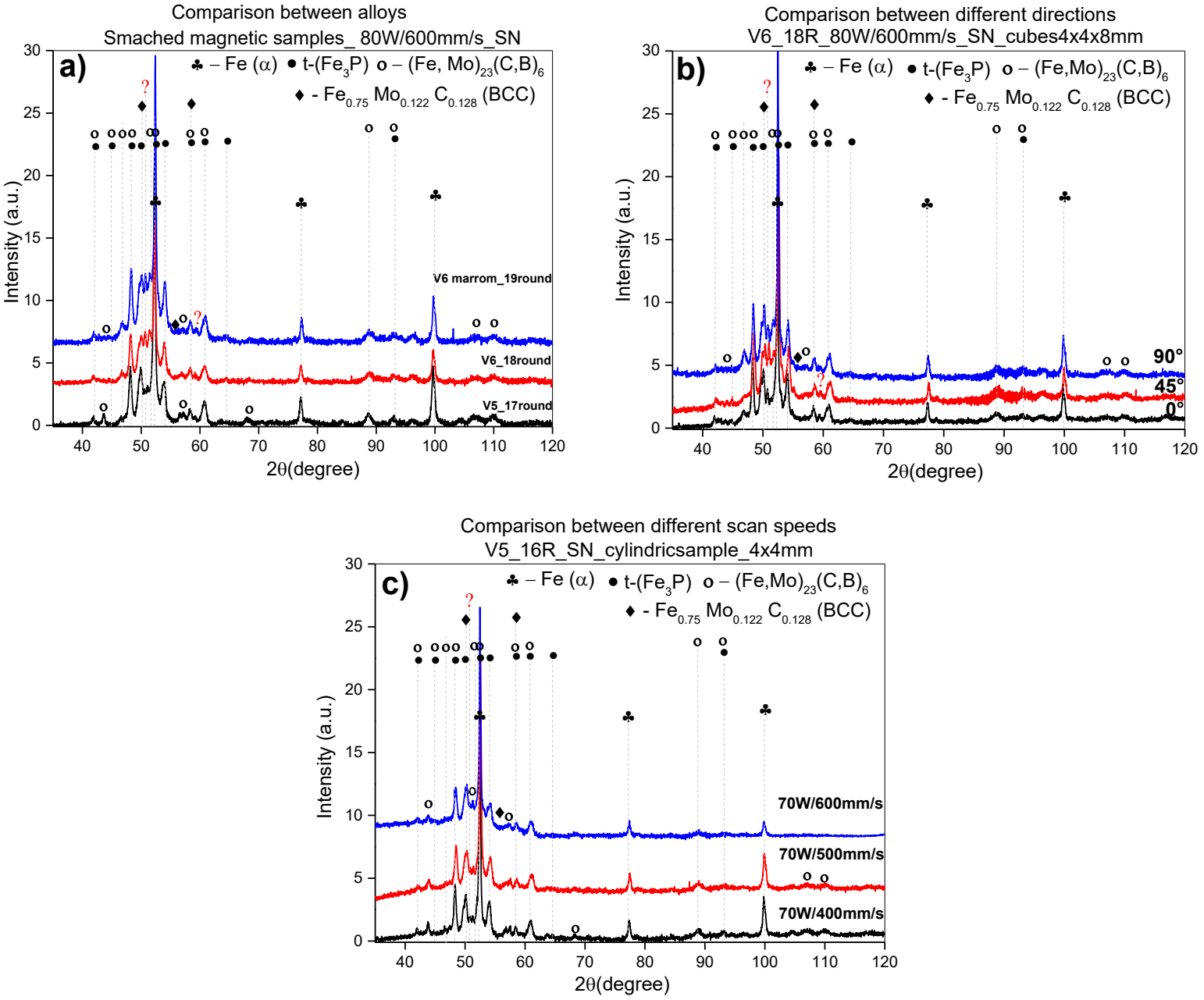

Figure 4.38- X-ray diffractograms of selected LPBF samples comparing: **a)** different alloys (V5, V6, and contaminated V6); **b)** different printing directions (0°, 45° and 90°); and **c)** different scan speeds (400, 500, and 600 mm/s).

To better understand the formation of the glassy phase in LPBF samples, the effects of laser power, scan speed, and laser scan strategy were investigated. **Figure 4.39** shows the XRD diffractograms of selected 4×4×8 mm LPBF samples

of V5 and V6 alloys. Since the identified crystalline phases are the same as those discussed in **Figure 4.38**, they will not be mentioned again here.

An increase in glassy phase content is indicated by a more pronounced glassy hump and a corresponding reduction in the intensity of crystalline peaks. Thus, regarding the glassy phase, it is evident that for both alloys, a high scan speed (500mm/s) and the use of a chessboard laser scan strategy promote glassy phase formation (see **Figure 4.39a)**) and **Figure 4.39c)**). Additionally, the 80W_600mm/s combination results in greater glassy phase formation than the 70W_400mm/s combination (see **Figure 4.39b)**) and **Figure 4.39d)**). The glassy phase content is further enhanced when these parameter combinations are used together with the chessboard scan strategy.

In conclusion, glassy phase formation is favored by higher scan speeds and the use of a chessboard laser scan strategy. In addition, the type of crystalline phases formed in the LPBF samples was found to be fairly independent of the processing conditions, suggesting that varying the process parameters primarily affects the proportion of glassy phase rather than the crystalline phases composition.

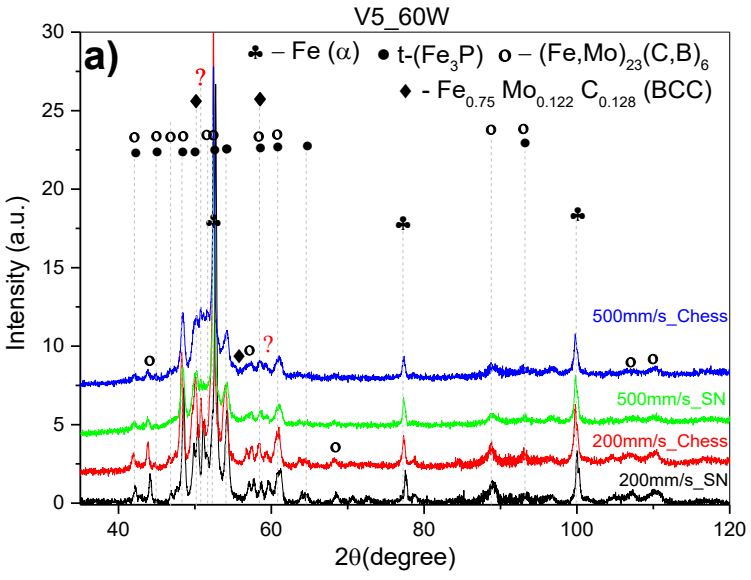

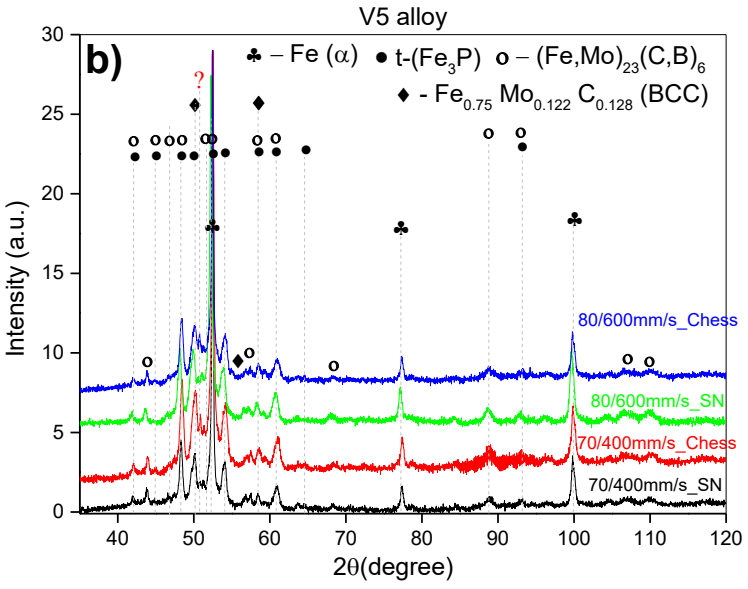

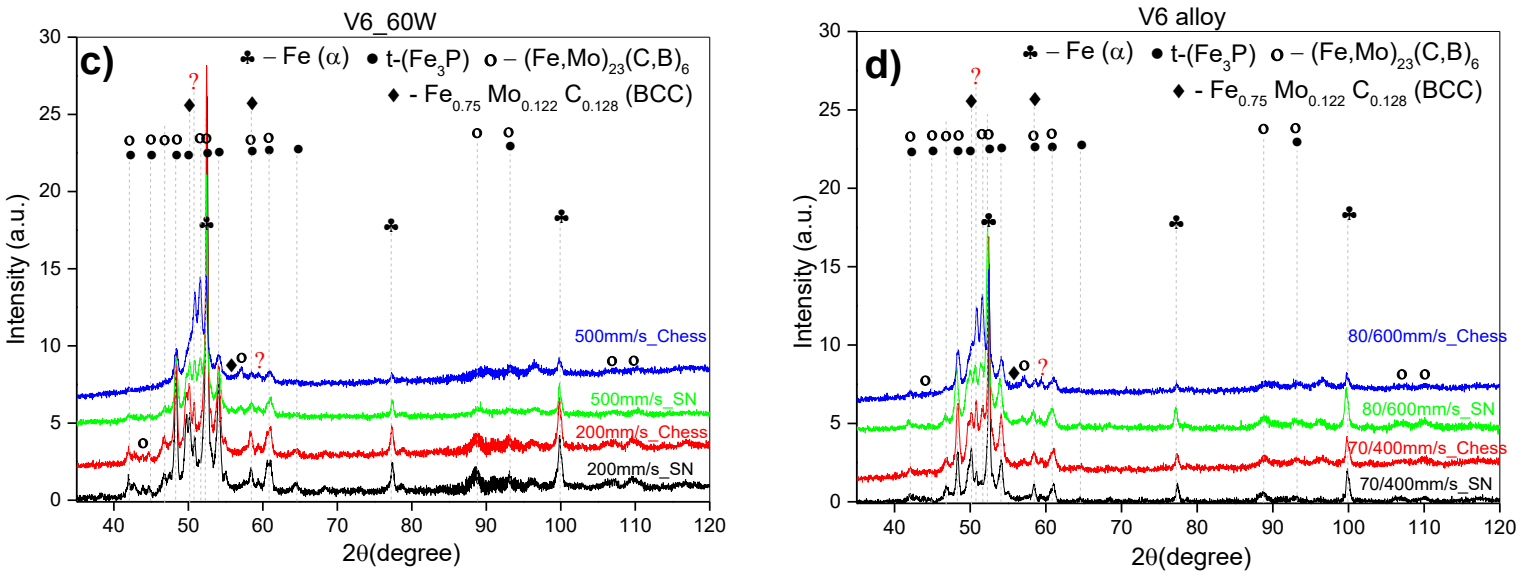

Figure 4.39- X-ray diffractograms of selected 4×4×8 mm LPBF samples investigating the influence of laser power (60W, 70W, and 80W), scan speed (200, 400, 500, and 600 mm/s), and laser scan strategy (SN and Chess) for: V5 alloy **a)** and **b)**, and V6 alloy **c)** and **d)**.

Confirming the XRD results, **Figure 4.40** depicts the variation in the volume fraction of the glassy phase, measured by DSC. From **Figure 4.40** a clear trace of the glass transition, with an apparent onset (T_g) at around 433°C, is observed for a heating rate of 20 K/min. As shown in the insets, a plateau indicating the super-cooled liquid region follows, succeeded by the first crystallization event, with the onset near 500 °C. At least three crystallization events can be identified, although they are superimposed and cannot be clearly distinguished. The subsequent small endothermic event corresponds to the ferrite (α-Fe) to austenite (γ-Fe) solid-state transformation, with an initial onset around 850 °C, consistent with previous reports [103], [231]. The second and third endothermic events are associated with alloy melting, with initial onsets near 920 °C and 1000 °C, respectively.

From **Figure 4.40a)**, it is evident that the V6 LPBF samples contain a significantly higher amount of glassy phase compared to the V5 samples. **Figure 4.40b)**, shows that increasing the printing angle from 0° to 90° leads to an

increase in glassy phase content. **Figure 4.40c)** confirms that higher scan speeds also promote glassy phase formation. **Figure 4.40d)** demonstrates that even with suboptimal parameters for glass formation (70 W_400 mm/s), the V6 alloy still achieves a higher glassy phase content than the V5 alloy.

In conclusion, the V6 alloy is a more effective glass-former than the V5 alloy when processed via LPBF. Both increased scan speed and higher printing angles contribute to enhanced glassy phase formation. For both alloys, the parameter combination of 80 W_600 mm/s results in a glassy richer microstructure than 70 W_400 mm/s.

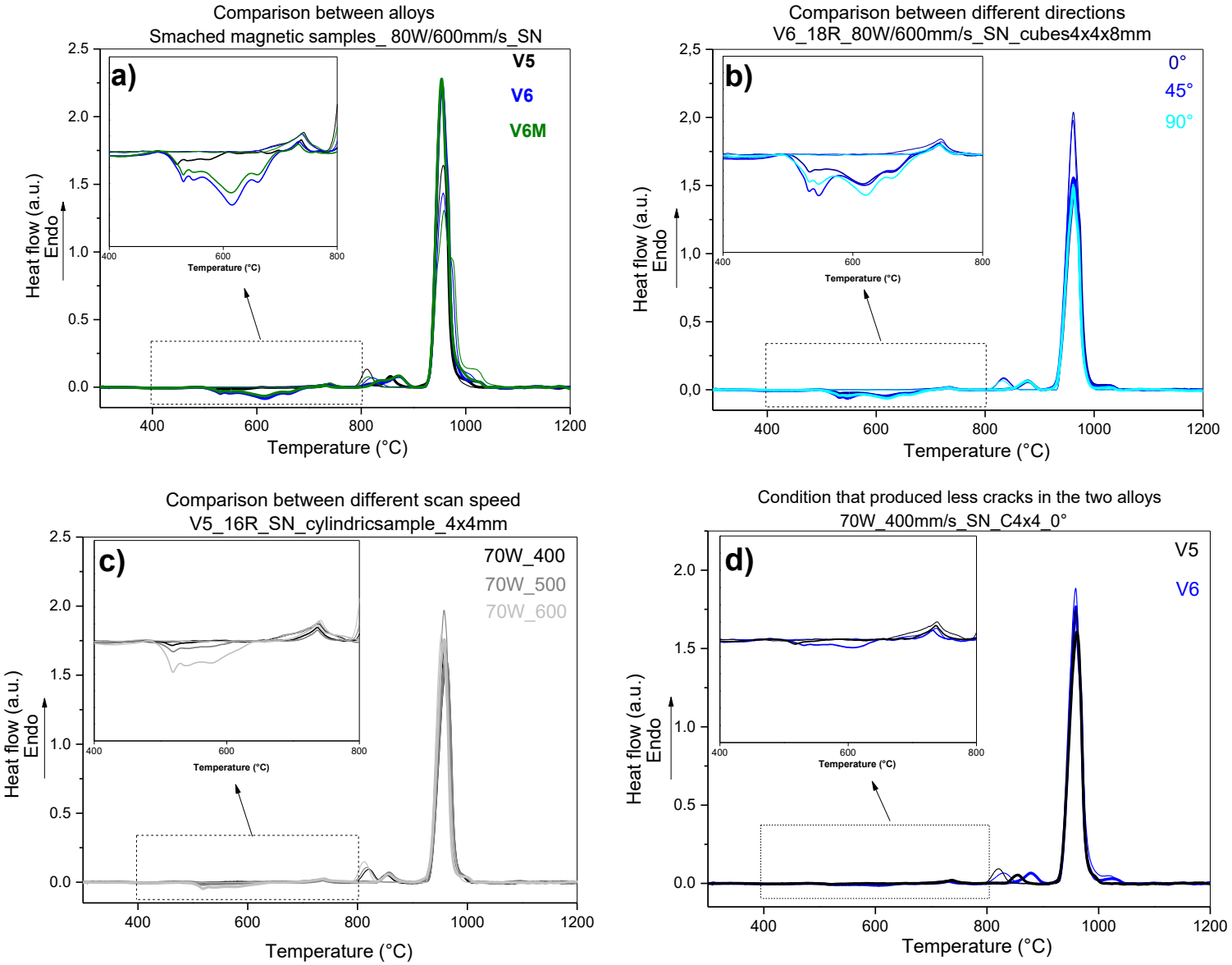

Figure 4.40- DSC curves of selected LPBF samples comparing: **a)** different

alloys (V5, V6, and contaminated V6); **b)** different printing directions (0°, 45° and 90°); **c)** different scan speeds (400, 500, and 600 mm/s), and **d)** V5 and V6 samples produced with the parameter combination (70W_400 mm/s) that resulted in the lowest amount of cracks. Heating rate of 20K/min.

The effect of laser scan strategy (SN and chessboard) and scan speed on glassy phase formation in V5 and V6 alloys was investigated using DSC measurements, as shown in **Figure 4.41**. Since the thermal events take place at temperatures equivalent to those reported in **Figure 4.40**, they will not be discussed again here.

Figure 4.41a) shows that, for both alloys, the use of the chessboard laser strategy significantly enhances glassy phase formation compared to the SN strategy. It also confirms that the 80 W_600 mm/s parameter combination is more favorable for glassy phase formation than 70 W_400 mm/s. By comparing **Figure 4.41b)** and **Figure 4.41c)** (for V5), as well as **Figure 4.41d)** and **Figure 4.41e)** (for V6), the positive influence of higher scan speeds and the chessboard laser strategy on glassy phase formation is clearly demonstrated.

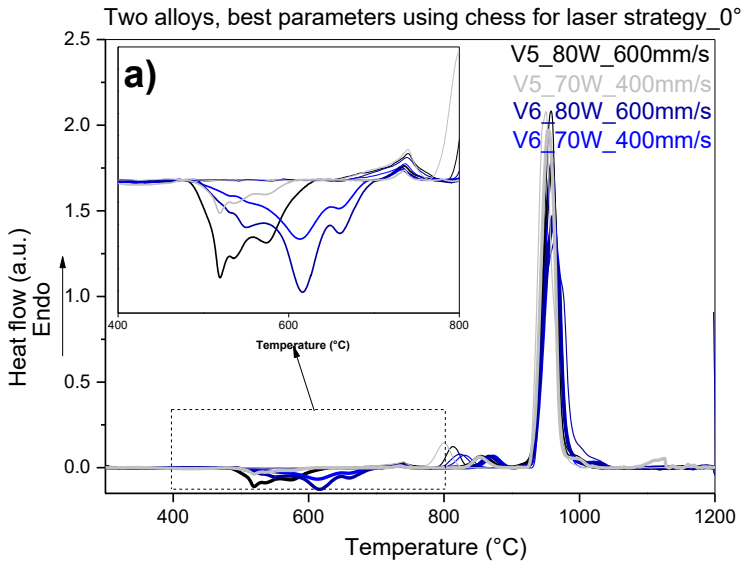

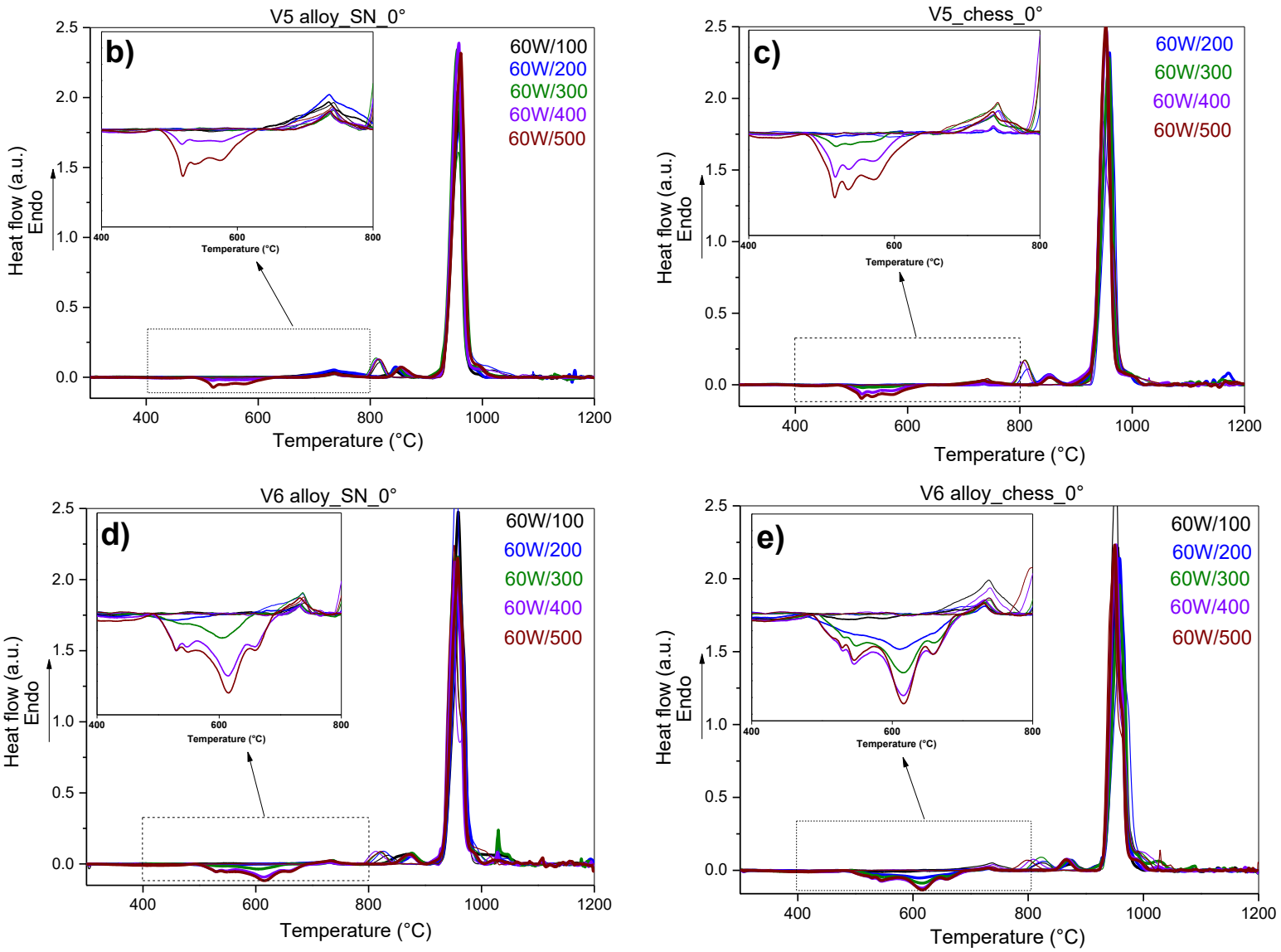

Figure 4.41- DSC curves of selected LPBF samples investigating the influence of: a) the chessboard laser strategy for V5 and V6 samples built with 80W_600 mm/s and 70W_400 mm/s; and scan speed (100-500 mm/s) at a laser power of 60 W using SN and chessboard laser strategies for: **b)** and **c)** V5 alloy, and **d)** and **e)** V6 alloy. Heating rate of 20K/min.

From the DSC results shown in **Figure 4.40** and **Figure 4.41**, all LPBF samples exhibited exothermic peaks near 500°C, which are associated with the crystallization of the glassy phase. The crystallization enthalpy (ΔH_{cry_LPBF}) was calculated for each LPBF sample and correlated with the crystallization enthalpy

(ΔH_{Cry_R}) of V5 and V6 melt-spun ribbons. The glassy fraction (%) was then determined using the formula: (ΔH_{cry_LPBF} alloy/ΔH_{cry_R}) x 100, similar to that reported by others [151], [153], [232], and the results are presented in **Table 4.13**.

Before discussing the results, it should be noted that:

1- V5 and V6 virgin powders had similar oxygen content (0.007–0.008 wt.%), and after all printing rounds, they showed equivalent oxygen content (~0.021 wt.%).
2- The oxygen level in the chamber at the start of processing was below 200 ppm for all LPBF samples analyzed in **Table 4.13**.

Therefore, the influence of oxygen content in the virgin powders or its uptake during processing can be considered negligible for both alloys.

Table 4.13 summarizes the variation of glassy fraction as a function of parameter combinations and correlates this with the percentage of porosity plus cracks (i.e., inverse of relative density) for all selected LPBF samples. Within the range of parameters investigated, the glassy phase fraction ranged from 0% to 18.6% for V5 and from 0% to 24.2% for V6. For all processing conditions, V6 samples consistently exhibited higher glassy content than V5 samples, indicating a superior glass-forming ability (GFA) for the V6 alloy when processed by LPBF. This can be attributed to the higher Mo content in the V6 alloy, as Mo is known to significantly enhance the GFA in Fe-P,C,B [63] and Fe-B-C-P-Si-Mo [204] alloys.

The results highlight the strong influence of scan speed on glassy phase formation, with higher scan speeds leading to a significant increase in glassy fraction. The effectiveness of the chessboard scan strategy in promoting glassy phase formation is also confirmed, along with a slight tendency for increased glassy phase with higher printing angles.

When comparing the glassy fraction with sample porosity, it becomes evident that the process parameter windows leading to the highest densities (e.g., 60_100_SN_0° or 60_100_chess_0°) and those producing the highest glassy fractions (e.g., 60_500_chess_0°) do not coincide. In fact, the highest glassy fractions were found in samples exhibiting the greatest porosity and cracking (i.e., lowest relative density). Within the same alloy, a clear trend is observed where

an increase in porosity and cracking is associated with a higher glassy phase fraction. According to the literature [146], pores may help preserve glassy regions by shielding them from devitrification during the melting of subsequent layers.

Table 4.13- Porosity+cracks fraction (%) and glassy phase fraction (%) in selected LPBF samples of V5 and V6 alloys, using V5 and V6 ribbons (100% glassy) as references.

Sample name	Glassy phase %		Porosity+cracks %	
	V5	V6	V5	V6
80_600_SN_0°	3.00	13.6	1.4	3.1
80_600_SN_45°	4.02	13.0	1.6	3.5
80_600_SN_90°	4.40	14.1	1.6	3.6
80_600_chess_0°	18.60	21.4	11	7.5
70_400_SN_0°	0.6	2.3	1.7	1.8
70_500_SN_0°	2.8	-	2.2	2.2
70_600_SN_0°	7.5	-	2.6	2.6
70_400_chess_0°	4.8	12.0	6.7	3.3
60_100_SN_0°	0.0	0.0	1.2	1.1
60_200_SN_0°	0.0	1.4	1.5	1.7
60_300_SN_0°	0.0	6.0	1.5	1.1
60_400_SN_0°	4.5	18.4	2.4	2.3
60_500_SN_0°	12.2	21.8	3.0	2.2
60_100_chess_0°	0.0	0.0	1.4	1.0
60_200_chess_0°	0.0	12.4	3.4	2.9
60_300_chess_0°	3.0	17.4	8.6	6.9
60_400_chess_0°	10.6	23.2	9.2	8.0
60_500_chess_0°	18.0	24.2	15	8.7

As shown by the XRD and DSC results, the microstructure of the LPBF samples varies only in terms of glassy phase fraction. Therefore, regardless of

the processing conditions, the composite microstructure is expected to consist of a glassy phase and largely the same crystalline phases. For this reason, only SEM images of the V6 LPBF sample containing 12% glassy phase (representing an intermediate glassy fraction) are presented here.

The microstructural evolution of bulk metallic glasses composites (BMGCs) during the LPBF process is a complex phenomenon, due to the heterogeneous nature of the complicated thermal treatments cycles, which develop during the printing process [180],[207],[232]. **Figure 4.42** present SEM-BSE images of V6 LPBF sample containing 12% of glassy phase. In **Figure 4.42a)**, a microstructure containing molten pools (MP) and heat affected zone (HAZ) can be distinctly observed. While the MP zone exhibits a featureless light gray contrast—typical of a glassy phase—the HAZ shows a darker gray contrast, which denotes the crystallization during the LPBF process. These microstructural differences can be attributed to the significantly different cooling rates experienced by the MP and HAZ regions, as has been reported by others [232], [233].

To highlight these microstructural differences, two representative regions (“1” and “2”) were examined. In region “1” (**Figure 4.42b)**), a large area rich in coarser dendrites is observed. At higher magnification (**Figure 4.42d)**) numerous white, rounded phases can be seen dispersed among the dendritic structures. In region “2” (**Figure 4.42c)**), crystalline phase with different sizes and shapes are especially evident in the HAZ contour. While the MP is predominantly composed of a homogeneous matrix (assumed to be glassy) with a few randomly dispersed gray spherulites, the HAZ contains many gray spherulites and dark blocky phases embedded in a similar matrix. These features often grow, and collide with each other within the HAZ region. Such microstructural characteristics are expected, as the MP undergoes rapid cooling rates sufficient to directly solidify the melt into a glassy state. Additionally, as previously reported [232], the cooling rate decreases from the MP toward the HAZ due to the high thermal gradients generated during laser scanning, thereby promoting crystallization within the HAZ.

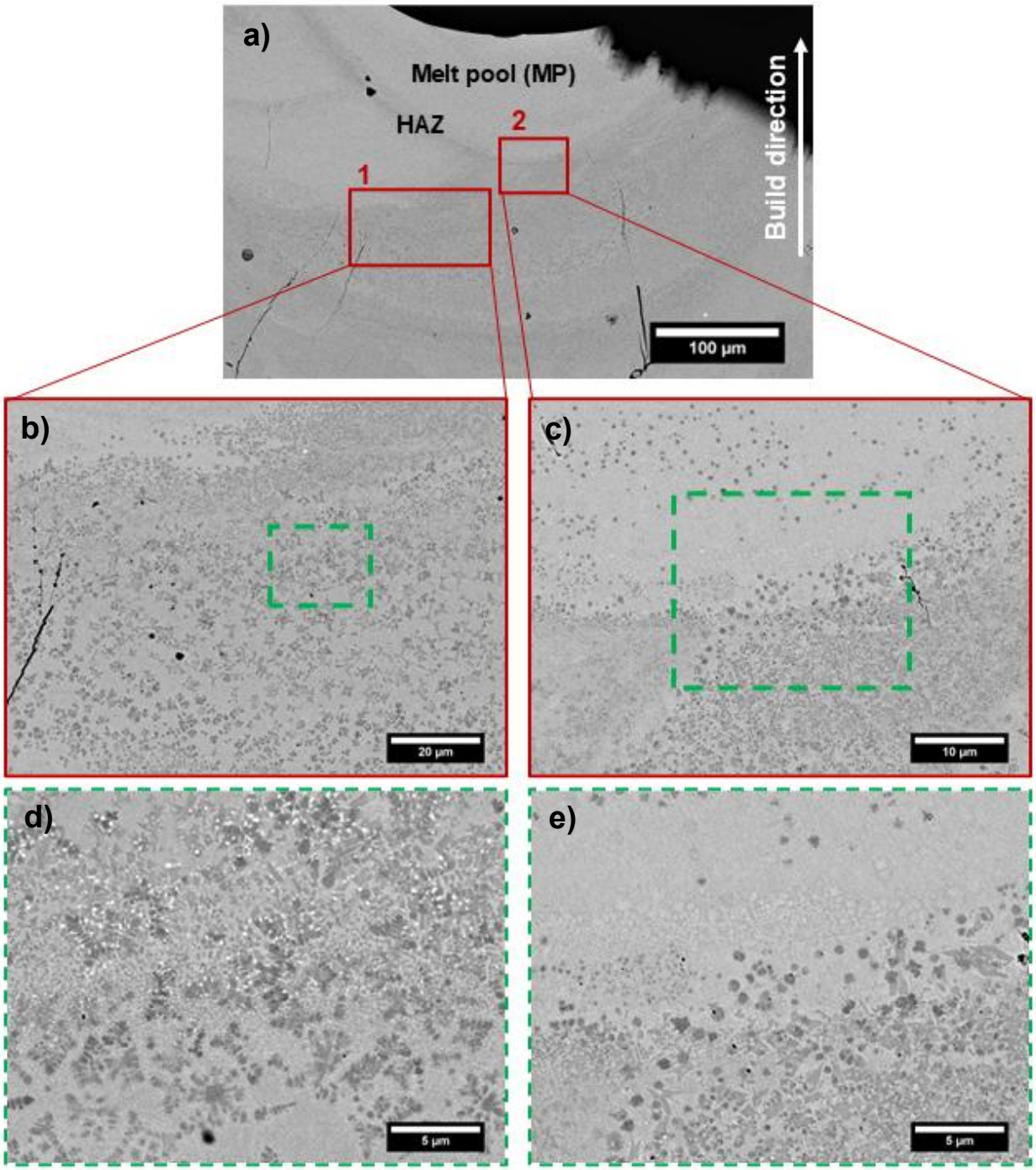

Figure 4.42- SEM-BSE micrographs of V6 LPBF sample containing 12% of glassy phase, showing: **a)** general view of melt pool zone (MP) and heat affected zone (HAZ), **b)** and **d)** HAZ with coarser microstructure, and **c)** and **e)** Intermediate region between the bottom of MP and the HAZ, exhibiting a finer microstructure.

A further microstructural investigation in the melt pool (MP) and in heat-affected zone (HAZ) was carried out using SEM-BSE imaging at higher magnification, along with their corresponding elemental mapping, as shown in **Figure 4.43**. In the MP region (**Figure 4.43a)**), the featureless matrix—assumed to be glassy—appears uniformly enriched in all detected elements (Fe, Mo, P, C, B, and Si), with no visible contrast variations. In contrast, the HAZ (**Figure 4.43b)**) reveals the presence of Fe- and Si-rich rounded phases, which are devoid of Mo and P, as well as elongated phases that are predominantly P-rich.

By correlating these findings with the XRD data, the Fe- and Si-rich phases are most likely the well-known α-Fe(Si) phase, which corresponds to α-Fe enriched with silicon in solid solution within a body-centered cubic (BCC) structure. According to the literature, silicon exhibits high solubility in the ferritic α-Fe phase [234], thus, in steels containing approximately 2–4 wt.% Si, the α-Fe(Si) is commonly found. This phase has also been reported in Fe-based BMGCs processed by LPBF in previous studies [146],[151][232],[235]. The elongated P-rich phase is most likely Fe_3P, a phase that has been consistently reported in Fe-Mo-P-C-B and Fe-Mo-P-C-B-Si systems [101], [103], [204], [236].

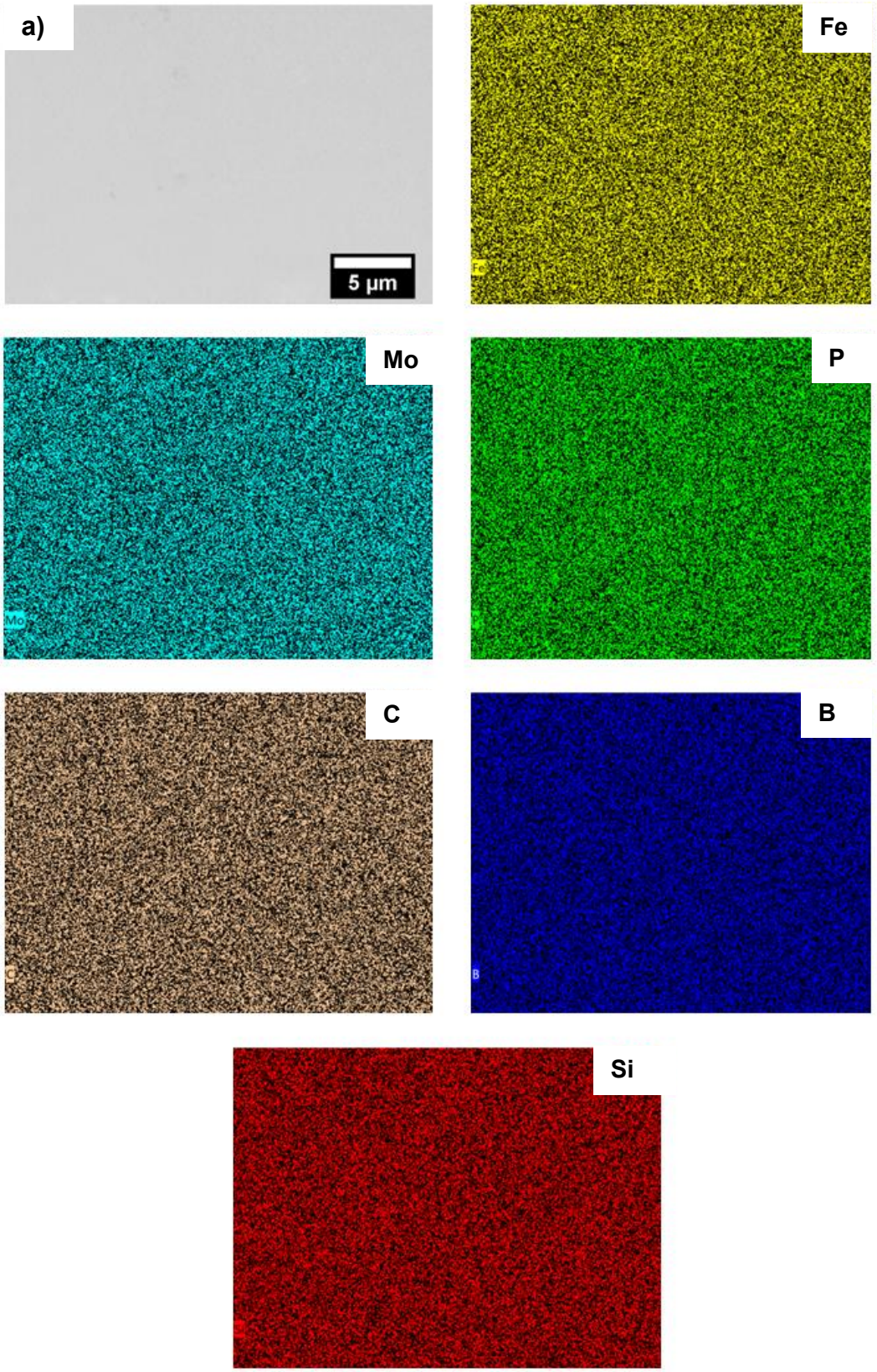
a)
5 µm
Fe
Mo
P
C
B
Si

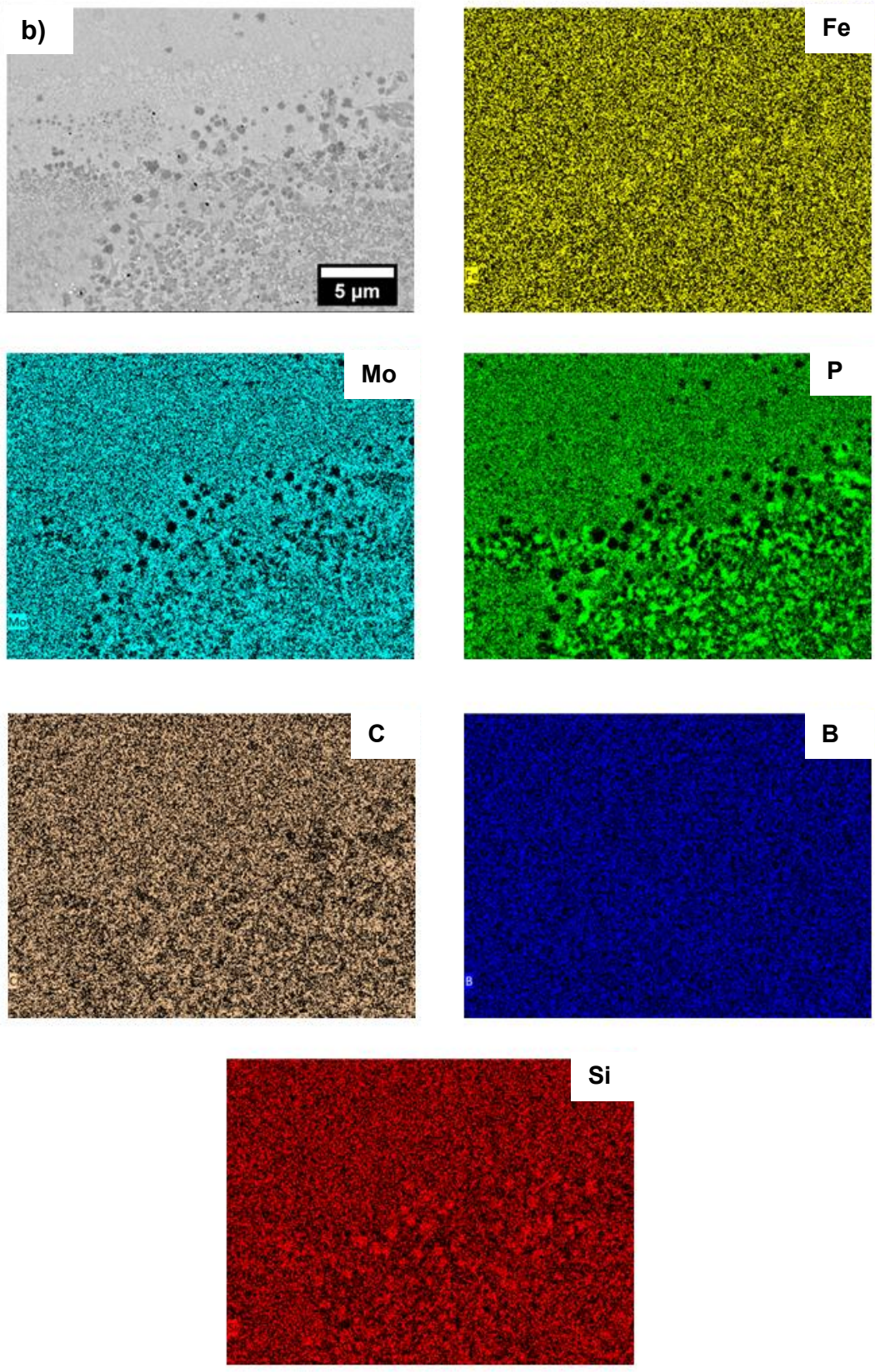

Figure 4.43- SEM-BSE micrographs and corresponding elemental EDX maps using Fe-K, Mo-L, P-K, C-K, B-K, and Si-K of V6 LPBF sample containing 12%

of glassy phase, showing the microstructure in: **a)** the melt pool zone (MP), and **b)** the heat affected zone (HAZ) near the bottom of the melt pool, exhibiting a finer microstructure.

In order to further analyze the composition of the melt pool (MP) and the heat-affected-zone (HAZ), TEM analyses provide more detailed and accurate proof. **Figure 4.44** presents TEM bright-field (BF) and dark-field (DF) images of the microstructures, along with the corresponding selected area electron diffraction patterns (SAEDPs) and elemental EDX maps of the MP and HAZ regions in a V6 LPBF sample containing 21% glassy phase.

In the MP region, a homogeneous microstructure full of equiaxed nano-scaled grains (30-100nm) was observed (**Figure 4.44a)**). The EDX elemental maps (**Figure 4.44b)**) indicate that these grains contain all elements, with a slightly higher contrast for Mo and Si. Additionally, P appears segregated at the grain boundaries/matrix. An area EDX analysis revealed a composition of $Fe_{79.14}Mo_{2.55}P_{5.64}C_{11.13}Si_{1.51}$ ($Fe_{88.10\pm0.3}Mo_{4.89\pm0.10}P_{3.48\pm0.06}C_{2.66\pm0.10}Si_{0.84\pm0.02}$ wt%), which is not significantly enriched in Si. As shown in **Figure 4.44c),** the nano-grains were identified as the $Fe_{0.75}Mo_{0.122}C_{0.128}$ (bcc) phase, with a fitting error below 1.2%. Additionally, closer to the MP boarder, the cluster-like “flower” phase shown in **Figure 4.44d)** was identified as α-Fe (bcc) phase (fitting error of 1.4%). Although it was not possible to isolate a diffraction pattern from just the grain boundary/matrix region, all SAED patterns obtained from within the MP revealed a halo ring, characteristic of an amorphous structure. This suggests that a glassy phase is a constituent phase in the matrix of the MP zone.

In contrast, the HAZ exhibits a heterogeneous microstructure consisting of phases of varying shapes and sizes (**Figure 4.44e)**). According to the EDX maps (**Figure 4.44f)**), the dendritic phases are Fe-rich with some C and Si, but depleted in Mo and P. The rounded phases—which decrease in size, from fine to ultra fine, when moving toward the MP—are rich in all elements except P, and again, the contrast for Mo and Si is evidenced. Three phases were identified in the HAZ:

1- $B_{50}Fe_{1.04}$ (tetragonal) phase—with an irregular shape (**Figure 4.44g)**) (fitting error of 1.58%),

2- α-Fe (bcc) phase—in flower-like/dendritic morphology (**Figure 4.44h)**) (fitting error of 1.2%), and

3- $Fe_{0.75}Mo_{0.122}C_{0.128}$ (bcc) phase—round phases ~200 nm in diameter (**Figure 4.44i)**) (fitting error of 3% and 0.8%).

The indexed α-Fe is likely α-Fe(Si), as Si has high solubility in α-Fe [234]. With Si in solid solution, this phase is commonly referred to as α-Fe(Si) [146],[151][232]. For instance, Özden and Morley [232] reported α-Fe(Si) nanograins (300–500 nm) in the MP and Fe_3Si nanocrystalline clusters (30–100 nm) alongside Fe_2B nano-needles (400–600 nm) in the HAZ of an LPBF-processed KUAMET 6B2 alloy ($Fe_{87.38}Si_{6.85}B_{2.54}Cr_{2.46}C_{0.77}$ in wt%). However, their phase identifications were based solely on SEM images without EDX confirmation or TEM validation. In another study [151], identified ordered Fe_3Si dendrites, glassy phase and disordered α-Fe(Si) equiaxed grains in the HAZ of LPBF Kuamet 52 ($Fe_{71}Si_{10}B_{11}C_6Cr_2$ (at. %)), though the provided TEM images did not clearly support what they claim.

In this work, the $Fe_{0.75}Mo_{0.122}C_{0.128}$ (bcc) phase—observed as nanograins in the MP region—exhibits a simple cubic structure, likely formed under the extremely high cooling rates in the melt pool center (~10^4°C/s [180]). Under such rapid solidification, phases with more complex crystal structures are unlikely to form due to insufficient time for atomic diffusion.

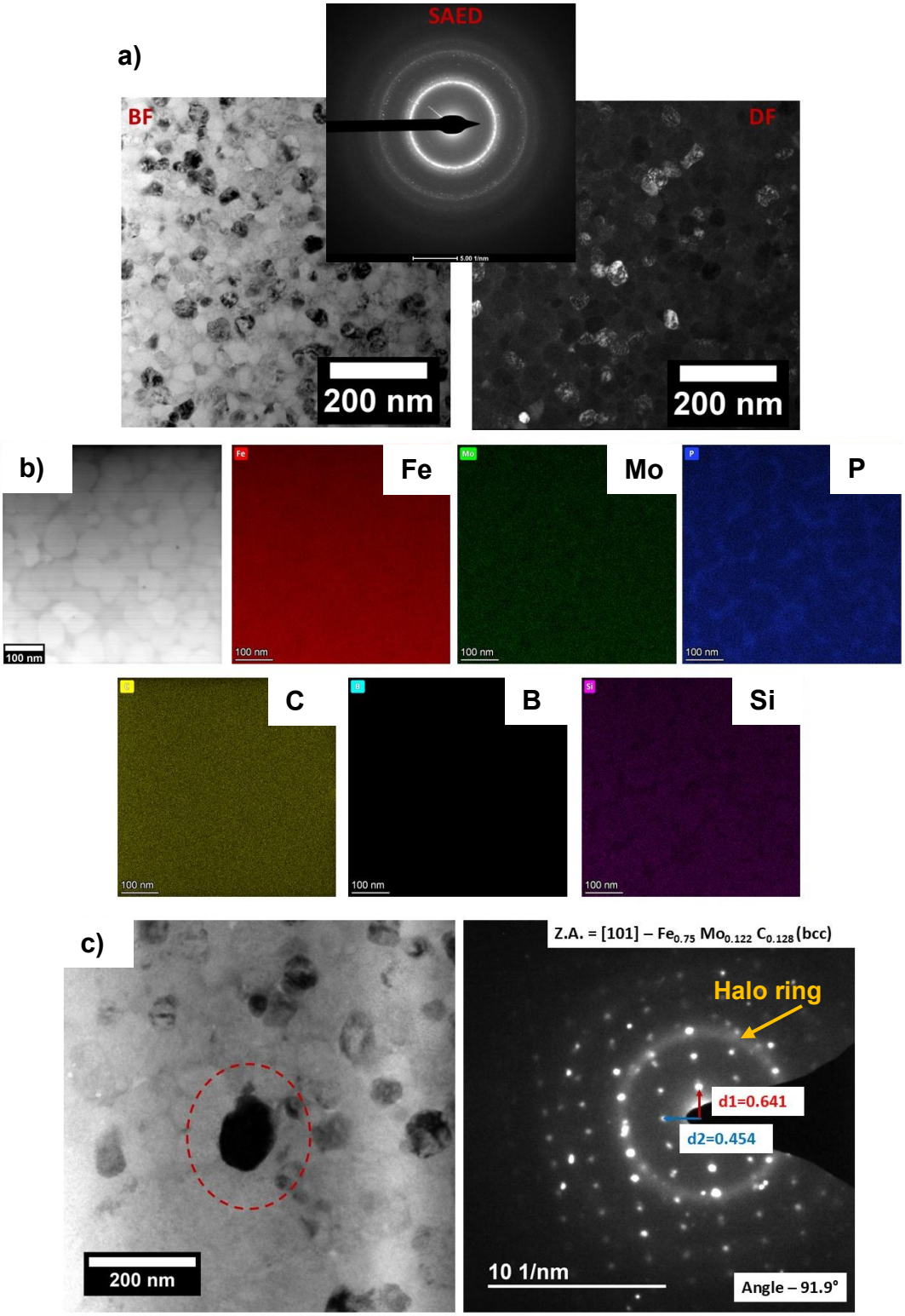
a)
SAED
BF
DF
200 nm
200 nm
b)
Fe
Mo
P
C
B
Si
100 nm
c)
200 nm
Z.A. = [101] – Fe0.75 Mo0.122 C0.128 (bcc)
Halo ring
d1=0.641
d2=0.454
10 1/nm
Angle – 91.9°

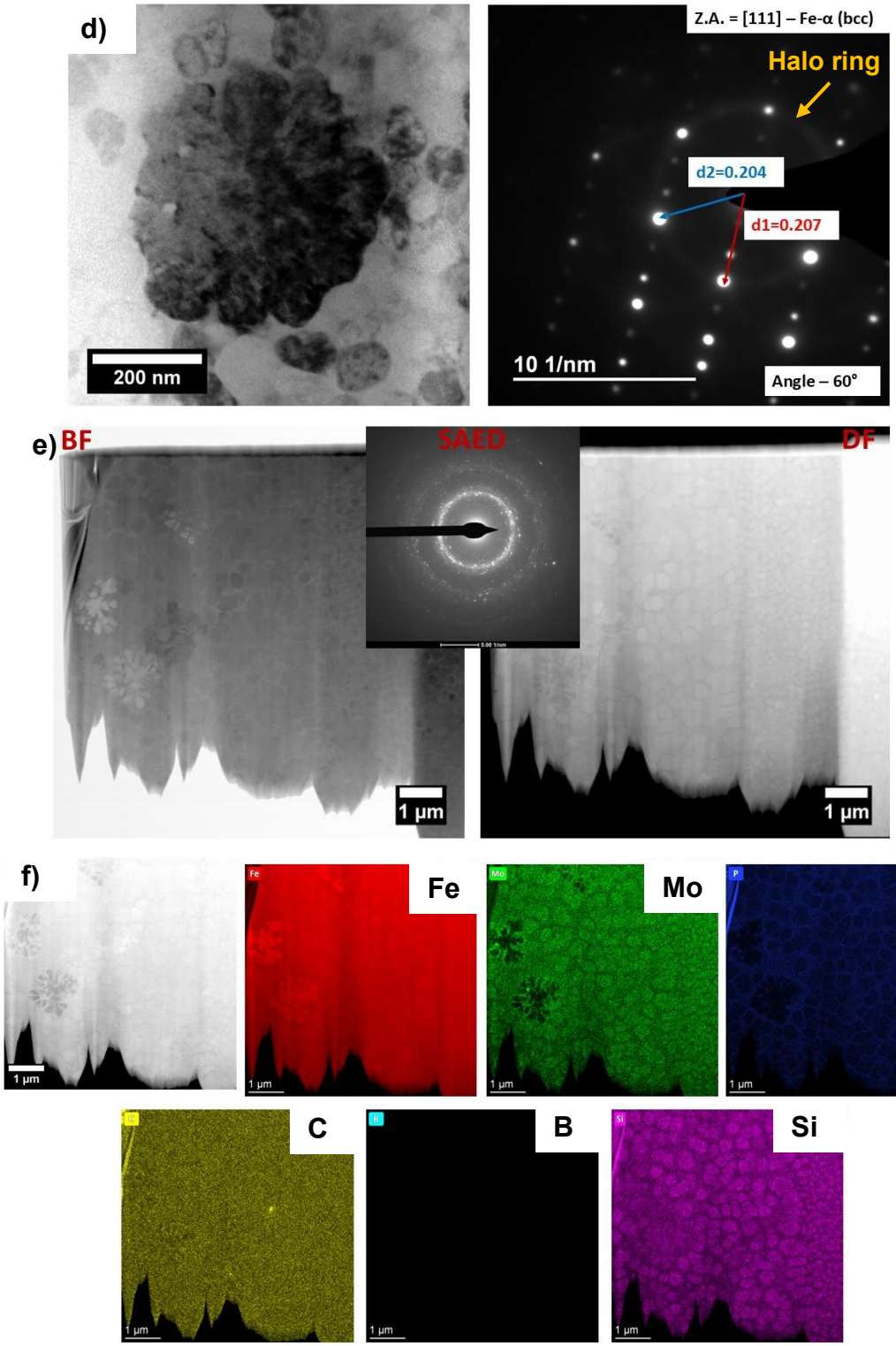
d)
200 nm
Z.A. = [111] – Fe-α (bcc)
Halo ring
d2=0.204
d1=0.207
10 1/nm
Angle – 60°
e)
BF
SAED
DF
1 µm
1 µm
f)
1 µm
Fe
1 µm
Mo
1 µm
P
1 µm
C
1 µm
B
1 µm
Si
1 µm

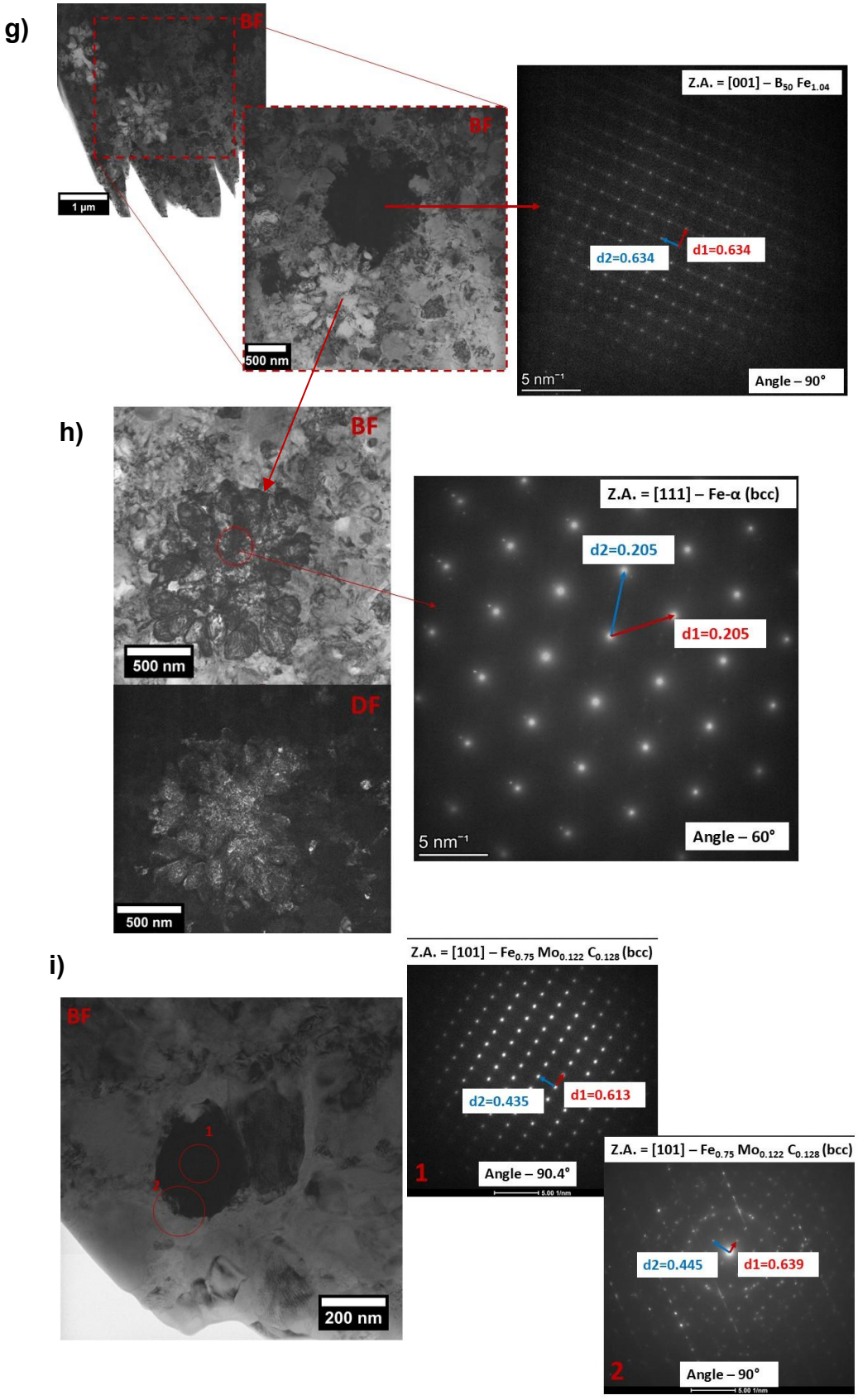

Figure 4.44- TEM bright-field (BF) and dark-field (DF) images of the microstructures, along with the corresponding selected area electron diffraction

patterns (SAEDPs) and elemental EDX maps (Fe-K, Mo-L, P-K, C-K, B-K, and Si-K) of a V6 LPBF sample containing 21% glassy phase: **a)**–**d)** melt pool (MP) zone, and **e)**–**i)** heat-affected zone (HAZ).

4.4.2.2. Mechanical characterization

To investigate the effect of processing parameters on the Vickers microhardness of the V5 and V6 LPBF samples, micro indentation experiments were conducted in the typical melt pool (MP) and heat-affected zone (HAZ) regions, which exhibit white and dark contrast, respectively, under optical microscopy (**Figure 4.45a)**). Measurements were performed along the cross-sections of the LPBF samples, and the variation in average microhardness for each region (MP and HAZ) as a function of processing parameters is shown in **Figure 4.45b)** for V5, and **Figure 4.45c)** for V6.

For a given alloy, the hardness values across different parameter combinations were quite similar, indicating that microhardness is largely independent of the processing conditions. This observation is consistent with previous results, which showed that samples produced under different parameters exhibited similar composite microstructures composed of the same phases, differing only in their volume fractions. Consequently, similar hardness values were expected across samples with comparable microstructural characteristics.

When comparing the two alloys, V6 samples exhibited consistently higher hardness values (~1100 HV) compared to V5 samples (~1050 HV) across all parameter combinations. In both alloys, the white regions (MP) generally displayed higher hardness than the dark regions (HAZ). This can be attributed to the presence of ultrafine grains in the MP (see TEM images), which contribute to grain refinement strengthening of the glassy matrix. Conversely, the HAZ undergoes matrix thermal relaxation and precipitation of coarser crystalline phases, which may reduce hardness in this region.

Nonetheless, considering the standard deviation, the hardness values of

both regions are very close, and the differences are almost negligible. The microhardness values obtained for the LPBF FeMoPBCSi composites produced in this work are comparable to those reported for LPBF Fe-Co-B-Si-Nb (~1200 HV) [207], and higher than those reported for LPBF-processed FeSiBCrC (~900 $HV_{0.1}$) [237]. Based on their high hardness, the LPBF FeMoPBCSi composites developed in this study show promise for applications requiring excellent wear resistance.

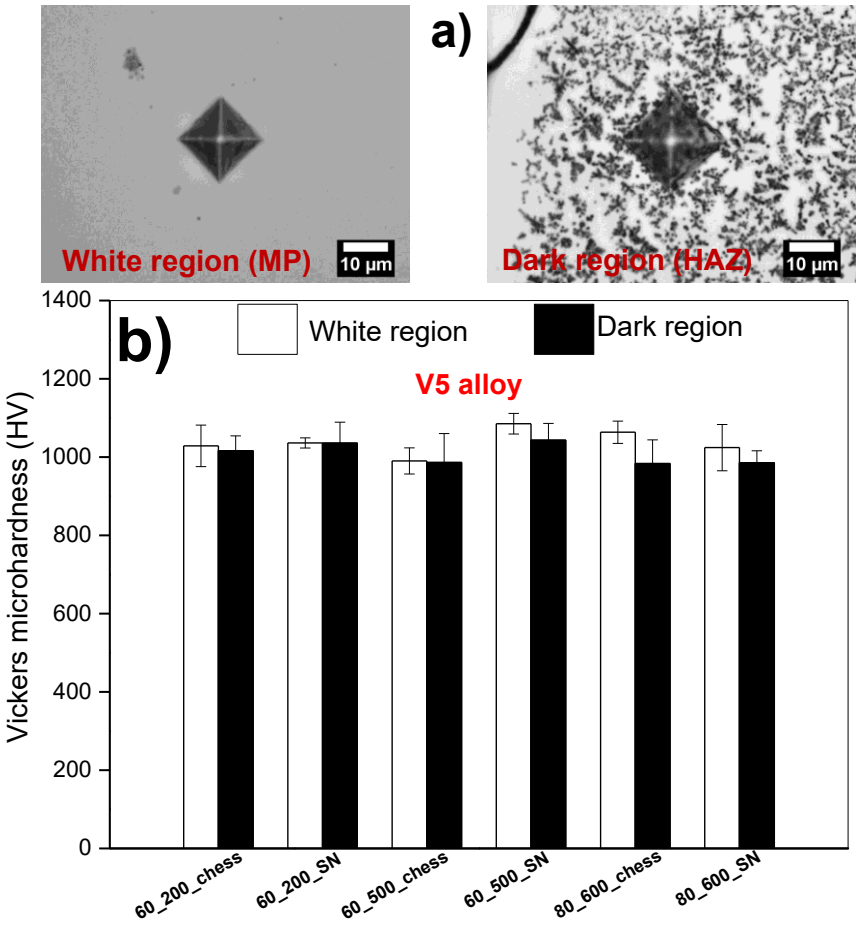

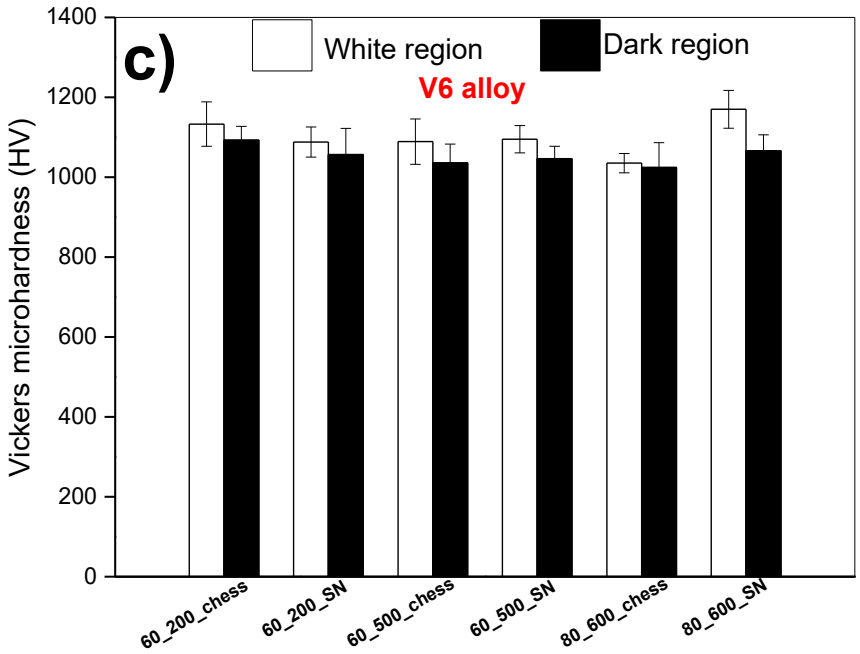

Figure 4.45- a) White (MP) and dark (HAZ) regions where Vickers microhardness measurements were taken in the selected LPBF samples as a function of processing parameter combinations for: **b)** V5 alloy, and **c)** V6 alloy.

To statistically compare and evaluate the equivalence of hardness in LPBF V5 and V6 samples produced under different conditions, the results presented in **Figure 4.45** were analyzed using one-way ANOVA. The corresponding p-values for the V5 and V6 alloys—considering the white regions, dark regions, as well as the average hardness of each sample— are summarized in **Table 4.14**. Since all p-values are greater than the significance level ($\alpha = 0.05$), there are no statistically significant differences in the hardness of the white or dark regions of the LPBF samples produced using different parameter combinations, nor in the average hardness of the LPBF samples produced using different parameter combinations, with 95% confidence. Therefore, for both alloys, the hardness of the LPBF samples remains unaffected by variations in the process parameters.

Table 4.14- Statistical comparison of Vickers microhardness for the white regions, dark regions, and average values (HV_{white}+HV_{dark}/2) of V5 and V6 LPBF samples produced using different parameter combinations, based on one-way ANOVA analysis.

	P-value	
Alloy	**V5**	**V6**
White area	0.431	0.119
Dark area	0.363	0.382
Average	0.123	0.054

The static uniaxial compression test was conducted at ambient temperature on a series of at least three samples for each parameter combination. The as-built rectangular samples, with a height-to-width ratio of 2, had their contact surfaces ground and polished to ensure low surface roughness and parallelism, as shown in **Figure 4.46a)**. The compression tests were carried out until fracture. Because all LPBF samples exhibited numerous cracks, the tests serve a comparative purpose rather than providing absolute values, and the corresponding results are shown in **Figure 4.46b)-e)**.

Since all selected LPBF samples from both studied alloys exhibited elastic-brittle behavior—with compression curves similar to those of bulk metallic glasses (BMGs) and maximum deformation of approximately 1.5%—only the ultimate compressive strength (UCS) is presented here for comparison.

In general, the mechanical properties of the V5 and V6 LPBF samples were significantly lower than those of their casted counterparts. As shown in **Figure 4.46b)-e)**, the highest UCS values were obtained from the densest LPBF samples of both alloys. Among the best-performing samples, V5 achieved approximately 49% and V6 about 34% of the UCS of their respective cast counterparts.

The results also reveal several trends:

1. Using the 80 W_600 mm/s or 70 W_400 mm/s combinations, V5 samples showed higher UCS compared to the equivalent V6 samples (see **Figure**

4.46b) and **d)**).

2. At a laser power of 60 W, regardless of scan speed or laser strategy, V6 samples exhibited higher UCS than V5 (see **Figure 4.46c)** and **e)**).
3. Samples built at 0° demonstrated better mechanical performance than those built at 45° and 90°; between the latter two, the results were similar, with a slight advantage for 90°, especially in V6 alloy (see **Figure 4.46b)** and **d)**).
4. The chessboard laser strategy resulted in lower UCS compared to the SN strategy, possibly due to a higher percentage of defects.
5. Regardless of laser strategy, at a constant power of 60 W, increasing scan speed led to reduced mechanical strength (see **Figure 4.46c)** and **e)**).

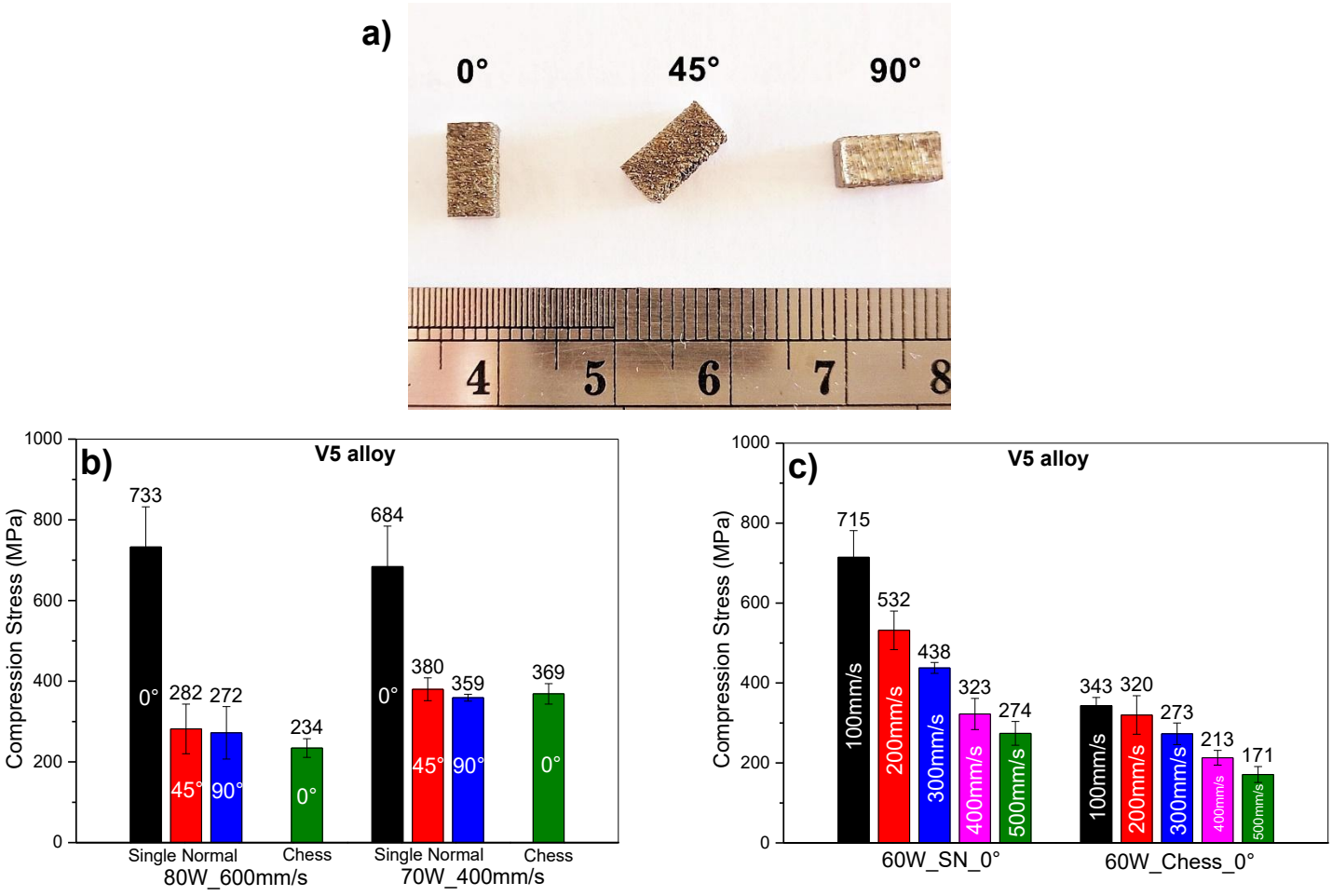

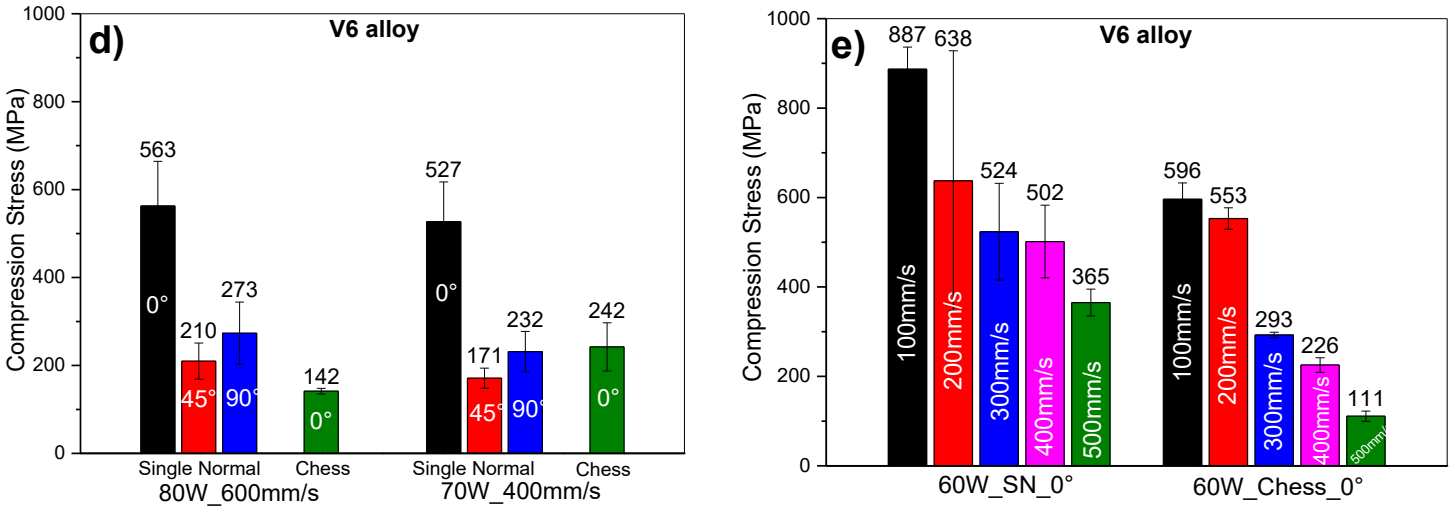

Figure 4.46- a) Picture of the as-built LPBF samples submitted to static uniaxial compression testing at room temperature. Ultimate compressive strength results of the LPBF samples produced using different parameter combinations for: **b)** and **c)** V5 alloy, and **d)** and **e)** V6 alloy.

4.4.2.3. Fracture behavior

Figure 4.47 shows the visual appearance of representative LPBF samples built at 0°, 45°, and 90° after compression testing, along with schematic illustrations of their corresponding fracture behavior and SEM micrographs of the fracture surfaces. From the visual inspection of fracture behavior (**Figure 4.47a)**), it is evident that the cracks propagate along the layers, i.e., parallel to the building direction (BD). It is likely that these cracks follow the heat-affected zones (HAZ), which contain coarser phases and, as shown in the microhardness tests, exhibit slightly lower hardness compared to the melt pool (MP) zone.

As a result, while the load in the 45° and 90° samples is applied at an angle to the BD, for the 0° samples, the load is applied parallel to the layers (i.e., along the BD), which makes crack propagation more difficult. This can explain why the 0° samples exhibited the highest ultimate compressive strength (UCS) and fractured into multiple pieces (as seen in **Figure 4.47a)**).

Regarding the SEM images of the fracture surfaces, none displayed the vein-like patterns typical of ductile BMGs. Moreover, no single dominant shear

plane was observed. The fracture surfaces of all samples were smooth, featuring mist and hackle regions. These characteristics indicate brittle cleavage fracture, with a generally faceted appearance (see **Figure 4.47b), e)** and **h)**), where river patterns are evident (**Figure 4.47d), g)** and **j)**), consistent with the fracture behavior of brittle metallic glasses [225], [238], [239], [240], [241].

In the 0° sample, the presence of separated cuboids along the crack path is clearly visible (**Figure 4.47b)**), which explains why the sample broke into many pieces after catastrophic failure. The presence of defects (such as pores and cracks) likely contributed to the increased number of fracture initiation sites, thereby reducing the overall mechanical strength of the samples.

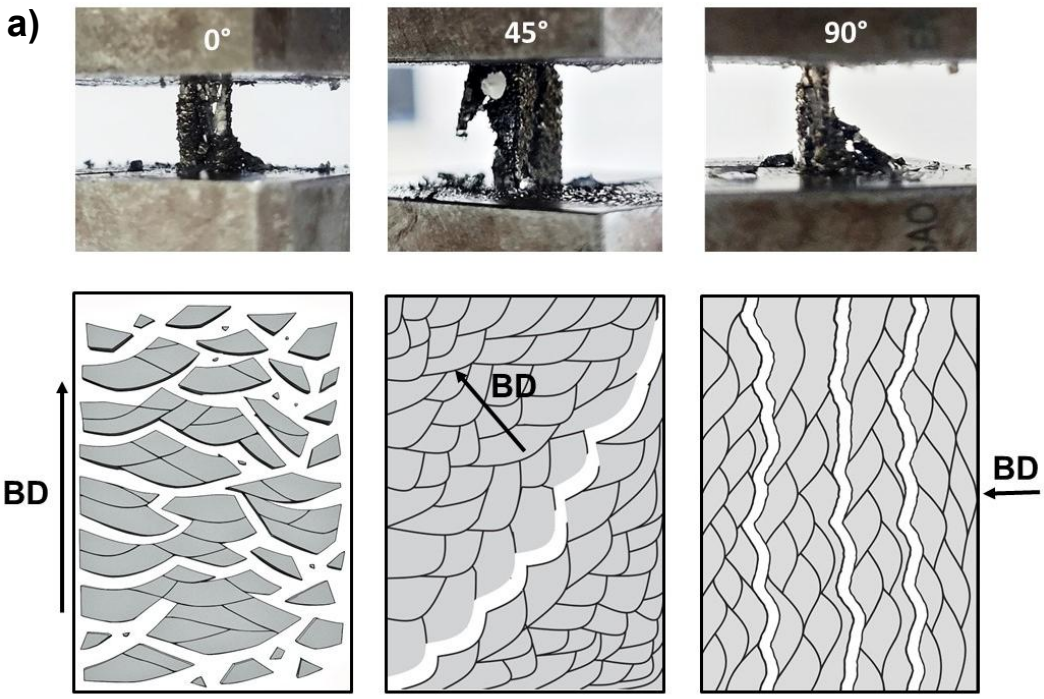

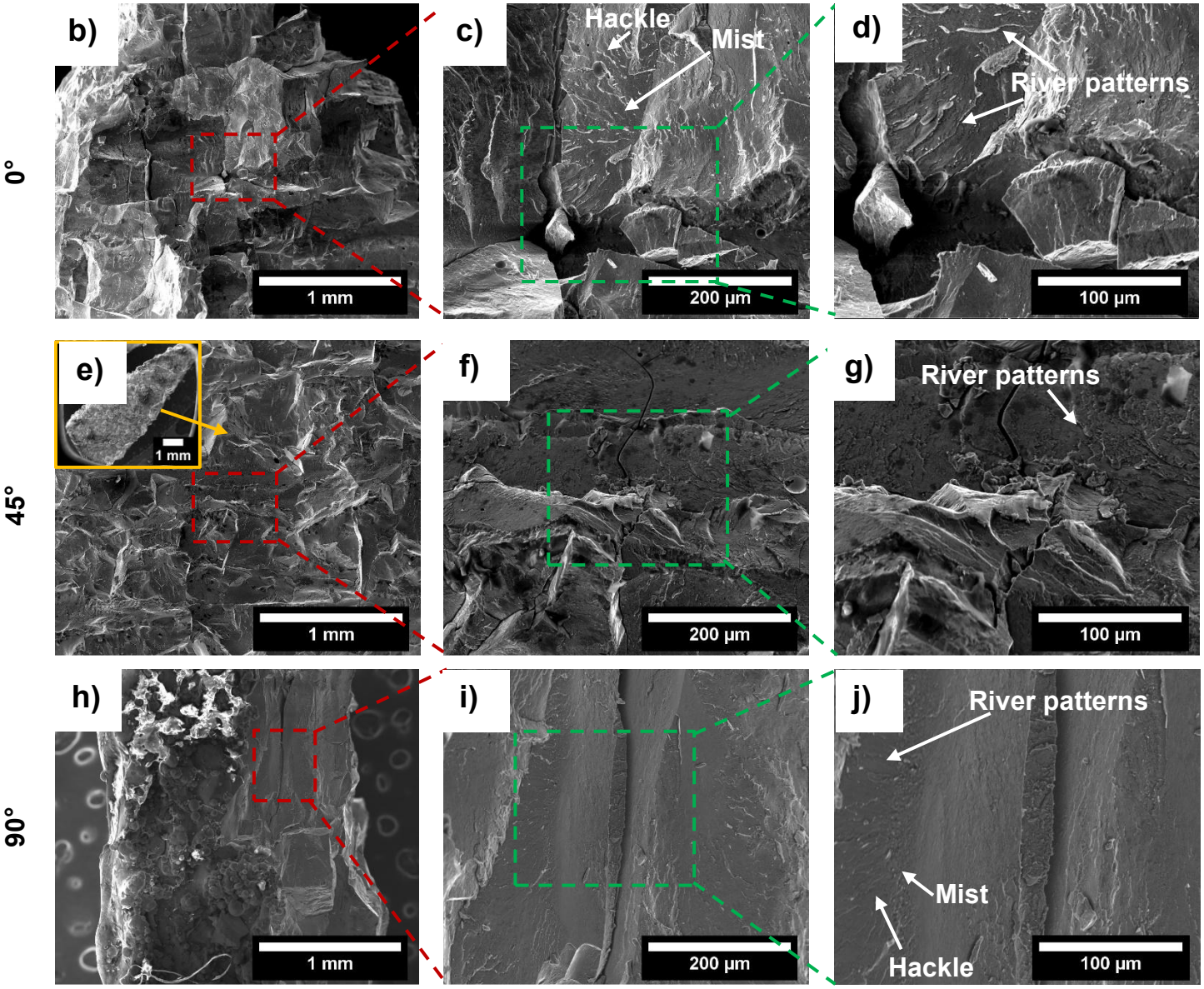

Figure 4.47- a) Visual appearance of representatives LPBF samples built at 0°, 45°, and 90° after compression testing, along with schematic illustrations of their corresponding fracture behavior. SEM micrographs of fracture surface of LPBF samples built at: **b)-d)** 0°; **e)-g)** 45°, and **h)-j)** 90° with respect to the build Z-axis.

4.4.2.4. Wear resistance

V5 and V6 LPBF samples produced using 80 W_600 mm/s at 0°, 45°, and 90°, with both SN and chessboard laser strategies, were subjected to wear tests. **Figure 4.48a)** shows a representative optical microscopy (OM) image of the initial

sample surfaces where the tests were performed. **Figure 4.48b)** and **c)** depict the average curves of the coefficient of friction (COF) as a function of sliding distance for V5 and V6 samples, respectively. As shown, all curves exhibit a rapid increase to a certain value at the running-in stage, after which the friction relatively stabilizes due to improved surface roughness and the formation of a tribolayer that provides lubrication effect as the sliding distance increases.

It is noteworthy that fluctuations in the COF during the running-in stage are mainly attributed to the inhomogeneous microstructure of the composite [242], while in the stable wear stage, COF variations are caused by changes in the contact area and the periodic formation of wear debris on the worn surface [243].

Table 4.15 presents the volume loss, Vickers microhardness, specific wear rate, and average COF for each sample. Except for the V5 LPBF_45° sample, all LPBF samples exhibited lower COF values compared to the ingot samples, indicating that the presence of defects (e.g., pores and cracks) in the LPBF samples did not significantly influence the COF values, or, at least it was not apparent. When comparing V5 and V6 samples, V6 exhibited lower COF values overall. A decreasing trend in COF was observed in the order: ingot > 0° > 0°_chess > 45° > 90°, suggesting that increasing the printing angle significantly reduces the COF.

For the V6 alloy, the SN_90° sample exhibited the lowest COF value of 0.032 ± 0.007. In contrast, the V5 alloy showed its lowest COF (0.075 ± 0.040) for the 0°_chess sample, without a clear overall trend. Regarding the specific wear rate (k) (used to evaluate the wear resistance), the ingot samples showed the lowest values (in the order of 10^{-8} mm^3/Nm), while LPBF samples exhibited k values ranging from 10^{-7} to 10^{-6} mm^3/Nm.

Despite minor variations, the mean microhardness values across samples were relatively similar when accounting for standard deviation. Although literature generally suggests that higher hardness correlates with lower COF and improved wear resistance [244], the wear results in this study cannot be directly explained by hardness alone, as is commonly done [245]. Here, despite similar hardness, ingot samples had higher COF and lower k values. Among LPBF samples, a general trend of lower COF correlating with lower k was observed. Interestingly,

the V5 LPBF_45° sample, which had the highest COF (0.355 ± 0.054), also presented the lowest k (3.0 × 10^{-7} mm³/N·m) among the LPBF group, suggesting the need for further investigation into the wear mechanisms of these alloys.

Comparing these results with the only comparable study available [246], the combination of low COF and low k values observed here remains impressive. While Zou et al.[246], reported COF = 0.389 and k = 4.74 × 10^{-6} mm^3/Nm for an ex-situ additively manufactured $Fe_{44}Cr_{30}Mo_{30}C_3B_3$(wt%) / Cu bulk metallic glass composite under a 20 N load, the present work achieved COF = 0.075 and k = 7.5 ×10^{-7} mm^3/Nm for the V5 alloy, and COF = 0.032 with k = 1.4 ×10^{-6} mm^3/Nm for the V6 alloy, both under a 25 N load.

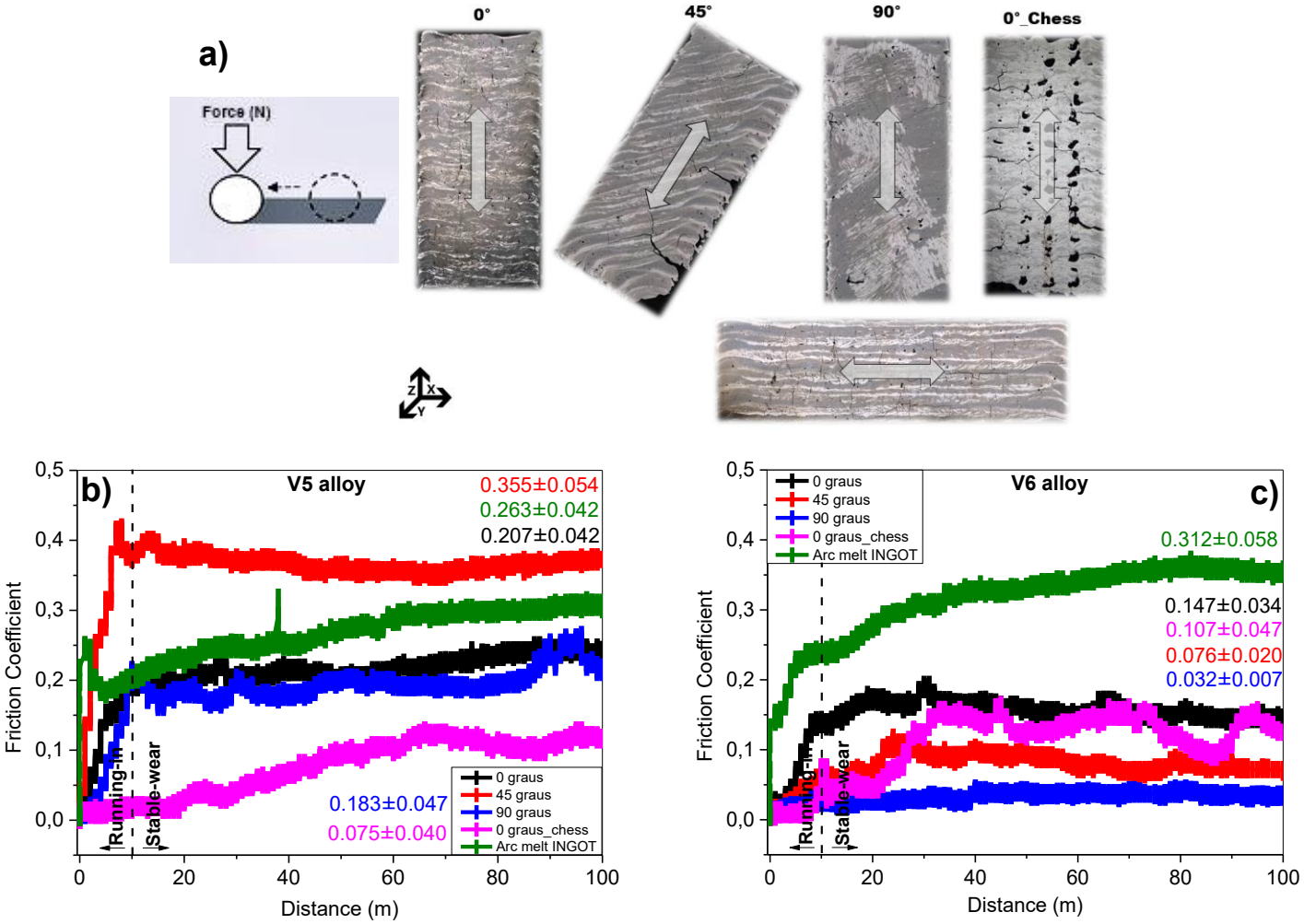

Figure 4.48- a) Schematic illustration of the sliding process and surface orientation during the wear testing for LPBF samples built at 0°, 45°, and 90° with

respect to the Z-axis. Representative (average) friction coefficient (COF) curves as a function of sliding distance (m) for: **b)** V5 alloy, and **c)** V6 alloy.

Table 4.15- Volume loss, Vickers hardness, specific wear rate, and coefficient of friction of the selected LPBF samples of V5 and V6 alloys.

Alloy	Sample name	Volume loss (mm^3)	$HV_{0.5}$	k (mm^3/ Nm)	COF
V5	**Arc melter ingot**	0.00005	1017±31	2.0×10^{-8}	0.263±0.042
	80_600_SN_0°	0.0061	970±51	2.4×10^{-6}	0.207±0.042
	80_600_SN_45°	0.0007	1012±54	3.0×10^{-7}	0.355±0.054
	80_600_SN_90°	0.0075	1001±79	3.0×10^{-6}	0.183±0.047
	80_600_chess_0°	0.0019	1016±64	7.5×10^{-7}	0.075±0.040
V6	**Arc melter ingot**	0.0002	1012±44	7.3×10^{-8}	0.312±0.058
	80_600_SN_0°	0.0100	1035±48	4.0×10^{-6}	0.147±0.034
	80_600_SN_45°	0.0068	988±51	2.7×10^{-6}	0.076±0.020
	80_600_SN_90°	0.0036	1029±44	1.4×10^{-6}	0.032±0.007
	80_600_chess_0°	0.0054	1024±57	2.2×10^{-6}	0.107±0.047

Figure 4.49 presents OM images showing the general aspects of the worn surfaces of V5 and V6 samples. From these images, it is evident that the LPBF samples exhibit more debris compared to the ingot samples. Although the presence of defects did not significantly affect the coefficient of friction (COF), they likely influenced the wear rate (k), particularly in the case of cracks, which are clearly visible in the LPBF samples (**Figure 4.49**). As reported in the literature, defects such as pores and cracks can alter the stress distribution, promote crack initiation, and work as channels for oxygen atom diffusion [247],[248], ultimately leading to embrittlement, fracture, and preferential material removal in those regions [249].

Furthermore, the increased presence of third bodies (debris) can modify the wear track morphology and increase wear severity during sliding, thereby increasing the wear rate (k) [250]. According to the literature, the width of the worn track—representing the effective contact area between the counter-body pin—can be reflected on the COF values [251]. Generally, lower COF is expected to be associated with reduced frictional force between surfaces, which can result in lower wear and, consequently, narrower and shallower worn tracks. In this study, considering the LPBF samples, the V5_45° sample exhibited the narrowest worn track width (537 ± 98 µm), yet showed the highest COF. In contrast, the V6_90° sample had the smallest track width (423 ± 45 µm) and the lowest COF. This indicates that the relationship between COF and worn track width is not always straightforward, as other factors—such as the dominant wear mechanisms—also influence the wear behavior. However, it is noteworthy that the two LPBF samples with the narrowest track widths (V5_45° and V6_90°) also had the lowest wear rates (k), suggesting that in this study, worn track width correlates more closely with wear rate than with COF.

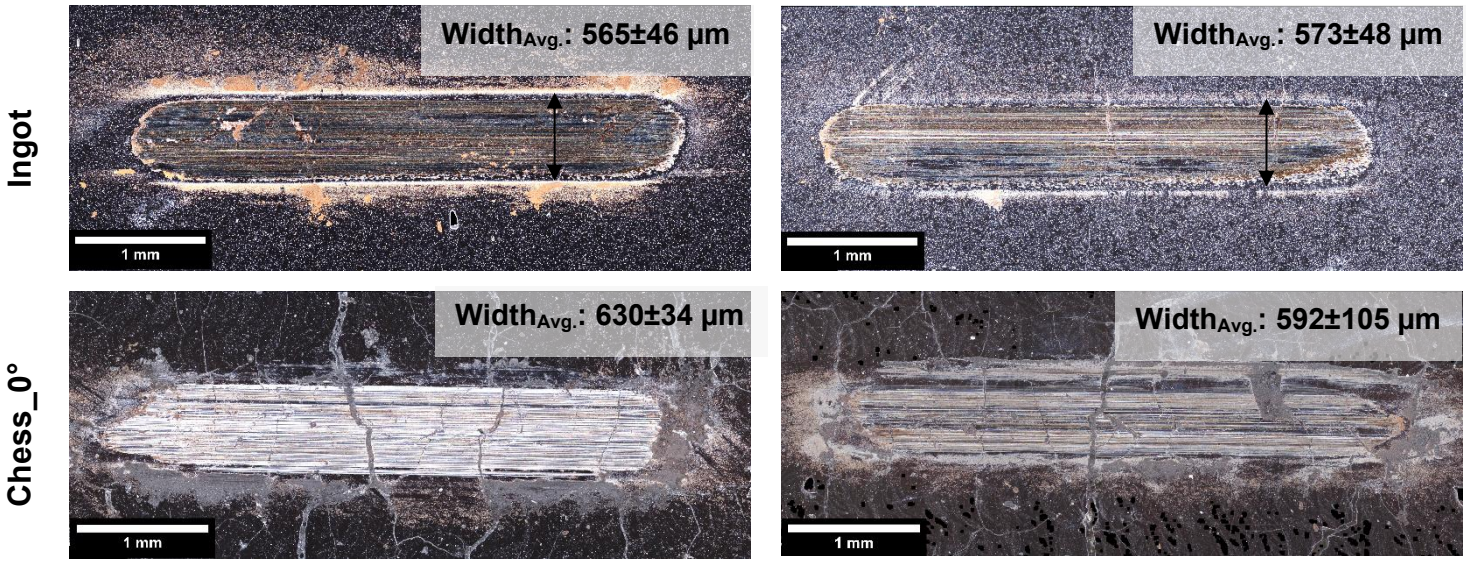

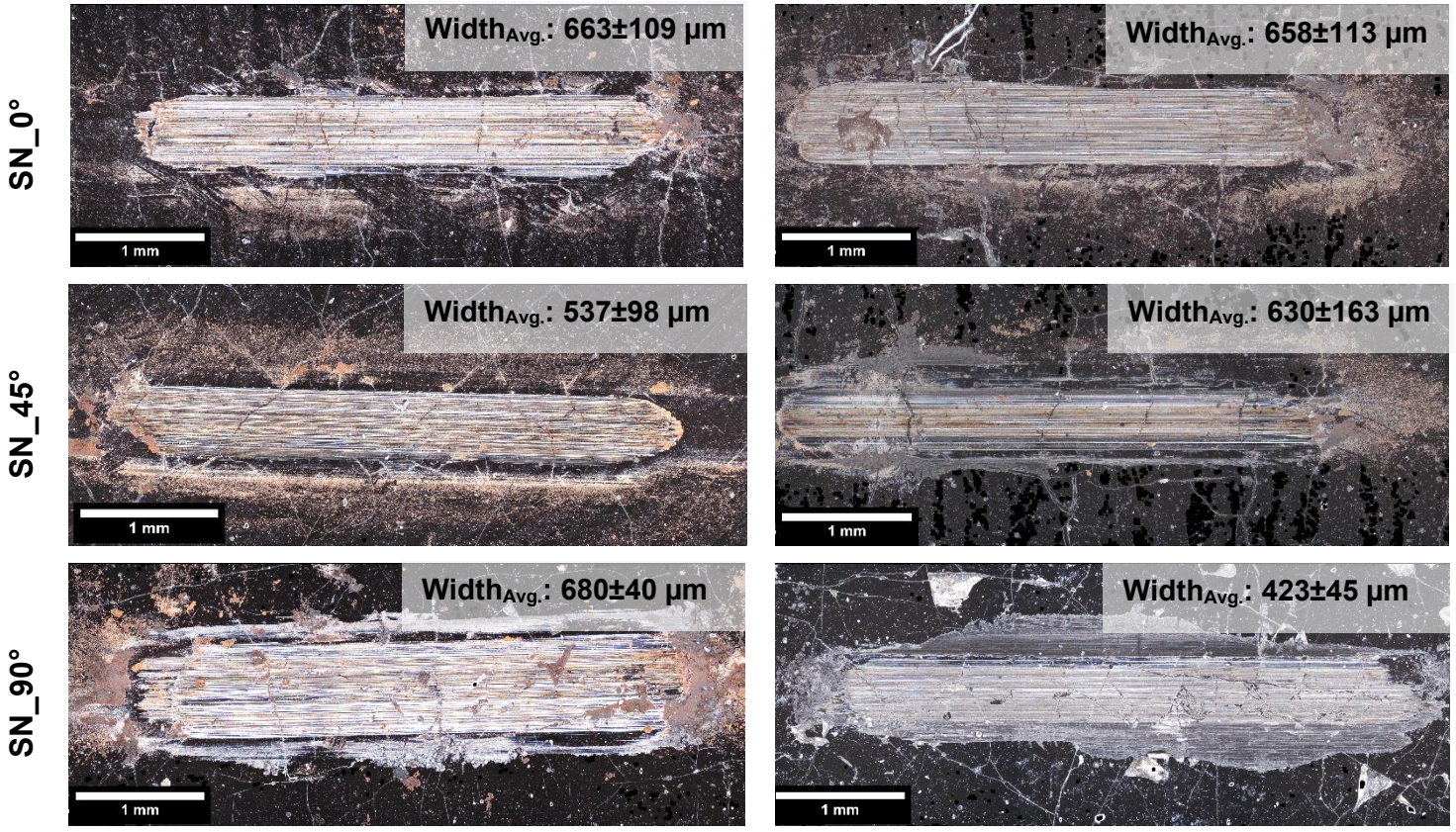

Figure 4.49- Optical microscopic images of the worn tracks of the ingots and LPBF samples built with 80W_600mm/s at 0°, 45° and 90° using SN laser strategy, and 0° using chessboard (chess) laser strategy: **a)** V5 alloy, and **b)** V6 alloy.

To address and discuss the wear mechanisms, the worn surfaces of the tested samples were examined using SEM. Due to the similarities observed between the worn surfaces of V5 and V6 samples, only the images of V6 are presented in **Figure 4.50a)-o)**. For all samples, the central region of the worn track was selected for comparison. The SEM images reveal that the primary wear mechanism was abrasive wear, as evidenced by the presence of grooves and abrasive debris (**Figure 4.50**). The severity of abrasive wear is indicated by the number and depth of grooves, while the presence of debris distinguishes between two-body and three-body abrasion [252].

The ingot sample exhibited mild abrasive wear, characterized by shallow

grooves and the absence of loose abrasive particles. This suggests direct contact between the sample surface and the Al pin, with minimal debris formation. In contrast, the LPBF samples showed numerous, deeper grooves and abundant loose debris, confirming a three-body abrasion mechanism type. The presence of hard debris can intensify the abrasive wear by producing deeper grooves [250].

Abrasive wear is primarily influenced by surface hardness and condition. However, as shown in **Table 4.15**, the samples exhibited similar microhardness values. In contrast, **Figure 4.49** shows that the LPBF samples contained numerous cracks on their initial surfaces. These pre-existing defects likely played a significant role in the observed abrasive wear, making the LPBF samples more susceptible to material removal. Therefore, the presence of such defects increased the severity of abrasive wear compared to that of the ingot sample. The absence of surface defects in the ingot sample contributed to its specific wear rate being one-two orders of magnitude lower than that of the LPBF samples (**Table 4.15**).

Notably, the exceptionally low specific wear rate of the ingot sample can also be attributed to the presence of light-gray round phases in its microstructure (**Figure 4.50c)**). These phases were identified by EDS as molybdenum borides, most likely $Mo_{23}B_6$, as supported by XRD analysis (**Figure 4.12**). These hard, refined, and homogeneously dispersed borides likely acted as reinforcements within the matrix. According to the literature [251],[253], the presence of rigid borides within the microstructure acts protecting the matrix from excessive material removal, thereby reducing the specific wear rate and improving wear resistance. This suggests that, in this study, wear resistance is more closely related to microstructural features than to microhardness alone.

Additionally, across all samples, no clear signs of plastic deformation were observed on the worn surfaces. However, the presence of oxidized debris suggests that oxidative wear also contributed to the wear mechanisms. The oxides were chemically analyzed by EDX, with results shown in **Figure 4.50p)** and **q)**. The oxide on the ingot sample was found to be mainly Fe-rich (63.20 ± 5.36 at. %), indicating iron oxide formation (**Figure 4.50p)**). In contrast, the oxide on the LPBF sample SN_0° was Fe-rich (47.74 ± 6.58 at. %) and

significantly enriched in carbon (27.59 ± 6.44 at. %) (**Figure 4.50q)**). Although it was not possible to confirm the exact carbonaceous compound formed, the presence of a C-rich oxide tribolayer is inferred to have provided a lubricating effect during sliding, contributing to the lower COF values observed for the LPBF samples. This finding aligns with previous studies [254],[255],[256],[257], which have shown that the friction coefficient values are influenced by the nature of oxides formed during wear.

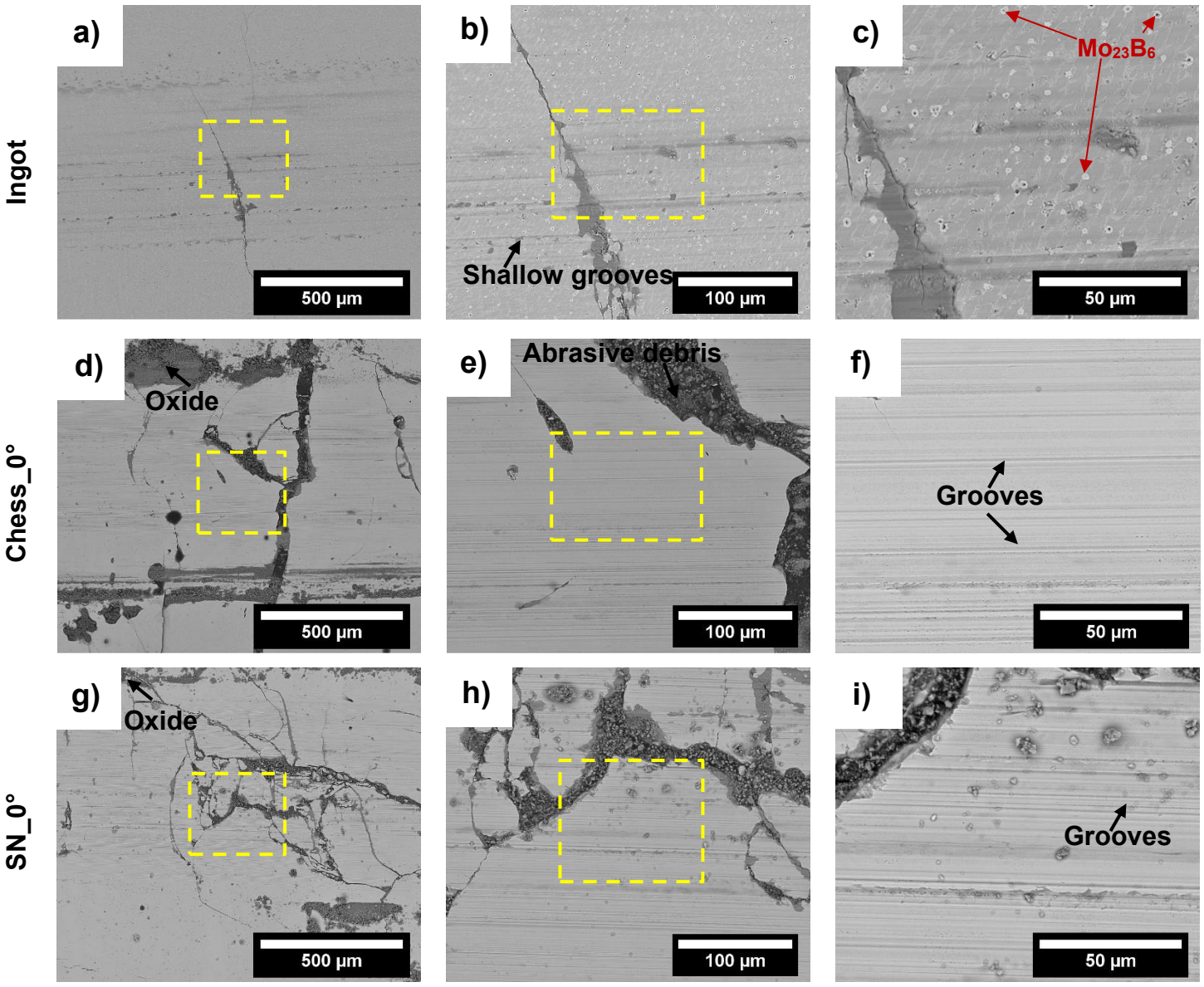

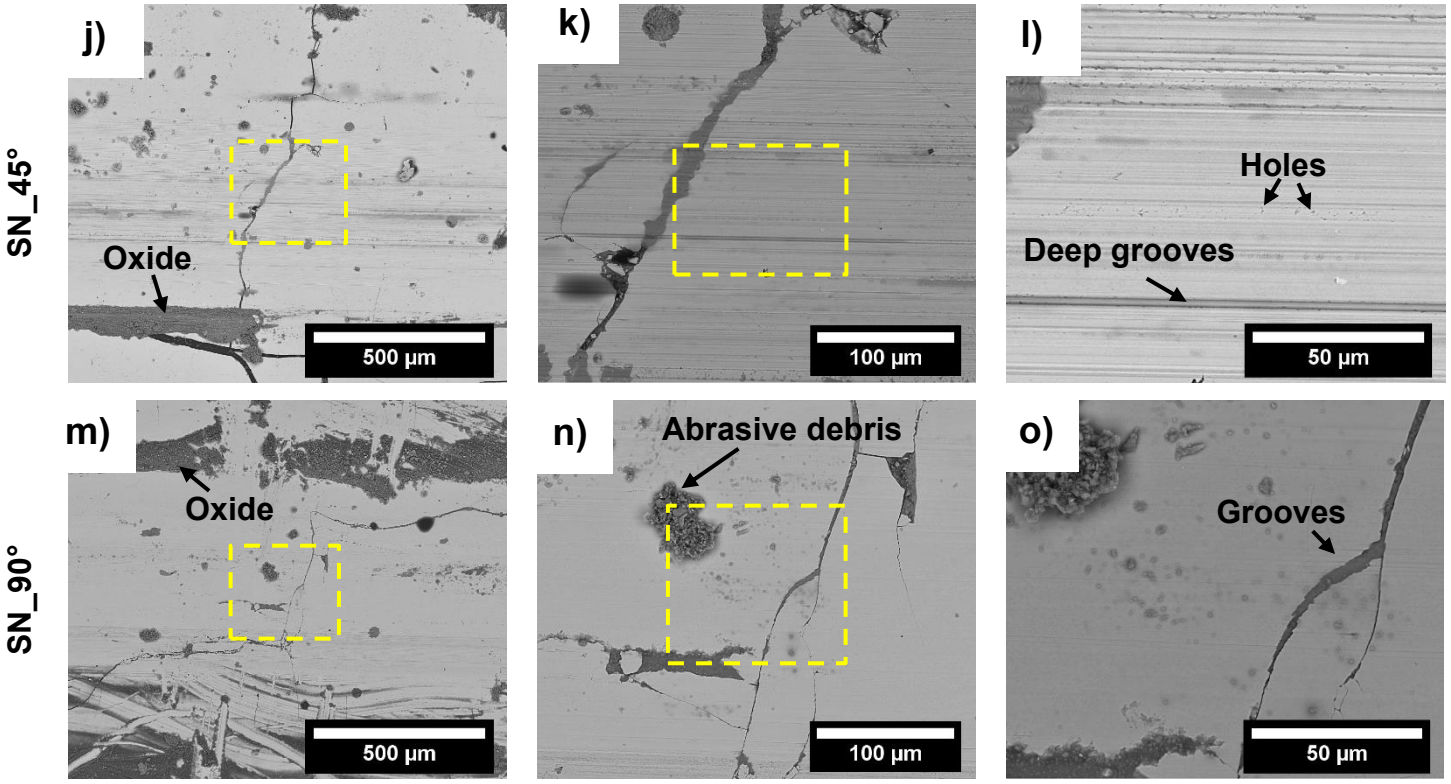

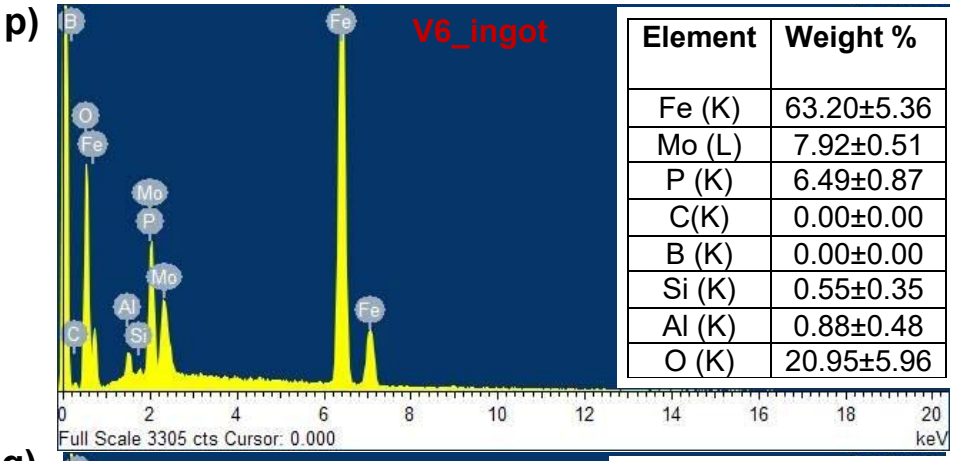

Element	Weight %
Fe (K)	63.20±5.36
Mo (L)	7.92±0.51
P (K)	6.49±0.87
C(K)	0.00±0.00
B (K)	0.00±0.00
Si (K)	0.55±0.35
Al (K)	0.88±0.48
O (K)	20.95±5.96

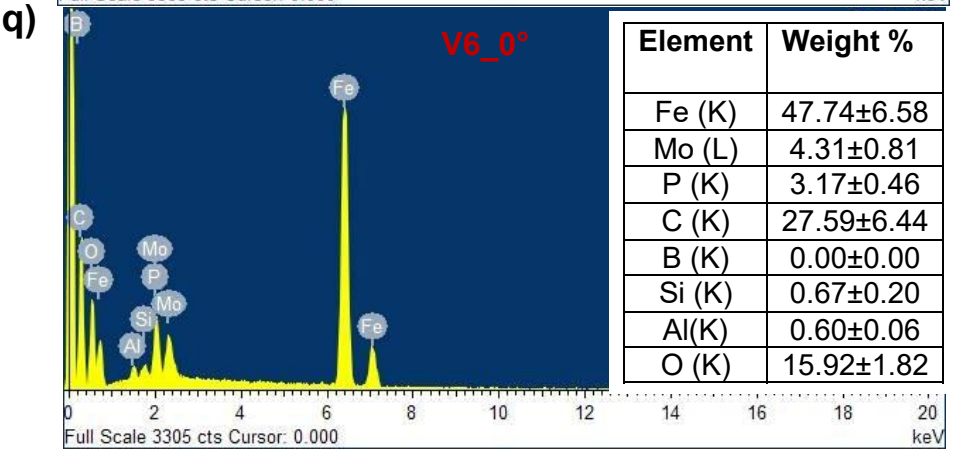

Element	Weight %
Fe (K)	47.74±6.58
Mo (L)	4.31±0.81
P (K)	3.17±0.46
C (K)	27.59±6.44
B (K)	0.00±0.00
Si (K)	0.67±0.20
Al(K)	0.60±0.06
O (K)	15.92±1.82

Figure 4.50- SEM micrographs of the worn surfaces of the V6 alloy as **a), b), c)** ingot, and LPBF 80W_600mm/s **d), e), f)** Chess built at 0°, **g), h), i)** SN built at

0°, **j), k), l)** SN built at 45°, **m), n), o)** SN built at 90°, and EDX results (in wt.%) of the oxides for: **p)** ingot and **q)** SN built at 0°.

5 CONCLUSION

The aim of this work was first to select and design, using theoretical and experimental methods, Fe-based alloys suitable for additive manufacturing. The selected FeMoPCB alloys were then investigated for their feasibility of processing via Laser Powder Bed Fusion (LPBF) additive manufacturing. With that goal, simple geometry specimens (toroidal, cylinders, cubes, parallelepiped) were produced using a wide range of processing parameters, including laser power (90W-330 W), scan speed (100-3000 mm/s), hatching distance (30, 40 and 50 µm), layer thickness (50, 70, 90 and 100 µm), laser scan strategy (single-unidirectional and chessboard/island), substrate (CK45 carbon and 316L steel, unheated and preheated to 150±20°C), with and without remelting step. The processing parameters were optimized to obtain intact samples containing the glassy phase. The best LPBF samples were selected, and their processing conditions were correlated with microstructure, mechanical, and wear behavior. The following conclusions can be drawn from the present study:

1- Six FeMoPCB alloy compositions with predicted good GFA and toughness were selected using the alloy design methodology. Experimental results from arc melting and suction casting confirmed glassy phase formation in all six compositions. Among them, $Fe_{79}Mo_3P_9C_{7.5}B_{1.5}$ (named as V5) and $Fe_{77}Mo_5P_9C_{7.5}B_{1.5}$ (at. %) (named as V6) were chosen for processing by LPBF.

2- The gas-atomized V5 and V6 powders exhibited excellent flowability and spreadability, particularly after the drying step, making them suitable for LPBF processing.

3- FeMoPCBSi LPBF samples were successfully manufactured with good dimensional accuracy within an optimized processing window, including laser powers ranging from 50 to 80 W and scan speeds between 100 and 700 mm/s.

4- Both porosity and glassy phase content increased under conditions of low laser power (P) and high scan speed (V). Within the explored parameters range, pore and crack area fractions as low as 1% and glassy phase fractions as high as 24% were achieved; however, these extremes did not

occur simultaneously. For achieving high density (i.e., pore and crack area fraction below 2%), the parameter combinations 70_400_SN, 60_100–300_SN, and 60_100_Chess were effective. In contrast, high glassy phase fractions (~20%) were obtained using the 80_600_Chess, 60_400–500_Chess, and 60_500_SN combinations.

5- The integrity, porosity and dimensional accuracy of the samples were more influenced by the specific combination of parameters than by the energy input alone. For example, under the same energy input (100 J/mm³), different parameter combinations yielded varying results:
    - 210 W / 700 mm/s: super-elevation phenomenon, ~5% porous area
    - 105 W / 350 mm/s: mostly flat surface, ~2% porous area
    - 90 W / 300 mm/s: flat surface, excellent dimensional accuracy, ~1% porous area
6- The glassy phase content depends on the energy input used to produce the samples. The content increases with decreasing energy input and vice versa.
7- Under the same parameter combinations, i.e., same energy input, increasing the build angle showed a slight tendency to increase glassy phase formation.
8- Even though the plasticity of the LPBF-processed FeMoPCBSi was not enhanced compared to their casted counterparts, FeMoPCBSi bulk metallic glass composites (BMGCs) as higher as 11mm were produced with great dimensional accuracy by LPBF using commercial and recycled iron as the raw materials.
9- The microstructure of the melt pool (MP) region was found to be formed by ultrafine, equiaxed grains, of $Fe_{0.75}$ $Mo_{0.122}$ $C_{0.128}$ (bcc) phase embedded in a glassy matrix, while the heat-affected-zone (HAZ) was formed by a mix of phases, including Fe(Si)-α (bcc), B_{50}-$Fe_{1.04}$ ((tetragonal), and $Fe_{0.75}$ $Mo_{0.122}$ $C_{0.128}$ (bcc) phase.
10- While the type of constituent phases (crystalline and glassy) remained unchanged across different parameter combinations, their relative fractions were dependent on the processing parameters.

11- To increase glassy phase content, low energy input is required. However, achieving high bulk density necessitates higher energy input, highlighting the inherent trade-off and difficulty in producing crack- and pore-free (intact) parts with high glass content.

12- The FeMoPCBSi BMGCs produced via LPBF in this study demonstrated excellent wear resistance:

- V5: COF = 0.075, $k = 7.5 \times 10^{-7}$ mm^3/Nm
- V6: COF = 0.032, $k = 1.4 \times 10^{-6}$ mm^3/Nm

6 RECOMMENDATIONS FOR FUTURE WORKS

- Fabricate LPBF FeMoPCBSi samples with the highest possible glassy phase content, followed by the application of porosity- and crack-reducing techniques such as Ultra-High-Pressure (UHP) processing and Hot Isostatic Pressing (HIP).
- Perform heat treatments and investigate the resulting microstructural evolution in correlation with wear resistance.
- Evaluate whether fabricating parts with honeycomb structures using the studied alloys can enhance glassy phase formation.
- Investigate the corrosion resistance of the new BMGCs fabricated by LPBF.
- Investigate the magnetic properties of the new BMGCs fabricated by LPBF.
- To improve the ductility and toughness of LPBF-processed FeMoPCBSi samples while reducing cracking, mixing 316L powder with FeMoPCBSi powder and performing the LPBF process using this mixture may be a promising strategy.
- In this work, it was observed that cylindrical samples exhibited more cracking than square samples, suggesting that it would be worthwhile to investigate the influence of sample geometry on FeMoPCBSi processed by LPBF.

7 REFERENCES

[1] M. F. Ashby and A. L. Greer, “Metallic glasses as structural materials,” *Scr Mater*, vol. 54, no. 3, pp. 321–326, Feb. 2006, doi: 10.1016/j.scriptamat.2005.09.051.

[2] J. J. Kruzic, “Bulk Metallic Glasses as Structural Materials: A Review,” *Adv Eng Mater*, vol. 18, no. 8, pp. 1308–1331, 2016, doi: 10.1002/adem.201600066.

[3] W. Klement, R. H. Willens, and P. O. L. Duwez, “Non-crystalline Structure in Solidified Gold–Silicon Alloys,” *Nature*, vol. 187, no. 4740, pp. 869–870, 1960, doi: 10.1038/187869b0.

[4] C. Suryanarayana and A. Inoue, *Bulk Metallic Glasses*, Second Edi. New York, NY: Taylor & Francis Group, LLC, 2018.

[5] A. Peker and W. L. Johnson, “A highly processable metallic glass: Zr41.2Ti13.8Cu12.5Ni10.0Be22.5,” *Appl Phys Lett*, vol. 63, no. 17, pp. 2342–2344, 1993, doi: 10.1063/1.110520.

[6] H. W. Kui, A. L. Greer, and D. Turnbull, “Formation of bulk metallic glass by fluxing,” *Appl Phys Lett*, vol. 45, no. 6, pp. 615–616, 1984, doi: 10.1063/1.95330.

[7] H. S. Chen, “Glassy metals,” *Reports on Progress in Physics*, vol. 43, no. 4, pp. 353–432, 1980, doi: 10.1088/0034-4885/43/4/001.

[8] A. Inoue and N. Nishiyama, “Extremely low critical cooling rates of new Pd-Cu-P base amorphous alloys,” *MATERIALS SCIENCE & ENGINEERING A*, vol. 226, pp. 401–405, 1997.

[9] W. Yang *et al.*, “Fluxing induced boron alloying in Fe-based bulk metallic glasses,” *Mater Des*, vol. 129, no. January, pp. 63–68, 2017, doi: 10.1016/j.matdes.2017.05.020.

[10] D. Turnbull, “Under What Conditions Can A Glass Be Formed?,” *Contemp Phys*, vol. 10, no. 5, pp. 473–488, 1969, doi: 10.1080/00107516908204405.

[11] S. Ueno and Y. Waseda, “Evaluation of the optimum solute concentration for good glass formability in multi-component alloys,” *Journal of Materials Engineering*, vol. 9, no. 2, pp. 199–204, 1987, doi: 10.1007/BF02833711.

[12] T. Egami and Y. Waseda, “Atomic size effect on the formability of metallic glasses,” *J Non Cryst Solids*, vol. 64, no. 1, pp. 113–134, 1984, doi: https://doi.org/10.1016/0022-3093(84)90210-2.

[13] W. J. Botta, F. S. Pereira, C. Bolfarini, C. S. Kiminami, and M. F. de Oliveira, “Topological instability and electronegativity effects on the glass-forming ability of metallic alloys,” *Philos Mag Lett*, vol. 88, no. 11, pp. 785–791, 2008, doi: 10.1080/09500830802375622.

[14] M. de Oliveira, “A simple criterion to predict the glass forming ability of metallic alloys,” *J Appl Phys*, vol. 111, no. 2, p. 23509, 2012, doi: 10.1063/1.3676196.

[15] M. F. de Oliveira, “A new correlation between electronic parameters and glass forming ability of metallic alloys,” *Philos Mag Lett*, vol. 91, no. 6, pp. 418–422, 2011, doi: 10.1080/09500839.2011.579078.

[16] H. S. Chen, “Thermodynamic considerations on the formation and stability of metallic glasses,” *Acta Metallurgica*, vol. 22, no. 12, pp. 1505–1511, Dec. 1974, doi: 10.1016/0001-6160(74)90112-6.

[17] A. L. Greer and E. Ma, “Bulk Metallic Glasses: At the Cutting Edge of Metals Research,” *MRS Bull*, vol. 32, no. 8, pp. 611–619, Aug. 2007, doi: 10.1557/mrs2007.121.

[18] A. Inoue, “Stabilization of metallic supercooled liquid and bulk amorphous alloys,” *Acta Mater*, vol. 48, no. 1, pp. 279–306, Jan. 2000, doi: 10.1016/S1359-6454(99)00300-6.

[19] J. Z. Jiang, D. Hofmann, D. J. Jarvis, and H. J. Fecht, “Low-density high-strength bulk metallic glasses and their composites: A review,” *Adv Eng Mater*, vol. 17, no. 6, pp. 761–780, 2015, doi: 10.1002/adem.201400252.

[20] C. A. Schuh, T. C. Hufnagel, and U. Ramamurty, “Mechanical behavior of amorphous alloys,” *Acta Mater*, vol. 55, no. 12, pp. 4067–4109, Jul. 2007, doi: 10.1016/j.actamat.2007.01.052.

[21] D. Singh, R. K. Mandal, R. adhey Tiwari, and O. N. Srivastava, “Mechanical Behavior of Zr-Based Metallic Glasses and Their Nanocomposites,” 2016, pp. 109–132. doi: 10.5772/64221.

[22] G. N. Yang *et al.*, “Serration behaviours in metallic glasses with different

plasticity," *Philosophical Magazine*, vol. 96, no. 21, pp. 2243–2255, 2016, doi: 10.1080/14786435.2016.1197434.

[23] B. Sarac *et al.*, "Origin of large plasticity and multiscale effects in iron-based metallic glasses," *Nat Commun*, vol. 9, no. 1333, pp. 1–10, 2018, doi: 10.1038/s41467-018-03744-5.

[24] A. L. Greer, Y. Q. Cheng, and E. Ma, "Shear bands in metallic glasses," *Materials Science and Engineering R: Reports*, vol. 74, no. 4, pp. 71–132, Apr. 2013, doi: 10.1016/j.mser.2013.04.001.

[25] E. Ma, "Tuning order in disorder Spectrum of atomic-packing motifs," 2015. doi: 10.1038/nmat4300.

[26] D. Pan, A. Inoue, T. Sakurai, and M. W. Chen, "Experimental characterization of shear transformation zones for plastic flow of bulk metallic glasses," *Proc Natl Acad Sci U S A*, vol. 105, no. 39, pp. 14769–14772, 2008, doi: 10.1073/pnas.0806051105.

[27] A. S. Argon, "Plastic deformation in metallic glasses," *Acta Metallurgica*, vol. 27, no. 1, pp. 47–58, Jan. 1979, doi: 10.1016/0001-6160(79)90055-5.

[28] C. A. Schuh and A. C. Lund, "Atomistic basis for the plastic yield criterion of metallic glass," *Nat Mater*, vol. 2, no. 7, pp. 449–452, 2003, doi: 10.1038/nmat918.

[29] A. S. Argon and L. T. Shi, "Development of visco-plastic deformation in metallic glasses," *Acta Metallurgica*, vol. 31, no. 4, pp. 499–507, Apr. 1983, doi: 10.1016/0001-6160(83)90038-X.

[30] A. S. Argon and H. Y. Kuo, "Plastic flow in a disordered bubble raft (an analog of a metallic glass)," *Materials Science and Engineering*, vol. 39, no. 1, pp. 101–109, Jul. 1979, doi: 10.1016/0025-5416(79)90174-5.

[31] M. L. Falk and J. S. Langer, "Dynamics of viscoplastic deformation in amorphous solids," *Phys. Rev. E*, vol. 57, no. 6, pp. 7192–7205, Jun. 1998, doi: 10.1103/PhysRevE.57.7192.

[32] D. Şopu, A. Stukowski, M. Stoica, and S. Scudino, "Atomic-Level Processes of Shear Band Nucleation in Metallic Glasses," *Phys Rev Lett*, vol. 119, no. 19, p. 195503, Nov. 2017, doi: 10.1103/PhysRevLett.119.195503.

[33] Y. Chen, M. Q. Jiang, Y. J. Wei, and L. H. Dai, “Failure criterion for metallic glasses,” *Philosophical Magazine*, vol. 91, no. 36, pp. 4536–4554, 2011, doi: 10.1080/14786435.2011.613859.

[34] W. (汪卫华) Hua Wang, “Properties inheritance in metallic glasses,” *J Appl Phys*, vol. 111, no. 12, p. 123519, 2012, doi: 10.1063/1.4730441.

[35] J. Das, W. Löser, U. Kühn, J. Eckert, S. K. Roy, and L. Schultz, “High-strength Zr-Nb-(Cu,Ni,Al) composites with enhanced plasticity,” *Appl Phys Lett*, vol. 82, no. 26, pp. 4690–4692, 2003, doi: 10.1063/1.1587254.

[36] C. C. Hays, C. P. Kim, and W. L. Johnson, “Microstructure controlled shear band pattern formation and enhanced plasticity of bulk metallic glasses containing in situ formed ductile phase dendrite dispersions,” *Phys Rev Lett*, vol. 84, no. 13, pp. 2901–2904, Mar. 2000, doi: 10.1103/PhysRevLett.84.2901.

[37] J. Eckert, J. Das, S. Pouly, and C. Duhamel, “Processing routes/ microstructure and mechanical properties of metallic glasses and their composites,” *Adv Eng Mater*, vol. 9, no. 6, pp. 443–453, 2007, doi: 10.1002/adem.200700043.

[38] U. Kühn, J. Eckert, N. Mattern, and L. Schultz, “ZrNbCuNiAl bulk metallic glass matrix composites containing dendritic bcc phase precipitates,” *Appl Phys Lett*, vol. 80, no. 14, pp. 2478–2480, 2002, doi: 10.1063/1.1467707.

[39] K. Kosiba, D. Şopu, S. Scudino, L. Zhang, J. Bednarcik, and S. Pauly, “Modulating heterogeneity and plasticity in bulk metallic glasses: Role of interfaces on shear banding,” *Int J Plast*, vol. 119, pp. 156–170, Aug. 2019, doi: 10.1016/j.ijplas.2019.03.007.

[40] P. Gargarella *et al.*, “Ti-Cu-Ni shape memory bulk metallic glass composites,” *Acta Mater*, vol. 61, no. 1, pp. 151–162, Jan. 2013, doi: 10.1016/j.actamat.2012.09.042.

[41] Z. Y. Zhang *et al.*, “Effects of Sn addition on phase formation and mechanical properties of TiCu-based bulk metallic glass composites,” *Intermetallics (Barking)*, vol. 42, pp. 68–76, 2013, doi: 10.1016/j.intermet.2013.05.009.

[42] F. Szuecs, C. P. Kim, and W. L. Johnson, “Mechanical properties of

Zr56.2Ti13.8Nb5.0Cu6.9 Ni5.6Be12.5 ductile phase reinforced bulk metallic glass composite," *Acta Mater*, vol. 49, no. 9, pp. 1507–1513, 2001, doi: 10.1016/S1359-6454(01)00068-4.

[43] A. Inoue, "Mechanical properties of Zr-based bulk glassy alloys containing nanoscale compound particles," *Intermetallics (Barking)*, vol. 8, no. 5–6, pp. 455–468, 2000, doi: 10.1016/s0966-9795(99)00150-8.

[44] M. Ferry *et al.*, "Recent developments in ductile bulk metallic glass composites," *MRS Commun*, vol. 3, no. 1, pp. 1–12, 2013, doi: 10.1557/mrc.2012.32.

[45] D. C. Hofmann *et al.*, "Designing metallic glass matrix composites with high toughness and tensile ductility," *Nature*, vol. 451, no. 7182, pp. 1085–1089, 2008, doi: 10.1038/nature06598.

[46] K. Kosiba and S. Pauly, "Inductive flash-annealing of bulk metallic glasses," *Sci Rep*, vol. 7, no. 1, p. 2151, 2017, doi: 10.1038/s41598-017-02376-x.

[47] C. Fan and A. Inoue, "Ductility of bulk nanocrystalline composites and metallic glasses at room temperature," *Appl Phys Lett*, vol. 77, no. 1, pp. 46–48, 2000, doi: 10.1063/1.126872.

[48] A. Leonhard, L. Q. Xing, M. Heilmaier, A. Gebert, J. Eckert, and L. Schultz, "Effect of crystalline precipitations on the mechanical behavior of bulk glass forming Zr-based alloys," *Nanostructured Materials*, vol. 10, no. 5, pp. 805–817, Jul. 1998, doi: 10.1016/S0965-9773(98)00117-2.

[49] D. Wang, J. Mu, Q. Xie, H. Xu, Y. Wang, and H. Zhang, "A study of CuZr-based bulk metallic glass composite dispersed by in-situ Ta particles," *AIP Conf Proc*, vol. 1846, no. 1, p. 20004, 2017, doi: 10.1063/1.4983585.

[50] Y. L. Huang *et al.*, "Dendritic microstructure in the metallic glass matrix composite Zr 56Ti14Nb5Cu7Ni6Be 12," *Scr Mater*, vol. 53, no. 1, pp. 93–97, 2005, doi: 10.1016/j.scriptamat.2005.03.005.

[51] Z. Bian, H. Kato, C. Qin, W. Zhang, and A. Inoue, "Cu-Hf-Ti-Ag-Ta bulk metallic glass composites and their properties," *Acta Mater*, vol. 53, no. 7, pp. 2037–2048, 2005, doi: 10.1016/j.actamat.2005.01.015.

[52] G. Y. Sun, G. Chen, and G. L. Chen, "Comparison of microstructures and properties of Zr-based bulk metallic glass composites with dendritic and

spherical bcc phase precipitates," *Intermetallics (Barking)*, vol. 15, no. 5–6, pp. 632–634, 2007, doi: 10.1016/j.intermet.2006.10.026.

[53] M. L. Lee, Y. Li, and C. A. Schuh, "Effect of a controlled volume fraction of dendritic phases on tensile and compressive ductility in La-based metallic glass matrix composites," *Acta Mater*, vol. 52, no. 14, pp. 4121–4131, 2004, doi: 10.1016/j.actamat.2004.05.025.

[54] S. F. Guo, L. Liu, N. Li, and Y. Li, "Fe-based bulk metallic glass matrix composite with large plasticity," *Scr Mater*, vol. 62, no. 6, pp. 329–332, 2010, doi: 10.1016/j.scriptamat.2009.10.024.

[55] S. Guo and C. Su, "Micro/nano ductile-phases reinforced Fe-based bulk metallic glass matrix composite with large plasticity," *Materials Science and Engineering A*, vol. 707, pp. 44–50, 2017, doi: 10.1016/j.msea.2017.09.036.

[56] S. F. Guo, J. F. Wang, H. J. Zhang, and S. H. Xie, "Enhanced plasticity of Fe-based bulk metallic glass by tailoring microstructure," *Transactions of Nonferrous Metals Society of China (English Edition)*, vol. 22, no. 2, pp. 348–353, Feb. 2012, doi: 10.1016/S1003-6326(11)61182-5.

[57] P. Gargarella *et al.*, "Formation of Fe-based glassy matrix composite coatings by laser processing," *Surf Coat Technol*, vol. 240, pp. 336–343, Feb. 2014, doi: 10.1016/j.surfcoat.2013.12.049.

[58] A. Inoue, Y. Shinohara, and J. S. Gook, "Thermal and Magnetic Properties of Bulk Fe-Based Glassy Alloys Prepared by Copper Mold Casting," *Materials Transactions, JIM*, vol. 36, no. 12, pp. 1427–1433, 1995, doi: 10.2320/matertrans1989.36.1427.

[59] A. Inoue and A. Takeuchi, "Recent development and application products of bulk glassy alloys," *Acta Mater*, vol. 59, no. 6, pp. 2243–2267, 2011, doi: 10.1016/j.actamat.2010.11.027.

[60] A. Inoue *et al.*, "Development and application of Fe-based soft magnetic bulk metallic glassy inductors," *J Alloys Compd*, vol. 731, pp. 1303–1309, 2018, doi: 10.1016/j.jallcom.2017.08.240.

[61] S. F. Guo, J. L. Qiu, P. Yu, S. H. Xie, and W. Chen, "Fe-based bulk metallic glasses: Brittle or ductile?," *Appl Phys Lett*, vol. 105, no. 16, 2014, doi:

10.1063/1.4899124.

[62] Y. C. Li, C. Zhang, W. Xing, S. F. Guo, and L. Liu, “Design of Fe-Based Bulk Metallic Glasses with Improved Wear Resistance,” *ACS Appl Mater Interfaces*, vol. 10, no. 49, pp. 43144–43155, 2018, doi: 10.1021/acsami.8b11561.

[63] B. Shen, M. Akiba, and A. Inoue, “Effects of Si and Mo additions on glass-forming in FeGaPCB bulk glassy alloys with high saturation magnetization,” *Phys Rev B Condens Matter Mater Phys*, vol. 73, no. 10, p. 104204, Mar. 2006, doi: 10.1103/PhysRevB.73.104204.

[64] T. D. Shen and R. B. Schwarz, “Bulk ferromagnetic glasses prepared by flux melting and water quenching,” *Appl Phys Lett*, vol. 75, no. 1, pp. 49–51, 1999, doi: 10.1063/1.124273.

[65] F. Li, B. Shen, A. Makino, and A. Inoue, “Excellent soft-magnetic properties of (Fe,Co)-Mo-(P,C,B,Si) bulk glassy alloys with ductile deformation behavior,” *Appl Phys Lett*, vol. 91, no. 23, p. 234101, 2007, doi: 10.1063/1.2820608.

[66] M. Askari-Paykani, M. Nili Ahmadabadi, and A. Seiffodini, “The effect of liquid phase separation on the Vickers microindentation shear bands evolution in a Fe-based bulk metallic glass,” *Materials Science and Engineering A*, vol. 585, pp. 363–370, 2013, doi: 10.1016/j.msea.2013.07.045.

[67] A. Inoue, A. Makino, and T. Mizushima, “Ferromagnetic bulk glassy alloys,” 2000. doi: 10.1016/S0304-8853(00)00127-X.

[68] Q. Li, J. Li, P. Gong, K. Yao, J. Gao, and H. Li, “Formation of bulk magnetic ternary Fe 80P 13C 7 glassy alloy,” *Intermetallics (Barking)*, vol. 26, no. Complete, pp. 62–65, 2012, doi: 10.1016/j.intermet.2012.03.045.

[69] J. Wang, R. Li, N. Hua, L. Huang, and T. Zhang, “Ternary Fe-P-C bulk metallic glass with good soft-magnetic and mechanical properties,” *Scr Mater*, vol. 65, no. 6, pp. 536–539, 2011, doi: 10.1016/j.scriptamat.2011.06.020.

[70] M. Stoica, K. Hajlaoui, A. Lemoulec, and A. R. Yavari, “New ternary Fe-based bulk metallic glass with high boron content,” *Philos Mag Lett*, vol. 86,

no. 4, pp. 267–275, 2006, doi: 10.1080/09500830600696344.

[71] J. Chipman, “Thermodynamics and phase diagram of the Fe-C system,” *Metallurgical Transactions*, vol. 3, no. 1, pp. 55–64, 1972, doi: 10.1007/BF02680585.

[72] O. K. von Goldbeck, “Iron—Boron Fe—B,” in *IRON—Binary Phase Diagrams*, Berlin, Heidelberg: Springer Berlin Heidelberg, 1982, pp. 15–18. doi: 10.1007/978-3-662-08024-5_8.

[73] H. Okamoto, “The Fe-P (iron-phosphorus) system,” *Bulletin of Alloy Phase Diagrams*, vol. 11, no. 4, pp. 404–412, 1990, doi: 10.1007/BF02843320.

[74] Y. Wu, X. D. Hui, Z. P. Lu, Z. Y. Liu, L. Liang, and G. L. Chen, “Effects of metalloid elements on the glass-forming ability of Fe-based alloys,” *J Alloys Compd*, vol. 467, no. 1–2, pp. 187–190, 2009, doi: 10.1016/j.jallcom.2007.12.002.

[75] J. E. Gao *et al.*, “Fe-based bulk metallic glass composites without any metalloid elements,” *Acta Mater*, vol. 61, no. 9, pp. 3214–3223, 2013, doi: 10.1016/j.actamat.2013.02.009.

[76] K. F. Yao and C. Q. Zhang, “Fe-based bulk metallic glass with high plasticity,” *Appl Phys Lett*, vol. 90, no. 6, p. 61901, 2007, doi: 10.1063/1.2437722.

[77] X. Li, H. Kato, K. Yubuta, A. Makino, and A. Inoue, “Effect of Cu on nanocrystallization and plastic properties of FeSiBPCu bulk metallic glasses,” *Materials Science and Engineering A*, vol. 527, no. 10–11, pp. 2598–2602, Apr. 2010, doi: 10.1016/j.msea.2009.12.026.

[78] J. M. Park, D. H. Kim, and J. Eckert, “Enhanced plasticity of Fe-Nb-B-(Ni, Cu) bulk metallic glasses by controlling the heterogeneity and elastic constants,” *J Alloys Compd*, vol. 536, no. SUPPL.1, pp. 70–73, 2012, doi: 10.1016/j.jallcom.2011.10.026.

[79] X. J. Gu, A. G. McDermott, S. J. Poon, and G. J. Shiflet, “Critical Poisson’s ratio for plasticity in Fe-Mo-C-B-Ln bulk amorphous steel,” *Appl Phys Lett*, vol. 88, no. 21, p. 211905, 2006, doi: 10.1063/1.2206149.

[80] X. J. Gu, S. J. Poon, G. J. Shiflet, and M. Widom, “Ductility improvement of amorphous steels: Roles of shear modulus and electronic structure,” *Acta*

Mater, vol. 56, no. 1, pp. 88–94, 2008, doi: 10.1016/j.actamat.2007.09.011.

[81] J. J. Lewandowski, X. J. Gu, A. Shamimi Nouri, S. J. Poon, and G. J. Shiflet, “Tough Fe-based bulk metallic glasses,” *Appl Phys Lett*, vol. 92, no. 9, p. 91918, 2008, doi: 10.1063/1.2890489.

[82] M. E. McHenry, F. Johnson, H. Okumura, T. Ohkubo, V. R. V. Ramanan, and D. E. Laughlin, “The kinetics of nanocrystallization and microstructural observations in FINEMET, NANOPERM and HITPERM nanocomposite magnetic materials,” *Scr Mater*, vol. 48, no. 7, pp. 881–887, 2003, doi: 10.1016/S1359-6462(02)00597-3.

[83] F. Yang, S. feng Guo, A. dong Lan, H. jun Yang, and H. feng Zhou, “Corrosion Behavior of Fe-based Bulk Metallic Glass and In-situ Dendrite-reinforced Metallic Glass Matrix Composites in Acid Solution,” *Journal of Iron and Steel Research International*, vol. 23, no. 11, pp. 1200–1205, Nov. 2016, doi: 10.1016/S1006-706X(16)30176-5.

[84] A. Zarebidaki, A. Seifoddini, and T. Rabizadeh, “Corrosion resistance of Fe77Mo5P9C7.5B1.5 in-situ metallic glass matrix composites,” *J Alloys Compd*, vol. 736, pp. 17–21, 2018, doi: 10.1016/j.jallcom.2017.11.138.

[85] S. F. Guo, K. C. Chan, and L. Liu, “Notch toughness of Fe-based bulk metallic glass and composites,” *J Alloys Compd*, vol. 509, no. 39, pp. 9441–9446, 2011, doi: 10.1016/j.jallcom.2011.07.016.

[86] T. Wang, L. Zhang, Q. Hou, Q. Hao, and J. Qiao, “Improvement the plasticity of Fe-based bulk metallic glass via low temperature annealing,” *J Non Cryst Solids*, vol. 569, p. 120965, 2021, doi: 10.1016/j.jnoncrysol.2021.120965.

[87] S. Hasani, M. Ansariniya, and A. Seifoddini, “Enhancement of mechanical properties of a soft magnetic Fe-based metallic glass,” *Materials Science and Technology (United Kingdom)*, vol. 35, no. 7, pp. 865–871, 2019, doi: 10.1080/02670836.2019.1594552.

[88] Y. Lv and Q. Chen, “Internal friction behavior and thermal conductivity of Fe-based bulk metallic glasses with different crystallization,” *Thermochim Acta*, vol. 666, pp. 36–40, 2018, doi: 10.1016/j.tca.2018.05.025.

[89] J. E. Gao *et al.*, “Effects of nanocrystal formation on the soft magnetic

properties of Fe-based bulk metallic glasses," *Appl Phys Lett*, vol. 99, no. 5, p. 52504, 2011, doi: 10.1063/1.3621832.

[90] Y. Yoshizawa, S. Oguma, and K. Yamauchi, "New Fe-based soft magnetic alloys composed of ultrafine grain structure," *J Appl Phys*, vol. 64, no. 10, pp. 6044–6046, 1988, doi: 10.1063/1.342149.

[91] M. A. Willard *et al.*, "Magnetic properties of HITPERM (Fe, Co)88Zr7B4Cu1 magnets," *J Appl Phys*, vol. 85, no. 8, pp. 4421–4423, 1999, doi: 10.1063/1.369804.

[92] K. Suzuki *et al.*, "High Saturation Magnetization and Soft Magnetic Properties of bcc Fe-Zr-B Alloys with Ultrafine Grain Structure," *Materials Transactions, JIM*, vol. 31, no. 8, pp. 743–746, 1990, doi: 10.2320/matertrans1989.31.743.

[93] M. M. A. Rafique, *Bulk metallic glasses and their composites: additive manufacturing and modeling and simulation*. Walter de Gruyter GmbH & Co KG, 2021.

[94] F. G. Caballero, M. J. Santofimia, C. García-Mateo, J. Chao, and C. G. de Andrés, "Theoretical design and advanced microstructure in super high strength steels," *Mater Des*, vol. 30, no. 6, pp. 2077–2083, 2009, doi: https://doi.org/10.1016/j.matdes.2008.08.042.

[95] S. F. Guo, J. L. Qiu, P. Yu, S. H. Xie, and W. Chen, "Fe-based bulk metallic glasses: Brittle or ductile?," *Appl Phys Lett*, vol. 105, no. 16, 2014, doi: 10.1063/1.4899124.

[96] C. Wan *et al.*, "Ductile Fe-based bulk metallic glasses at room temperature," *Materials Science and Technology (United Kingdom)*, vol. 34, no. 6, pp. 751–756, 2018, doi: 10.1080/02670836.2017.1412037.

[97] F. Liu, S. Pang, R. Li, and T. Zhang, "Ductile Fe–Mo–P–C–B–Si bulk metallic glasses with high saturation magnetization," *J Alloys Compd*, vol. 483, no. 1, pp. 613–615, 2009, doi: https://doi.org/10.1016/j.jallcom.2008.07.164.

[98] T. Zhang, F. Liu, S. Pang, and R. Li, "Ductile Fe-Based Bulk Metallic Glass with Good Soft-Magnetic Properties," *Mater Trans*, vol. 48, no. 5, pp. 1157–1160, 2007, doi: 10.2320/matertrans.48.1157.

[99] R. Liu, R. He, J. Xiao, M. Tang, H. Zhang, and S. Guo, “Development of Fe-based bulk metallic glass composite as biodegradable metal,” *Mater Lett*, vol. 247, pp. 185–188, 2019, doi: https://doi.org/10.1016/j.matlet.2019.03.118.

[100] Z. B. Jiao, H. X. Li, J. E. Gao, Y. Wu, and Z. P. Lu, “Effects of alloying elements on glass formation, mechanical and soft-magnetic properties of Fe-based metallic glasses,” *Intermetallics (Barking)*, 2011, doi: 10.1016/j.intermet.2011.05.020.

[101] W. Zhang, X. Jia, Y. Li, and C. Fang, “Effects of Mo addition on thermal stability and magnetic properties of a ferromagnetic Fe75P10C10B5 metallic glass,” *J Appl Phys*, vol. 115, no. 17, p. 17A768, 2014, doi: 10.1063/1.4869161.

[102] M. Telford, “The case for bulk metallic glass,” *Materials Today*, vol. 7, no. 3, pp. 36–43, Mar. 2004, doi: 10.1016/S1369-7021(04)00124-5.

[103] M. Stoica, *Fe-Based Bulk Metallic Glasses: Understanding the Influence of Impurities on Glass Formation*. Wiesbaden: Springer Fachmedien Wiesbaden, 2017. doi: 10.1007/978-3-658-17018-9.

[104] I. ASTM52900-15, “Standard Terminology for Additive Manufacturing – General Principles – Terminology,” West Conshohocken, PA, 2015.

[105] T. DebRoy *et al.*, “Additive manufacturing of metallic components – Process, structure and properties,” *Prog Mater Sci*, vol. 92, pp. 112–224, 2018, doi: 10.1016/j.pmatsci.2017.10.001.

[106] Y. Li and D. Gu, “Parametric analysis of thermal behavior during selective laser melting additive manufacturing of aluminum alloy powder,” *Mater Des*, vol. 63, pp. 856–867, 2014, doi: 10.1016/j.matdes.2014.07.006.

[107] S. Pauly, P. Wang, U. Kühn, and K. Kosiba, “Experimental determination of cooling rates in selectively laser-melted eutectic Al-33Cu,” *Addit Manuf*, vol. 22, pp. 753–757, 2018, doi: 10.1016/j.addma.2018.05.034.

[108] D. Dai and D. Gu, “Influence of thermodynamics within molten pool on migration and distribution state of reinforcement during selective laser melting of AlN/AlSi10Mg composites,” *Int J Mach Tools Manuf*, vol. 100, pp. 14–24, 2016, doi: 10.1016/j.ijmachtools.2015.10.004.

[109] P. Lu, Z. Cheng-Lin, W. Liang, L. Tong, and L. Jiang-Lin, “Molten pool structure, temperature and velocity flow in selective laser melting AlCu5MnCdVA alloy,” *Mater Res Express*, vol. 7, no. 8, 2020, doi: 10.1088/2053-1591/abadcf.

[110] J. Gunasekaran, P. Sevvel, and I. J. Solomon, “Metallic materials fabrication by selective laser melting: A review,” *Mater Today Proc*, vol. 37, no. Part 2, pp. 252–256, 2020, doi: 10.1016/j.matpr.2020.05.162.

[111] H. Shipley *et al.*, “Optimisation of process parameters to address fundamental challenges during selective laser melting of Ti-6Al-4V: A review,” *Int J Mach Tools Manuf*, vol. 128, pp. 1–20, 2018, doi: 10.1016/j.ijmachtools.2018.01.003.

[112] J. Zhang, B. Song, Q. Wei, D. Bourell, and Y. Shi, “A review of selective laser melting of aluminum alloys: Processing, microstructure, property and developing trends,” *J Mater Sci Technol*, vol. 35, no. 2, pp. 270–284, Feb. 2019, doi: 10.1016/j.jmst.2018.09.004.

[113] S. D. Jadhav, L. R. Goossens, Y. Kinds, B. Van Hooreweder, and K. Vanmeensel, “Laser-based powder bed fusion additive manufacturing of pure copper,” *Addit Manuf*, vol. 42, p. 101990, Jun. 2021, doi: 10.1016/j.addma.2021.101990.

[114] X. Su and Y. Yang, “Research on track overlapping during Selective Laser Melting of powders,” *J Mater Process Technol*, vol. 212, no. 10, pp. 2074–2079, 2012, doi: 10.1016/j.jmatprotec.2012.05.012.

[115] D. Wang, Y. Yang, X. Su, and Y. Chen, “Study on energy input and its influences on single-track,multi-track, and multi-layer in SLM,” *International Journal of Advanced Manufacturing Technology*, vol. 58, no. 9–12, pp. 1189–1199, 2012, doi: 10.1007/s00170-011-3443-y.

[116] C. Chen, J. Yin, H. Zhu, Z. Xiao, L. Zhang, and X. Zeng, “Effect of overlap rate and pattern on residual stress in selective laser melting,” *Int J Mach Tools Manuf*, vol. 145, 2019, doi: 10.1016/j.ijmachtools.2019.103433.

[117] T. Gustmann *et al.*, “Influence of processing parameters on the fabrication of a Cu-Al-Ni-Mn shape-memory alloy by selective laser melting,” *Addit Manuf*, vol. 11, pp. 23–31, 2016, doi: 10.1016/j.addma.2016.04.003.

[118] L. N. Carter, C. Martin, P. J. Withers, and M. M. Attallah, “The influence of the laser scan strategy on grain structure and cracking behaviour in SLM powder-bed fabricated nickel superalloy,” *J Alloys Compd*, vol. 615, pp. 338–347, Dec. 2014, doi: 10.1016/j.jallcom.2014.06.172.

[119] A. G. Demir and B. Previtali, “Investigation of remelting and preheating in SLM of 18Ni300 maraging steel as corrective and preventive measures for porosity reduction,” *International Journal of Advanced Manufacturing Technology*, vol. 93, no. 5–8, pp. 2697–2709, 2017, doi: 10.1007/s00170-017-0697-z.

[120] J. Vaithilingam, R. D. Goodridge, R. J. M. Hague, S. D. R. Christie, and S. Edmondson, “The effect of laser remelting on the surface chemistry of Ti6al4V components fabricated by selective laser melting,” *J Mater Process Technol*, vol. 232, pp. 1–8, Jun. 2016, doi: 10.1016/j.jmatprotec.2016.01.022.

[121] K. G. Prashanth, S. Scudino, and J. Eckert, “Defining the tensile properties of Al-12Si parts produced by selective laser melting,” *Acta Mater*, vol. 126, pp. 25–35, 2017, doi: 10.1016/j.actamat.2016.12.044.

[122] H. H. Zhu, J. Y. H. Fuh, and L. Lu, “The influence of powder apparent density on the density in direct laser-sintered metallic parts,” *Int J Mach Tools Manuf*, vol. 47, no. 2, pp. 294–298, 2007, doi: 10.1016/j.ijmachtools.2006.03.019.

[123] A. P. M. de Araujo *et al.*, “Additive manufacturing of a quasicrystal-forming Al95Fe2Cr2Ti1 alloy with remarkable high-temperature strength and ductility,” *Addit Manuf*, vol. 41, p. 101960, 2021, doi: 10.1016/j.addma.2021.101960.

[124] N. Vlachos and I. T. H. Chang, “Investigation of flow properties of metal powders from narrow particle size distribution to polydisperse mixtures through an improved Hall-flowmeter,” *Powder Technol*, vol. 205, no. 1–3, pp. 71–80, 2011, doi: 10.1016/j.powtec.2010.08.067.

[125] A. T. Sutton, C. S. Kriewall, M. C. Leu, and J. W. Newkirk, “Powder characterisation techniques and effects of powder characteristics on part properties in powder-bed fusion processes,” *Virtual Phys Prototyp*, vol. 12,

no. 1, pp. 3–29, 2017, doi: 10.1080/17452759.2016.1250605.

[126] A. Simchi, “The role of particle size on the laser sintering of iron powder,” 2004. doi: 10.1007/s11663-004-0088-3.

[127] E. O. Olakanmi, R. F. Cochrane, and K. W. Dalgarno, “A review on selective laser sintering/melting (SLS/SLM) of aluminium alloy powders: Processing, microstructure, and properties,” *Prog Mater Sci*, vol. 74, pp. 401–477, 2015, doi: 10.1016/j.pmatsci.2015.03.002.

[128] A. T. Clare *et al.*, “Alloy design and adaptation for additive manufacture,” *J Mater Process Technol*, vol. 299, p. 117358, 2021, doi: 10.1016/j.jmatprotec.2021.117358.

[129] R. Srivastava, J. Eckert, W. Löser, B. Dhindaw, and L. Schultz, “Cooling Rate Evaluation for Bulk Amorphous Alloys from Eutectic Microstructures in Casting Processes,” *Mater Trans*, vol. 43, no. 7, pp. 1670–1675, 2002, doi: 10.2320/matertrans.43.1670.

[130] N. Ciftci, N. Ellendt, E. Soares Barreto, L. Mädler, and V. Uhlenwinkel, “Increasing the amorphous yield of {(Fe0.6Co0.4)0.75B0.2Si0.05}96Nb4 powders by hot gas atomization,” *Advanced Powder Technology*, vol. 29, no. 2, pp. 380–385, 2018, doi: 10.1016/j.apt.2017.11.025.

[131] M. J. Kramer, H. Mecco, K. W. Dennis, E. Vargonova, R. W. McCallum, and R. E. Napolitano, “Rapid solidification and metallic glass formation - Experimental and theoretical limits,” *J Non Cryst Solids*, vol. 353, no. 32–40, pp. 3633–3639, 2007, doi: 10.1016/j.jnoncrysol.2007.05.172.

[132] P. Fischer, V. Romano, A. Blatter, and H. P. Weber, “Highly precise pulsed selective laser sintering of metallic powders,” *Laser Phys Lett*, vol. 2, no. 1, pp. 48–55, Jan. 2004, doi: 10.1002/lapl.200410118.

[133] N. Sohrabi *et al.*, “Additive manufacturing of a precious bulk metallic glass,” *Appl Mater Today*, vol. 24, p. 101080, Sep. 2021, doi: 10.1016/j.apmt.2021.101080.

[134] S. M. Kelly, “Fabrication of fe-based bulk metallic glass components using laser additive manufacturing,” *ICALEO 2006 - 25th International Congress on Applications of Laser and Electro-Optics, Congress Proceedings*, vol. 2006, no. 1, p. P539, 2006, doi: 10.2351/1.5060946.

[135] K. Kosiba, L. Deng, and S. Scudino, “Viscous flow of supercooled liquid in a Zr-based bulk metallic glass synthesized by additive manufacturing,” *Materials*, vol. 13, no. 17, 2020, doi: 10.3390/MA13173803.

[136] P. Bordeenithikasem, M. Stolpe, A. Elsen, and D. C. Hofmann, “Glass forming ability, flexural strength, and wear properties of additively manufactured Zr-based bulk metallic glasses produced through laser powder bed fusion,” *Addit Manuf*, vol. 21, pp. 312–317, May 2018, doi: 10.1016/j.addma.2018.03.023.

[137] Y. Li, Y. Shen, M. C. Leu, and H. L. Tsai, “Mechanical properties of Zr-based bulk metallic glass parts fabricated by laser-foil-printing additive manufacturing,” *Materials Science and Engineering A*, vol. 743, pp. 404–411, 2019, doi: 10.1016/j.msea.2018.11.056.

[138] X. Lu, M. Nursulton, Y. Du, and W. Liao, “Structural and mechanical characteristics of Cu50Zr43Al7 bulk metallic glass fabricated by selective laser melting,” *Materials*, vol. 12, no. 5, 2019, doi: 10.3390/ma12050775.

[139] X. Gao *et al.*, “Selective laser melting of CuZr-based metallic glass composites,” *Mater Lett*, vol. 259, 2020, doi: 10.1016/j.matlet.2019.126724.

[140] S. Pauly, C. Schricker, S. Scudino, L. Deng, and U. Kühn, “Processing a glass-forming Zr-based alloy by selective laser melting,” *Mater Des*, vol. 135, pp. 133–141, 2017, doi: 10.1016/j.matdes.2017.08.070.

[141] X. P. Li, M. P. Roberts, S. O’Keeffe, and T. B. Sercombe, “Selective laser melting of Zr-based bulk metallic glasses: Processing, microstructure and mechanical properties,” *Mater Des*, vol. 112, pp. 217–226, Dec. 2016, doi: 10.1016/j.matdes.2016.09.071.

[142] D. Ouyang, N. Li, and L. Liu, “Structural heterogeneity in 3D printed Zr-based bulk metallic glass by selective laser melting,” *J Alloys Compd*, vol. 740, pp. 603–609, 2018, doi: 10.1016/j.jallcom.2018.01.037.

[143] D. Ouyang *et al.*, “3D printing of crack-free high strength Zr-based bulk metallic glass composite by selective laser melting,” *Intermetallics (Barking)*, vol. 90, pp. 128–134, 2017, doi: 10.1016/j.intermet.2017.07.010.

[144] X. P. Li, C. W. Kang, H. Huang, and T. B. Sercombe, “The role of a low-energy–density re-scan in fabricating crack-free Al85Ni5Y6Co2Fe2 bulk

metallic glass composites via selective laser melting," *Mater Des*, vol. 63, pp. 407–411, 2014, doi: 10.1016/j.matdes.2014.06.022.

[145] X. P. Li, C. W. Kang, H. Huang, L. C. Zhang, and T. B. Sercombe, "Selective laser melting of an Al86Ni6Y4.5Co2La1.5 metallic glass: Processing, microstructure evolution and mechanical properties," *Materials Science and Engineering A*, vol. 606, pp. 370–379, 2014, doi: 10.1016/j.msea.2014.03.097.

[146] Ł. Żrodowski, B. Wysocki, R. Wróblewski, K. J. Kurzydłowski, and W. Święszkowski, "The Novel Scanning Strategy For Fabrication Metallic Glasses By Selective Laser Melting," in *Presented at the Fraunhofer Direct Digital Manufacturing Conference 2016.*, Presented at the Fraunhofer Direct Digital Manufacturing Conference 2016., 2016.

[147] X. D. Nong, X. L. Zhou, and Y. X. Ren, "Fabrication and characterization of Fe-based metallic glasses by Selective Laser Melting," *Opt Laser Technol*, vol. 109, pp. 20–26, 2019, doi: 10.1016/j.optlastec.2018.07.059.

[148] H. Y. Jung *et al.*, "Fabrication of Fe-based bulk metallic glass by selective laser melting: A parameter study," *Mater Des*, vol. 86, pp. 703–708, 2015, doi: 10.1016/j.matdes.2015.07.145.

[149] S. Pauly *et al.*, "Processing metallic glasses by selective laser melting," *Materials Today*, vol. 16, no. 1–2, pp. 37–41, Jan. 2013, doi: 10.1016/j.mattod.2013.01.018.

[150] D. C. Hofmann, P. Bordeenithikasem, A. Pate, S. N. Roberts, and E. Vogli, "Developing Processing Parameters and Characterizing Microstructure and Properties of an Additively Manufactured FeCrMoBC Metallic Glass Forming Alloy," *Adv Eng Mater*, vol. 20, no. 10, p. 1800433, 2018, doi: https://doi.org/10.1002/adem.201800433.

[151] Ł. Żrodowski *et al.*, "New approach to amorphization of alloys with low glass forming ability via selective laser melting," *J Alloys Compd*, vol. 771, pp. 769–776, Jan. 2019, doi: 10.1016/j.jallcom.2018.08.075.

[152] L. Wang *et al.*, "Selective laser melting helps fabricate record-large bulk metallic glass: Experiments, simulation and demonstrative part," *J Alloys Compd*, vol. 808, p. 151731, Nov. 2019, doi:

10.1016/j.jallcom.2019.151731.

[153] Y. G. Nam *et al.*, “Selective laser melting vitrification of amorphous soft magnetic alloys with help of double-scanning-induced compositional homogeneity,” *Mater Lett*, vol. 261, 2020, doi: 10.1016/j.matlet.2019.127068.

[154] N. Li, J. Zhang, W. Xing, D. Ouyang, and L. Liu, *3D printing of Fe-based bulk metallic glass composites with combined high strength and fracture toughness*, vol. 143. Elsevier Ltd, 2018, pp. 285–296. doi: 10.1016/j.matdes.2018.01.061.

[155] W. Xing, D. Ouyang, N. Li, and L. Liu, “Insight into micro-cracking in 3D-printed Fe-based BMGs by selective laser melting,” *Intermetallics (Barking)*, vol. 103, pp. 101–106, 2018, doi: 10.1016/j.intermet.2018.10.011.

[156] H. Liu, Q. Jiang, J. Huo, Y. Zhang, W. Yang, and X. Li, “Crystallization in additive manufacturing of metallic glasses: A review,” *Addit Manuf*, vol. 36, p. 101568, Dec. 2020, doi: 10.1016/j.addma.2020.101568.

[157] T. Mukherjee, W. Zhang, and T. DebRoy, “An improved prediction of residual stresses and distortion in additive manufacturing,” *Comput Mater Sci*, vol. 126, pp. 360–372, Jan. 2017, doi: 10.1016/j.commatsci.2016.10.003.

[158] Y. J. Liu, Z. Liu, Y. Jiang, G. W. Wang, Y. Yang, and L. C. Zhang, “Gradient in microstructure and mechanical property of selective laser melted AlSi10Mg,” *J Alloys Compd*, vol. 735, pp. 1414–1421, Feb. 2018, doi: 10.1016/j.jallcom.2017.11.020.

[159] D. Dai, D. Gu, R. Poprawe, and M. Xia, “Influence of additive multilayer feature on thermodynamics, stress and microstructure development during laser 3D printing of aluminum-based material,” *Sci Bull (Beijing)*, vol. 62, no. 11, pp. 779–787, Jun. 2017, doi: 10.1016/j.scib.2017.05.007.

[160] H. Rao, S. Giet, K. Yang, X. Wu, and C. H. J. Davies, “The influence of processing parameters on aluminium alloy A357 manufactured by Selective Laser Melting,” *Mater Des*, vol. 109, pp. 334–346, Nov. 2016, doi: 10.1016/j.matdes.2016.07.009.

[161] S. Cao, D. Gu, and Q. Shi, “Relation of microstructure, microhardness and underlying thermodynamics in molten pools of laser melting deposition processed TiC/Inconel 625 composites,” *J Alloys Compd*, vol. 692, pp. 758–769, Jan. 2017, doi: 10.1016/j.jallcom.2016.09.098.

[162] G. Yang *et al.*, “Laser solid forming Zr-based bulk metallic glass,” *Intermetallics (Barking)*, vol. 22, pp. 110–115, Mar. 2012, doi: 10.1016/j.intermet.2011.10.008.

[163] X. P. Li, M. Roberts, Y. J. Liu, C. W. Kang, H. Huang, and T. B. Sercombe, “Effect of substrate temperature on the interface bond between support and substrate during selective laser melting of Al-Ni-Y-Co-La metallic glass,” *Mater Des*, vol. 65, pp. 1–6, Jan. 2015, doi: 10.1016/j.matdes.2014.08.065.

[164] P. Fischer, A. Blatter, V. Romano, and H. P. Weber, “Selective laser sintering of amorphous metal powder,” *Appl Phys A Mater Sci Process*, vol. 80, no. 3, pp. 489–492, 2005, doi: 10.1007/s00339-004-3062-7.

[165] C. Yang, C. Zhang, W. Xing, and L. Liu, “3D printing of Zr-based bulk metallic glasses with complex geometries and enhanced catalytic properties,” *Intermetallics (Barking)*, vol. 94, pp. 22–28, Mar. 2018, doi: 10.1016/j.intermet.2017.12.018.

[166] B. Zheng, Y. Lin, Y. Zhou, and E. J. Lavernia, “Gas atomization of amorphous aluminum powder: Part II. experimental investigation,” *Metallurgical and Materials Transactions B: Process Metallurgy and Materials Processing Science*, vol. 40, no. 6, pp. 995–1004, 2009, doi: 10.1007/s11663-009-9277-4.

[167] S. Mukherjee, J. Schroers, Z. Zhou, W. L. Johnson, and W.-K. Rhim, “Viscosity and specific volume of bulk metallic glass-forming alloys and their correlation with glass forming ability,” *Acta Mater*, vol. 52, no. 12, pp. 3689–3695, 2004, doi: https://doi.org/10.1016/j.actamat.2004.04.023.

[168] A. Malachowska, G. Paczkowski, T. Lampke, and A. Ambroziak, “Characterization of FeP-based metallic glass coatings prepared with laser cladding,” *Surf Coat Technol*, vol. 405, no. November 2020, p. 126733, Jan. 2021, doi: 10.1016/j.surfcoat.2020.126733.

[169] F. Xie, Q. Chen, and J. Gao, “Brittle-ductile transition in laser 3D printing of

fe-based bulk metallic glass composites," *Metals (Basel)*, vol. 9, no. 1, 2019, doi: 10.3390/met9010078.

[170] I. Yadroitsev, A. Gusarov, I. Yadroitsava, and I. Smurov, "Single track formation in selective laser melting of metal powders," *J Mater Process Technol*, vol. 210, no. 12, pp. 1624–1631, Sep. 2010, doi: 10.1016/j.jmatprotec.2010.05.010.

[171] Y. L. Guo, L. N. Jia, B. Kong, Y. L. Huang, and H. Zhang, "Energy Density Dependence of Bonding Characteristics of Selective Laser-Melted Nb–Si-Based Alloy on Titanium Substrate," *Acta Metallurgica Sinica (English Letters)*, vol. 31, no. 5, pp. 477–486, 2018, doi: 10.1007/s40195-017-0670-8.

[172] A. Simchi, "Direct laser sintering of metal powders: Mechanism, kinetics and microstructural features," *Materials Science and Engineering A*, vol. 428, no. 1–2, pp. 148–158, Jul. 2006, doi: 10.1016/j.msea.2006.04.117.

[173] Y. Zhang, X. Lin, L. Wei, F. Liu, and W. Huang, "Influence of powder size on the crystallization behavior during laser solid forming Zr55Cu30Al10Ni5 bulk amorphous alloy," *Intermetallics (Barking)*, vol. 76, pp. 1–9, Sep. 2016, doi: 10.1016/j.intermet.2016.06.006.

[174] V. K. Balla and A. Bandyopadhyay, "Laser processing of Fe-based bulk amorphous alloy," *Surf Coat Technol*, vol. 205, no. 7, pp. 2661–2667, Dec. 2010, doi: 10.1016/j.surfcoat.2010.10.029.

[175] H. Li, Z. Lu, and S. Yi, "Estimation of the glass forming ability of the Fe-based bulk metallic glass Fe68.8C7.0Si3.5B5.0P 9.6Cr2.1Mo2.0Al2.0 that contains non-metallic inclusions," *Metals and Materials International*, vol. 15, no. 1, pp. 7–14, 2009, doi: 10.1007/s12540-009-0007-x.

[176] B. S. Murty, D. H. Ping, K. Hono, and A. Inoue, "Influence of oxygen on the crystallization behavior of Zr65Cu27.5Al7.5 and Zr66.7Cu33.3 metallic glasses," *Acta Mater*, vol. 48, no. 15, pp. 3985–3996, Sep. 2000, doi: 10.1016/S1359-6454(00)00190-7.

[177] Y. Zhang, X. Lin, L. Wang, L. Wei, F. Liu, and W. Huang, "Microstructural analysis of Zr55Cu30Al10Ni5 bulk metallic glasses by laser surface remelting and laser solid forming," *Intermetallics (Barking)*, vol. 66, pp. 22–

30, Nov. 2015, doi: 10.1016/j.intermet.2015.06.007.

[178] H. X. Li, J. E. Gao, Z. B. Jiao, Y. Wu, and Z. P. Lu, “Glass-forming ability enhanced by proper additions of oxygen in a Fe-based bulk metallic glass,” *Appl Phys Lett*, vol. 95, no. 16, p. 161905, 2009, doi: 10.1063/1.3248186.

[179] L. Deng, S. Wang, P. Wang, U. Kühn, and S. Pauly, “Selective laser melting of a Ti-based bulk metallic glass,” *Mater Lett*, vol. 212, pp. 346–349, Feb. 2018, doi: 10.1016/j.matlet.2017.10.130.

[180] D. Ouyang, W. Xing, N. Li, Y. Li, and L. Liu, “Structural evolutions in 3D-printed Fe-based metallic glass fabricated by selective laser melting,” *Addit Manuf*, vol. 23, pp. 246–252, 2018, doi: 10.1016/j.addma.2018.08.020.

[181] H. X. Li, Z. C. Lu, S. L. Wang, Y. Wu, and Z. P. Lu, “Fe-based bulk metallic glasses: Glass formation, fabrication, properties and applications,” *Prog Mater Sci*, vol. 103, pp. 235–318, 2019, doi: 10.1016/j.pmatsci.2019.01.003.

[182] P. Zhang, J. Tan, Y. Tian, H. Yan, and Z. Yu, “Research progress on selective laser melting (SLM) of bulk metallic glasses (BMGs): a review,” *The International Journal of Advanced Manufacturing Technology*, 2021, doi: 10.1007/s00170-021-07990-8.

[183] Z. Mahbooba *et al.*, “Additive manufacturing of an iron-based bulk metallic glass larger than the critical casting thickness,” *Appl Mater Today*, vol. 11, pp. 264–269, Jun. 2018, doi: 10.1016/j.apmt.2018.02.011.

[184] Ł. Szczepański, M. Bambach, F. Jensch, A. Ambroziak, and T. Kurzynowski, “Structural investigations of Fe-Zr-Si-Cu metallic glass with low glass-forming ability produced in laser powder bed fusion technology,” *Mater Des*, vol. 210, p. 110112, Nov. 2021, doi: 10.1016/j.matdes.2021.110112.

[185] S. X. Liang, X. Wang, W. Zhang, Y. J. Liu, W. Wang, and L. C. Zhang, “Selective laser melting manufactured porous Fe-based metallic glass matrix composite with remarkable catalytic activity and reusability,” *Appl Mater Today*, vol. 19, p. 100543, 2020, doi: 10.1016/j.apmt.2019.100543.

[186] N. Li, S. Wu, D. Ouyang, J. Zhang, and L. Liu, “Fe-based metallic glass reinforced FeCoCrNiMn high entropy alloy through selective laser melting,”

J Alloys Compd, vol. 822, p. 153695, May 2020, doi: 10.1016/j.jallcom.2020.153695.

[187] Y. Zou, Z. Qiu, C. Tan, Y. Wu, K. Li, and D. Zeng, “Microstructure and mechanical properties of Fe-based bulk metallic glass composites fabricated by selective laser melting,” *J Non Cryst Solids*, vol. 538, p. 120046, Jun. 2020, doi: 10.1016/j.jnoncrysol.2020.120046.

[188] Y. M. Zou, Y. S. Wu, K. F. Li, C. L. Tan, Z. G. Qiu, and D. C. Zeng, “Selective laser melting of crack-free Fe-based bulk metallic glass via chessboard scanning strategy,” *Mater Lett*, vol. 272, p. 127824, Aug. 2020, doi: 10.1016/j.matlet.2020.127824.

[189] M. T. Clavaguera-Mora, N. Clavaguera, D. Crespo, and T. Pradell, “Crystallisation kinetics and microstructure development in metallic systems,” *Prog Mater Sci*, vol. 47, no. 6, pp. 559–619, Jan. 2002, doi: 10.1016/S0079-6425(00)00021-9.

[190] W. H. Wang, “Roles of minor additions in formation and properties of bulk metallic glasses,” *Prog Mater Sci*, vol. 52, no. 4, pp. 540–596, May 2007, doi: 10.1016/j.pmatsci.2006.07.003.

[191] W. L. Johnson, “Thermodynamic and kinetic aspects of the crystal to glass transformation in metallic materials,” *Prog Mater Sci*, vol. 30, no. 2, pp. 81–134, Jan. 1986, doi: 10.1016/0079-6425(86)90005-8.

[192] J. Wu, W. Li, Y. Pan, J. Qi, and J. Wang, “Microalloying and microstructures of Cu-based bulk metallic glasses & composites and relevant mechanical properties,” *Mater Des*, vol. 89, pp. 1130–1136, 2016, doi: 10.1016/j.matdes.2015.10.054.

[193] Z. B. Jiao, H. X. Li, J. E. Gao, Y. Wu, and Z. P. Lu, “Effects of alloying elements on glass formation, mechanical and soft-magnetic properties of Fe-based metallic glasses,” *Intermetallics (Barking)*, vol. 19, no. 10, pp. 1502–1508, Oct. 2011, doi: 10.1016/J.INTERMET.2011.05.020.

[194] W. Cao *et al.*, “PANDAT software with PanEngine, PanOptimizer and PanPrecipitation for multi-component phase diagram calculation and materials property simulation,” *CALPHAD*, vol. 33, no. 2, pp. 328–342, Jun. 2009, doi: 10.1016/j.calphad.2008.08.004.

[195] “PanIron 2021: Thermodynamic database for multi-component Fe-rich alloys.” [Online]. Available: https://computherm.com/

[196] C. Walter, B. Hallstedt, and N. Warnken, “Simulation of the solidification of CMSX-4,” *Materials Science and Engineering A*, vol. 397, no. 1–2, pp. 385–390, Apr. 2005, doi: 10.1016/j.msea.2005.02.056.

[197] M. D. Demetriou and W. L. Johnson, “Tough iron-based bulk metallic glass alloys-Wo 2010/135415 A2,” 2010

[198] X. Q. Chen, H. Niu, D. Li, and Y. Li, “Modeling hardness of polycrystalline materials and bulk metallic glasses,” *Intermetallics (Barking)*, vol. 19, no. 9, pp. 1275–1281, Sep. 2011, doi: 10.1016/j.intermet.2011.03.026.

[199] “Designation: C702/C702M − 18 Standard Practice for Reducing Samples of Aggregate to Testing Size”, doi: 10.1520/C0702_C0702M-18.

[200] B. K. Panigrahi, “Microstructure-mechanical property relationships for a Fe/Mn/Cr rock bolt reinforcing steel,” *J Mater Eng Perform*, vol. 19, no. 6, pp. 885–893, 2010, doi: 10.1007/s11665-009-9540-5.

[201] C. H. Won *et al.*, “Effect of annealing on mechanical properties and microstructure evolution of borated stainless steels,” *Journal of Nuclear Materials*, vol. 515, pp. 206–214, Mar. 2019, doi: 10.1016/j.jnucmat.2018.12.039.

[202] M. Shaker and H. Abd El-Hafez, “Effect of Austempering Time on the Workability and Mechanical Properties of the Ductile Iron,” *ERJ. Engineering Research Journal*, vol. 33, no. 1, pp. 31–38, 2010, doi: 10.21608/erjm.2010.67302.

[203] A. Seifoddini, M. Stoica, M. Nili-Ahmadabadi, S. Heshmati-Manesh, U. Kühn, and J. Eckert, “New (Fe0.9Ni0.1)77Mo5P9C7.5B1.5 glassy alloys with enhanced glass-forming ability and large compressive strain,” *Materials Science and Engineering: A*, vol. 560, pp. 575–582, Jan. 2013, doi: 10.1016/J.MSEA.2012.09.104.

[204] R. Wang, L. Shi, Y. Wu, J. Jia, Y. Shao, and K. Yao, “Effects of Mo on the glass forming ability and properties of Fe-B-C-P-Si-Mo bulk metallic glasses,” *J Non Cryst Solids*, vol. 629, p. 122868, 2024, doi: https://doi.org/10.1016/j.jnoncrysol.2024.122868.

[205] J. Zhou, B. Sun, Q. Wang, Q. Yang, W. Yang, and B. Shen, “Effects of Ni and Si additions on mechanical properties and serrated flow behavior in FeMoPCB bulk metallic glasses,” *J Alloys Compd*, vol. 783, pp. 555–564, Apr. 2019, doi: 10.1016/J.JALLCOM.2018.12.331.

[206] C. Yang, T. Wei, J. Zeng, L. H. Liu, S. G. Qu, and Y. Y. Li, “Microstructure evolution and thermal properties in FeMoPCB alloy during mechanical alloying,” *J Non Cryst Solids*, vol. 358, no. 12–13, pp. 1459–1464, Jul. 2012, doi: 10.1016/J.JNONCRYSOL.2012.03.024.

[207] N. Luo *et al.*, “Preparation of Fe-Co-B-Si-Nb bulk metallic glasses by laser powder bed fusion: Microstructure and properties,” *Mater Charact*, vol. 162, p. 110206, Apr. 2020, doi: 10.1016/J.MATCHAR.2020.110206.

[208] N. Sohrabi, J. E. K. Schawe, J. Jhabvala, J. F. Löffler, and R. E. Logé, “Critical crystallization properties of an industrial-grade Zr-based metallic glass used in additive manufacturing,” *Scr Mater*, vol. 199, p. 113861, 2021, doi: https://doi.org/10.1016/j.scriptamat.2021.113861.

[209] N. Sohrabi *et al.*, “Quantitative prediction of crystallization in laser powder bed fusion of a Zr-based bulk metallic glass with high oxygen content,” *Mater Des*, vol. 239, p. 112744, 2024, doi: https://doi.org/10.1016/j.matdes.2024.112744.

[210] A. Lekatou, A. K. Sfikas, C. Petsa, and A. E. Karantzalis, “Al-Co Alloys Prepared by Vacuum Arc Melting: Correlating Microstructure Evolution and Aqueous Corrosion Behavior with Co Content,” *Metals (Basel)*, vol. 6, no. 3, 2016, doi: 10.3390/met6030046.

[211] J. Lentz, A. Röttger, and W. Theisen, “Mechanism of the Fe3(B,C) and Fe23(C,B)6 solid-state transformation in the hypoeutectic region of the Fe-C-B system,” *Acta Mater*, vol. 119, pp. 80–91, 2016, doi: https://doi.org/10.1016/j.actamat.2016.08.009.

[212] M. A. Kaleem, M. Z. Alam, M. Khan, S. H. I. Jaffery, and B. Rashid, “An experimental investigation on accuracy of Hausner Ratio and Carr Index of powders in additive manufacturing processes,” *Metal Powder Report*, vol. 76, pp. S50–S54, Dec. 2021, doi: 10.1016/J.MPRP.2020.06.061.

[213] N. Sohrabi, J. Jhabvala, and R. E. Logé, “Additive manufacturing of bulk

metallic glasses—process, challenges and properties: A review," *Metals (Basel)*, vol. 11, no. 8, 2021, doi: 10.3390/met11081279.

[214] S. V Madge and A. L. Greer, "Laser additive manufacturing of metallic glasses: issues in vitrification and mechanical properties," *Oxford Open Materials Science*, 2021, doi: 10.1093/oxfmat/itab015.

[215] C. P. Harmer *et al.*, "Pseudo-Polymorphism in Layered FeS Intercalates: A Competition between Charged and Neutral Guest Species," *Chemistry of Materials*, vol. 34, no. 12, pp. 5397–5408, Jun. 2022, doi: 10.1021/acs.chemmater.2c00270.

[216] S. Kavita *et al.*, "On the table-like magnetocaloric effect, microstructure and mechanical properties of LaxFe11.6 Si1.4 system," *J Alloys Compd*, vol. 895, p. 162597, 2022, doi: https://doi.org/10.1016/j.jallcom.2021.162597.

[217] G. Pradelli, C. Gianoglio, and E. Quadrini, "Borocarburi cubici del tipo Cr23C6 - Studio della fase (Cr, Mn)23(B, C)6," *Atti della Accademia Nazionale dei Lincei. Classe di Scienze Fisiche, Matematiche e Naturali. Rendiconti*, vol. Serie 8, no. 65, pp. 177–184, 1978.

[218] S. Rundqvist, "X-ray investigations of the ternary system Fe-PB. Some features of the systems Cr-PB, Mn-PB, Co-PB and Ni-PB," *Acta Chem. Scand*, vol. 16, no. 1, pp. 1–19, 1962.

[219] F. Römer *et al.*, "Crystallization of Fe74Mo4P10C7.5B2.5Si2 metallic glass: Insights from in-situ synchrotron diffraction and Flash DSC," *Mater Today Adv*, vol. 25, p. 100550, 2025, doi: https://doi.org/10.1016/j.mtadv.2024.100550.

[220] T. H. Courtney, *Mechanical behavior of materials*. Waveland Press, 2005.

[221] D. Turnbull and M. H. Cohen, "On the Free-Volume Model of the Liquid-Glass Transition," *J Chem Phys*, vol. 52, no. 6, pp. 3038–3041, Mar. 1970, doi: 10.1063/1.1673434.

[222] W. Pilarczyk, O. Starczewska, and D. Łukowiec, "Nanoindentation characteristic of Fe-based bulk metallic glass laser weld," *physica status solidi (b)*, vol. 252, no. 11, pp. 2598–2601, Nov. 2015, doi: https://doi.org/10.1002/pssb.201552231.

[223] Q. Jiang *et al.*, "Influence of the microstructure on mechanical properties of

SLM additive manufacturing Fe-based bulk metallic glasses," *J Alloys Compd*, vol. 894, p. 162525, Feb. 2022, doi: 10.1016/J.JALLCOM.2021.162525.

[224] H.-S. Park and D.-S. Nguyen, "Study on Flaking Behavior in Selective Laser Melting Process," *Procedia CIRP*, vol. 63, pp. 569–572, 2017, doi: https://doi.org/10.1016/j.procir.2017.03.146.

[225] A. Małachowska, Ł. Żrodowski, B. Morończyk, Ł. Maj, A. Kuś, and T. Lampke, "Selective Laser Melting of Fe-Based Metallic Glasses With Different Degree of Plasticity," *Metallurgical and Materials Transactions A*, vol. 54, no. 2, pp. 658–670, 2023, doi: 10.1007/s11661-022-06913-w.

[226] P. Ponnusamy, S. H. Masood, D. Ruan, S. Palanisamy, and R. Rashid, "High strain rate dynamic behaviour of AlSi12 alloy processed by selective laser melting," *The International Journal of Advanced Manufacturing Technology*, vol. 97, no. 1, pp. 1023–1035, 2018, doi: 10.1007/s00170-018-1873-5.

[227] H. Roirand, A. Hor, B. Malard, and N. Saintier, "Effect of laser-scan strategy on microstructure and fatigue properties of 316L additively manufactured stainless steel," *Fatigue Fract Eng Mater Struct*, vol. 46, no. 1, pp. 32–48, Jan. 2023, doi: https://doi.org/10.1111/ffe.13845.

[228] C. Tan, Q. Shi, K. Li, K. Khanlari, and X. Liu, "Effect of oxygen content of tantalum powders on the characteristics of parts processed by laser powder bed fusion," *Int J Refract Metals Hard Mater*, vol. 110, p. 106008, 2023, doi: https://doi.org/10.1016/j.ijrmhm.2022.106008.

[229] O. A. Quintana, J. Alvarez, R. Mcmillan, W. Tong, and C. Tomonto, "Effects of Reusing Ti-6Al-4V Powder in a Selective Laser Melting Additive System Operated in an Industrial Setting," *JOM*, vol. 70, no. 9, pp. 1863–1869, 2018, doi: 10.1007/s11837-018-3011-0.

[230] V. N. Eremenko and T. Velikanova, "Intrusion Phases Based on Metallides in Ternary Systems of Transition Metals with Carbon," *Soviet Progress in Chemistry*, vol. 56, no. 4, pp. 21–28, 1990.

[231] F. Khodabakhshi and M. Kazeminezhad, "Differential scanning calorimetry study of constrained groove pressed low carbon steel:

Recovery, recrystallisation and ferrite to austenite phase transformation," *Materials Science and Technology*, vol. 30, no. 7, pp. 765–773, Jun. 2014, doi: 10.1179/1743284713Y.0000000388.

[232] M. G. Özden and N. A. Morley, "Optimizing laser additive manufacturing process for Fe-based nano-crystalline magnetic materials," *J Alloys Compd*, vol. 960, p. 170644, Oct. 2023, doi: 10.1016/J.JALLCOM.2023.170644.

[233] C. Zhang, D. Ouyang, S. Pauly, and L. Liu, "3D printing of bulk metallic glasses," *Materials Science and Engineering R: Reports*, vol. 145, 2021, doi: 10.1016/j.mser.2021.100625.

[234] L. T. Khajavi and M. Barati, "Thermodynamics of Phosphorus Removal from Silicon in Solvent Refining of Silicon," *High Temperature Materials and Processes*, vol. 31, no. 4–5, pp. 627–631, 2012, doi: doi:10.1515/htmp-2012-0100.

[235] M. Rodríguez-Sánchez *et al.*, "Relating laser powder bed fusion process parameters to (micro)structure and to soft magnetic behaviour in a Fe-based bulk metallic glass," *Materialia (Oxf)*, vol. 35, p. 102111, 2024, doi: https://doi.org/10.1016/j.mtla.2024.102111.

[236] J. Löfstrand *et al.*, "Stress related magnetic imaging of iron-based metallic glass produced with laser beam powder bed fusion," *Mater Des*, vol. 244, p. 113199, 2024, doi: https://doi.org/10.1016/j.matdes.2024.113199.

[237] S. Gao *et al.*, "Microstructure and magnetic properties of FeSiBCrC soft magnetic alloy manufactured by selective laser melting," *Mater Lett*, vol. 290, p. 129469, 2021, doi: https://doi.org/10.1016/j.matlet.2021.129469.

[238] R. Raghavan, P. Murali, and U. Ramamurty, "On factors influencing the ductile-to-brittle transition in a bulk metallic glass," *Acta Mater*, vol. 57, no. 11, pp. 3332–3340, 2009, doi: https://doi.org/10.1016/j.actamat.2009.03.047.

[239] T. Xu, S. Pang, and T. Zhang, "Glass formation, corrosion behavior, and mechanical properties of novel Cr-rich Cr–Fe–Mo–C–B–Y bulk metallic glasses," *J Alloys Compd*, vol. 625, pp. 318–322, 2015, doi: https://doi.org/10.1016/j.jallcom.2014.09.166.

[240] M. Q. Jiang, Z. Ling, J. X. Meng, J. B. Gao, and L. H. Dai, “Nanoscale periodic corrugation to dimple transition due to ‘beat’ in a bulk metallic glass,” *Scr Mater*, vol. 62, no. 8, pp. 572–575, 2010, doi: https://doi.org/10.1016/j.scriptamat.2009.12.046.

[241] S. Hasani, P. Rezaei-Shahreza, A. Seifoddini, and M. Hakimi, “Enhanced glass forming ability, mechanical, and magnetic properties of Fe41Co7Cr15Mo14Y2C15B6 bulk metallic glass with minor addition of Cu,” *J Non Cryst Solids*, vol. 497, pp. 40–47, 2018, doi: https://doi.org/10.1016/j.jnoncrysol.2018.05.021.

[242] H. Huang *et al.*, “Note: A novel rotary actuator driven by only one piezoelectric actuator,” *Review of Scientific Instruments*, vol. 84, no. 9, p. 096105, Sep. 2013, doi: 10.1063/1.4821495.

[243] G. Deng *et al.*, “Effects of normal load and velocity on the dry sliding tribological behaviour of CoCrFeNiMo0.2 high entropy alloy,” *Tribol Int*, vol. 144, p. 106116, 2020, doi: https://doi.org/10.1016/j.triboint.2019.106116.

[244] Y. Liu, Z. Yitian, L. Xuekun, and Z. Liu, “Wear behavior of a Zr-based bulk metallic glass and its composites,” *J Alloys Compd*, vol. 503, no. 1, pp. 138–144, 2010, doi: https://doi.org/10.1016/j.jallcom.2010.04.217.

[245] W. Dong, M. Dong, D. Qian, Z. Wang, Y. Yang, and S. Zhu, “Consolidation and wear resistance of Fe based bulk metallic glass composites by spark plasma sintering,” *J Non Cryst Solids*, vol. 623, p. 122687, 2024, doi: https://doi.org/10.1016/j.jnoncrysol.2023.122687.

[246] Y. Zou *et al.*, “Ex-situ additively manufactured FeCrMoCB/Cu bulk metallic glass composite with well wear resistance,” *Tribol Int*, vol. 162, p. 107112, 2021, doi: 10.1016/j.triboint.2021.107112.

[247] N. Wang *et al.*, “Effects of Various Processing Parameters on Mechanical Properties and Biocompatibility of Fe-based Bulk Metallic Glass Processed via Selective Laser Melting at Constant Energy Density,” *Chinese Journal of Mechanical Engineering: Additive Manufacturing Frontiers*, vol. 1, no. 3, p. 100038, 2022, doi: https://doi.org/10.1016/j.cjmeam.2022.100038.

[248] W. Yuan, K. S. Chin, G. Dong, and M. Hua, “Assessment of surface wear properties with initial macro crack defects using on-line visual ferrography

and SEM methods," *Industrial Lubrication and Tribology*, vol. 67, no. 6, pp. 538–548, 2015.

[249] G. Y. Koga, G. Zepon, L. S. Santos, C. Bolfarini, C. S. Kiminami, and W. J. Botta, "Wear Resistance of Boron-Modified Supermartensitic Stainless Steel Coatings Produced by High-Velocity Oxygen Fuel Process," *Journal of Thermal Spray Technology*, vol. 28, no. 8, pp. 2003–2014, 2019, doi: 10.1007/s11666-019-00961-2.

[250] X. Hou, D. Du, K. Wang, Y. Hong, and B. Chang, "Microstructure and Wear Resistance of Fe-Cr-Mo-Co-C-B Amorphous Composite Coatings Synthesized by Laser Cladding," *Metals (Basel)*, vol. 8, no. 8, 2018, doi: 10.3390/met8080622.

[251] B. J. Martins Freitas, G. Yuuki Koga, L. C. Miguel Rodrigues, W. J. Botta Filho, S. de Traglia Amancio-Filho, and C. Bolfarini, "Ultrafine-grained stainless steel with wear-resistant nanoborides decorating grain boundaries produced by laser powder bed fusion," *Materialia (Oxf)*, vol. 34, p. 102079, 2024, doi: https://doi.org/10.1016/j.mtla.2024.102079.

[252] I. D. Marinescu, W. B. Rowe, B. Dimitrov, and H. Ohmori, "13 - Loose abrasive processes," in *Tribology of Abrasive Machining Processes (Second Edition)*, I. D. Marinescu, W. B. Rowe, B. Dimitrov, and H. Ohmori, Eds., Oxford: William Andrew Publishing, 2013, pp. 399–421. doi: https://doi.org/10.1016/B978-1-4377-3467-6.00013-6.

[253] B. J. M. Freitas, V. A. de Oliveira, P. Gargarella, G. Y. Koga, and C. Bolfarini, "Microstructural characterization and wear resistance of boride-reinforced steel coatings produced by Selective Laser Melting (SLM)," *Surf Coat Technol*, vol. 426, p. 127779, 2021, doi: https://doi.org/10.1016/j.surfcoat.2021.127779.

[254] J. H. Hsieh, C. Li, A. L. K. Tan, C. K. Poh, and N. J. Tan, "Study of oxidation and wear behaviors of (Nb,Cr)N thin films using Raman spectroscopy," *Surf Coat Technol*, vol. 177–178, pp. 299–305, 2004, doi: https://doi.org/10.1016/j.surfcoat.2003.09.008.

[255] R. Ramadoss, N. Kumar, S. Dash, D. Arivuoli, and A. K. Tyagi, "Wear mechanism of CrN/NbN superlattice coating sliding against various

counterbodies," *Int J Refract Metals Hard Mater*, vol. 41, pp. 547–552, 2013, doi: https://doi.org/10.1016/j.ijrmhm.2013.07.005.

[256] B. Biswas, Y. Purandare, A. Sugumaran, I. Khan, and P. Eh. Hovsepian, "Effect of chamber pressure on defect generation and their influence on corrosion and tribological properties of HIPIMS deposited CrN/NbN coatings," *Surf Coat Technol*, vol. 336, pp. 84–91, 2018, doi: https://doi.org/10.1016/j.surfcoat.2017.08.021.

[257] B. Biswas, Y. Purandare, I. Khan, and P. Eh. Hovsepian, "Effect of substrate bias voltage on defect generation and their influence on corrosion and tribological properties of HIPIMS deposited CrN/NbN coatings," *Surf Coat Technol*, vol. 344, pp. 383–393, 2018, doi: https://doi.org/10.1016/j.surfcoat.2018.03.009.

APPENDIX

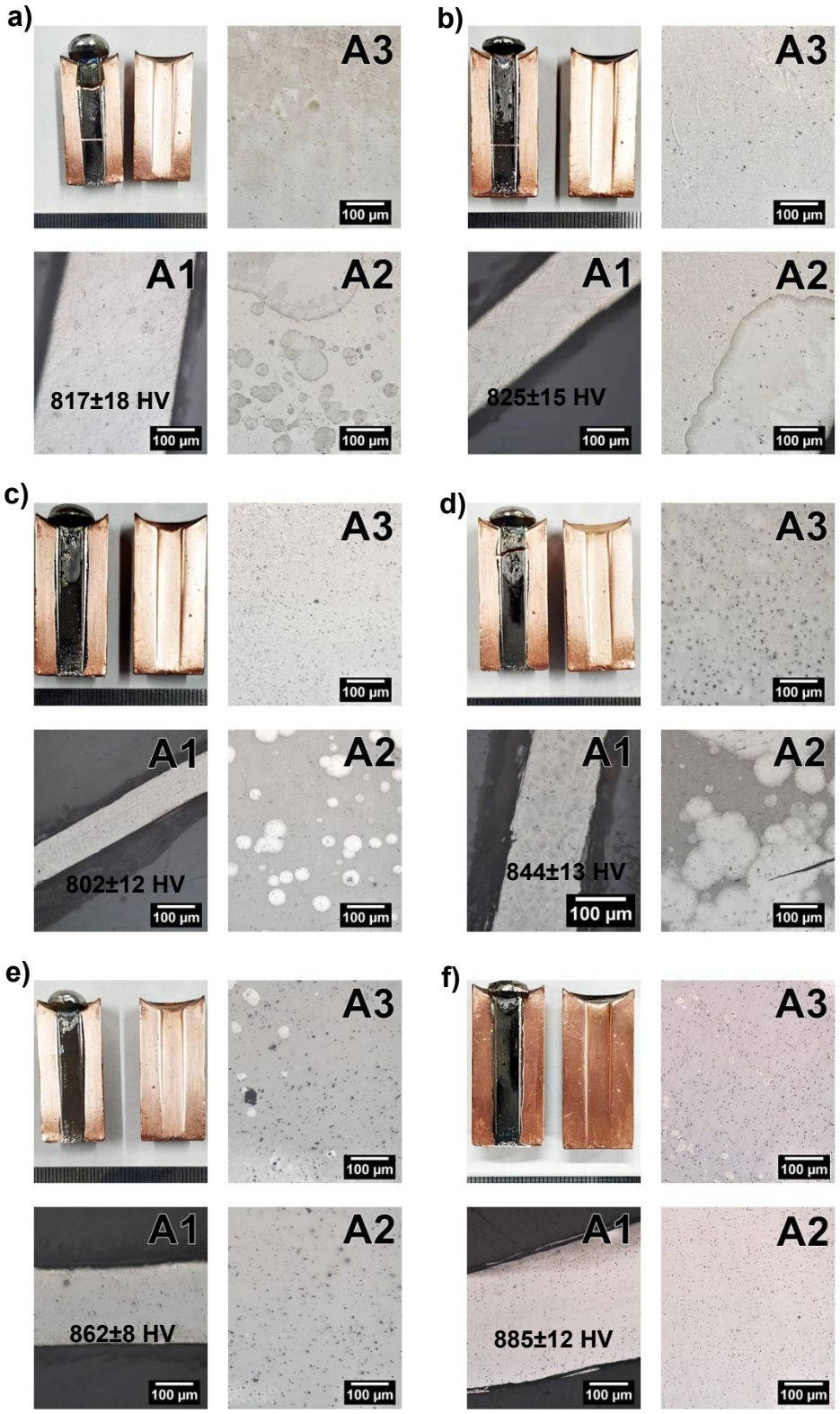

Figure A.1- Images of the wedges as-produced and microstructure by OM of the A1, A2 and A3 areas of the wedges for **a)** V1, **b)** V2, **c)** V3, **d)** V4, **e)** V5, and **f)**

V6 alloys.

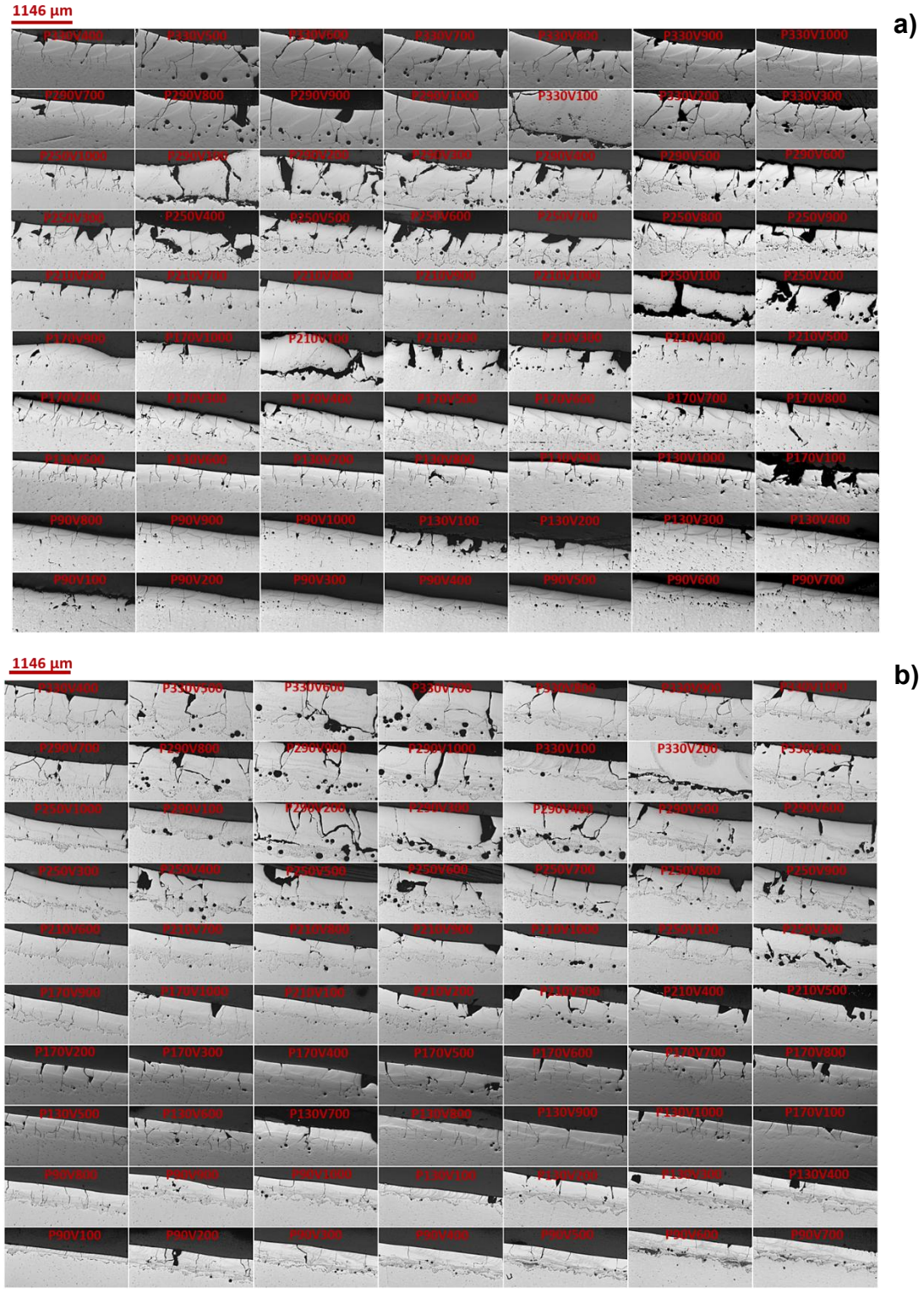

Figure A.2- Optical microscopy images of the cross-sections of LPBF samples produced using the Omnitek machine on an unheated substrate, employing a

chessboard-like scanning strategy with a remelting step, for **a)** V5 and **b)** V6 alloys.

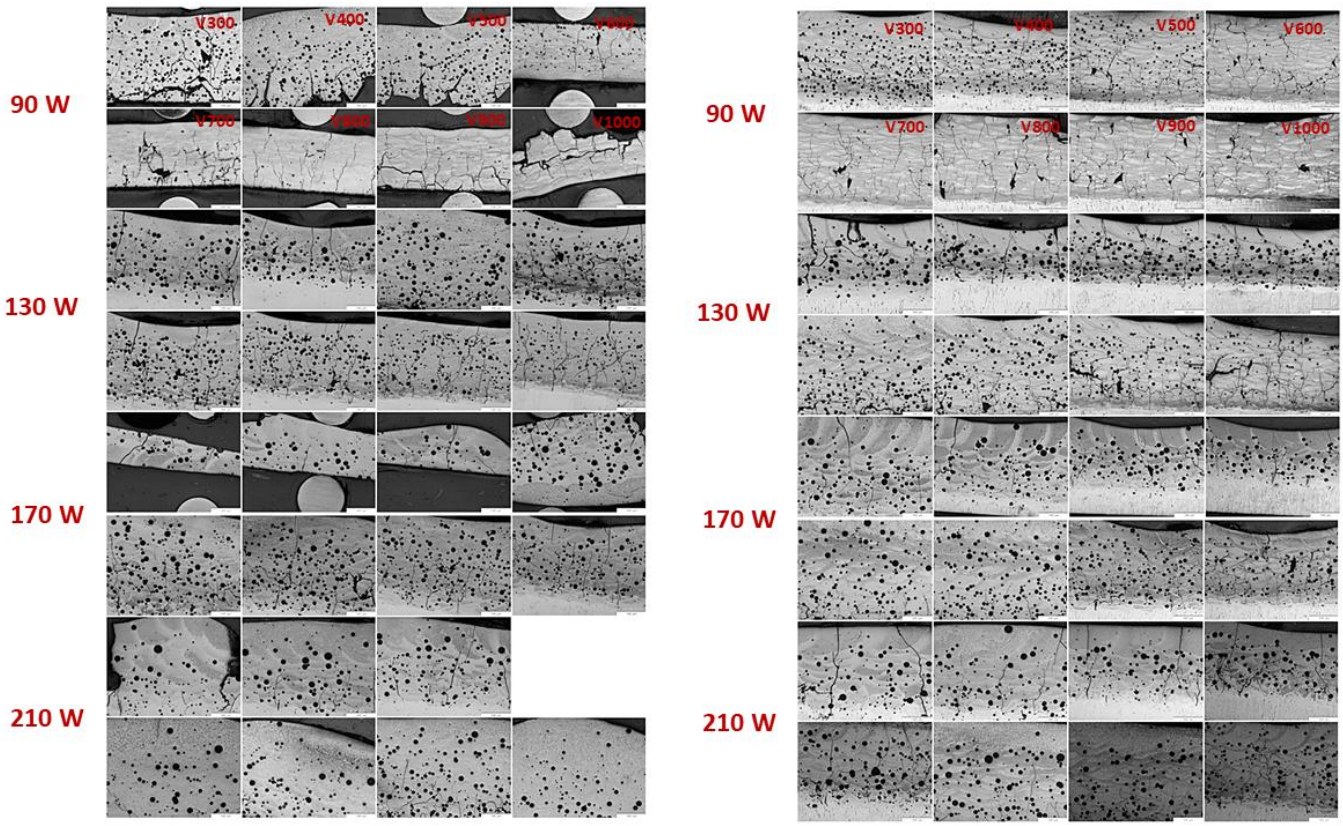

LPBF V5 samples **LPBF V6 samples**

Figure A.3- Optical microscopy images of the cross-sections of V5 and V6 LPBF samples, produced using the AconityMini machine on a heated 316L steel substrate (200 °C) with a remelting step. Scale bar: 500 µm (white bar at the lower right of the images).

1° round: Investigation of remelting, laser power, and laser scanning strategy. **Results**: All the samples were really bad regarding their integrity.	1-3: 90/700_no contour_simple79_h30_remelted 4-6: 130/700_no contour_simple79_h30_remelted 7-9: 170/700_no contour_simple79_h30_remelted 10-12: 210/700_no contour_simple79_h30_remelted 13-15: 90/700_no contour_simple79_h30_remelted_random 16-18: 130/700_no contour_simple79_h30_remelted_random 19-21: 170/700_no contour_simple79_h30_remelted_random 22-24: 210/700_no contour_simple79_h30_remelted_random 25,26: 90/700_no contour_chess5v_79_h30 27,28: 130/700_no contour_chess5v_79_h30 29,30: 170/700_no contour_chess5v_79_h30 31,32: 210/700_no contour_chess5v_79_h30 33,34: 90/700_no contour_chess5v_79_h30_remelted 35,36: 130/700_no contour_chess5v_79_h30_remelted 37,38,39: 170/700_no contour_chess5v_79_h30_remelted 40,41: 210/700_no contour_chess5v_79_h30_remelted	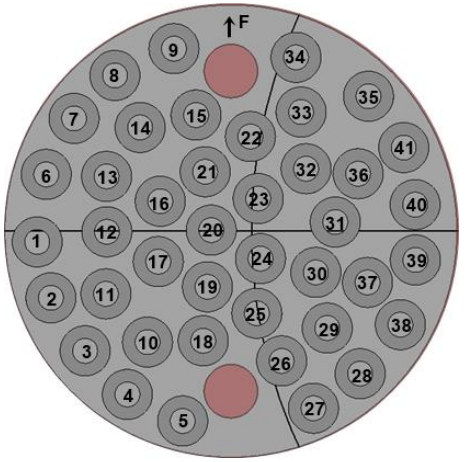	
2° round: Investigation of remelting, combination of different laser powers, and laser scanning strategies. **Results**: All the samples were bad as well.	1-3: 90/700_ 170/700_no contour_simple79_h30_remelted 4-6: 170/700_ 90/700_no contour_simple79_h30_remelted 7-9: 90/700_ 210/700_no contour_simple79_h30_remelted 10-12: 210/700_ 90/700_no contour_simple79_h30_remelted 13-15: 90/700_ 210/700_no contour_simple79_h30_remelted_random 16-18: 210/700_ 90/700_no contour_simple79_h30_remelted_random 19-21: 90/700_ 170/700_no contour_simple79_h30_remelted_random 22-24: 170/700_ 90/700_no contour_simple79_h30_remelted_random 25,26: 90/700_no contour_chess5v_79_h30 27,28: 110/700_no contour_chess5v_79_h30 29,30: 130/700_no contour_chess5v_79_h30 31,32: 150/700_no contour_chess5v_79_h30 33,34, 40: 90/700_ 90/700_ no contour_chess5v_79_h30_remelted 35,36,41: 90/700_ 130/700_ no contour_chess5v_79_h30_remelted 37,38,39: 130/700_ 90/700_ no contour_chess5v_79_h30_remelted	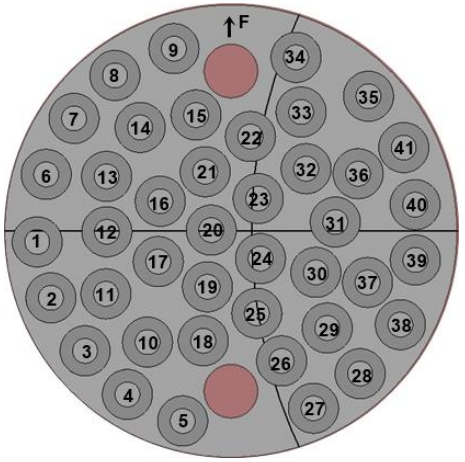	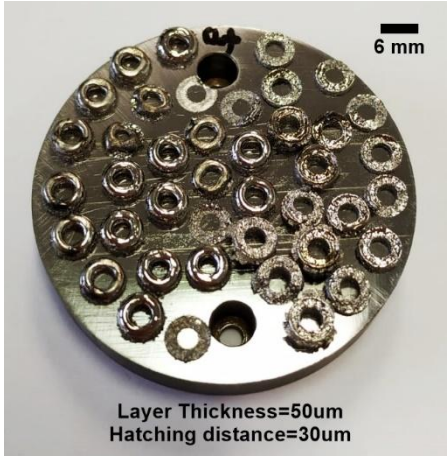

1-3: 90/700_ 170/700_no contour_simple79_h30_remelted 4-6: 170/700_ 90/700_no contour_simple79_h30_remelted 7-9: 90/700_ 210/700_no contour_simple79_h30_remelted 10-12: 210/700_ 90/700_no contour_simple79_h30_remelted 13-15: 90/700_ 210/700_no contour_simple79_h30_remelted_random 16-18: 210/700_ 90/700_no contour_simple79_h30_remelted_random 19-21: 90/700_ 170/700_no contour_simple79_h30_remelted_random 22-24: 170/700_ 90/700_no contour_simple79_h30_remelted_random 25,26: 90/700_no contour_chess5v_79_h30 27,28: 110/700_no contour_chess5v_79_h30 29,30: 130/700_no contour_chess5v_79_h30 31,32: 150/700_no contour_chess5v_79_h30 33,34, 40: 90/700_ 90/700_ no contour_chess5v_79_h30_remelted 35,36,41: 90/700_ 130/700_ no contour_chess5v_79_h30_remelted 37,38,39: 130/700_ 90/700_ no contour_chess5v_79_h30_remelted **3° round**: Investigation of the increase of the layer thickness (from 50um to 70um), using the same parameters as 2° round. **Results**: same samples presented Residual stress/distortion, super-elevation and Flaking phenomenon.	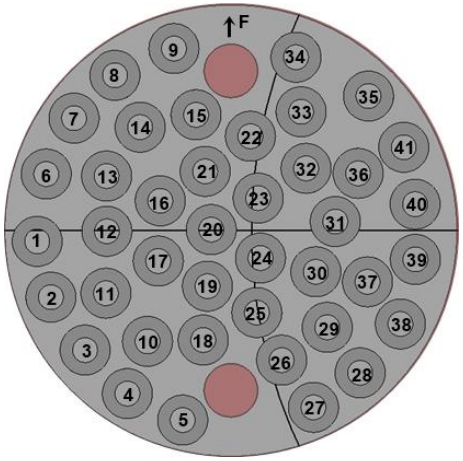	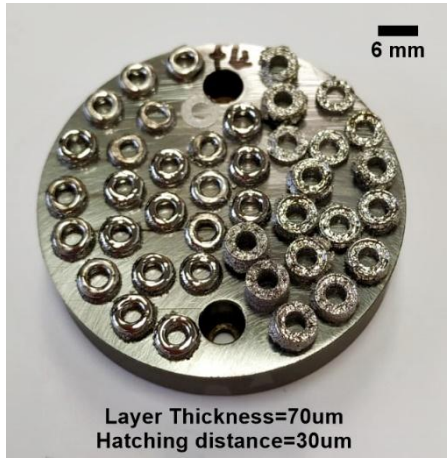
1-12: 210/700_ 90/700_nocontour_simple79_h30_remelted **13-24**: 210/700_ 90/700_nocontour_simple79_h30_remelted_random **1-3 cubes**: 210/700_ 90/700_nocontour_simple79_h30_remelted **4-6 cubes**: 210/700_ 90/700_nocontour_simple79_h30_remelted_random **4° round**: Investigation of the effect of layer thickness (from 70um to 90um), using the best parameters from the 3° round, and changing the sample geometry. **Results**: All the samples presented super-elevation.	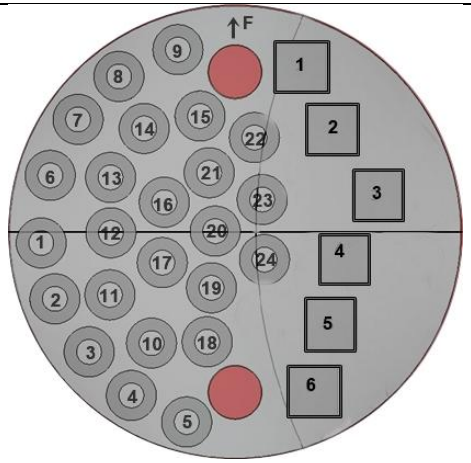	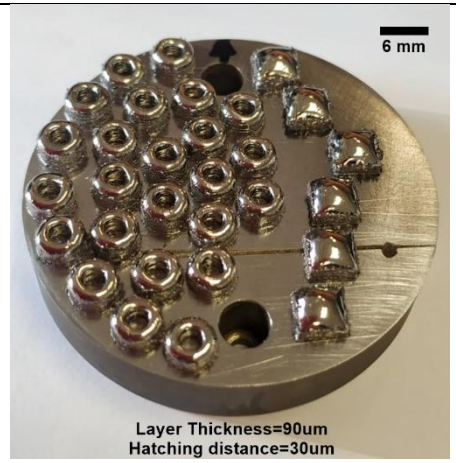

1-12: 210/700_ 90/700_nocontour_simple79_h30_remelted **13-24**: 210/700_ 90/700_nocontour_simple79_h30_remelted_random **1-3 cubes**: 210/700_ 90/700_nocontour_simple79_h30_remelted **4-6 cubes**: 210/700_ 90/700_nocontour_simple79_h30_remelted_random **5° round**: Investigation of the effect of layer thickness (from 90um to 100um), using the same geometries and parameters from the 4° round. **Results**: All the samples presented super-elevation.	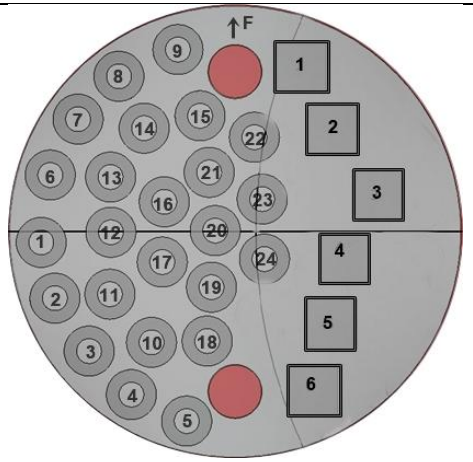	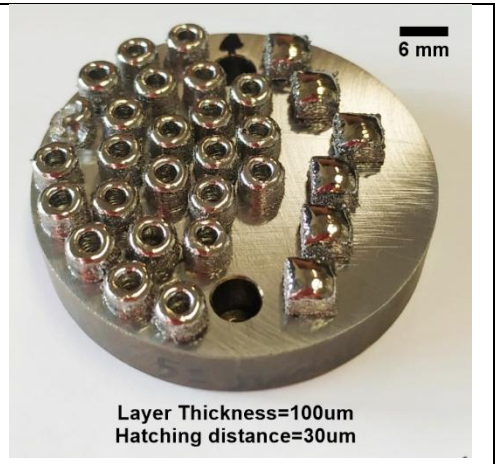
All samples were **melted** using 210w/700_single and **remelted** using 90w/700_single_random **6° round**: Investigation of the influence of hatching distance and geometries, using the best parameters from round 5°. **Results**: All the samples presented super-elevation.	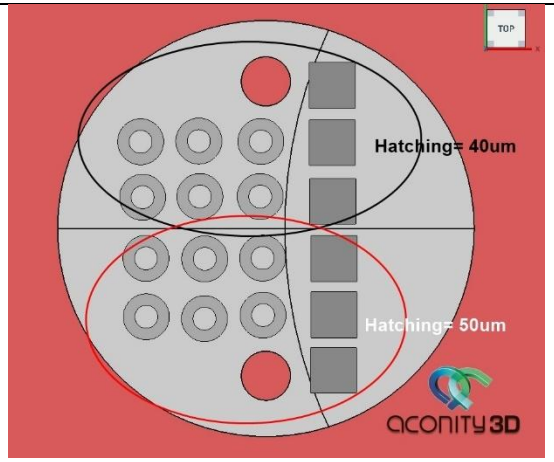	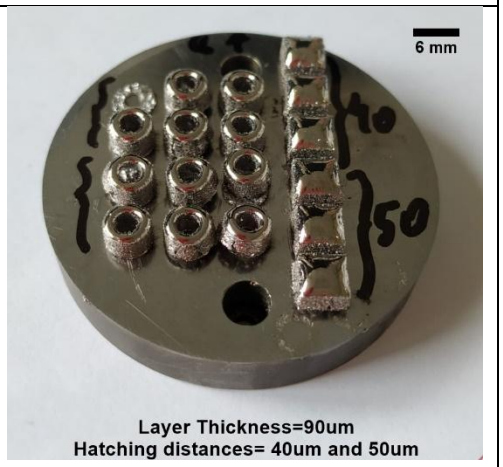

All samples were **melted** using different laser power_700mm/s_single and **remelted** using 90w_700_single_random **7° round**: Investigation of the influence of different laser power for melting, and staying with the best parameters from 6° round, with different sample sizes and geometries. **Results**: All the samples presented super-elevation, especially the small ones, and distortion, especially the big ones.	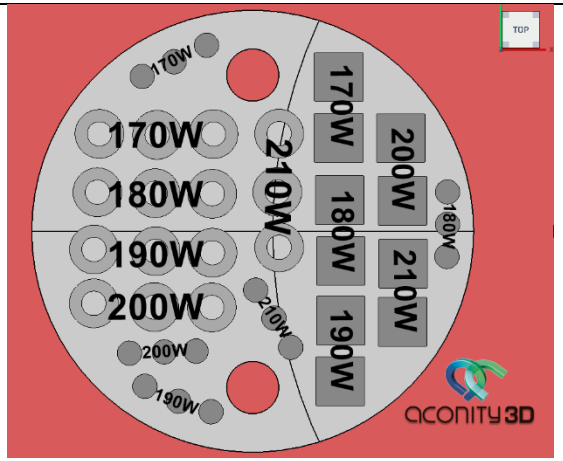	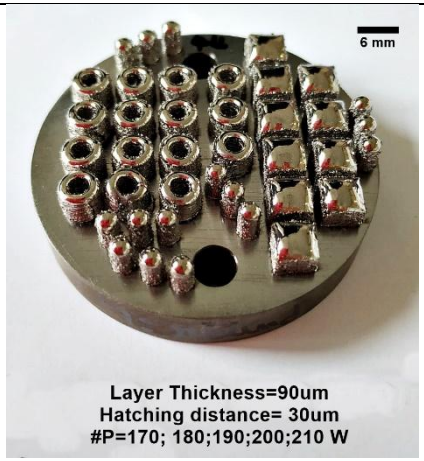
Different scan speeds for the melting **For all samples** **Melting**: 210W_single strategy **Remelting**: 90W/700_single random strategy **8° round**: Investigation of the influence of different scan speeds for melting, and staying with the best parameters from 7° round, with different sample sizes and geometries. **Results**: All the samples presented super-elevation, especially the small ones and distortion, especially the big ones.	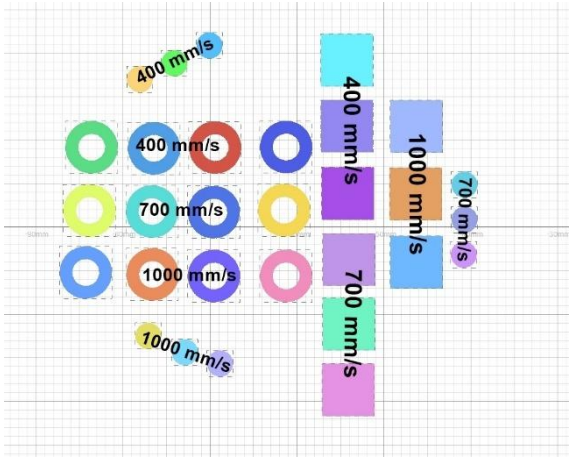	

9° round: Investigation of the influence of different scan speeds for melting and remelting, and staying with the best parameters from 8° round, different sample sizes, geometries, laser strategies and layer thickness of 100um. So far, a CK45 carbon steel substrate has been used without heating. **Results**: All the samples presented super-elevation, especially the small ones, and distortion, especially the big ones.	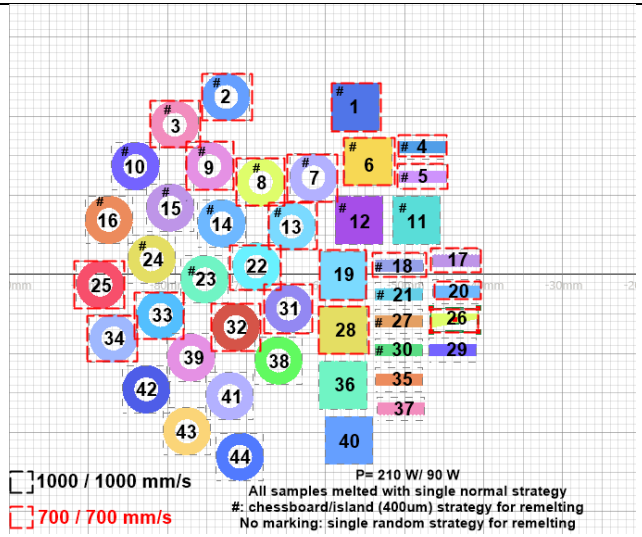	
10° round: Investigation of the influence of different scan speeds for melting and remelting, and staying with the best parameters from 9° round, different sample sizes, geometries, and laser strategies, using 316L substrate heated at 150±20°C. **Results**: All the samples presented super-elevation, especially the small ones, while distortion was decreased. Fewer cracks were observed by eyes.	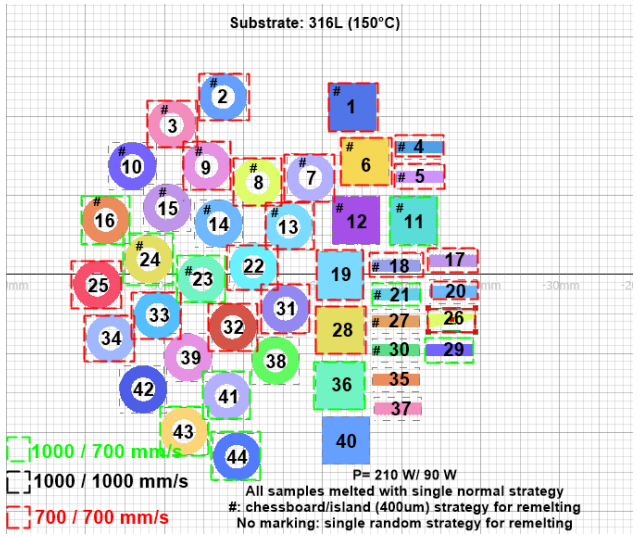	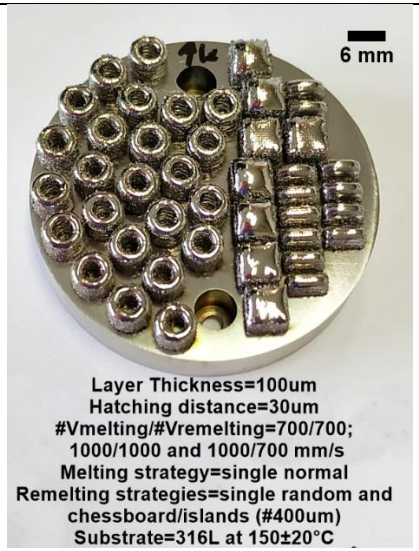

11° round: Investigation of the influence of different combinations of laser power and scan speed for melting, using the same conditions as round 10°. **Results**: All the samples presented super-elevation, especially the small ones, while distortion was decreased. Fewer cracks were observed by eyes.	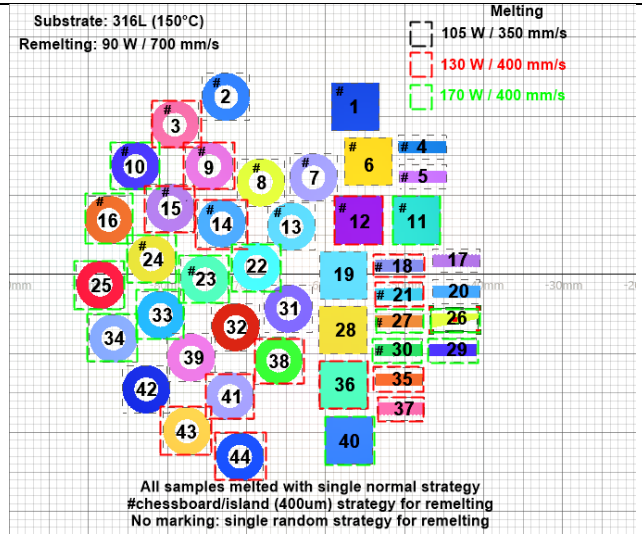	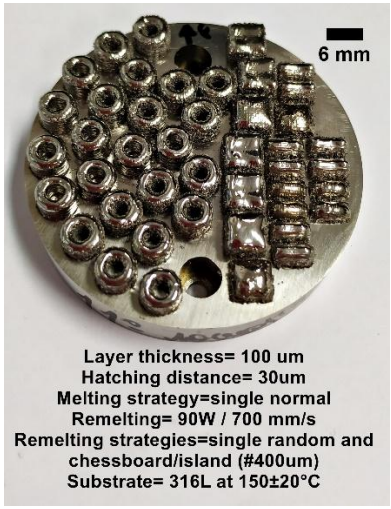
12° round: **V5** alloy powder. Investigation of the influence of different combinations of laser power and scan speed for melting, using the same conditions of round 11°. **Results**: All the samples presented super-elevation, especially the small ones, while distortion was decreased. Fewer cracks were observed by eyes.	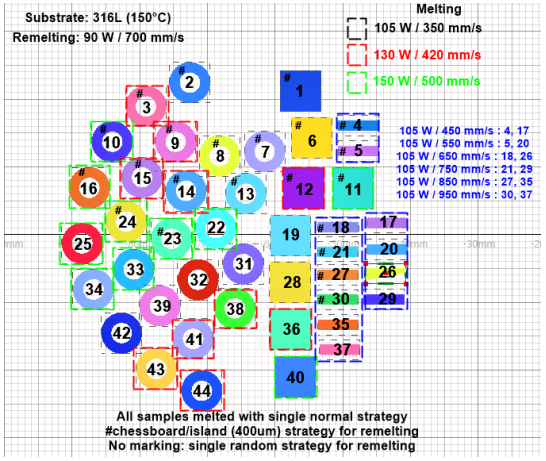	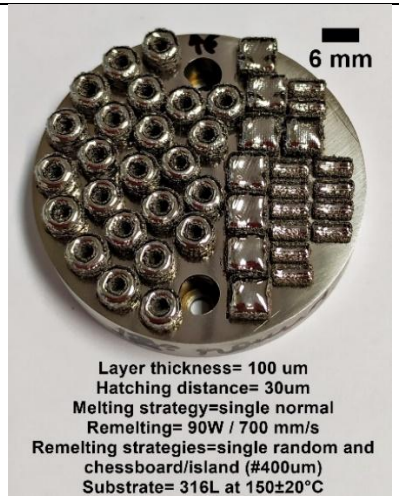

13° round: **V6** alloy powder. Investigation of the influence of different combinations of laser power and scan speed for melting. **Results**: Super-elevation was reduced but still present, especially for the small ones, while distortion was decreased. Fewer cracks were observed by eyes.	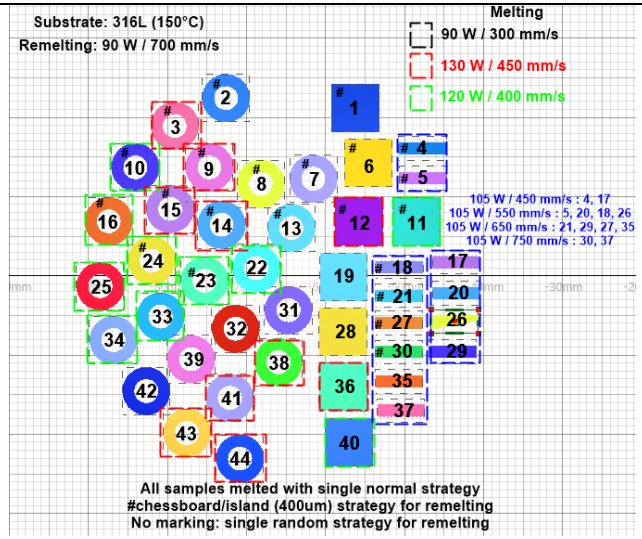	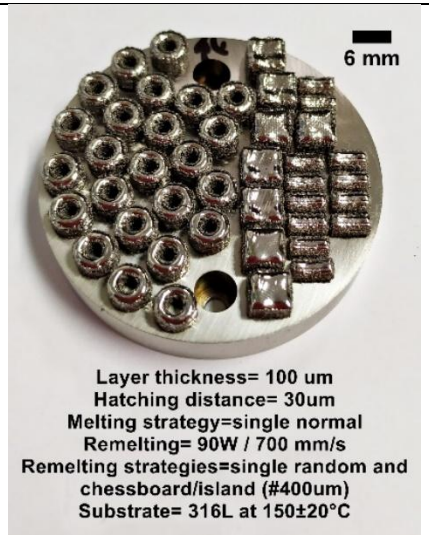
14° round: **V6** alloy powder. Investigation of the influence of different combinations of laser power and high scan speed for remelting, influence of the geometry of the samples, and the behavior of samples produced without remelting. **Results**: Super-elevation was presented only for the remelted samples, those melted with 90w_300mm/s. The samples produced without remelting were quite flat and presented many fewer cracks by eyes. Here it was proved that cylindrical samples cracked much more than square samples.	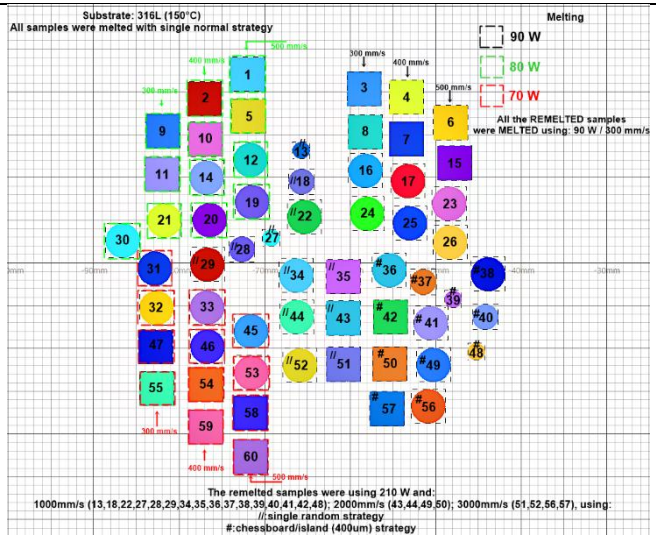	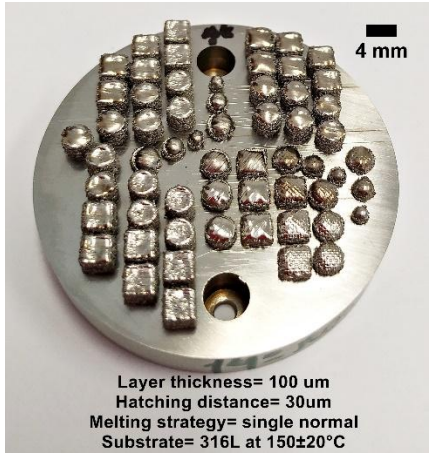

15° round: **V6** alloy powder. Investigation of the influence of different combinations of laser power and high scan speed for remelting, influence of the geometry of the samples, and the behavior of samples produced without remelting. **Results**: Super-elevation was not observed anymore. The samples produced without remelting were quite flat and presented many fewer cracks by eyes. Here was confirmed that cylindrical samples cracked much more than square samples, and they crack even more if the remelting step is used, especially with the chessboard scan strategy for remelting.	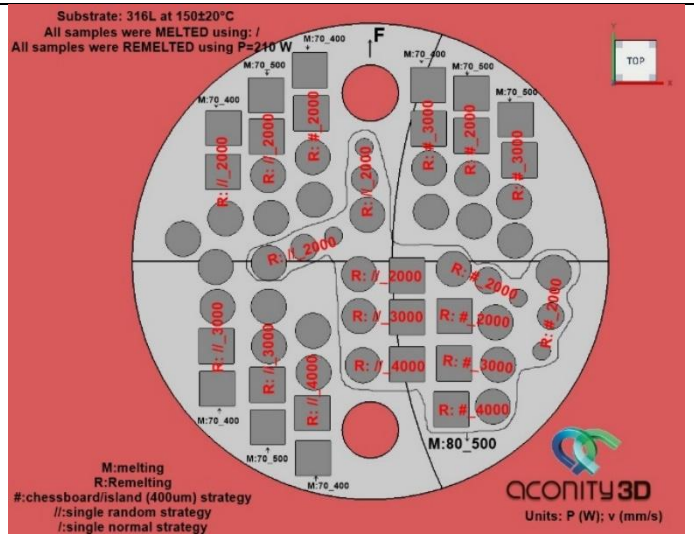	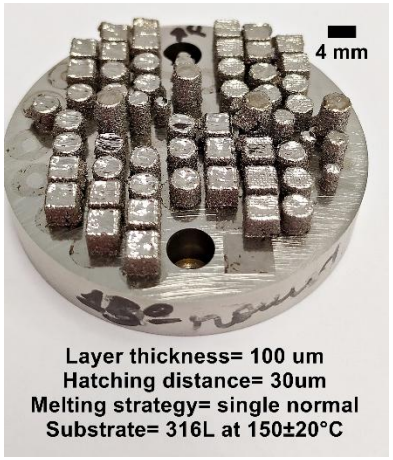
16° round: **V5** alloy powder. Investigation of the influence of different combinations of laser power and high scan speed for remelting, the effect of sample geometry, and the behavior of samples produced without remelting. **Results**: Super-elevation was no longer observed. Samples produced without remelting were relatively flat and showed significantly fewer visible cracks. It was confirmed that cylindrical samples exhibited more cracking than square ones, and this effect was exacerbated when remelting was applied—particularly with the chessboard scan strategy. Overall, samples produced without remelting demonstrated better structural integrity than those subjected to remelting.	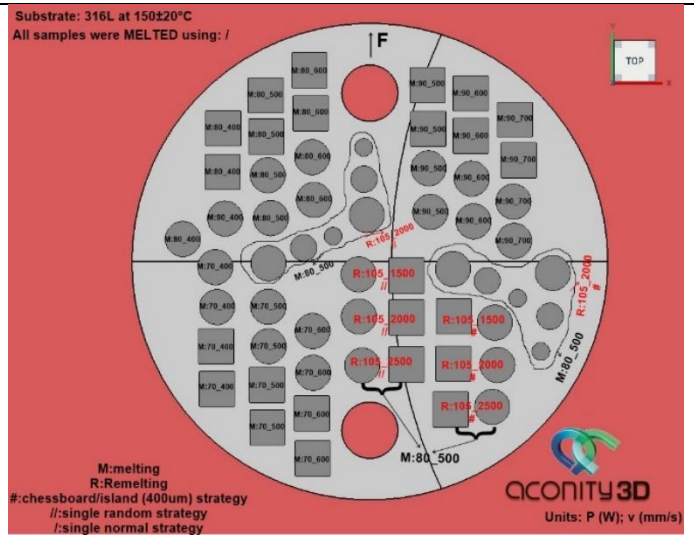	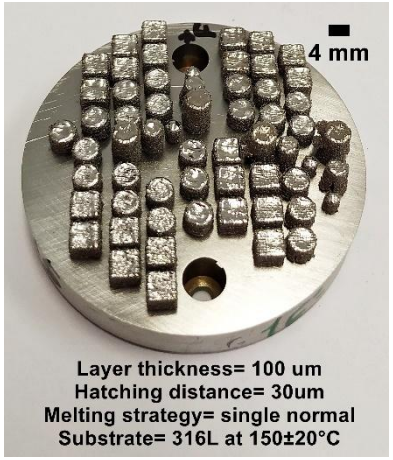

-Cubes with: 3x3x6; 4x4x8 and 5x5x10 mm at 0°, 45° and 90° related to Z axis. -Small magnetic samples 6x4 mm **17° round**: **V5** alloy powder. Printing with the best parameter combination regarding the integrity of the samples. **Results**: The samples were super flat, no cracks were observed by eye and no distortions occurred, independently of the geometry or size of the sample.	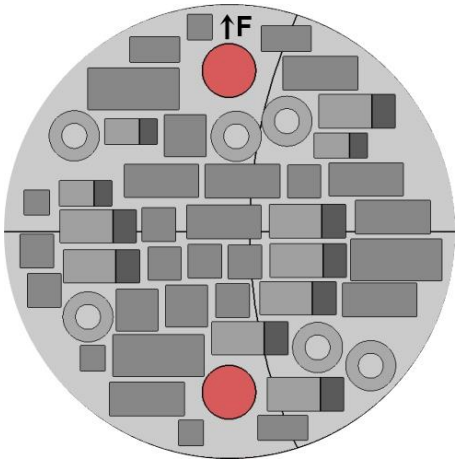	
- Cubes with: 3x3x6; 4x4x8 and 5x5x10 mm at 0°, 45° and 90° related to Z axis. - Small magnetic samples 6x4 mm **18° round**: **V6** alloy powder. Printing with the best parameter combination regarding the integrity of the samples. **Results**: The samples were super flat, no cracks were observed by the eyes and no distortions occurred, independently of the geometry or size of the sample.	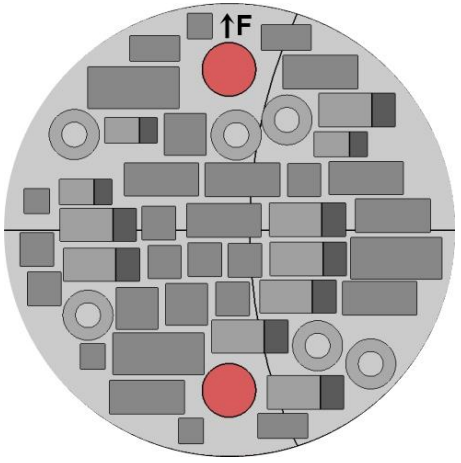 -	

- Cubes with: 3x6; 4x8 and 5x10 mm at 0°, 45° and 90° related to Z axis. - Small magnetic samples 3x4 mm **19° round**: **V6** alloy powder contaminated with oxygen. Printing with the best parameter combination regarding the integrity of the samples. **Results**: The samples were super flat, no cracks were observed by the eye and no distortions occurred, independently of the geometry or size of the sample.	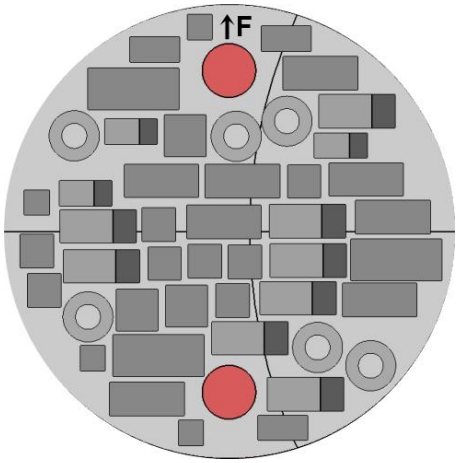 -	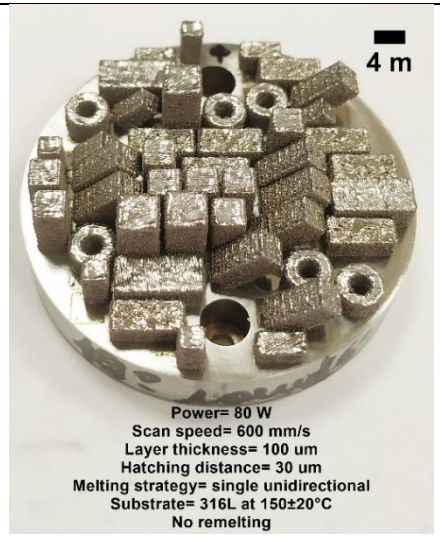
- Only cubes 4x4x8 mm and big magnetic samples 13x3 mm **20° round**: **V6** alloy powder. Printing with the two best parameter combinations with regard to the integrity of the samples. Here, big samples for magnetic measurements were printed. **Results**: The samples were super flat, no cracks were observed by eye and no distortions occurred, independently of the geometry or size of the sample.	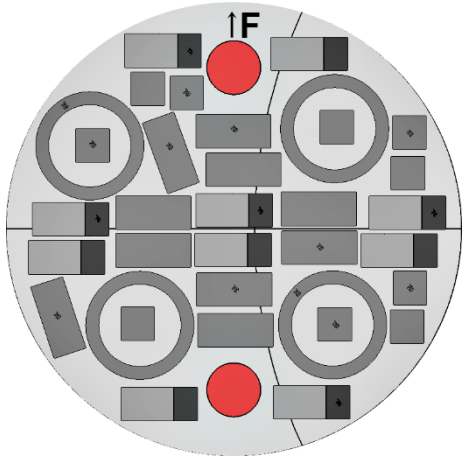	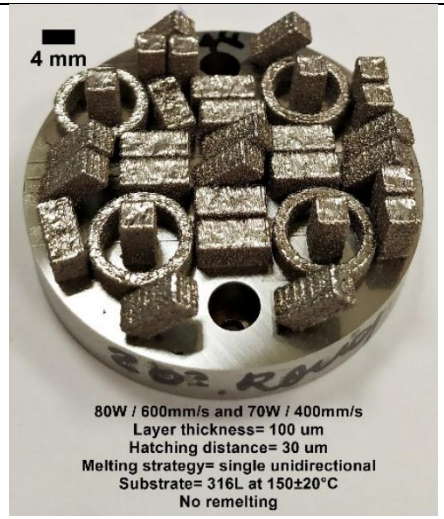

- Only cubes 4x4x8 mm and big magnetic samples 13x3 mm. **21° round**: **V5** alloy powder. Printing with the two best parameter combinations with regard to the integrity of the samples. Here, big samples for magnetic measurements were printed. **Results**: The samples were super flat, no cracks were observed by eye and no distortions occurred, independently of the geometry or size of the sample.	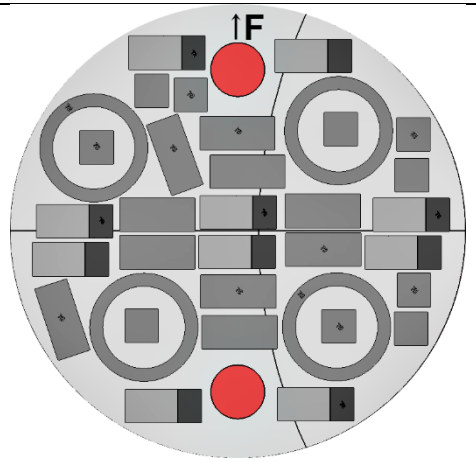	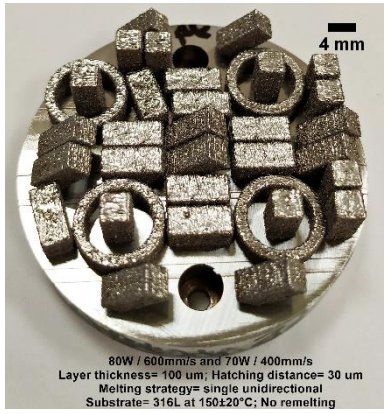
- Only cubes 4x4x8 mm and big magnetic samples 13x3 mm **22° round**: **V6** alloy powder contaminated with oxygen. Printing with the two best parameter combinations with regard to the integrity of the samples. Here, big samples for magnetic measurements were printed. **Results**: The samples were super flat, no cracks were observed by eye and no distortions occurred, independently of the geometry or size of the sample.	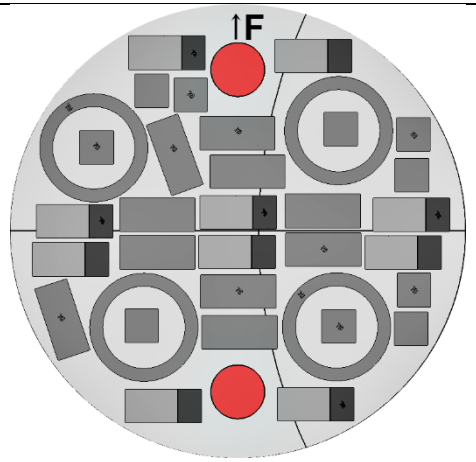	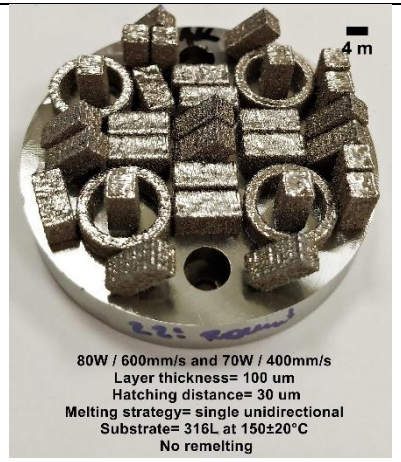

23° round: **V6** alloy powder. Printing with low laser power, with and without remelting and using different laser scan strategies. Cubes 4x4x8 mm at 0° and 90° were printed. **Results**: Samples subjected to remelting exhibited extensive cracking, with severity increasing as the remelting scan speed decreased. The use of a chessboard laser strategy for remelting resulted in particularly severe cracking.	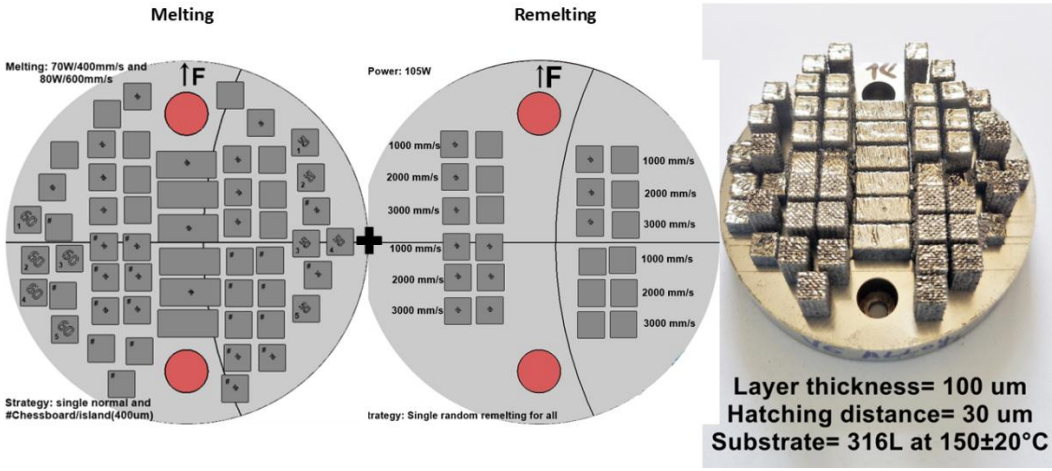
24° round: **V5** alloy powder. Printing with low laser power, without remelting and using different laser scan strategies. Cubes 4x4x8 mm at 0° and 90° were printed. **Results**: with low laser power and low scan speed, the samples are yellowish, and the finishing surface is really rough. Considering the same laser power, the high scan speed promotes more cracks.	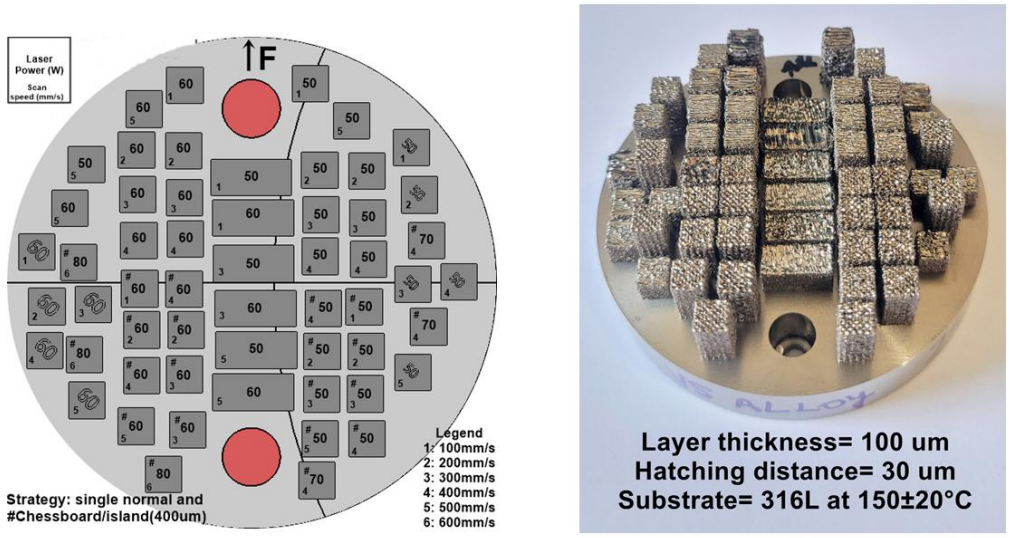

25° round: **V6** alloy powder. Printing with the best laser power (60w) combined with different scan speeds, without remelting and using different laser scan strategies. Cubes 4x4x8 mm at 0° and 90° were printed. **Results**: scan speed higher than 400 mm/s promotes cracks in the samples, especially if the chessboard strategy is used.	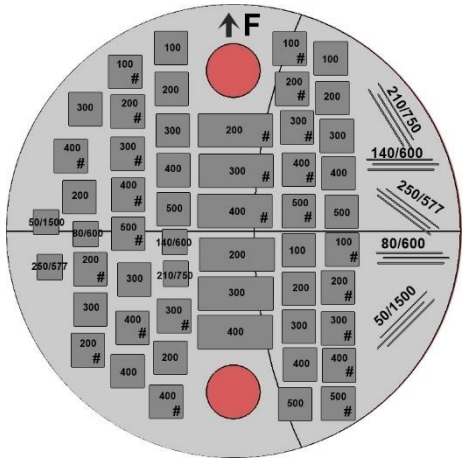	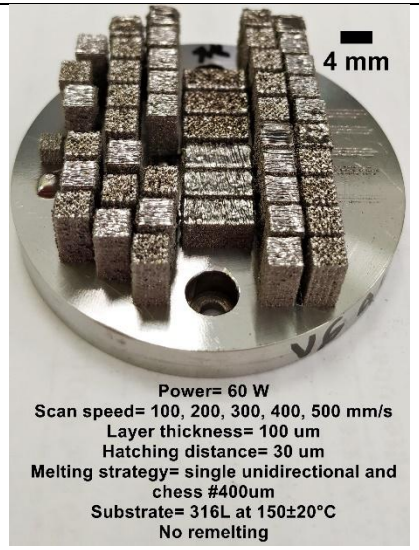
26° round: **V5** alloy powder. Printing with the best laser power (60w) combined with different scan speeds, without remelting and using different laser scan strategies. Cubes 4x4x8 mm at 0° and 90° were printed. **Results**: scan speed higher than 400 mm/s promotes cracks in the samples, especially if the chessboard strategy is used.	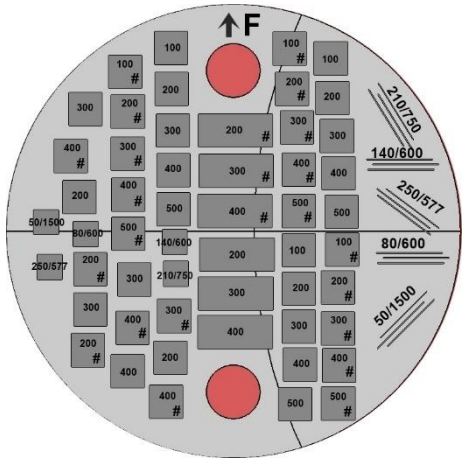	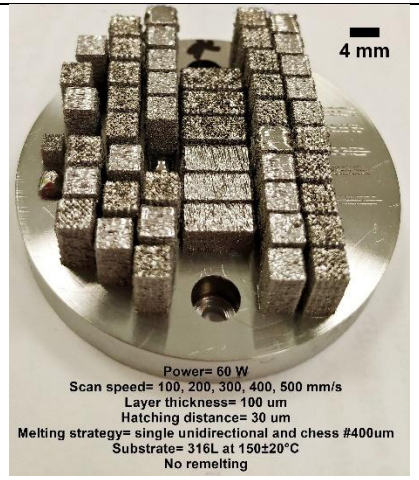

27° round: **V5** alloy powder. Printing with the same parameters used in round 26° in order to have more samples for mechanical tests. **Results**: samples with the same visual characteristics as those obtained in round 26°. Using the same combination of parameters, there are more cracks in those samples produced with a single normal laser scanning strategy than using a chessboard laser strategy.	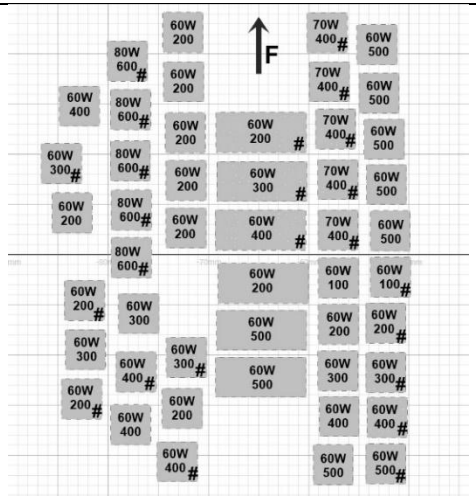	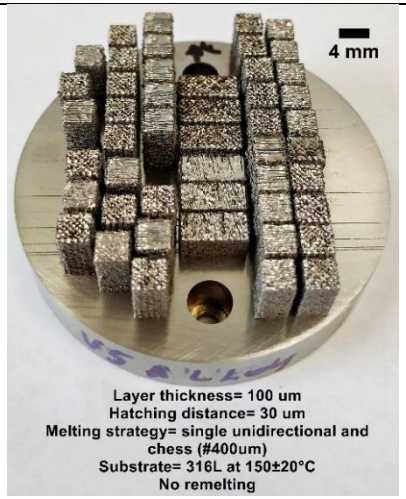
28° round: **V6** alloy powder. Printing with the best parameters in order to have more samples for mechanical tests. **Results**: Samples with similar characteristics to the samples produced previously were obtained.	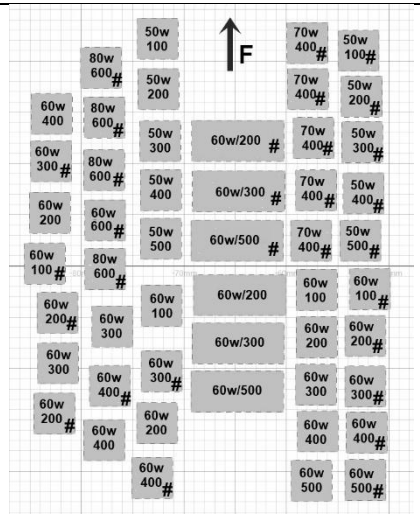	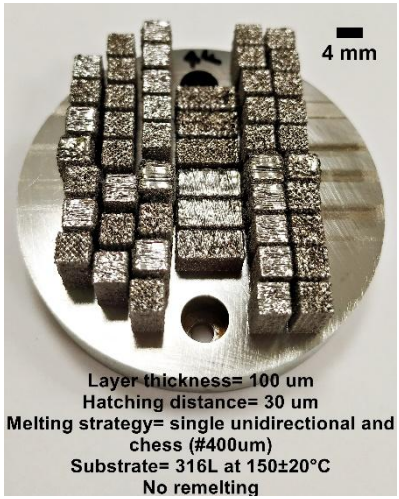

Figure A.4- LPBF sample printing rounds presented in the sequence of tested parameters, visually illustrating the influence of each parameter. Legend: **F**= direction of the fume extractor in the LPBF machine.

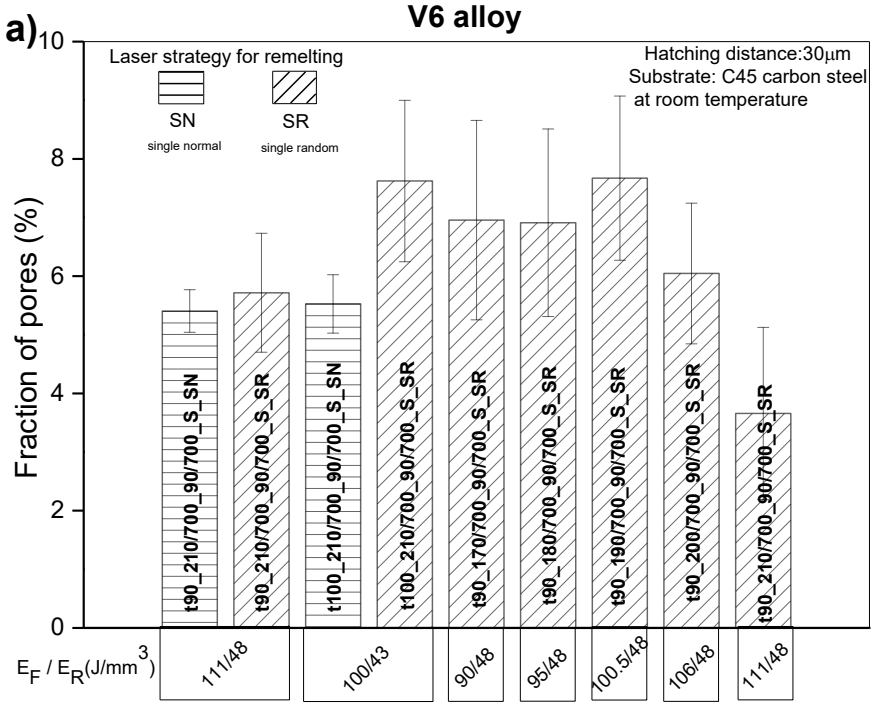
a)
V6 alloy
Laser strategy for remelting
SN
single normal
SR
single random
Hatching distance:30μm
Substrate: C45 carbon steel
at room temperature
Fraction of pores (%)
0
2
4
6
8
10
t90_210/700_90/700_S_SN
t90_210/700_90/700_S_SR
t100_210/700_90/700_S_SN
t100_210/700_90/700_S_SR
t90_170/700_90/700_S_SR
t90_180/700_90/700_S_SR
t90_190/700_90/700_S_SR
t90_200/700_90/700_S_SR
t90_210/700_90/700_S_SR
E_F / E_R(J/mm^3)
111/48
100/43
90/48
95/48
100.5/48
106/48
111/48

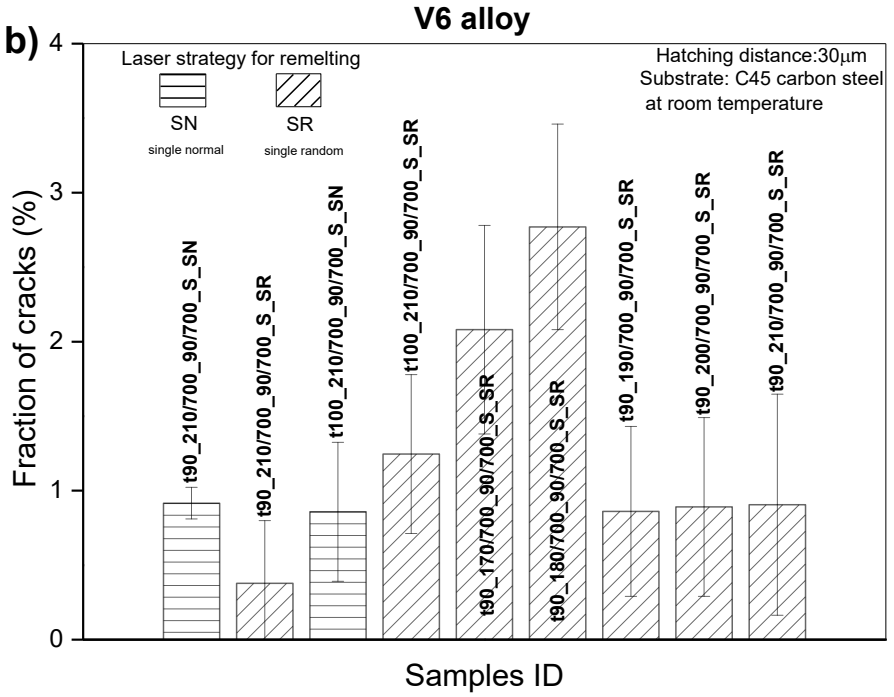
b)
V6 alloy
Laser strategy for remelting
SN
single normal
SR
single random
Hatching distance:30μm
Substrate: C45 carbon steel
at room temperature
Fraction of cracks (%)
0
1
2
3
4
t90_210/700_90/700_S_SN
t90_210/700_90/700_S_SR
t100_210/700_90/700_S_SN
t100_210/700_90/700_S_SR
t90_170/700_90/700_S_SR
t90_180/700_90/700_S_SR
t90_190/700_90/700_S_SR
t90_200/700_90/700_S_SR
t90_210/700_90/700_S_SR
Samples ID

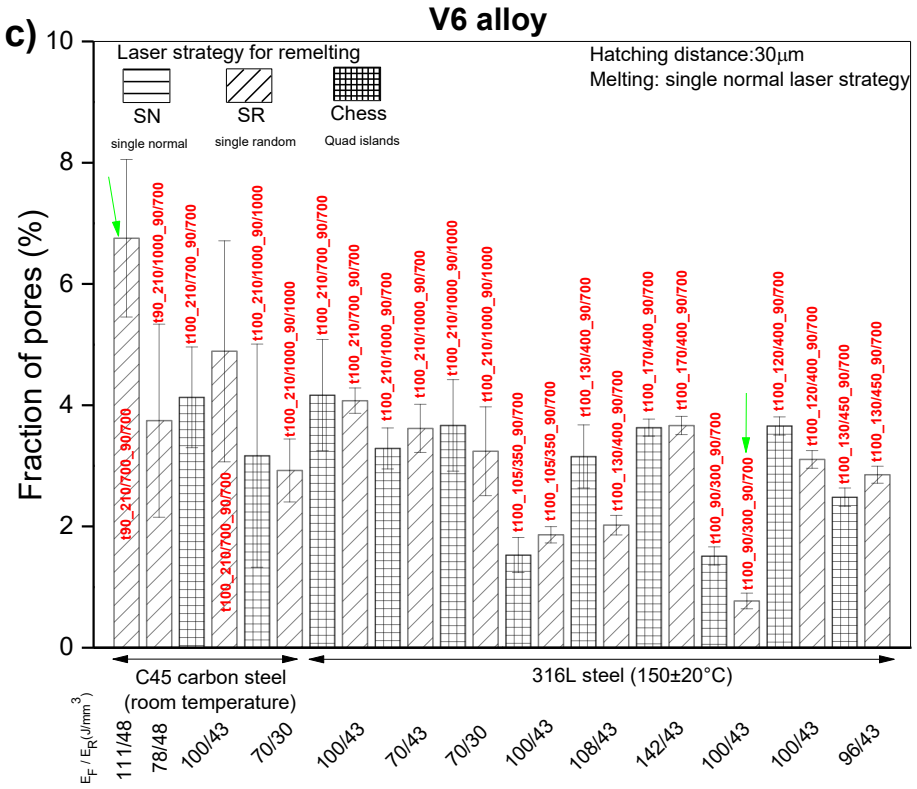
c)
V6 alloy
Laser strategy for remelting
SN
single normal
SR
single random
Chess
Quad islands
Hatching distance:30µm
Melting: single normal laser strategy
Fraction of pores (%)
0
2
4
6
8
10
t90_210/700_90/700
t90_210/1000_90/700
t100_210/700_90/700
t100_210/1000_90/700
t100_210/1000_90/1000
t100_210/700_90/700
t100_210/1000_90/700
t100_210/700_90/700
t100_210/1000_90/700
t100_210/1000_90/1000
t100_210/1000_90/1000
t100_105/350_90/700
t100_105/350_90/700
t100_130/400_90/700
t100_130/400_90/700
t100_170/400_90/700
t100_170/400_90/700
t100_90/300_90/700
t100_90/300_90/700
t100_120/400_90/700
t100_120/400_90/700
t100_130/450_90/700
t100_130/450_90/700
C45 carbon steel
(room temperature)
316L steel (150±20°C)
E_F / E_R (J/mm^3)
111/48
78/48
100/43
70/30
100/43
70/43
70/30
100/43
108/43
142/43
100/43
100/43
96/43

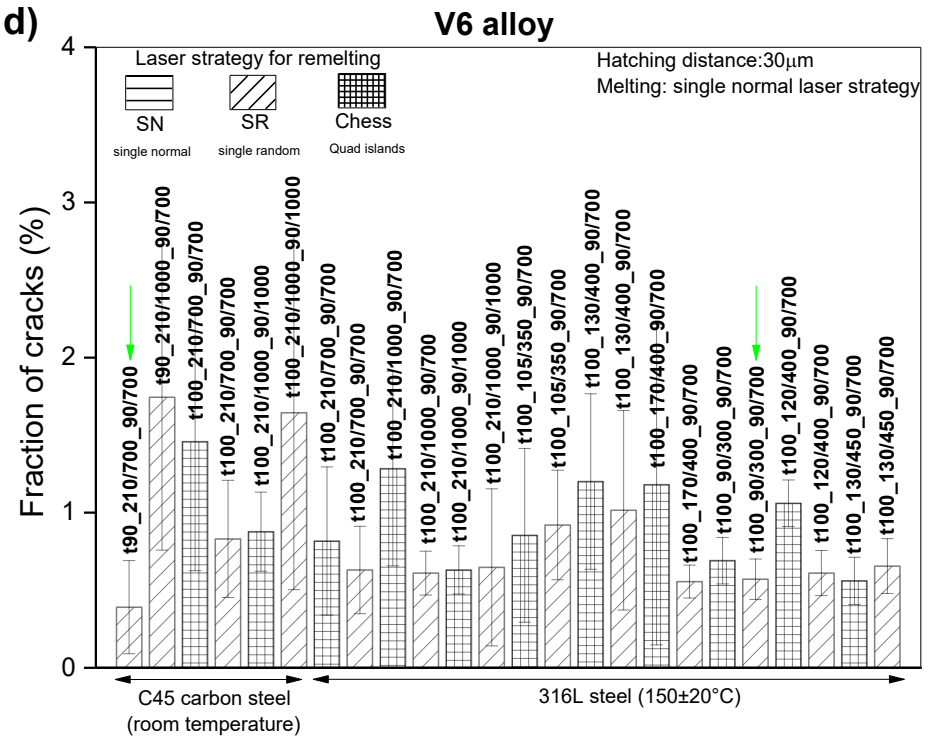
d)
V6 alloy
Laser strategy for remelting
SN
single normal
SR
single random
Chess
Quad islands
Hatching distance:30µm
Melting: single normal laser strategy
Fraction of cracks (%)
0
1
2
3
4
t90_210/700_90/700
t90_210/1000_90/700
t100_210/700_90/700
t100_210/700_90/700
t100_210/1000_90/1000
t100_210/1000_90/1000
t100_210/700_90/700
t100_210/700_90/700
t100_210/1000_90/700
t100_210/1000_90/700
t100_210/1000_90/1000
t100_105/350_90/700
t100_105/350_90/700
t100_130/400_90/700
t100_130/400_90/700
t100_170/400_90/700
t100_170/400_90/700
t100_90/300_90/700
t100_90/300_90/700
t100_120/400_90/700
t100_120/400_90/700
t100_130/450_90/700
t100_130/450_90/700
C45 carbon steel
(room temperature)
316L steel (150±20°C)

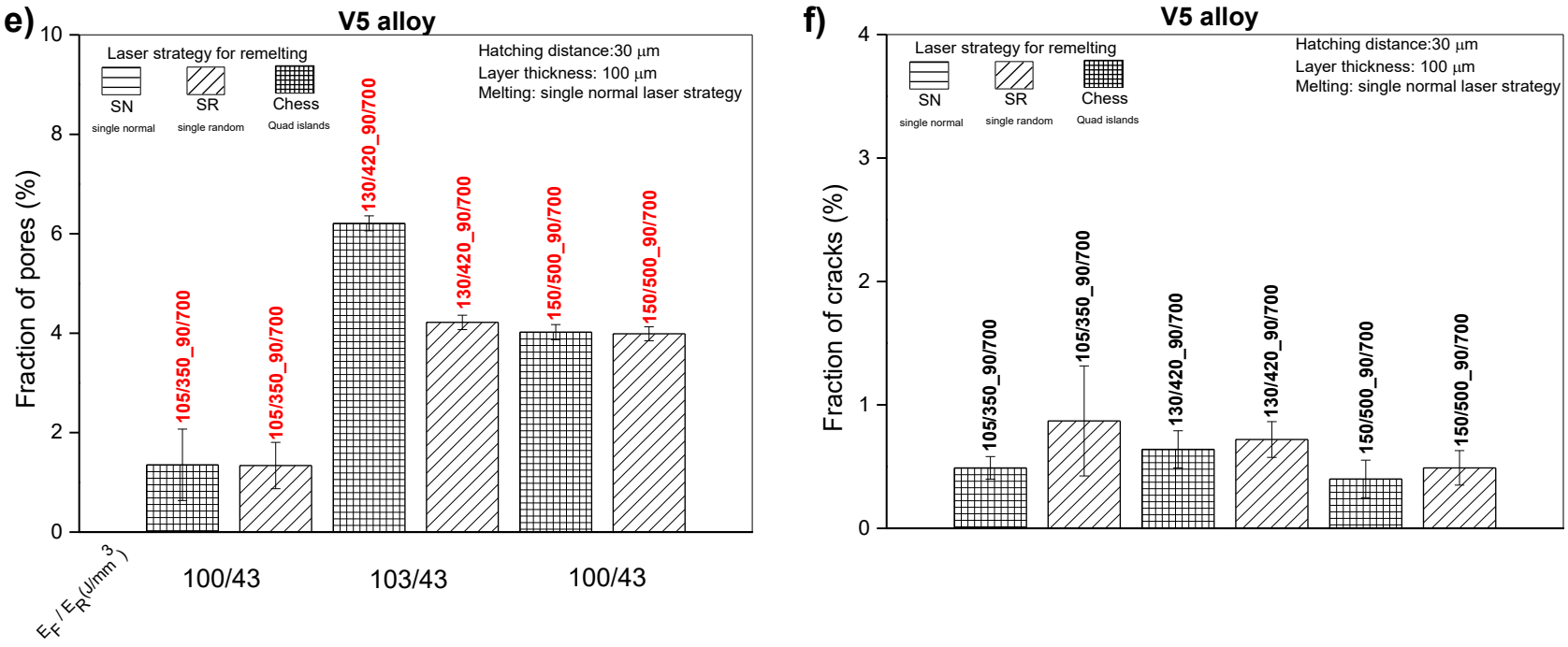

Figure A.5 - Fraction of pores (**a, c, e**) and cracks (**b, d, f**) in the first group of intact samples for V5 and V6 alloys.

Image Analysis Procedure for Measuring Pores or Cracks Using ImageJ/Fiji (WEKA)

⚙️ Initial Setup (First Sample Only)

- Open the image in ImageJ or Fiji.
- Load the image by dragging it into ImageJ/Fiji.
- Select the entire sample area using the Freehand Selections Tool.
- Go to: Edit → Clear Outside, then: Image → Crop
- Convert image type: Image → Type → 16-bit
- Open the segmentation plugin: Plugins → Segmentation → Trainable Weka Segmentation
- Rename classes:
  - Class 1: Rename to Pores or Cracks
  - Class 2: Rename to Matrix (Without Pores/Cracks)
- Train the classifier:
  - Select 5 to 8 pores or cracks and add them to the Pores or Cracks class.
  - Select 5 to 8 defect-free areas (no pores or cracks) and add them to the Matrix class.
- Click Train Classifier (wait for it to finish training).
- If needed, refine class selections and retrain the classifier.
- Click Create Result.
- Convert result to 16-bit: Image → Type → 16-bit
- Set threshold: Image → Adjust → Threshold
- Analyze features: Analyze → Analyze Particles
  - Circularity: 0.00–1.00
  - Check the box “Exclude on edges” → Only check this if you're analyzing pores, not cracks.
- In the Summary window, record the total percentage of area occupied by pores or cracks.
- Save your results (e.g., % of defects).
- Save the trained classifier: Save Classifier

🔁 For Subsequent Samples

- Open and load the next image in Fiji.
- Repeat the following steps:
  - Select the whole sample with Freehand Selections → Edit → Clear Outside → Image → Crop
  - Convert image: Image → Type → 16-bit
- Load the saved classifier: Plugins → Segmentation → Trainable Weka Segmentation → Load Classifier
- Optionally, check the selection quality with Toggle Overlay.
- Click Create Result and wait for it to finish.
- Convert result to 16-bit: Image → Type → 16-bit
- Set threshold: Image → Adjust → Threshold
- Analyze particles: Analyze → Analyze Particles
  - Circularity: 0.00–1.00
  - Check “Exclude on edges” → only if analyzing pores
- Record the total area % of defects from the Summary window.
- Save your results and classifier if updated: Save Classifier

🔁 Notes on Improving the Classifier

You can keep improving your AI model by:
- Adding more regions to the classes.
- Adjusting for sample-to-sample variations.

Just don’t forget to save the classifier after making changes: → Save Classifier